Development of a bifunctional oxygen electrode for Zn/Air batteries

Dissertation zur Erlangung des Doktorgrades

Doktor der Naturwissenschaftem (Dr. rer. nat.)

an der Fakultät für Naturwissenschaften der Universität Ulm

vorgelegt von

Emanuele Marini

Ulm, 2021

Amtierender Dekan: Prof. Dr. Thorsten Bernhardt

Erste Gutachter: Prof. Dr. Werner Tillmetz

Zweiter Gutachter: Prof. Dr. Carsten Streb

Datum der Promotionsprüfung: 29.06.2021

Erklärung/Declaration

Ich versichere hiermit, dass ich die Arbeit selbständig angefertigt habe und keine anderen als die angegebenen Quellen und Hilfsmittel benutzt sowie die wörtlich oder inhaltlich übernommenen Stellen als solche kenntlich gemacht habe und die Satzung der Universität Ulm zur Sicherung guter wissenschaftlicher Praxis in der jeweils gültigen Fassung beachtet habe.

I declare that I prepared this doctoral thesis independently and did not use any sources or means other than those indicated by me and, furthermore, I cited the passages where I quoted or referred to works by other people and their contents and I comply with the Statutes of Ulm University on Safeguarding Good Scientific Practice in the applicable version.

Ulm,

……

Abstract

Economic viability of the electrochemical stationary storage of electricity produced by intermittent renewables is the bottleneck for a transition towards a fully green energy landscape. Abundance, inexpensiveness and facile preparation for novel active materials and performant electrodes facilitate scale-up and costs lowering upon their further integration into already existing manufacturing processes. Herein, we demonstrate the relevance of a low-cost approach and a design strategy for the preparation of an efficient material for bifunctional O_2 electrocatalysis, and detail its further embedding into a gas diffusion electrode (GDE) architecture tested under relevant load conditions for rechargeable zinc-air battery application. One of the most promising ORR electrocatalyst, α-MnO_2, was synthetized through a microwave-assisted hydrothermal process, which delivered highly reproducible, rapid and scalable synthesis products. The physical, chemical and electrochemical properties of the electrocatalyst were then investigated. The synthetized α-MnO_2 was further combined with commercially available carbon black and Ni/NiO nanoparticles to create the bifunctional catalyst composite. A systematic optimization of the surface concentration of the most active catalytic ensemble and synergetic effects for both oxygen reduction and oxygen evolution reactions, taken separately, shapes the design of a bifunctional electrocatalyst. Performances of GDEs surpass the vast majority of the previous concepts, with stable overpotentials (ca. 0.35 V for each reaction, 55 % energy efficiency) over 400 h at 20 $mAh \cdot cm^{-2}$ load cycles (for both charge and discharge), bridging the gap between promising electrocatalyst material and realistic functional electrode. Finally, this thesis investigates the different degradation processes occurring at the GDE under successive charge/discharge current loads, and of their interactions/relationships. This study reveals the interplay between the four major degradation processes that contribute to the deterioration of the ORR/OER electrocatalysts and ultimately to the overall GDE failure: i) chemically- and (partially electrochemically)-driven degradation of the polytetrafluoroethylene binder component, ii) incremental surface restructuring of the Ni/NiO nanoparticles, iii) formation of carbonate / hydrogen carbonate through oxidation of the carbon component, iv) pore clogging of the GDE by potassium carbonate / hydrogen carbonate formed by the reaction of the alkaline electrolyte with the CO_2 from the ambient air. Last, this work provides a roadmap of where to act/leverage for enhancing the stability of the electrode, in which the composition should be tailored according to the specific application.

Parts of this dissertation have already been published in [E. Marini, L. Jörissen, S. Brimaud, Rational design of a low-cost, durable and efficient bifunctional oxygen electrode for rechargeable metal-air batteries, J. Power Sources. 482 (2021) 228900. https://doi.org/10.1016/j.jpowsour.2020.228900]. © 2020 Elsevier B.V. Reuse under author rights.

Table of Contents

1. Introduction 1

1.1. Overview of batteries chemistries and their applications 3

1.2. Zn-air batteries 13

1.2.1. Parameters affecting the operating cell voltage 17

1.2.2. Designing principles of the gas diffusion electrode 21

1.2.3. Benchmarking the GDE performance 23

1.3. Oxygen electrocatalysis 25

1.3.1. Theoretical insights on the oxygen reduction (ORR) and oxgen evolution (OER) reactions 25

1.3.2. The ideal bifunctional eletrocatalyst 34

1.4. Research objectives 36

2. Experimental Methods 39

2.1. Microwave-assisted synthesis of α-MnO_2 39

2.2. Physical and chemical characterization methods 40

2.2.1. X-ray powder diffraction (XRD) 40

2.2.2. Inductively coupled plasma-optical emission spectroscopy (ICP-OES) 41

2.2.3. Brunauer-Emmett-Teller (BET) analysis via N_2 adsorption isotherms 41

2.2.4. Scanning electron microscopy (SEM) 42

2.2.5. X-ray photoelectron spectroscopy (XPS) 44

2.2.6. X-ray absorption spectroscopy (XAS) 45

2.3. Electrochemical techniques and electrode preparation methods 49

2.3.1. Rotating disk (RDE) and ring disk (RRDE) electrode methods 49

2.3.2. GDE Testing 53

2.3.3. Electrochemical setup for *in operando* XAS 56

3. Results and Discussion 59

3.1. Synthesis and chemical-physical characterization of α-MnO_2 59

3.2. A Comprehensive study on the ORR activity and selectivity of α-MnO_2/C catalyst composite via RDE and RRDE techniques 65

3.3. Optimization of a ternary catalyst composite for enhanced ORR and OER activities 74

3.3.1. Physical-chemical characteristics of the catalyst materials 74

3.3.2. Electrocatalytic properties of binary mixtures 76

3.3.3. Design, activity and stability of the performances of the bifunctional catalyst materials 84

3.3.4. ORR/OER activities comparison with commercial MnO_2 88

3.4. Architecting and performances of gas diffusion electrode 91

3.5. The influence of aging on the air electrode components 102

3.5.1. Electrode performance and stability upon galvanostatic charge-discharge 102
3.5.2. Insights on the processes during the electrode aging from EIS and SEM 104
3.5.3. Insights on electrode components degradation from ex-situ XPS and in operando XANES investigations 108
3.6. Monitoring the structural and electronic changes of the α-MnO_2 under battery application condition via operando extended X-ray absorption fine structure (EXAFS) analysis 119
3.6.1. *In operando* EXAFS investigation of the α-MnO_2 GDE component 119
3.6.2. Probing oxidation state and local structural changes at the α-MnO_2 surface via differential EXAFS analysis 125
3.7. Mapping of the different degradation processes occurring at the GDE under successive charge/discharge current loads 132
4. Conclusion and outlook 135
5. References 137
6. Annex 154
Curriculum Vitae 183
List of Publications 185
Posters 185
Oral Contributions 186

1. Introduction

With growing world population and expanding industrialization, over the past decade global generation of electricity has grown rapidly. Since 2013, gross annual electricity production exceeded 18 TW, of which fossil resources (coal, oil, and gas) accounted for approximately 80 % of global electricity generation[1]. Furthermore, the global electric power demand is projected to further increase to 24 or 26 TW in 2040, with a corresponding increase in CO_2 emission from 32 Gt in 2013 to 37 or 44 Gt in 2040[2,3]. To meet the goal of reducing carbon dioxide emissions, future generation of electricity must advance through decreased dependence on fossil fuels, increasing the use of renewable energy resources (such as solar, wind and hydroelectric power), and improved environmental regulation. However, the intermittent nature of most renewable energy sources poses a major challenge in energy production and load balance management, which are of crucial importance in ensuring the stability and reliability of the power grid. Electrical energy storage may not be the answer for all the global energy concerns, but it provides a well-established solution to improve the grid stability and use. Electrical energy storage (EES) technology is the process of energy conversion from one form (mainly electrical energy) to a storable one, which can be then converted back into electricity when needed. The available energy storage solutions for stationary applications can be categorized into five types: mechanical (pumped hydroelectric storage, compressed air energy storage and flywheels), electrical (capacitors and superconducting magnets), chemical, electrochemical (fuel cells, supercapacitors, rechargeable batteries and flow batteries) and thermal energy storage[1,3]. In general, electrochemical energy storage systems (ECES) have a variety of appealing features, such as high round-trip efficiency, versatile power and energy controls, which can satisfy different grid purposes, long cycle life and low maintenance.

Electrochemical energy storage systems can store energy using a wide range of mechanisms. ECES systems usually consist of electrochemical cells that are connected in parallel and/or in series in order to supply the required capacity and voltage when needed, respectively. These systems can be

classified in three main categories: namely i) hydrogen storage/electrocatalysis (fuel cells and electrolyzers), ii) supercapacitors and iii) secondary (rechargeable) batteries. Hydrogen uses separate processes for its production, storage and use. The electrolyzer produces hydrogen and oxygen from water by mean of electrical current. A conventional H_2 fuel cell (FC) converts hydrogen (that is typically stored in a dedicated pressurized tank) and oxygen back to water to release energy[4]. Hydrogen storage can have a very high energy density of 0.6-1.2 $kWh \cdot kg^{-1}$ among other types of ECES, and the ability to be implemented across a wide range of scales into a variety of systems, from kW to multi-MW capacity[5]. Supercapacitors store energy through a capacitive process that takes place at the electrode-electrolyte interface, where the electrochemical double layer is formed. They can be charged significantly faster than other conventional ECES, surviving several thousands of charge-discharge cycles. They have an extremely high power density of 10 $kW \cdot kg^{-1}$, but at the cost of low specific energy density (1-30 $Wh \cdot kg^{-1}$[6]), as well as high dissipation rates of 5-40 $\% \cdot day^{-1}$, making them best used for fast cycling applications.

A battery is another form of electrochemical storage system that stores energy within its structure through charge transfer reactions. The transfer of ions between the two electrodes happens by means of an electrolyte that usually consists of ionically conductive species. A separator, consisting of a semi-permeable membrane, is placed between the battery's electrodes. The main function of the separator is to prevent electrical short circuits while allowing the transport of ionic species throughout the cell. Once the electrodes are connected to an external load, a spontaneous redox process, which inherently dependent on the type of battery, occurs between the two electrodes. Rechargeable batteries are readily employed to regulate the fluctuations in the production of solar and wind energy. However, this type of energy storage is quite expensive, which in turn hinders its large deployment. On the other hand, due to the fast response time, modularity and scalability of numerous battery systems, a drop in costs is expected in the coming years[1]. Therefore, this sector is experiencing significant growth, with several battery installations deployed worldwide typically grid storage applications.

1.1. Overview of batteries chemistries and their applications

Lead-acid battery

The lead-acid battery is the most widely employed rechargeable battery for small-medium scale energy storage applications[5,6]. In 2008, the lead-acid battery market share of all secondary batteries worldwide was about 70 %[7]. The battery consists of a PbO_2 cathode, a Pb anode and uses sulfuric acid as electrolyte. The redox process of the lead-acid battery can be described as follows:

Eq. 1) $$\text{Anode: } Pb + SO_4^{2-} \underset{Charge}{\overset{Discharge}{\rightleftharpoons}} PbSO_4 + 2e^-$$

Eq. 2) $$\text{Cathode: } PbO_2 + SO_4^{2-} + 4H^+ + 2e^- \underset{Charge}{\overset{Discharge}{\rightleftharpoons}} PbSO_4 + 2H_2O$$

Eq. 3) $$\text{Overall reaction: } Pb + PbO_2 + 2H_2SO_4 \underset{Charge}{\overset{Discharge}{\rightleftharpoons}} 2PbSO_4 + 2H_2O$$

The nominal voltage of the lead-acid cell is 2 V[7]. A special feature of lead-acid batteries is that the electrolyte takes part of the electrode reaction (formation of $PbSO_4$). This type of battery have quick response times, small self-discharge rates, high cycling efficiency (60-90 %) and marginal capital costs, ranging from 50 to 600 $/KW·h[4,5]. Typically, this type of battery is used as stationary back-up power supply for data and telecommunication systems. Due to their relatively low cycle life (<2000 cycles), volumetric (50-90 $Wh·L^{-1}$) and gravimetric (25-50 $Wh·kg^{-1}$) energy densities, lead-acid batteries have been rarely employed as utility-scale EES. In addition, their performance is severely affected under low temperature conditions, which is why a thermal management system is normally required, thereby increasing their capital costs[1]. State-of-the-art lead-acid batteries, with rapid response times, are being recently developed and are now in the demonstration phase[1,8].

Nickel-cadmium battery

A nickel-cadmium (NiCd) battery uses metallic Cd and nickel hydroxide as anode and cathode materials, while the electrolyte is typically an aqueous alkaline solution. The charge and discharge electrochemical reactions of the NiCd battery are illustrated in the following equations:

Eq. 4) $$\text{Anode: } Cd + 2OH^- \underset{Charge}{\overset{Discharge}{\rightleftharpoons}} Cd(OH)_2 + 2e^-$$

Eq. 5) $$\text{Cathode: } NiOOH + H_2O + e^- \underset{Charge}{\overset{Discharge}{\rightleftharpoons}} Ni(OH)_2 + OH^-$$

Eq. 6) $$\text{Overall reaction: } 2NiOOH + 2H_2O + Cd \underset{Charge}{\overset{Discharge}{\rightleftharpoons}} 2Ni(OH)_2 + Cd(OH)_2$$

The nominal voltage of the NiCd cell is 1.2 V[7]. The NiCd battery is a relatively robust and reliable system and therefore requires low maintenance. The reported specific (50-75 $Wh \cdot kg^{-1}$) and volumetric (60-150 $Wh \cdot L^{-1}$) energy densities of NiCd battery type are both higher than the lead-acid battery system, as well as the cycle life is medium range (2000-3500[8,9]) The main drawback of the NiCd battery lies in the use of Cd that is an environmental hazardous element[10]. In addition, the NiCd system is also known to suffer from memory effects[1], where a significant reduction of the capacity occurs when the battery is repeatedly charged at low deep of discharge (DoD) states. It is therefore not surprising that so far very few technological developments have been made in the use of NiCd batteries for stationary EES applications on a utility scale[11].

Nickel-metal hydride battery

The working principle of nickel-metal hydride (NiMH) battery is very similar to the NiCd system, but a hydrogen adsorbing alloy is used as anode material instead of the metallic cadmium. The redox process of the NiMH battery can be described by the following reactions:

Eq. 7) $$\text{Anode: } MH + OH^- \underset{Charge}{\overset{Discharge}{\rightleftharpoons}} M + H_2O + e^-$$

Eq. 8) $$\text{Cathode: } NiOOH + H_2O + e^- \underset{Charge}{\overset{Discharge}{\rightleftharpoons}} Ni(OH)_2 + OH^-$$

Eq. 9) $$\text{Overall reaction: } MH + NiOOH \underset{Charge}{\overset{Discharge}{\rightleftharpoons}} M + Ni(OH)_2$$

The nominal voltage of the NiMH cell is 1.35 V[7]. The NiMH battery generally has specific energy (70-100 $Wh \cdot kg^{-1}$[12,13]) and volumetric energy (170-420 $Wh \cdot L^{-1}$[12,13]) densities greater than those of NiCd battery with comparable cycle durability. The advantages of NiMH batteries are also reduced memory effect and lower (improved) environmental impact (benignity) than NiCd. However, its high rate of self-discharge is the main obstacle to EES for stationary applications, where a loss of capacity of 5- 20 % occurs on the first day after charging. Finally, the NiMH is sensitive to deep DoD, which can cause a significant drop in performances after only few hundreds charge-discharge cycles[12,13].

Nickel-zinc battery

Nickel-zinc (NiZn) batteries are one of the best choices when a small, lightweight energy storage with a high-rate discharge capability is required at a significantly lower cost than a lithium-ion. It is an abuse-tolerant battery that can also replace nickel-cadmium and nickel-metal hydride batteries in most high-volume applications[7]. The redox process of the NiZn battery is described by the following equations:

Eq. 10) $$\text{Anode: } Zn + 2OH^- \underset{Charge}{\overset{Discharge}{\rightleftharpoons}} Zn(OH)_2 + 2e^-$$

Eq. 11) $\text{Cathode: } 2NiOOH + 2H_2O + 2e^- \underset{Charge}{\overset{Discharge}{\rightleftharpoons}} 2Ni(OH)_2 + 2OH^-$

Eq. 12) $\text{Overall reaction: } 2NiOOH + 2H_2O + Zn \underset{Charge}{\overset{Discharge}{\rightleftharpoons}} Zn(OH)_2 + 2Ni(OH)_2$

The NiZn battery has a nominal voltage of 1.73 V[7]. Due to its superior power density and high specific energy density, which currently ranges between 70 $Wh \cdot kg^{-1}$ and 110 $Wh \cdot kg^{-1}$, lightweight systems with high-current drains (*e.g.* power tools, lawn and garden tools, light electric vehicles) are well suited to nickel-zinc batteries. NiZn batteries have a typical cycle life of more than 900 cycles at 80 % depth of discharge, thus making them competitive with modern nickel-cadmium and lithium-ion technologies.

Lithium-ion battery

In lithium-ion batteries, common cathode materials are lithium metal oxides, such as Lithium Cobalt Oxide (LCO), Lithium Manganese Oxide (LMO), and Lithium Nickel Manganese Cobalt (NMC). More recently, Lithium Iron Phosphate (LFP) has been introduced. LFP is a comparatively inexpensive material that provides high-rate capability and long cycle life. As anode material, graphitic carbon is typically employed. These electrodes are usually impregnated with an aprotic organic liquid electrolyte where lithium salts (*e.g.* $LiClO_4$) are dissolved. The conventional Li-ion cell operates via an intercalation process, where lithium ions are intercalated and de-intercalated, in a reversible manner, into the host material without undergoing major structural transformations of the latter. During discharge, Li ions are de-intercalated from the anode and intercalated into the cathode, as indicated by the following equations:

Eq. 13) $\text{Anode: } Li_yC \underset{Charge}{\overset{Discharge}{\rightleftharpoons}} C + yLi^+ + ye^-$

Eq. 14) $\text{Cathode: } Li_{1-x}MO_2 + xLi^+ + xe^- \underset{Charge}{\overset{Discharge}{\rightleftharpoons}} LiMO_2$

Eq. 15) $$\text{Overall reaction: } \frac{x}{y}Li_yC + Li_{1-x}MO_2 \underset{Charge}{\overset{Discharge}{\rightleftharpoons}} LiMO_2 + \frac{x}{y}C$$

Where $LiMO_2$ represents the metal oxide cathode material and C corresponds the carbon-based anode material. Common values for x and y are approximately 0.5 and 0.16, respectively, and both depend on the molar capacity of the electrode materials. According to Dunn et. al[3], Li-ion batteries can deliver energy densities 2.5 times higher than other competing technologies, such as NiMH, NiCd and lead-acid batteries, while still providing high specific power. The great advantage of lithium electrochemistry resides in the combination of low negative electrode potential and low molecular weight of its ions, thus providing high-output voltages and high energy densities[3]. In addition, the small lithium ion radius is beneficial for diffusion, which is advantageous for faster reaction kinetics. Such appealing properties make the lithium-ion battery one of the best candidates for applications where rapid response time, high volumetric (250-690 $Wh \cdot L^{-1}$) and gravimetric energy (100-265 $Wh \cdot kg^{-1}$) densities matters. The latter, coupled with excellent rate capability and extended cycle life, has enabled the Li-ion battery technology to capture the market for portable electronic applications. Despite significant improvements have been made in the field of electrode materials and architectures over the last two decades, a number of key issues remain of concern. The main disadvantages of Li-ion batteries are that i) the battery pack often demands an on-board computer to maintain safe operation, thus increasing its overall capital cost (600-3800 $\$ \cdot KWh^{-1}$[5,8]), ii) battery aging is severely affected by the degree of Deep of Discharge (DoD), iii) the use of raw materials, such as lithium and cobalt. Several companies worldwide succeeded in implementing lithium-ion batteries for utility-scale applications, where Li-ion battery EES is being readily employed to balance the intermittency of wind, solar and other renewables, helping their integration into the grid[11,14–16].

Sodium-sulfur battery

This type of battery is constructed from molten sodium (Na) and sulfur (S) that are used as anode and cathode materials, respectively. The two electrodes are separated by beta-alumina solid electrolyte (BASE). Half-cell reactions and full-cell reactions of the sodium-sulfur (NaS) battery can be described by the following equations:

Eq. 16) $$\text{Anode: } 2Na \underset{Charge}{\overset{Discharge}{\rightleftharpoons}} 2Na^{+} + 2e^{-}$$

Eq. 17) $$\text{Cathode: } xS + 2e^{-} \underset{Charge}{\overset{Discharge}{\rightleftharpoons}} S_x^{2-}$$

Eq. 18) $$\text{Overall reaction: } 2Na + xS \underset{Charge}{\overset{Discharge}{\rightleftharpoons}} Na_2S_x$$

Where x ranges between 3 and 5 and with a nominal voltage of 2.076 V. This system requires operating temperatures between 300-350°C to ensure that Na and S are in their molten states[1]. The advantages of the NaS battery are i) relatively high energy densities (150-300 $Wh \cdot L^{-1}$ and 150-240 $Wh \cdot kg^{-1}$)[5,17], ii) negligible daily self-discharge, iii) use of low-cost and environmentally friendly materials, thus facilitating their recyclability (99%)[5,18]. However, high annual operating costs and the need of temperature control systems are the main drawbacks of this battery[1]. NaS battery is an emerging technology and it is considered one of the most promising candidates for high power EES applications. Today, more than 200 NaS installations have been deployed worldwide and they account for a total discharge power capacity of 315 MW[3].

Redox-flow battery

A redox-flow battery uses two circulating soluble redox couples as electroactive species, which are oxidized and reduced to store or supply energy, respectively. This device has an ion-selective membrane separating the positive and negative redox species contained in separate storage tanks. When the battery is in use, the redox-active ions undergo oxidation or reduction reactions when in

contact with or near the current collector. Ions that do not participate to the redox process (such as H^+ and Na^+) can pass through the membrane to preserve electroneutrality and balance of the electrolyte[3]. There are currently two main types of redox-flow batteries under development: zinc/bromine (1.85 V) and vanadium-redox (1.26 V) batteries[7]. The electrochemical reactions of the zinc/bromine system can be described as follows:

Eq. 19) $$\text{Anode: } Zn \underset{Charge}{\overset{Discharge}{\rightleftharpoons}} Zn^{2+} + 2e^-$$

Eq. 20) $$\text{Cathode: } Br_2(aq) + 2e^- \underset{Charge}{\overset{Discharge}{\rightleftharpoons}} 2Br^-$$

Eq. 21) $$\text{Overall reaction: } Zn + Br_2(aq) \underset{Charge}{\overset{Discharge}{\rightleftharpoons}} ZnBr_2$$

For the vanadium-redox battery, the electrolytes in the anode and cathode compartments have vanadium ion species (typically sulfates) with different oxidation numbers, and the corresponding electrochemical reactions are expressed as follows[19]:

Eq. 22) $$\text{Anode: } V^{2+} \underset{Charge}{\overset{Discharge}{\rightleftharpoons}} V^{3+} + e^-$$

Eq. 23) $$\text{Cathode: } VO_2^+ + e^- + H^+ \underset{Charge}{\overset{Discharge}{\rightleftharpoons}} VO^{2+} + H_2O$$

Eq. 24) $$\text{Overall reaction: } VO_2^+ + V^{2+} + 2H^+ \underset{Charge}{\overset{Discharge}{\rightleftharpoons}} VO^{2+} + V^{3+} + H_2O$$

Advantages of this type of batteries are i) simplicity of the electrode reaction (robustness), thus avoiding undesired phenomena, such as phase transformation, electrolyte degradation, and morphological changes of the electrode materials, ii) easy and flexible battery design[3], since power and energy of this system can be uncoupled. Disadvantages are i) the requirement of pumps, sensors, reservoirs and flow management[20,21], ii) membrane inefficiency for controlling long-term ion cross-over, iii) low specific energy density (< 25 $Wh \cdot kg^{-1}$) due to the limited solubility (8 M) of the

redox couples. Consequently, notwithstanding the benefits of redox-flow batteries, the application of this technology to stationary energy storage remains uncertain.

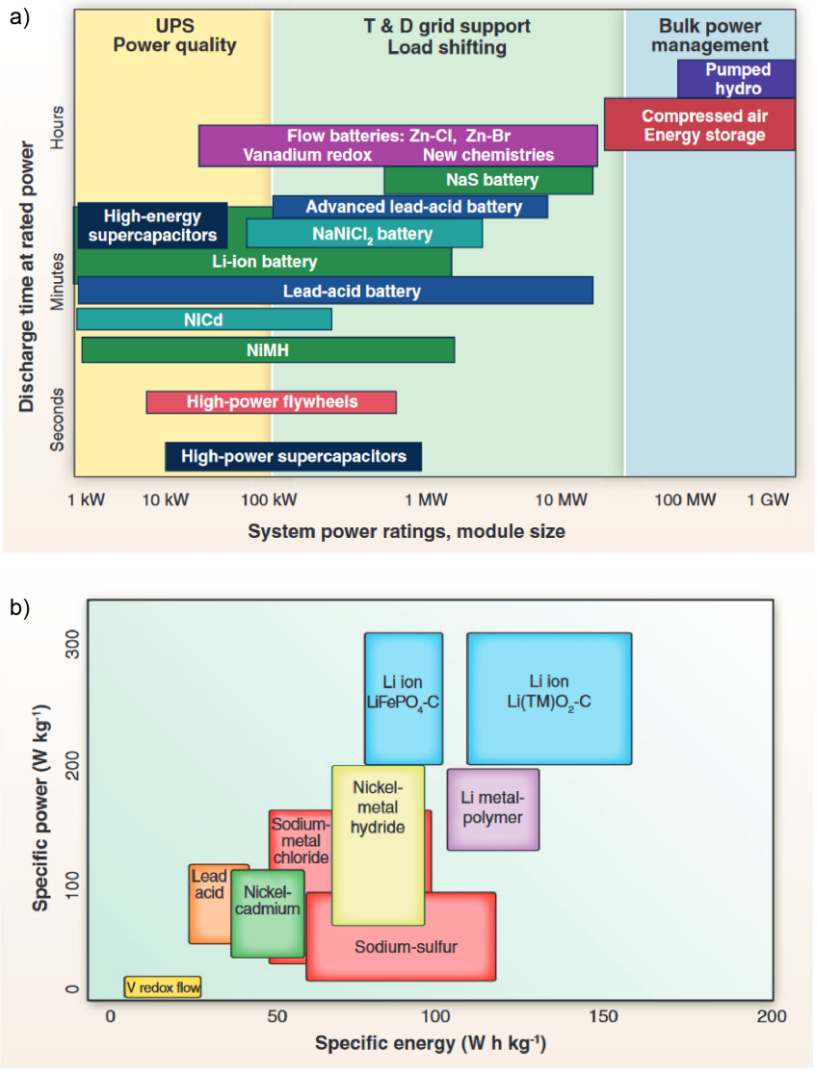

Figure 1: **(a)** Discharge time vs. power rate comparison of various electrical energy storage technologies. **(b)** Comparison of specific power and energy densities for various secondary battery systems currently being studied for grid storage applications. Figures taken from [3].

It is very unlikely that the power rate, energy density and cycle life needed by the wide range of existing stationary applications will be achieved by a single type of battery technology (Figure 1). The success of one battery system over another will depend on how well certain key expectations can be met, such as i) low installation, maintenance and operating costs, ii) high cycle life and reliability, as well as iii) high energy density and efficiency. In addition, the ideal battery should also be easy to

manufacture and made from cost-effective and environmentally friendly materials. Moreover, sensitive aspects concerning the secured supply of critical raw materials are now at the forefront of the discussions and need to be addressed natively to any battery technology to be developed. This has led to a renewed interest in new concepts for alternative rechargeable battery technologies.

Metal-air batteries

Metal-air batteries are one of the most promising EES battery systems still in the early research phase. So far, only primary cell reached to the market. The main advantage of metal-air batteries lies in the fact that only the metal anode must be placed in the battery, since oxygen accessed from the air is used as the active species for the cathode, thus reducing the battery weight and freeing up more space dedicated to the storage of energy. This is the fundamental reason why metal-air batteries can achieve higher values of specific and volumetric energy densities than most of the current rechargeable battery systems (Figure 2).

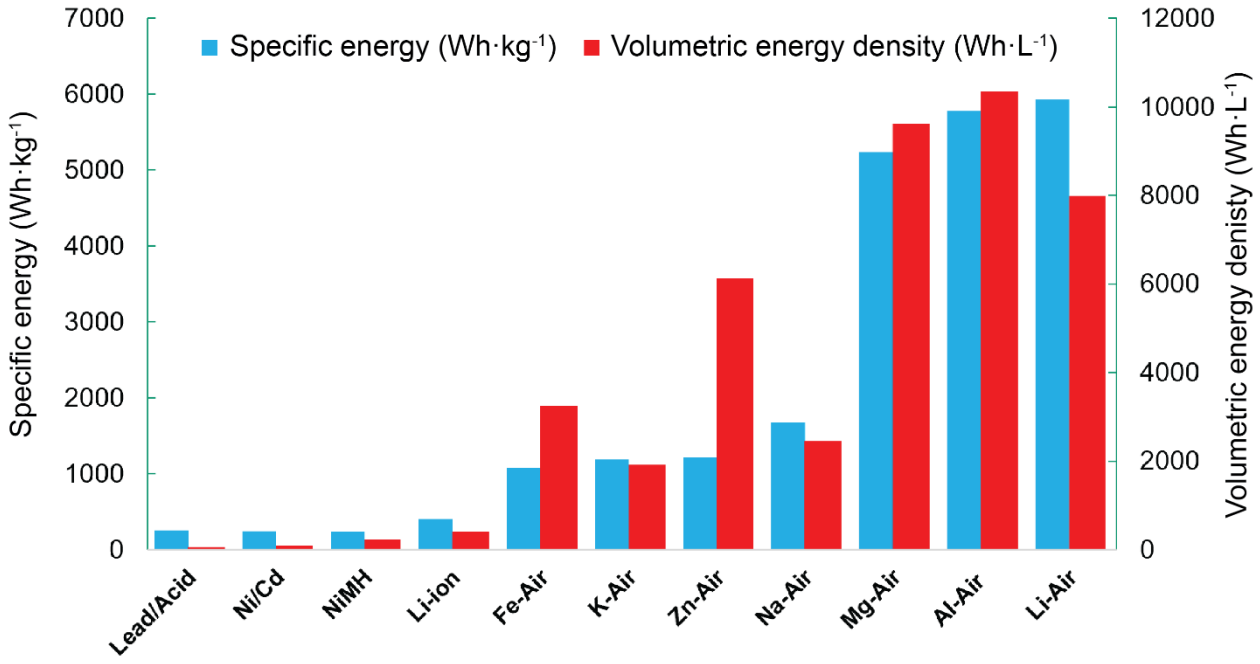

Figure 2: Comparison between different types of secondary battery according to their theoretical specific energy density. Data taken from [7,22].

Metal-air batteries are usually classified into two groups, depending on their electrolytes. The first cell system uses aqueous electrolytes since the metal anode does not react vigorously, or even explosively, when in contact with water. Oxygen is reduced to hydroxide ions in aqueous alkaline electrolyte while the metal anode (M) is transformed into a metal oxide- or a metal hydroxide species. In aqueous solvent, the general redox process of a metal-oxygen cell can be described by the following equations:

Eq. 25) $$\text{Anode: } M + nOH^- \underset{Charge}{\overset{Discharge}{\rightleftharpoons}} MO_{n/2} + \frac{n}{2}H_2O + ne^- \text{ or}$$

$$M + nOH^- \underset{Charge}{\overset{Discharge}{\rightleftharpoons}} M(OH)_n + ne^-$$

Eq. 26) $$\text{Cathode: } \frac{1}{2}O_2 + H_2O + 2e^- \underset{Charge}{\overset{Discharge}{\rightleftharpoons}} 2OH^-$$

Eq. 27) $$\text{Overall reaction: } M + \frac{n}{4}O_2 \underset{Charge}{\overset{Discharge}{\rightleftharpoons}} MO_{n/2} \text{ or}$$

$$M + \frac{n}{4}O_2 + \frac{n}{2}H_2O \underset{Charge}{\overset{Discharge}{\rightleftharpoons}} M(OH)_n$$

The second cell system uses aprotic solvents which make it water-sensitive and degrade when in contact with moisture. In this case, the oxidized metal M^{n+} formed at the anode reaches the cathode forming the oxides $MO_{n/2}$. Metals such as Ca, Al, Fe, Mg, Cd and Zn generally belong to the aqueous system[23–26]. Common metals that use aprotic solvents are K and Na[22]. Lithium-oxygen cell can operate in both aqueous and aprotic solvents, and is considered one of the best candidates for rechargeable metal-air batteries, as it has the highest theoretical specific energy (5928 $Wh \cdot kg^{-1}$) and high nominal cell voltage of 2.96 V (non-aqueous) and 3.45 V (aqueous). However, practical energy densities of aprotic systems are far below these values, when considering the air supply. In addition, lithium metal experiences significant deterioration when exposed to air and water electrolytes. Furthermore, this battery (like other metal-air batteries) suffers from irreversible discharge products

and electrolyte evaporation. Mg and Al-air batteries have comparable energy densities to Li-air, but their low reduction potential typically results in rapid self-discharge and poor Coulombic charging efficiency[27].

1.2. Zn-air batteries

Among all metal-air systems, the aqueous alkaline zinc-air battery (ZAB) has received far more interest because of the several benefits of using metallic zinc as anode material combined with highly ionic conductive alkaline electrolyte. Zinc is a quite inexpensive element due to its relatively high abundancy in the earth's crust. In addition, metallic zinc is non-toxic and environmentally friendly, which is of paramount importance for renewable energy storage and grid balancing applications[22]. Moreover, a metal-air battery mounting zinc as anode material possess exceptionally high theoretical volumetric (6136 $Wh \cdot L^{-1}$) and specific (1218 $Wh \cdot kg^{-1}$ and 1353 $Wh \cdot kg^{-1}$ excluding oxygen[28]) energy densities. Primary Zn-air battery is not a new technology, since the concept of using oxygen as cathode material was already reported for the first time in 1840 by Smee[28,29]. Then, this effect was observed in 1866 with the advent of the wet-Leclanché cell[30], which absorbed oxygen from the atmosphere into the cathode material, consisting of a mixture of carbon and MnO_2. Maiche[31] patented the first practical primary zinc-air battery in 1878, where the carbon-based cathode had a design similar to that of Leclanché cell, but with the difference that platinum replaced the manganese dioxide. However, technological limitations prevented the widespread of Zn-air batteries into the market until the 20th century. In 1932, the commercialization of primary Zn-air batteries began with Heise and Schumacher, who applied hydrophobic wax into their air cathodes to avoid electrolyte's flooding. Nowadays, virtually the same battery model is used to produce large industrial primary Zn-air batteries with high energy densities and low power rate capabilities, making the application spectrum of this battery type very limited. This type of Zn-air battery is mainly used as electrochemical EES for remote railway signalling and navigation aid applications. A thin, robust and high-performance air cathode suitable for zinc-air button cells was realized in the early 1970s thanks

to the technological advancements made in fuel-cell research, which introduced the use of fluoropolymers, such as polytetrafluoroethylene (PTFE), for the manufacturing of Teflon bonded catalyst structure[32] and hydrophobic cathode composite[7,33]. Today, the Zn-air system is mostly successful in the fabrication of primary button cells, leading the market of hearing aid applications, and providing practical volumetric energy densities beyond 1300 $Wh \cdot L^{-1}$[23]. In the two decades preceding the 21st century, major research incentives have been devoted to the development of rechargeable zinc-air batteries for applications in the field of electrical mobility. One of the main strategies adopted to build a rechargeable zinc-air battery is to mechanically replace the oxidized zinc anode with a fresh one after complete discharge of the battery. This type of battery is usually referred to mechanically rechargeable Zn-air battery or Zn-air fuel cell. However, this concept never reached the market due to the high costs of creating a network of battery production and refuelling stations, as well as damaging during the recharge of the battery pack. At the same time, numerous attempts were made to create a fully secondary zinc-air battery, but developments in this direction nearly stopped at the end of the 20th century mainly due to problems related to the stability of the electrodes, as well as the introduction of the Li-ion battery technology launched by Sony in 1991. Recent advances in the field of battery research, in conjunction with the growing awareness of scarcity, safety-issues and high costs of lithium and cobalt, the latter being one of the main ingredients of cathode material for Li-ion batteries, have renewed interest in the development of electrically rechargeable zinc-air batteries. Companies including NantEnergy[34] (before known as Fluidic Energy), EOS Energy Storage[35] and MGX Renewables Inc./DBA Zinc8 Energy Solutions[36] (formerly ZincNyx Energy Solutions) have recently developed unique zinc-air battery systems that attempt to break into the global market for utility scale grid storage applications. In Europe, Zinium is the registered trademark of ZnR Batteries. It is a young and innovative French company, created in 2016 by Électricité de France (EDF) as a spin-off to develop rechargeable Zn-air batteries. A recent economic study revealed that the Zn-air battery is one of the very few electrochemical EES systems that are actually economically feasible for grid applications[37], hence further justifying this revived

interest. Therefore, it is believed that a rechargeable zinc-air battery, being made of abundant, environmentally friendly, intrinsically safe and robust materials, without issues for recycling step and presenting auspicious life cycle costs, could be more advantageous than state-of-the-art Li-ion batteries for the stationary electricity storage applications.

The four building blocks that typically constitute a zinc-air battery are the metallic Zn anode, the air cathode (also known as gas diffusion electrode), an electrolyte and a membrane separator. The electrolyte employed is generally a strongly alkaline aqueous solution consisting of concentrated potassium hydroxide (KOH) or sodium hydroxide (NaOH). A schematic representation of the operating principle of a secondary Zn-air battery is shown in Figure 3. While the battery is discharging, oxidation of the metallic zinc anode occurs, releasing electrons to an external load. The oxidation of the Zn anode generates zinc cations (Zn^{2+}) that then reacts with the hydroxide ions (OH^-) present in the aqueous electrolyte, forming zincate ($Zn(OH)_4^{2-}$) ions, as described as follows:

Eq. 28) $$\text{Anode: } Zn \underset{Charge}{\overset{Discharge}{\rightleftharpoons}} Zn^{2+} + 2e^-$$

Eq. 29) $$Zn^{2+} + 4OH^- \underset{Charge}{\overset{Discharge}{\rightleftharpoons}} Zn(OH)_4^{2-}, E_0 = -1.26 \text{ V vs SHE}$$

The zincate ion eventually spontaneously precipitates into insoluble zinc oxide (ZnO) onto the zinc electrode surface at supersaturated $Zn(OH)_4^{2-}$ conditions (Eq. 30):

Eq. 30) $$Zn(OH)_4^{2-} \underset{Charge}{\overset{Discharge}{\rightleftharpoons}} ZnO + H_2O + 2OH^-$$

The discharge products form a passivating layer of ZnO which in turn (because of its intrinsic insulating properties) increases the internal resistance of the zinc electrode, which inevitably results in voltage losses during discharge and increases in voltage during charging. Furthermore, the deposition of ZnO precipitates cannot be controlled, and therefore the local distribution of Zn re-deposited on the electrode surface during battery charge will vary from cycle to cycle, leading to

morphological changes (shape changes) in the Zn electrode. Another problem of the Zn anode is the evolution of hydrogen (hydrogen evolution reaction, HER) induced by metal corrosion in alkaline electrolytes:

Eq. 31) $$Zn + 2H_2O \rightarrow Zn(OH)_2 + H_2 \uparrow$$

During discharge, at the air cathode side, oxygen molecules (diffusing into the porous structure from the atmosphere) the electrons (released by the anode) meet at triple-phase boundary zone (TPB), a region where the gas (O_2), liquid (electrolyte) and solid (catalyst) phases are in contact. There, the oxygen is reduced into OH^- via the so-called oxygen reduction reaction (ORR), which can be written as follows (Eq. 32):

Eq. 32) $$\text{Cathode: } O_2 + 2H_2O + 4e^- \underset{Charge}{\overset{Discharge}{\rightleftharpoons}} 4OH^-, \quad E_0 = 0.40 \text{ V vs SHE}$$

The overall balance reaction is formulated as follows:

Eq. 33) $$\text{Overall reaction: } 2Zn + O_2 \underset{Charge}{\overset{Discharge}{\rightleftharpoons}} 2ZnO, \quad E_0 = 1.66 \text{ V vs SHE}$$

During battery charging, oxygen is formed at the air electrode by the so-called oxygen evolution reaction (OER) and the electrons return to the positive electrode, thus reducing ZnO back into metallic zinc. The electrochemical redox reactions described above result in a theoretical cell voltage of 1.66 V. In practice, because of the slow kinetics of redox reactions involving oxygen electrochemistry, a zinc air battery will never reach such high operating voltage. In practical systems, typical discharge and charge voltages are 1.0-1.2 V and 2.0 V, respectively. Moreover, the high overpotentials at which OER takes place causes gradual degradation of the air cathode properties, leading to a rapid decrease of the battery performance and, eventually, to its failure.

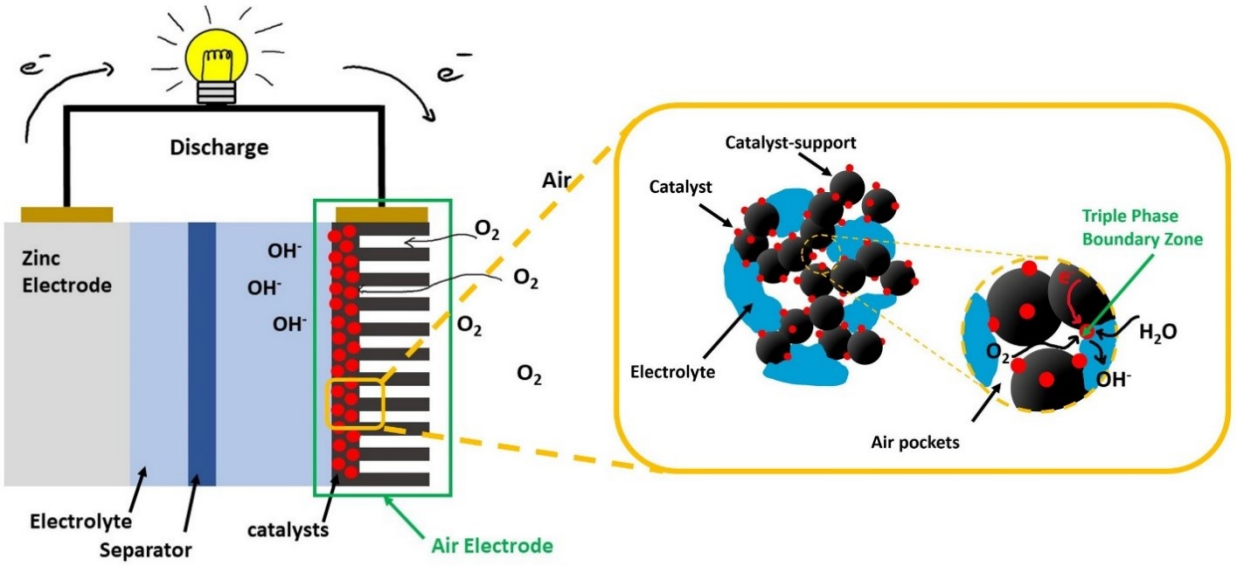

Figure 3: Schematic representation of the main components of a zinc air cell under discharge, adopted from [38,39].

Several approaches have been proposed over the past two decades to improve the efficiency and stability of the O_2-electrode, such as i) by changing the electrode design, and ii) by developing new materials, the electro-catalysts, to accelerate the sluggish ORR and OER processes. As this research focuses primarily on the development of an efficient and durable bi-functional O_2-electrode, a description of the main processes impacting electrode efficiency, such as electrode kinetics and mass-transport related phenomena, will be addressed in the next subsection.

1.2.1. Parameters affecting the operating cell voltage

When the electrochemical conditions differ from the standard conditions, the Nernst equation expresses the cell voltage E:

Eq. 34) $$E = E^0 - \frac{RT}{nF} \ln \frac{a_C^c a_D^d}{a_A^a a_B^b}$$

where a_i is the activity of species i, R is the ideal gas constant (8.314 $J \cdot K^{-1} \cdot mol^{-1}$), and the absolute temperature is represented by T. The thermodynamics presented above only describes the system at equilibrium condition, and it would correspond to the ideal case where during discharge the chemical energy of the cell could be fully converted into electrical energy without any losses. However, when

a current load is applied, the system goes out of its equilibrium and polarization losses arise while the electrochemical reactions take place. These energy losses include: i) kinetics limitation due to the finite rate of the reaction, and ii) decrease of reactant concentrations due to mass-transport limitations. The so-called internal resistance, which induces a characteristic voltage drop of the cell during operation is another critical factor that affects the cell's performance. The voltage drop induced by the internal resistance is usually referred to as "iR-drop" or "ohmic polarization". The total internal resistance is the sum of several resistances, where the major contributors are the ionic resistance of the electrolyte, the electronic resistances of the active mass, the current collectors and electrical tabs of both electrodes, and the contact resistance between the active mass and the current collector[7]. All of these resistances follow the Ohm's law in which the voltage drop is linearly proportional to the current load applied.

The operating cell voltage E can be defined as follows[7]:

Eq. 35) $$E = E_0 - [(\eta_{ct})_a + (\eta_c)_a] - [(\eta_{ct})_c + (\eta_c)_c] - iR_i$$

where E_0 is the open-circuit voltage (OCP), $\left(\eta_{ct,c}\right)_a$ and $\left(\eta_{ct,c}\right)_c$ are the activation and concentration polarizations at the cathode and anode, respectively. The operating cell current is expressed by i and R_i is the total internal resistance. The effect of the different contributions on the working cell voltage is also schematically shown in Figure 4. Yet, the phenomenological description of the system requires additional parameters that consider the kinetics and mass-transport processes involved during the electrochemical reaction. These will be addressed in more detail in the following paragraphs.

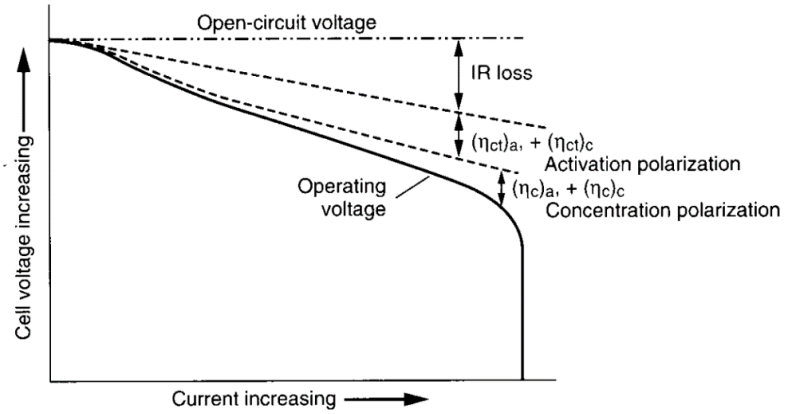

Figure 4: Schematics of the different resistances that affect the operating cell voltage. Taken from [7].

The concept of electrode kinetics can be expressed as the transition from electronic to ionic conduction, its regulation and other associated phenomena[40]. Since the type of conduction in the electrolyte is ionic while it is electrical in the electrode material, the transition from one conduction mode to another involves a charge transfer process across the solid-liquid interface. The rate of a kinetic process in controlled by several parameters, such as surface catalytic activity and concentration of the active species. Moreover, the overall rate of the electrochemical process is determined by the slowest step in multi-steps sequence of reactions[7], that is the so-called rate-determining step (RDS). Another important parameter that regulates the reaction rate is the potential difference across the interface, which is expressed in terms of overpotential η for the reaction. The latter is defined as the degree of departure of the potential from its equilibrium when an electrochemical reaction takes place with a net current flow across the electrode/solution interface. For a kinetically controlled process, i.e. when the rate of the reaction is controlled by the charge transfer process, the overpotential is defined as activation polarization (or activation overpotential). The central equation governing the electrode kinetics is the Butler-Volmer (B-V) equation[41]:

Eq. 36) $$i = i_0\left(e^{\beta\eta/FT} - e^{-(1-\beta)\eta F/RT}\right)$$

where i is a cathodic current flow, i_0 is the exchange current, and β represents a symmetry factor. There are two limiting cases for the B-V equation, one for the low overpotential region (usually η <

50 mV) and the other for the high overpotential region. In the high overpotential region, the B-V equation simplifies into the Tafel equation[42]:

Eq. 37) $$\eta = a \pm b \cdot \log i$$

where the constant b is usually referred to as the Tafel slope. A change in Tafel slope may be indicative for a change in the rate determining step or the occurrence of a different reaction mechanism. Detailed information on the derivation of the Tafel equation, as well as its interpretation for processes involving single- and multi-steps reactions are described elsewhere[7,41,43].

The kinetics of an electrochemical system can be enhanced by increasing the potential across the electrode/electrolyte interface. However, the charge transfer process only works over a very limited distance (about 0.5 nm) and a mass transport process is needed to bring the active species to the electrode surface, as well as to release the generated reaction products to the bulk electrolyte. Charge transfer and mass transport are two consecutive processes, where the overall reaction rate is determined by the slowest of the two. At low overpotentials, the charge transfer process is slower than the motion of the active species from the bulk to the electrode surface, thus mass transport is negligible compared to kinetics limitations. At higher overpotentials, the charge transfer process is faster than the rate of supply of the active species to the electrode surface, that is why mass transport is now reaction-rate limiting.

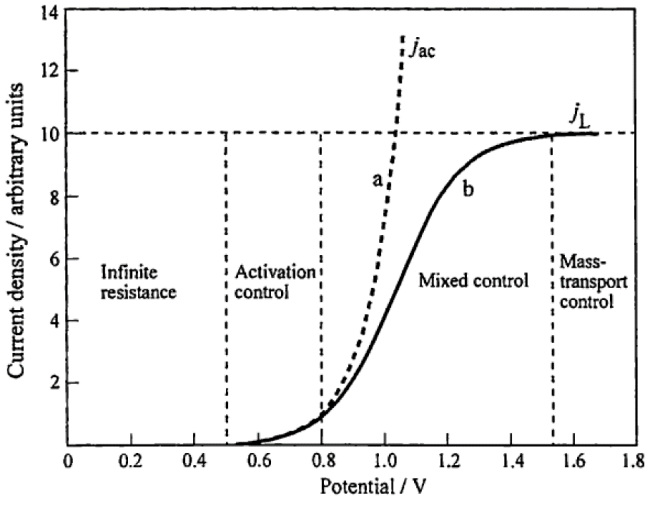

Figure 5: Illustration of the different electrode regimes, from activation (kinetics) to mass transport control process. Taken from [40].

As illustrated in Figure 5, a further increase of the overpotential enhances the charge-transfer rate, but the observed current eventually remains unchanged since it is still limited by the mass transport. This effect results in a current density that does not depend on the potential applied, which is defined as the limiting current density, j_L. The experimentally observed current density j_L (via rotating disk electrode (RDE) technique, see chapter Experimental Methods) can be then expressed by the Levich equation[44]:

Eq. 38) $$j_L = 0.62nFD^{2/3}\nu^{-1/6}C_0\omega^{1/2} = BC_0\omega^{1/2}$$

where B is referred to as to the Levich-constant. The full description of both the above equation and the RDE method will be discussed in the Experimental Methods chapter.

1.2.2. Designing principles of the gas diffusion electrode

The structural, chemical and electrical characteristics of the electrode play a decisive role in determining the overall battery performance. The electrode architecture must ensure optimal utilization of the electrocatalysts involved by maximizing the concentration of the so-called triple-phase boundaries (TPBs). This is typically controlled by the addition of fluoropolymers, such as PTFE[45,46] in the catalyst mixture. As previously described, knowledge gained through extensive research on fuel cell technology were directly implemented to develop efficient air cathodes for ZAB[7]. However, the only requirement for GDEs used in fuel cells is to be highly active towards ORR. For bifunctionality, the GDE must be both ORR and OER active, as well as stable towards repeated charge-discharge cycling. Different electrode architectures have been proposed to tackle these issues[47], such as i) by adopting a bi-cathode configuration that physically decouples the ORR and OER reaction into separate electrodes[48,49], ii) by using a multi-layered electrode with separate layers for ORR and OER[50] and iii) by merging the bifunctional catalysts into a single layered

electrode (Figure 6). Even though configurations i) and ii) enable to achieve improved performances, they come at the expense of additional complexity during fabrication, weight, battery size and lower energy density. To the best of our knowledge, the single layered electrode structure with an efficient, robust and convenient bifunctional catalysts represent the best choice for practical and cost-effective design for electrically rechargeable ZABs[47]. A typical design of GDE comprises a stack of two layers: the active layer (AL) including catalyst material, and a gas diffusion layer (GDL) for the supply and the release of O_2 during discharge and charge, respectively, as well as for the electrons- and heat transports.

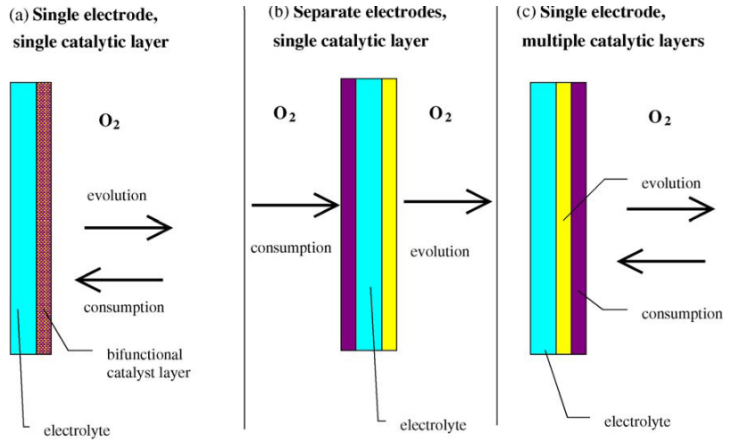

Figure 6: Design strategies of the bifunctional gas diffusion electrodes. Taken from [47].

The AL commonly contains fluoropolymers (e.g. PTFE), which i) makes the catalysts tightly stick to carbon supports[45] and improves the adhesion of the AL onto the GDL, thus enhancing the mechanical stability of the electrode, ii) tunes the hydrophobicity/hydrophilicity of the AL (which can also be achieved by tuning the pore size distribution in the electrode), relevant to reduce evaporation loss and leakage of the electrolyte, and iii) (thanks to its hydrophobic nature) helps the formation of reaction sites, the TPBs, which are crucial for efficient ORR. During battery discharge (ORR), high concentration of TPBs is beneficial for improving mass-transport limitations because of reduced diffusion-layer-thickness. The latter refers to the region close to the electrode where the concentration of the reactant is different from the bulk. Oxygen molecules dissolve at the gas-liquid

interface and then diffuse to the catalyst surface. The distance from the gas-liquid interface to the catalyst sites also contributes to the final ORR performance[51–53]. The gas diffusion layer (GDL) also plays a major role in determining the electrode stability and performance since it provides a physical support for the AL and it allows for a homogeneous transport of active species and reaction products throughout the electrode. Similar to the AL, the GDL also contains a hydrophobic polymer, which functions as a physical hindrance against leakage of the electrolyte[23]. Therefore, the wettability of the AL and gas permeability of the GDL are considered to be the two key factors determining the GDE performance[54], which largely depends on the design and morphology of the two layers. The manufacturing process, as well as the GDE composition (e.g. carbon/PTFE ratio) influence the electrode's structure and they must be optimized to achieve the best electrode performance[55]. Ancillary materials, such as polymeric additives (e.g. perfluorinated Nafion, Tokuyama AS4 alkaline ionomers[23]), electronic conductive catalyst support (acetylene black), pore forming agents (*e.g.* ammonium bicarbonate) are required to tune the ionic and electronic conductivity, as well as the porosity of the GDE, respectively. Common techniques for the manufacturing of GDEs include the pressing[51,56], rolling[56,57], decal[58], drop-casting[59], doctor blade[60], screen-printing[61,62], and spray-coating[63] methods. It is often the case that more than one method is used in sequence to produce the GDE to achieve the desired structural properties[56,57]. Novel approaches for the development of binder-free, integrative (i.e. carbon-free) bi-functional GDEs, including magnetron sputtering[64], one-step[65] and sequential[66] electrodeposition, chemical vapor deposition[67] (CVD), electrospinning[68], hydrothermal[69], have recently been reported in order to avoid issues related to the degradation of polymeric binders and carbon support corrosion.

1.2.3. Benchmarking the GDE performance

Nowadays, a growing number of researchers worldwide are developing new electrode concepts and revealing them to the scientific community as new breakthrough technologies for practical energy-

storage applications. However, unfamiliarity at the cell-level (e.g. by not taking into account the loading of active materials, or by applying current densities that are too low for practical purposes, etc.), may result in reporting mistranslations at the materials-level or bench-scale test findings when forecasting performance in practical batteries[70]. In this scenario, Parker and coworkers[70] established useful guidelines for testing new cell components, such as novel bifunctional air cathodes, in such a way that the results will provide a rational basis for bringing rechargeable zinc-air batteries to a practical performance level. Eventually, they defined the minimum metric j x $t_{discharge} \geq 11.7$ $mAh \cdot cm^{-2}$ for an air-cathode to meet the technologically relevant threshold value of 100 $Wh \cdot kg^{-1}$ to compete favourably with Li-ion batteries. To emphasize this concept, we compared the performance of bifunctional air cathodes that have been recently reported on peer-reviewed scientific journals in terms of cycle life (numbers of cycles) and areal capacity, which is defined as the applied geometric current density multiplied by the time of discharge (j x $t_{discharge}$). As shown by Figure 7, the vast majority of the reported air cathodes have been tested at areal capacities that are one to two orders of magnitude below the minimum threshold value of 11.7 $mAh \cdot cm^{-2}$, as indicated by the vertical black-dashed line in the same figure. Moreover, this metric has been calculated by estimating an average cell voltage of 1.25 V, required to achieve a minimum specific energy density of 100 $Wh \cdot kg^{-1}$. Given that i) the overpotential at the Zn anode in negligible compared to that of the air cathode and also ii) the ORR and OER overpotentials have similar magnitudes ($\eta_{ORR} \approx \eta_{OER}$), an operating cell voltage of 1.25 V can only be reached if the sum of the ORR and OER overpotentials is $\Delta E < 0.8$ V. The colour code in Figure 7, namely red, orange and blue indicate overpotential ranges of $\Delta E > 0.9$ V, $0.9 \text{ V} \geq \Delta E \geq 0.8$, and $\Delta E < 0.8$ V, respectively. It can be seen that only five of the air cathodes with j x $t_{discharge} \geq 11.7$ $mAh \cdot cm^{-2}$ are also capable of meeting the requirement of $\Delta E < 0.8$ V. All of these electrodes, though, utilize rare earth elements (e.g. La[57]) or large amounts of cobalt[57,67,71–73] and/or Ba[73], making them not the right choice for potential price-competing and environmentally friendly post-lithium-ion energy storage systems.

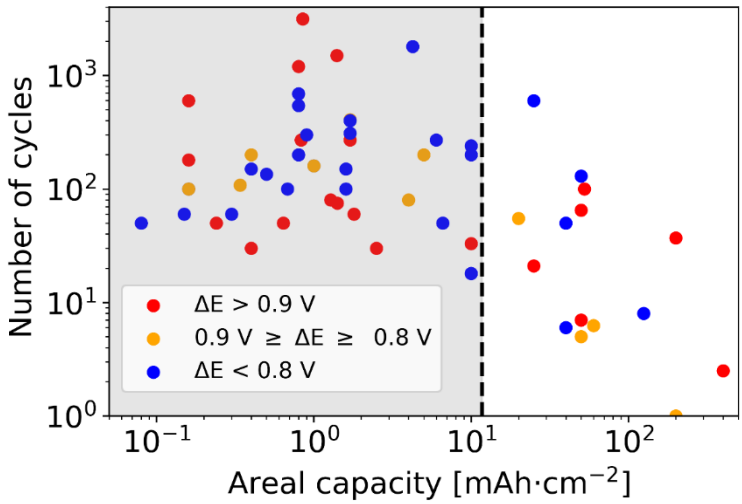

Figure 7: Overview of published bifunctional GDE performances and stabilities. The number of stable load cycles is plotted versus the charge-discharge loads (j x t, areal capacity), and for each scatter x-y coordinates are tabulated in Annex Table A1 together with references. The color code, namely red, orange and blue colors indicates $\Delta E > 0.9$ V, $0.9\ V \geq \Delta E \geq 0.8$, and $\Delta E < 0.8$ V, respectively, as qualitative descriptor for the efficiency (see text for details). The vertical dashed line crossing the x-axis at 11.7 mAh·cm^{-2} indicates the threshold metric developed by Parker and co-workers[70] to meet the minimum technologically relevant value of 100 Wh·kg^{-1} for ZAB.

1.3. Oxygen electrocatalysis

One of the most commonly studied electrochemical reactions is the cathodic oxygen reduction reaction (ORR), perhaps second to the anodic oxidation of hydrogen (HOR)[74], and there is still controversy where a number of mechanisms have been proposed. The pathways for the ORR and the anodic evolution of oxygen (OER) are discussed in this section.

1.3.1. Theoretical insights on the oxygen reduction (ORR) and oxgen evolution (OER) reactions

Both the ORR kinetics and mechanisms are functions of many experimental conditions, such as the nature of cathode material (such as the electrocatalyst) as well as electrolyte. In aqueous electrolytes, the reduction of oxygen can proceed through two main pathways, namely the *direct 4-e$^-$ pathway* and the *peroxide (or 2e$^-$) pathway*. The direct 4-electron process comprises a sequence of steps, where oxygen O_2 is reduced to either hydroxide ion OH^- or water H_2O. Some of the reduction steps may

involve the adsorption/desorption of intermediate peroxide molecules, but these are not released into the aqueous electrolyte at the end of the process. In alkaline solution, the general ORR equation can be described as follows:

Eq. 39) $O_2 + 2H_2O + 4e^- \rightleftharpoons 4OH^-, \quad E_0 = 0.40$ V vs SHE

Whereas in acid electrolyte the ORR process can be described by the following equation:

Eq. 40) $O_2 + 4H^+ + 4e^- \rightleftharpoons 2H_2O, \quad E_0 = 1.229$ V vs SHE

On the other hand, the peroxide pathway releases peroxide species in the aqueous solution. The ORR reaction in alkaline solution is presented as follows:

Eq. 41) $O_2 + H_2O + 2e^- \rightleftharpoons HO_2^- + OH^-, \quad E_0 = -0.065$ V vs SHE

Followed by either the electrochemical reduction of peroxide (Eq. 42) or its chemical decomposition by a disproportionation reaction (Eq. 43):

Eq. 42) $HO_2^- + H_2O + 2e^- \rightleftharpoons 3OH^-, \quad E_0 = 0.867$ V vs SHE

Eq. 43) $2HO_2^- \rightarrow 2OH^- + O_2$

In acidic solution, the 2-electron pathway can be described by the following equations:

Eq. 44) $O_2 + 2H^+ + 2e^- \rightleftharpoons H_2O_2, \quad E_0 = 0.67$ V vs SHE

Again, followed by either the reduction of peroxide:

Eq. 45) $H_2O_2 + 2H^+ + 2e^- \rightleftharpoons 2H_2O, \quad E_0 = 1.77$ V vs SHE

Or the decomposition of peroxide:

Eq. 46) $2H_2O_2 \rightarrow 2H_2O + O_2$

The four-electron reduction is primarily favored on noble metal catalysts, such as Pt, Ag, Au (100) and their alloys, while the two-electron peroxide route predominates on most carbonaceous materials

and transition metal oxides, mercury (Hg), Au (expect 100 facets), and some transition metal macrocycles[47,75]. However, for various transition metal oxides, such as perovskite-, pyrochlore- and spinel-type, the ORR pathway can either involve two or four electrons and may depend on various parameters, such as crystalline structure, molecular composition, and experimental conditions[23,75].

A number of reaction mechanisms for the ORR involving several intermediate reactions and rate-determining steps have been proposed. Oxygen reduction is a multi-electron process that may require various intermediate steps involving a variety of parallel-series pathways. Figure 8 shows a summary of the most relevant proposed models[74] for oxygen reduction in aqueous electrolytes. These models were obtained by comparing the theoretical work of Hsueh et al.[76] with experimental (based on rotating ring-disk electrode) measurements. It should be noticed that, in many instances, different models are able to describe the same ORR data, and that even more elaborate models are reported in the literature, as seen in Figure 8b. The latter also involves several other intermediate species, such as superoxide and oxygen ions, and differentiates between species that are strongly adsorbed and weakly adsorbed on the electro-catalyst surface. A summary of the mechanisms proposed for the oxygen reduction was compiled by Gnanamuthu and Petrocelli[77] and Damjanocic et al.[78]. The formers concluded that the rate-determining step (RDS) for the ORR on noble metals changes in acidic (H_2SO_4) and alkaline (NaOH) electrolytes.

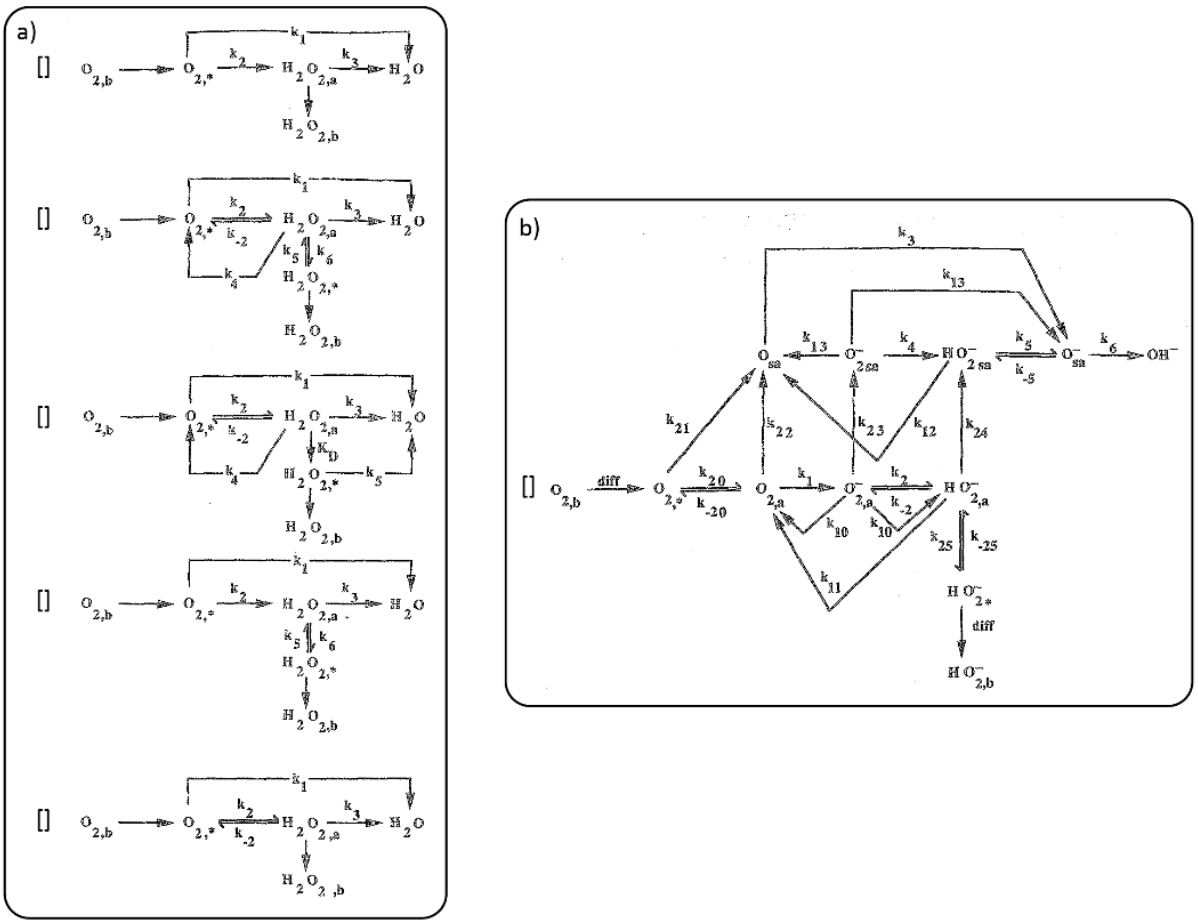

Figure 8: a) Different models proposed by Damjanovic et al.[79], Wroblowa et al.[80], Appleby and Savy[81], Zurilla et al.[82], and Bagotskii et al.[83], for the oxygen reduction reactions. The subscript "a" stands for species adsorbed on the electrode surface; "*" in the proximity of the surface and "b" in the bulk solution. b) Reaction scheme for the ORR in alkaline electrolyte[84]. Subscripts "sa" and "wa" refer to species that are strongly and weakly adsorbed to the electrode surface, respectively. Taken from [74].

However, the mechanism of the ORR is far more complex at the atomistic level and it involves a sequence of multi-steps reactions with various oxygen-containing intermediates, such as OOH*, OH* and O*. The theoretical approach used to estimate the ORR activity of various catalyst materials is to calculate the binding energy of the specific intermediates on the catalyst surface. Several studies have shown that there is a trend, resembling the shape of a volcano, between the ORR activity and the change in free energy of the various intermediates. Over the past decade, calculations based on density functional theory (DFT) have shown that the energetics of key reaction intermediates are linked by linear scaling relationships, which are crucial for describing trends in ORR catalytic activity of a

number of electro-catalysts[85]. Eventually, these studies result in a "volcano relation" between catalytic activity and main adsorption energies. These results enabled to elucidate several phenomena, such as i) why Pt, Pd and their alloys are the best ORR electro-catalysts, and ii) what are the key factors that restrict catalytic efficiency, explaining why the last decade of catalyst development has led to only a modest increase in intrinsic performance. Most of the theoretical/computational studies use the Pt(111) surface as an ideal benchmark electro-catalyst and the peroxide- and direct 4e- pathways to describe the ORR process are still considered, including both associative and dissociative mechanisms, depending on whether the O_2 molecule dissociates before reduction[86]. The associative mechanism, described in eq. 47, involves three different intermediates: *OOH, *O, and *OH:

Eq. 47) $O_2 + 4(H^+ + e^-) \rightleftharpoons *OOH + 3(H^+ + e^-) \rightleftharpoons *O + 2(H^+ + e^-) \rightleftharpoons *OH + H^+ + e^- \rightleftharpoons 2H_2O$

On the other hand, the dissociative pathway only includes *O and *OH:

Eq. 48) $\frac{1}{2}O_2 + 2(H^+ + e^-) \rightleftharpoons *O + 2(H^+ + e^-) \rightleftharpoons *OH + H^+ + e^- \rightleftharpoons H_2O$

At first it is necessary to consider the free energies of the intermediates, since the electrocatalytic current (related to the ORR kinetics) depends on the rate of the reaction that is mainly function of the potential-dependent energy activation barriers (between intermediates). DFT calculations work well in describing adsorption energies on metal surfaces; the challenge has been to describe the energy of the solvated protons and the electrons in the electrode at a given potential. DFT methods operate well in explaining adsorption energies on metal surfaces. Problems arise in determining the energy of the solvated protons and electrons in the electrode at a given potential. To address this issue, the computation hydrogen electrode (CHE) model is used as it allows the free energy of the proton-electron pairs (-*e*U) to be considered in the energy equations as a function of the potential (U) of the reversible hydrogen electrode (RHE):

Eq. 49) $\Delta G = \Delta E_{ele} + \Delta E_w + \Delta E_{field} + \Delta ZPE - T\Delta S - neU$

In the above calculation, the effects of adsorbate solvation (ΔE_w)[87], electric field effects (ΔE_{field})[88], zero-point energy (ΔZPE)[85], and entropic corrections (TΔS)[85] are also included to the DFT calculated binding energy ΔE_{ele}.

Figure 9 shows the DFT-calculated free energy diagram for the direct 4e- pathway over Pt(111) using the model described above. At 0.0 V vs. RHE, all the reaction steps are downhill. At the equilibrium potential (1.23 V vs. RHE), though, the energy path for the reduction of *OH to H_2O is uphill, implying that the surface will be occupied by *OH species, thus hampering the O_2 adsorption. The highest potential where all the steps are downhill in free energy is approx. 0.8 V, which is well in line with the experimentally reported optimum potential for high ORR current densities[89–91]. The thermodynamic limiting potential, U_L, is defined as the maximum potential where all the reaction steps are downhill in free energy. For the Pt(111) surface, U_L is equal to 0.8 V. The theoretical overpotential η_{theo} is the difference between the equilibrium potential 1.23 V and the limiting potential U_L, where for Pt(111) is about 1.23 – 0.8 V ≈ 0.4 V.

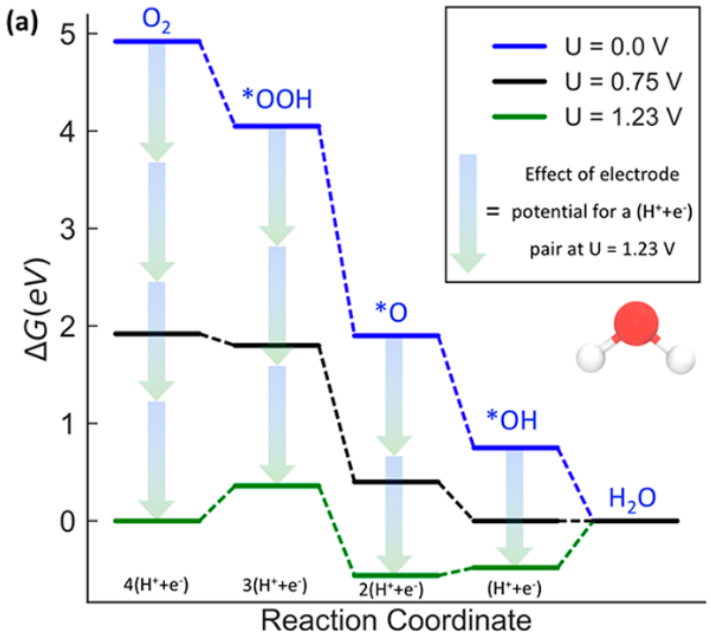

Figure 9: Free energy diagram for the four-electron associative ORR on Pt(111) for three different electrode potential vs. SHE. Taken from [86].

Linear scaling relationships, also obtained from CHE-based theory, show that binding energies for intermediates *OOH, *O, and *OH are strongly correlated and change monotonically for different metals (see Figure 10a). Such relations exist because the bond between the adsorbates and the surface always occurs through an oxygen atom. For instance, *OOH and *OH adsorbates have a similar metal-oxygen single bond and hence also their binding energies are similar, eventually resulting in a scaling line with slope close to unity ($\Delta G_{OOH} = \Delta G_{OH} + 3.2eV$). On the other side, *O adsorbate forms a double bond to the surface, resulting in binding energies that are almost two times (double) of single bonded metal-oxygen (*OH and *OOH) adsorbates ($\Delta G_O = 2\Delta G_{OH}$). This gives a *O vs *OH scaling line with slope close to 2.

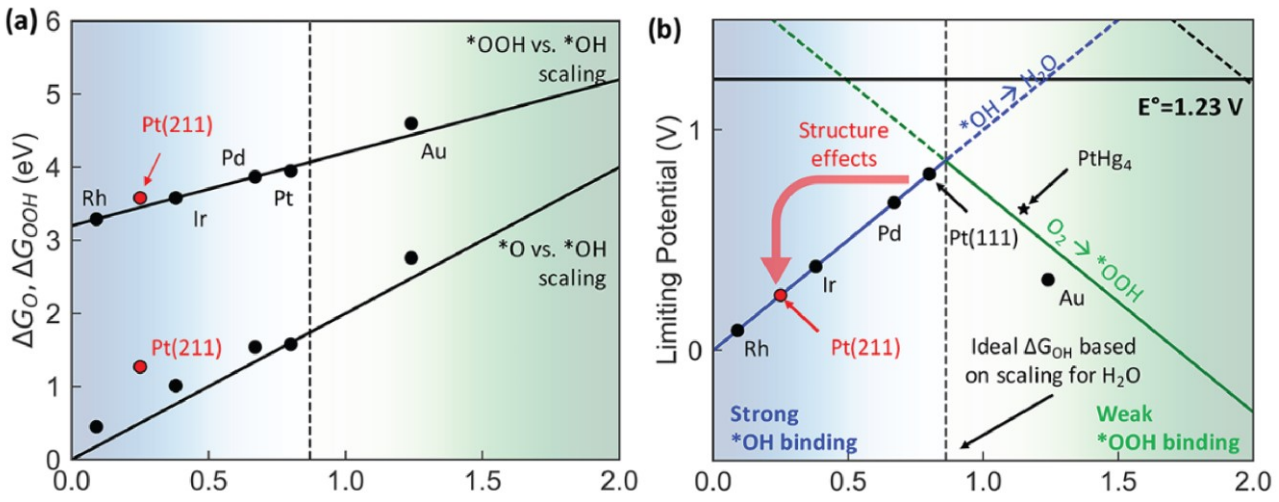

Figure 10: Scaling relationships for the *OOH and *O binding energies for the Pt(111) surface of different transition metals (black circles) with *OH chemisorption energy as descriptor. The two solid black lines represent binding energies ΔG_{OOH} and ΔG_O as a function of ΔG_{OH}. (b) Limiting potentials for individual steps including the strongly bound*OH region (solid blue line) and weakly bound*OOH region (solid green line) for the 4e-pathway. Taken from [86].

Linear scaling relationships are crucial to understand trends in catalytic activity for a wide range of electrocatalysts, which include transition metals and alloys[92], oxides[93–95], perovskites[96], sulfides[97], nitrides[98], and carbon-based materials[99].

The key message of the linear scaling relationships is that the binding energies of all intermediates (*OOH, *OH, and *O) to the catalyst surface can be described by a single independent variable,

where the most widely used is the *OH binding free energy, ΔG_{OH}. Therefore, one cannot tune independently the binding energies of the different adsorbed intermediates: As mentioned above, the catalytic activity (i.e. the theoretical overpotential) is a function of the binding energies of the three adsorbates. Therefore, the scaling relationships can be used to describe the limiting potentials for the four steps (U_{L1}-U_{L4}) as a function of ΔG_{OH} as follows:

Eq. 50) $$U_{L1} = -\Delta G_{OH} + 1.72$$

Eq. 51) $$U_{L2} = -\Delta G_{OH} + 3.3$$

Eq. 52) $$U_{L3} = \Delta G_{OH}$$

Eq. 53) $$U_{L4} = \Delta G_{OH}$$

Figure 10b shows a schematic representation of equations 50-53 for transition metals. These equations result in four limiting potential lines that define the four elementary steps of the 4e- direct ORR pathway. The solid green and blue lines correspond to the lowest limiting potential (i.e. the most energetically favorable) for the ORR reaction. It can be seen that the first (Eq. 50) and last steps (Eq. 53) are the potential limiting steps for all the transition metals. For metals with a strong *OH bond (solid blue line), the *OH → H_2O is the potential limiting steps. Instead, metals that are weakly bonded to *OH, the O_2 activation, O_2 → *OOH is the potential limiting (solid green line). Finally, the plot also demonstrates that, among all (111) facets of the other transition metals, Pt is nearest to the peak of the limiting potential volcano, thus confirming the experimental trends observed[89].

Since the ORR is the process responsible for the discharge of the Zn-air battery, the OER is the process required to charge it. The OER is also known to be of fundamental importance for other applications, such as water electrolysis. The mechanism of the OER, as is the case with the ORR, includes several intermediates and different reaction steps, which in turn control the rate of the reaction. The most relevant OER mechanisms proposed over the last decades are described in the review article of Matsumoto and Sato[100]. What follows is a brief overview of one of the most

recognized concepts describing the OER mechanism in alkaline environments. Figure 11 displays the potential energy diagrams of the OER following the electrochemical oxide pathway in the alkaline solution[101]. This can be described by the following equations:

Eq. 54) $M + OH^- \rightleftharpoons M\text{-}OH + e^-$

Eq. 55) $M\text{-}OH + OH^- \rightleftharpoons M\text{-}O + H_2O + e^-$

Eq. 66) $2M\text{-}O \rightarrow 2M + O_2$

It is proposed from Figure 11 that the OER electrocatalysis is determined by at least two main factors. One relates to the strength of the M-O bond of the adsorbed intermediate states, such as M-O and M-OH. This strength could affect the rate of desorption and/or adsorption of the OER process. The second main factor depends on the electron transfer rate between the intersections of the energy diagram shown in Figure 11. The Franck-Condon principle[100] states that the rate of electron transfer is primarily determined by the electron density of state at the Fermi level and the degree of overlap between the active site orbitals and the adsorbates at the electrode surface.

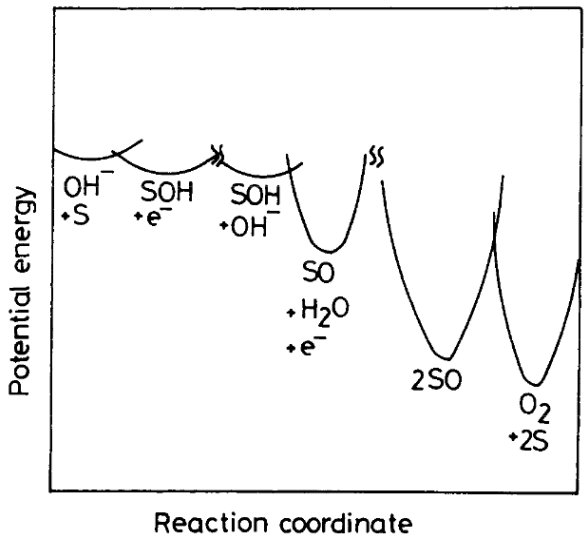

Figure 11: Schematic of the potential energy diagrams for the electrochemical oxide path described in Eq. 54-56 where the rate determining step is the desorption of oxygen from the metal surface. Taken from [100].

Platinum exhibits relatively poor OER electrocatalytic activity because of the formation of a stable oxide layer[47], although being an excellent ORR catalyst material. Noble-metal oxides, such as IrO_2 and RuO_2 have outstanding OER activity and are typically regarded as benchmark OER catalysts, but

they are rather expensive. Earth-abundant transition metal oxides have recently gained much attention as cost-effective OER electrocatalysts, the most notable of which are ABO_3 perovskite- ($LaNiO_3$, $La_{0.6}Ca_{0.4}CoO_3$[102]) and spinel-type (Co_3O_4[103–105], $NiCo_2O_4$[106]) metal oxides.

1.3.2. The ideal bifunctional eletrocatalyst

Aiming to the realization of rechargeable Zn-air batteries, large research incentives have been devoted to the development of more performant bifunctional catalysts for both ORR and OER that were recently reviewed[23,45,75,107–109]. Theoretical approach developed by Rossmeisl and co-workers[110] to rationalize changes in catalyst activities asserts that the optimum binding energies for the same reaction intermediate serving as descriptor for ORR and OER activities differs by 0.7 eV. In their work, OER and ORR are considered to be two reversed sequences of the same four coupled proton and electron transfer processes[110], as previously shown in Eq. 47 for the case of ORR. They first assumed that all reaction energies ΔG, which include the *OH, *O, and *OOH intermediates, could be tuned independently with the only restriction that the binding energy of *OH is equal to half the binding of the double-bonded *O intermediate. This assumption enables to have an ideal single active site mechanism with perfect ORR/OER catalytic activities. The resulting energy landscape for the OER (green pyramid) and ORR (blue pyramid) is shown in Figure 12a. The ideal catalyst will be found on the common vertices of both pyramids, i.e. where the two apexes (apices) meet. However, this catalyst would only exist if the *OH binding energy (ΔG_1) and ΔG_3 (the transition from *O to *OOH) have the same value, and therefore if the two binding energies can be tuned independently. This is not the case, though, because the scaling relationship between *OH and *-OOH implies that the energy difference between these intermediates is a constant of approximately 3.2 eV[111,112]. The red plane of Figure 12b indicates the restriction imposed by the constant offset of 3.2 eV between ΔG_1 and ΔG_3. The intersection between the red plane and the two pyramids creates two separate volcanos for ORR and OER, respectively (Figure 12c).

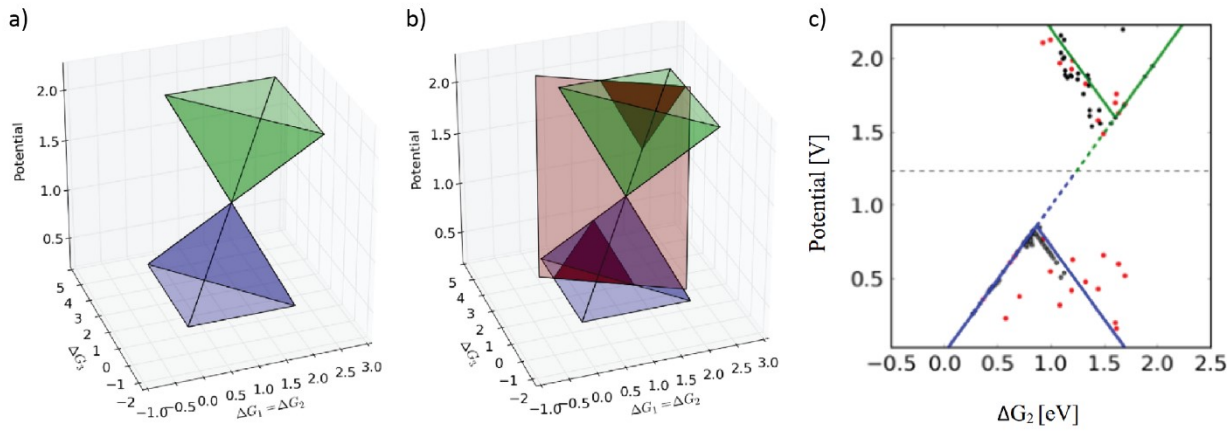

Figure 12: (a) Two pyramids that represent the best possible ORR- (blue) and OER (green) potentials for the determining step as a function of function reaction free energies ΔG_1 and ΔG_3. **(b)** Same plot shown in (a) but including a red plane representing the restriction imposed by the constant offset of 3.2 eV between ΔG_1 and ΔG_3. **(c)** Two-dimensional cross-section of the two pyramids at the intersection with the red plane. This forms two volcanos, one for the ORR (blue) and the other for the OER (green). The black dotted line visualizes the theoretical electrode potential of 1.23 V for both ORR and OER processes. Taken from [110].

Figure 12c reveals two important features: i) The apexes of the ORR and OER volcanos are far away from the optimum potential of 1.23 V (i.e. deviate from the apexes of the bipyramid), suggesting that single active site catalyst always requires a large driving force for both ORR/OER processes; ii) The two volcanos do not coincide (shifted on the ΔG_2 axis by about 0.7 eV), which means that a good ORR catalyst (on the top of the volcano) cannot be a good OER catalyst as well, and vice-versa. These two facts are direct effects of the linear scaling relations. This implies that between the two volcanos there is a so-called forbidden region in which the ideal reversible ORR and OER catalyst is located. The main implications for electrolyzers, fuel cells and metal-air batteries are that high current densities can only be achieved at high overpotentials for the reaction. More importantly, concerning the development of a bifunctional electrocatalyst for rechargeable Zn-air battery, creating a material with a single active site having ideal ORR and OER activities is unrealistic.

It follows that for the development of a performant bifunctional catalyst material for an O_2 electrode the catalytic sites for both ORR and OER should differ structurally and chemically at the atomic scale

level. A relatively straightforward approach to attain bifunctionality is the hybridization of complementary electrocatalysts with enhanced ORR and OER activities[23,48,113]. This approach allows to rationally design the bifunctional material since the catalysts can be optimized individually and then combined into an efficient bifunctional catalyst mixture. Among low-cost alternatives to state-of-the-art Pt (ORR), RuO_2 and IrO_2 (OER) noble-metal electrocatalysts, transition metal oxides based on manganese[114–130] and nickel-based oxides/hydroxides[131–140] have recently gained much attention due to their remarkable catalytic activity for ORR and OER, respectively. Several attempts have been made to associate the electrocatalytic properties of these two metal oxides, *e.g.* by doping MnO_2 with perovskite structure such as. $LaNiO_3$[130] or spinel structure such as $NiCoMnO_4$[141], by sequential co-electrodeposition technique on conductive substrates for the preparation of $MnNiO_x$[142], or by decorating MnO_2 with Ni nanoparticles via electroless nickel deposition[64]. However, a durable and efficient hybrid MnO_x/NiO_y catalyst composite mixture has still to be identified and, furthermore, to be prepared by methods that are robust and simple enough to maintain low-costs and to ease potential scale-up.

1.4. Research objectives

The main objective of this study is to develop a durable, efficient and cost-effective bifunctional electrode for rechargeable zinc air batteries, first by systematically exploring the influence of the catalyst properties on the ORR and OER activities and secondly by integrating the most active bifunctional catalyst into the GDE design. The goals of the thesis can be further described as follows:

Several ORR electrocatalysts have been proposed to be implemented in air cathodes for Zn-air battery applications. However, most of them have drawbacks, such as elevated costs (especially for noble and rare-earth elements), low-abundancy, toxicity and other issues related their synthesis/fabrication and scaling-up. First, this study aims to find a facile, reproducible, fast and scalable method for the synthesis of one of the most promising earth-abundant transition metal oxide-based catalyst for the ORR, the cryptomelane type manganese dioxide, α-MnO_2. This will also include a detailed physical,

chemical characterization of the material using several techniques that are available in our laboratories, including X-ray powder diffraction (XRD), scanning electron microscopy (SEM), inductively coupled plasma-optical emission spectroscopy (ICP-OES) and N_2-sorption method.

A comprehensive study on the electrochemical properties of the synthetized ORR electrocatalyst, α-MnO_2 will be presented. For the assessment of the ORR activity, a description of the rotating disk- (RDE) and rotating ring disk electrode (RRDE) techniques is also provided. This also includes the optimization of key parameters, such as the preparation of catalyst layer, as well as the refinement of the experimental electrochemical conditions. A rigorous investigation on the reproducibility of the measurements conducted with the RDE and RRDE techniques will also be discussed.

Second, an effective ORR/OER bifunctional electrocatalyst composite was produced by mixing the α-MnO_2 mixture with OER active nickel-based oxides. The most promising electrocatalysts were finally incorporated into the electrode architecture and tested under relevant conditions for practical energy storage applications. The architecture of the gas diffusion electrode is as important as the choice of the electrocatalysts in determining the final ORR and OER performances. Numerous strategies have been developed to improve the activity and stability of the air cathode, e.g. by introducing ancillary additives, adopting novel fabrication routes, and using advanced electrode configurations. Moreover, the majority of the literature available on this topic do not provide extended details on the manufacturing parameters and other relevant information, such as catalyst loading and testing conditions. When the latter are specified, it is often the case that the applied testing conditions are neither relevant nor sufficient for practical Zn-air battery applications, as pointed out by Parker et al.[70] Thus, a standardized protocol for manufacturing and evaluating this type of electrode is a priority and would benefit the entire scientific community.

Third, this work aims to investigate the main degradation processes that determine the longevity of our O_2-electrode, initially by discriminating between the degradation of the active materials and the degradation of the electrode structure. *Operando* XAS on a dedicated Zn-air cell were carried out to obtain direct bulk and surface structural-electronic information at the atomic level of the

electrocatalyst under application relevant conditions. The study shows that α-MnO_2 is the center of electrode activity and stability (lifetime) and it is susceptible to irreversible phase restructuring. Finally, it was demonstrated that the degradation of α-MnO_2 can be opportunely prevented when a supporting catalyst is added in the catalyst mixture.

2. Experimental Methods

2.1. Microwave-assisted synthesis of α-MnO_2

For more than 50 years, microwave radiation has been in use for many processes, including drying, calcination, decomposition, powder synthesis, sintering and others[143]. Nowadays, microwave energy has been found to be particularly interesting for the preparation of inorganic materials[144,145], and it is typically more effective than other conventional hydrothermal methods, especially in minimizing the reaction times and improving the homogeneity of the synthesis product (e.g. narrower size distribution and absence of byproducts). In microwave-based synthesis energy is transferred directly to the reagents without constraints related to thermal conductivity, resulting in a more uniform internal heating. Microwave heating is based on a substance's ability to absorb microwave energy and turn it into heat, where the magnitude of interaction between the electromagnetic radiation and the solvent depends on the polarity of the latter. The larger the dipole moment of a molecule, the more polar it is, and the stronger the microwave heat reaction[143,146,147]. Examples of polar solvents are ethanol, acetone and water, while common non-polar solvents are benzene and hexane.

A rapid method to synthesize cryptomelane-type manganese dioxide (α-MnO_2) using microwave-assisted hydrothermal (MW-HT) techniques has recently been introduced in the work of Huang and his coworkers[148]. It is reported[148] that the preparation of α-MnO_2 can be as fast as 10 s, while the reaction time of conventional methods, such as reflux, hydrothermal, solvent-free, high-temperature calcination, and sol-gel, may range from hours to days. In our study, the α-MnO_2 was prepared by a MW-HT method according to the procedure proposed by Huang et al.[149] and it can be summarized as follows. First, 314 mg K_2SO_4 (Merck, Emsure®, ACS, ISO, Reag. Ph. Eur) 486 mg $K_2S_2O_8$ (Fluka, puriss. P.a.) and 203 mg $MnSO_4 \cdot H_2O$ (Merck, ACS, Reag. Pg Eur) were added to 10 mL deionized water (Milli-Q® water, TKA, water conductivity 0.055 $\mu S \cdot cm^{-1}$) under stirring for 10 min in a 30 mL quartz reaction vial and then sealed with a cap. The mixture was transferred in a

microwave reactor (Monowave 400, Anton Paar GmbH) followed by hydrothermal treatment at 200°C for 10 min. The sample was collected by centrifugation and washed three times with deionized water. Finally, the synthesis product was dried overnight in a vacuum-oven at 60°C.

2.2. Physical and chemical characterization methods

2.2.1. X-ray powder diffraction (XRD)

X-ray powder diffraction (XRD) is a rapid analytical method used primarily to classify the phase of a crystalline sample and can also provide details on its unit cell size. This method is based on constructive interference of a crystalline material and the monochromatic X-rays, which are electromagnetic radiations with wavelengths comparable to the distance between crystal lattice planes. A cathode ray tube is responsible for the generation of X-rays that are then transmitted through a monochromator, which ultimately creates monochromatic radiation that is finally collimated and directed toward the sample. Constructive interference only arises when the difference in path length between wavelengths that are reflected on crystal lattice planes with diffraction angle θ and lattice spacing is d_{hkl}, is equivalent to a multiple integer of the X-ray wavelength λ of the incident beam. This yields to the Bragg equation:

Eq. 1) $$2d_{hkl}\sin\theta = n\lambda$$

According to the random orientation of the powdered sample, the variation of the diffraction angle through a specific 2θ range enables to attain all possible diffraction directions of the crystal lattice. Converting the diffraction peaks to d-spacings allows the sample identification since each mineral has a set of unique d-spacings, which can be used as a fingerprint. This is usually done by matching d-spacing with standard reference patterns. A detailed description of this technique is summarized in the textbooks of Hammond[150] and Glusker et al[151]. In this study, X-ray powder diffraction patterns were recorded on a X-ray powder diffractometer (Bruker XS D8 Advance) equipped with a

Cu Kα radiation (40 kV, 40 mA, λ = 0.154060 Å) at a step size of 0.01° with a time per step of 0.6 sec in the 2θ range from 10° to 100°.

2.2.2. Inductively coupled plasma-optical emission spectroscopy (ICP-OES)

Inductively coupled plasma-optical emission spectroscopy is a powerful analytical tool for the determination of the chemical composition and of trace elements of a large variety of samples, which can either be a gas, liquid or solid. However, the latter requires an acid digestion in order to make the analytes present in a form of solution[152]. The solution is then converted into an aerosol and guided towards the plasma's main channel. The inductively coupled plasma (ICP) maintains a temperature of about 10000 K at its core, so that the aerosol is vaporized easily. Analyte elements are formed in the gaseous state as free atoms and ions that are further driven to their excited states through collisions with each other. Upon emitting a photon, both the excited atomic and ionic species eventually return to the energy ground state. The energy of the photons is determined by the electronic structure of the atom / ion and each element has its characteristic energy levels. The wavelength of the photons can therefore be used to define the components from which they came. The total number of photons is directly proportional to the concentration of the source element in the sample[152]. In this study, a SPECTRO ARCOS ICP-OES was used to determine the chemical composition of the as-synthetized α-MnO_2, to measure the K^+ content intercalated in its structure (derived from the synthesis procedure), and to identify other trace elements, such as Co, Fe, Ni and S, regarded as impurities.

2.2.3. Brunauer-Emmett-Teller (BET) analysis via N_2 adsorption isotherms

The theory of BET, developed by Brunauer, Emmett, and Teller[153], is the most commonly used method to determine the specific surface area of a sample and it is based on the molecular-kinetic adsorption model introduced by Langmuir[154,155]. The adsorption of gases on solid surfaces is typically induced by physical- or chemical forces. The former is called physisorption and it is surface non-specific, while the latter is called chemisorption and is highly specific[156]. Physisorption is a reversible process that provides important information on the solid under study, such as pore volume,

surface area, adsorbent-adsorbate interaction energy, etc. The BET theory offers a mathematical description of the adsorption isotherm that is the plot of the amount of adsorbate on the solid (adsorbent) versus the equilibrium pressure at constant temperature, which can be described by the well-known BET equation:

Eq. 2) $$\frac{P}{n(P^0-P)} = \frac{1}{n_m C} + \frac{C-1}{n_m C}\frac{P}{P^0}$$

Where n is the quantity of gas physiosorbed at equilibrium vapor pressure P, n_m is the amount adsorbed per gram of solid when the adsorbent surface is covered with a monolayer, and C is a constant related to the heat of adsorption. Equation 9 provides a linear relationship between $\frac{P}{n(P^0-P)}$ and $\frac{P}{P^0}$, where the slope is $\frac{C-1}{n_m C}$ and the intercept with the Y axis is $\frac{1}{n_m C}$, thus allowing the numerical estimation of n_m and C. However, the description of the adsorption isotherm with the equation above is valid only over a limited range of relative pressure, usually for $0.05 < P/P^0 < 0.35$, owing to the constrains of the BET theory. The specific surface area of the sample, S can be obtained by applying the following equation[157]:

Eq. 3) $$S = n_m A_m N_A \cdot 10^{-18}$$

where A_m is the cross-sectional area of the adsorbate, which is approximately 0.167 nm^2 for a closely packed N_2 molecule at 77 K, N_A is the Avogadro number, and n_m can be obtained by applying equation 3 to the adsorption isotherm. In this study, specific surface area was determined using a surface area system of 3Flex (micrometrics®) using N_2 gas as the adsorbate at 77 K. All samples were degassed at 150°C for 12 hours prior to starting the N_2 adsorption measurement.

2.2.4. Scanning electron microscopy (SEM)

Nowadays, scanning electron microscopy (SEM) is one of the standard methods used in materials science for the characterization of the topography and composition of the sample. Instead of light,

electrons are used for imaging. According to De Broglie, the wavelength λ for the radiation of matter is given by:

Eq. 4) $$\lambda = \frac{h}{mv}$$

where h is the Plank constant, and m and v are the electron mass and velocity, respectively. The wavelength can be varied by changing the velocity v for a given electron with mass m. The velocity of the electron can be tuned by selecting the acceleration voltage V of the electron microscope. With the following relationship:

Eq. 5) $$\frac{k}{2\pi} = \frac{1}{\lambda} = \sqrt{\frac{2mE}{h}}$$

where $E = eV = \frac{mv^2}{2}$ defines the energy of the electrons, then we obtain for the wavelength the following expression:

Eq. 6) $$\lambda = \frac{h}{\sqrt{2meV^*}}, \qquad V^* = V\left(1 + \frac{eV}{2mc^2}\right)$$

According to Ernst Abbe, the resolution power of a microscope $\delta_A = 0.61\ \frac{\lambda}{nsin\alpha}$ is determined by its numerical aperture $nsin\alpha$ and the wavelength. Since the electron wavelength is within the range of 0.01 Å while the visible light is roughly 5000 Å, electron microscopy can obtain theoretical resolution power that are orders of magnitude greater than standard optical microscopes. SEM produces images by scanning the surface of a sample with a focused beam of electrons. The electrons interact with the sample, which then releases different types of signals, where the most common are the secondary electrons (SE) and the back scattered electrons (BSE). The former are low energy electrons and have their origin mostly on the top few nanometers of the sample's surface, therefore they provide useful information about the morphology of the sample. Instead, the latter are beam electrons that are reflected by elastic scattering from the sample and typically emerge from deeper than SE locations within the specimen. The amplitude of the BSE signal is strongly associated with the specimen's

atomic number, thereby providing information on the sample's distribution of the various elements. In this work, the morphology of the samples was investigated using a Zeiss LEO Gemini 1530 VP SEM (Jena, Germany) and a S9000G TESCAN FIB-SEM (Brno, Czech).

2.2.5. X-ray photoelectron spectroscopy (XPS)

X-ray photoelectron spectroscopy (XPS) is an analytical method that utilizes X-ray stimulated photoelectrons that are released from the sample into the vacuum for surface characterization purposes. In the material, each electron has a characteristic binding energy, which depends on the element of its origin[158]. Elastically scattered electrons released from the sample reveal information on its composition because they have specific binding energies that function as an elemental fingerprint. An electron spectrometer allows the determination of binding energies by correlating the measured kinetic energy of the electrons with the energy of the X-ray photons used for excitation, as described by the following equation:

Eq. 7) $$E_k = hv - E_b$$

which defines the measured electron kinetic energy E_k as the difference of the energy of the incident X-ray photon hv and the binding energy of the electron E_b. XPS is a surface sensitive technique since elastically scattered electrons are characterized by their relatively low escape depth of 0.5-2 nm[158]. XPS analyses of samples were carried out with a Kratos Axis Ultra DLD (Kratos Ltd., Manchester, UK) using a monochromatic Al K_α X-ray source (1486.6 eV, emission current: 10 mA, anode voltage: 15 kV). The instrument base pressure remained below 1.1×10^{-9} Pa. The instrument work function was calibrated to a binding energy of 84.0 eV for metallic gold (Au $4f_{7/2}$). The charge neutralizer system was used for all analyses. The charge neutralization was monitored with the help of the C 1s peak for adventitious carbon (filament current: 1.6 A, charge balance: 2.2 V, filament bias: 1.3 V). Survey spectra were recorded at a pass energy of 80 eV with 5 sweeps and an energy step of 1 eV. High-resolution spectra were obtained at a pass energy of 20 eV and 10 sweeps with energy steps of 0.1 eV.

The analysis area was ≈ 300 × 700 μm^2. All spectra were recorded in the spectroscopy, hybrid lens mode. For each sample, at least three independent measurements were performed. The C1s line of adventitious carbon on the electrode surface with a binding energy of 284.8 eV was used as binding energy reference. Peak fitting was done using the XPSPEAK 4.1 free software (Shirley background subtraction, pseudo-Voigt analytical peak shape: 80% Gaussian / 20% Lorentzian). No argon ion sputter cleaning has been performed prior to analysis. The measurements were carried out in collaboration with the Max Planck Institute for Polymer Research in Mainz, Germany.

2.2.6. X-ray absorption spectroscopy (XAS)

Advanced studies of electrochemical processes require potential- and time dependent information regarding chemical state and structure. X-ray absorption spectroscopy (XAS) is the tool of choice for this approach and this is an intrinsically synchrotron-based analytic. The structural and functional complexity of the GDE as well as its proneness to degradation require the use of state-of-the-art spectro-electrochemical techniques in order to discern at the molecular level the fundamental physical and electrochemical processes taking place inside the electrode during cell's operation. XAS is a powerful tool used to obtain quantitative information on the chemical and structural nature (*e.g.* electronic structure, covalency, oxidation state, site symmetry, etc.) of the different species present in the system under investigation. The working principle of XAS is briefly explained in the following paragraph. When a monochromatic X-ray beam hits the sample, the oscillating electric field of the electromagnetic radiation will interact with the bound electrons of the atoms. This interaction leads to different processes, such as X-ray scattering and X-ray absorption. The initial intensity I_0 of the monochromatic X-ray beam and the resulting reduced intensity I after sample's penetration, t, are linked by the following equation:

Eq. 8) $$\ln\frac{I_0}{I} = \mu t$$

Where μ is the linear absorption coefficient, which describes the fraction of the beam that is absorbed or scattered per unit thickness, of the absorber. The process is illustrated in Figure 13. The constant

μ accounts for the number of atoms per unit volume of the material and the probability of a photon being scattered or absorbed from the nucleus or an electron of one of these atoms[159].

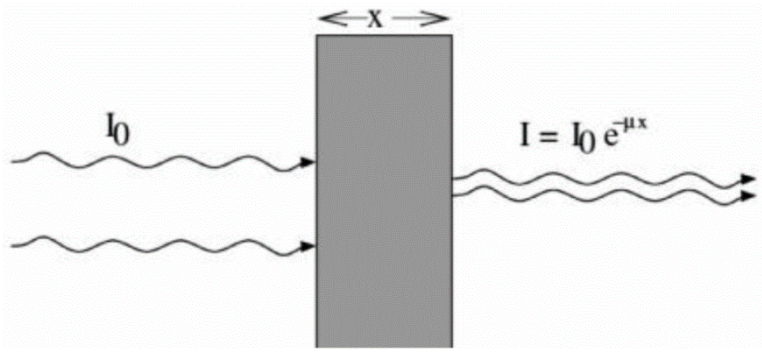

Figure 13: Schematic of the X-ray absorption measurement in transmission configuration. Taken from [160].

In a typical XAS experiment, the absorption coefficient μ is measured versus the energy of the X-ray beam. At specific wavelengths of the X-ray beam, μ increases drastically giving rise to the so-called absorption edge E_0, corresponding to the generation of photoelectrons. The energy of each absorption edge corresponds to the binding energy of an electron occupying a specific electronic state (shell) of the absorbing element. An example of an X-ray absorption spectrum at the Mn K-edge is shown in Figure 14a. The region of the spectrum nearest (approximately 50 eV above) to the absorption edge contains information on the electronic structure and local symmetry of the absorbing atom. This region is usually referred to as XANES (X-ray absorption near edge structure). By evaluating the position of the different absorption edges, it is possible to determine the oxidation state of the species in the system. The fine-structure of the spectra, called EXAFS (extended X-ray absorption fine structure), i.e. oscillations of the absorbance as a function of the incident photon extending up to 1000 eV above the absorption edge, conveys information on the chemical/structural environment of the absorbing atom.

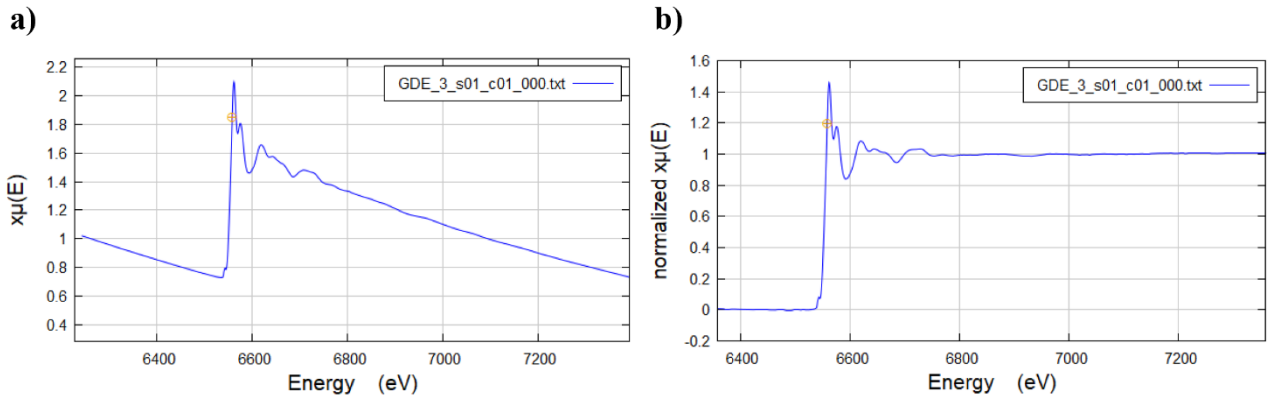

Figure 14: Acquired XAS spectrum at the Mn-K edge before **(a)** and after **(b)** normalization (Software: Athena[161]).

The analysis can be distinguished in three parts. First, all the acquired data (about 200 spectra) underwent the following iterative process: i) calibration, ii) alignment, iii) background subtraction, iv) deglitching and v) normalization. Figure 14a and Figure 14b show a XAS spectrum of the Mn-K edge before and after normalization, respectively. These set of transformations enables to properly convert the energy of the incident photon (E_{hv}) into k-space as follows:

Eq. 9) $$k = \left(\frac{2m_e}{\hbar}(E_{hv} - E_0)\right)^{1/2}$$

The EXAFS spectrum (i.e. the oscillation in the EXAFS region) is now function of k, $\chi(k)$, and it can be fitted using the EXAFS equation (Eq. 10), which is the product of the amplitude function $A_j(k)$ and phase function $\sin(\delta_j(k))$:

Eq.10) $$\chi(k) = \sum_{j=1}^{shells} A_j(k)\sin(\delta_j(k)) = \sum_{j=1}^{shells} \frac{N_j}{kR_j^2} S_0^2 F_j(k) e^{-2k^2\sigma_j^2} e^{-2R_j/\lambda(k)} \sin(2kR_j + \varphi_j(k))$$

where N_j is the number of atoms of type j at the distance R_j from the absorber atom, $F_j(k)$ is the backscattering amplitude from atom j, $\delta_j(k)$ is the backscattering phase shift, S_0 is the amplitude reduction factor (accounting for multielectron effects and other relaxation-related processes), σ_j^2 is the relative mean squared displacement (Debye-Waller factor) along the distance between the adsorber and scatterer atoms j due to static and thermal disorders, λ is the electron mean free path[162]. Second, we used the data available on the crystal structure of the electrocatalyst (see Figure 15a) to build a model that simulates the interaction between the X-rays (from the Synchrotron source) and the atoms in the crystal lattice. Third, we performed a fitting analysis of the normalized experimental

EXAFS oscillation χ(k) using Eq. 10 and the model described above, as shown in the example of Figure 15b.

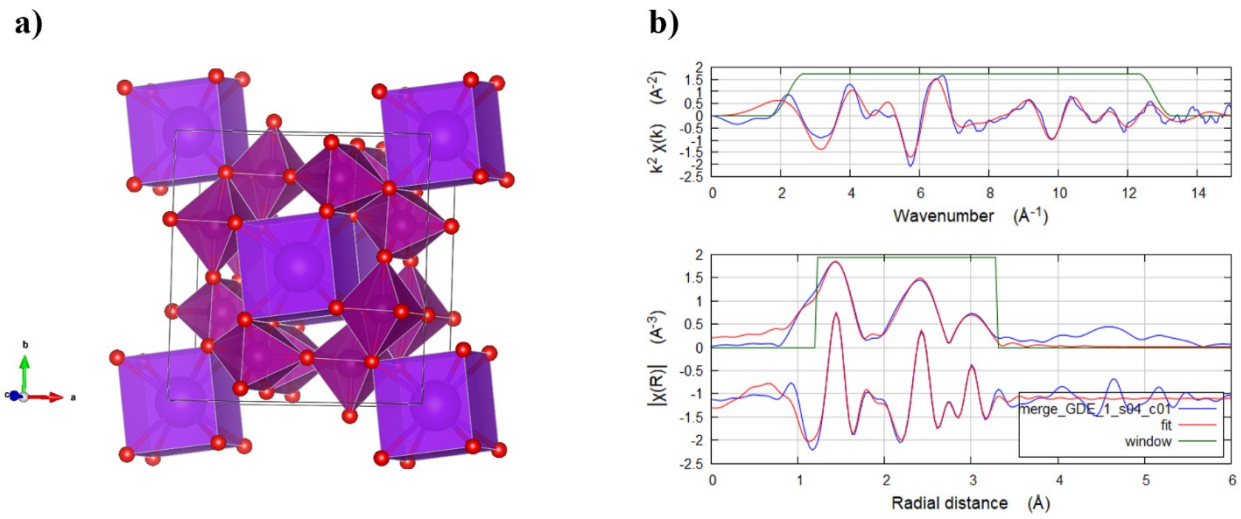

Figure 15: (a) 3D crystal structure of the electrocatalyst material used to create the model of the X-ray interaction paths (Software: VESTA[163]) and **(b)** example of the fit of the experimental k^2-weighted EXAFS oscillations χ(k) (top, blue) with the model (blue), as well as its Fourier transform components (bottom). Software: Artemis[164].

In our specific case, XAS enable to trace small changes in valence state, local symmetry and nearest coordination spheres of the different photoabsorbers incorporated in the electrode materials occurring during battery discharge (ORR) and charge (OER). X-ray absorption spectra (XAS) were collected at the Elettra synchrotron light source on the XAFS beamline[165] with an electron energy of 2.4-27 keV and an average current of 309 mA, with a typical photon flux of 10^{10} photon·s^{-1}. The radiation was monochromatized using a double-crystal Si (111) monochromator. The beam size was about 20 mm in width and 1.5 mm in height. During electrochemical experiments, the XAS data were acquired in transmission mode. The intensity of the incident X-ray was monitored by an ion chamber in front of the sample filled with a proper mixture of gases according to the energy. A second ionization chamber was placed after the sample to collect the transmitted intensity I_1. The energy was calibrated using the absorption edge of a Mn foil, which was also measured simultaneously. All data were collected at room temperature and in ambient air pressure. Data reduction, alignment, merging, deglitching, normalization and background removal were performed using the software Athena[161].

The EXAFS analysis was performed using ARTEMIS[164]. All spectra were fitted using scattering paths generated via FEFF6 code[166], which made use of the crystallographic data (model) adopted (derived) from the cryptomelane $K_{1.33}Mn_8O_{16}$ crystal structure[167].

2.3. Electrochemical techniques and electrode preparation methods

The reduction of overpotential during ORR (discharge) is one of the main challenges that still needs to be addressed for the realization of efficient air cathodes of practical Zn-air batteries. One of the main strategies employed to decrease the overpotential is by enhancing the electrocatalyst performances. The rotating disk electrode (RDE) is a principal tool used to determine the ORR activity of electrocatalysts rapidly and quantitatively. In order to attain information on the kinetics (i.e. charge transfer) of the system, the effect of the mass-transfer on the current-potential response must be properly quantified and decoupled.

2.3.1. Rotating disk (RDE) and ring disk (RRDE) electrode methods

The RDE is a hydrodynamic electrochemical method that enables to characterize the kinetic activity of electrocatalysts under defined mass-transport conditions by forced convection of the electrolyte for which hydrodynamic- and convective-diffusion equations have been solved. The rotation of the electrode provokes a convective flow of the electrolyte towards the electrode surface along the rotation axis. At the proximity of the electrode surface, the electrolyte is then flanged outward radially, as illustrated in Figure 16.

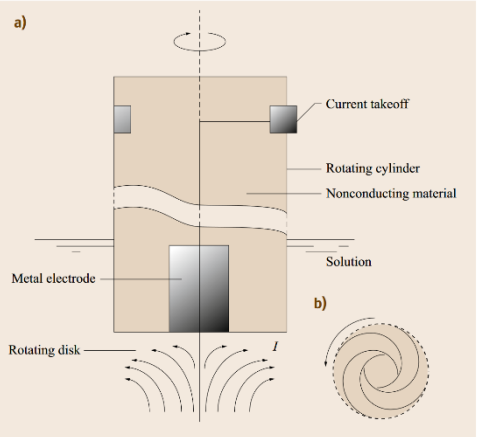

Figure 16: Sketch of the hydrodynamic flow over the rotating disk electrode tip in solution. Taken from [168].

When the vertical and radial velocities are known, the rate of mass-transport to the electrode surface can be estimated by calculating the thickness of the diffusion layer δ as follows[169]:

Eq. 11) $$\delta = \frac{1.61\nu^{1/6}D^{1/3}}{\omega^{1/2}}$$

where ν is the electrolyte kinematic viscosity and ω is the rotation speed (rad·s^{-1}) of the disk electrode. Therefore, the diffusion layer thickness can be adjusted by varying the rotation rate of the RDE. By considering that diffusion is governed by the Fick's laws, the limiting current density j_L, can be then expressed in terms of diffusion layer thickness as follows:

Eq. 12) $$j_L = nFC_0\frac{D}{\delta}$$

where n is the number of transferred electrons, D is the diffusion coefficient, and C_0 is the concentration of the active species in the bulk. The Levich equation, which describes the change in limiting current density as a function of rotation speed of the electrode, results from the combination of eq. 11 and eq. 12:

Eq. 13) $$j_L = 0.62nFD^{2/3}\nu^{-1/6}C_0\omega^{1/2} = BC_0\omega^{1/2}$$

where B is referred to as to the Levich-constant. By inserting the above expression for j_L in the Koutecky-Levich (KL) we obtain the following expression for the measured current density j:

Eq. 14) $$\frac{1}{j} = \frac{1}{j_{kin}} + \frac{1}{j_L} = \frac{1}{j_{kin}} + \frac{1}{B}\omega^{-1/2}$$

thus, the electron transfer number n and the reciprocal kinetic current density $\frac{1}{j_{kin}}$ can be retrieved from the slope and the Y-intercept of the linear plot of j^{-1} vs $\omega^{-1/2}$, respectively. Several studies on the development of efficient ORR catalysts used the KL plot to obtain the number of electrons exchanged by the reaction, n. The latter is one of the most important parameters, because it represents the efficiency of the reaction but also provides details on the ORR process. However, the validity of

the KL method is based upon the assumption of elementary single-step reactions, while the ORR mechanism is often a multistep process involving several intermediates. Moreover, it has been shown that the value of n may be affected by the rotation rate ω, meaning that the KL method, which needs a constant value of n, is not suitable for the ORR analysis. These often lead to inconsistencies, such as non-linear KL-plots and values of electron transfer number that exceeds the theoretical limit of 4[170]. Nonetheless, the KL equation can be very useful to obtain information on the dependence of the kinetic current on the overpotential by rearranging equation 14 to yield:

Eq. 15) $$j_{kin} = \frac{j_L \cdot j}{j_L - j}$$

Another method that is more suitable for the study of multistep process and the determination of the electron transfer number n, is the rotating ring disk electrode technique (RRDE), which was presented for the first time by Frumkin et al. in 1959 to qualitatively estimate the hydrogen peroxide produced during ORR in alkaline electrolyte[171]. Similar to the RDE, the RRDE technique is based on forced convection[170] where the reactants (O_2) are driven by convective hydrodynamic forces towards the disk electrode followed by reduction either into HO_2^- or OH^- through the 2e- or 4e- process, respectively. In addition to the disk electrode, the RRDE setup has a concentric ring-shaped electrode that enables to detect the produced HO_2^-, which can be directly measured by oxidizing it on the ring via:

Eq. 16) $$HO_2^- + OH^- \rightarrow O_2 + H_2O + 2e^-,\ E_0 = -0.065\ \text{V vs. SHE}$$

A schematic diagram of the working principle of the RRDE is illustrated in Figure 17. The HO_2^- ratio (p), which is defined as the fraction of O_2 reduced to HO_2^-, can be determined experimentally by using the following expression:

Eq. 17) $$p = 2 \cdot \frac{\frac{i_R}{N}}{i_D + \frac{i_R}{N}}$$

Where i_D and i_R are the disk and ring currents, respectively. The constant N is a geometric parameter defined as collection efficiency, which corresponds to the fraction of HO_2^- formed at the disk that arrives at the ring. The value of n can then be determined similarly as follows:

Eq. 18) $$n = 4 \cdot \frac{i_D}{i_D + \frac{i_R}{N}}$$

Finally, the values of n and p are related by the following mathematical expression:

Eq. 19) $$n = 4 - 2p$$

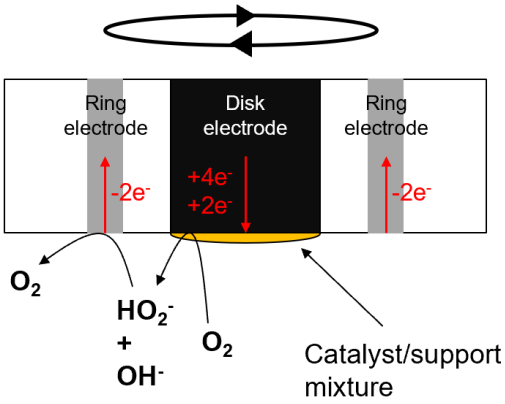

Figure 17: Schematic of the working principle of the RRDE technique. Adopted from [172].

Preparation of the RRDE measurement

The electrocatalytic properties of the materials were studied with a three-electrode cell in 0.1 M aqueous KOH solution (Merck, Titripur®, Reag. Ph Eur) using a rotating electrode setup (RDE710^{TM}, Gamry Instruments) coupled with a multichannel potentiostat (VMP3, Bio-logic Science Instruments). A Hg/HgO electrode and a Au wire served as the reference and the counter electrodes, respectively. All potentials in the text refer to the reversible hydrogen (RHE) scale. To prepare the working electrode, a total amount of 8 mg with different nominal ratios of synthetized α-MnO_2, carbon black (C-NERGY SUPER C65; Imerys Graphite & Carbon) and Ni(core)/NiO(shell) NPs (Alfa Aesar, 99.9 % trace metal basis) were dispersed in a 2 mL solution containing 1.586 mL deionized water, 0.4 mL ethanol and 14 µL of 5 wt.% Nafion solution (Fluka, Nafion® 117 Solution).

According to the supplier, the Ni/NiO particle size ranges between 5-20 nm, with a NiO shell of 0.5-1.5 nm thick (additional TGA measurements indicated a Ni : NiO weight ratio equal to 5 : 1, see Annex Figure A1, in good consistency with the specification of the supplier). The solution was magnetically stirred for 10 min, followed by 10 min sonication and then kept under stirring overnight to form a homogeneous catalyst ink. Afterwards, 25 µL of the prepared ink was drop-casted onto a glassy carbon-Pt RRDE disk (E7R9 RRDE Tip, Gamry Instruments) with a disk area of 0.2475 cm^2 and a collection efficiency of 39 %. The collection efficiency was determined from the ratio of the oxidation current of potassium ferrocyanide at the ring ($[Fe(II)(CN)_6]^{4-} \rightarrow [Fe(III)(CN)_6]^{3-} + e^-$) versus the reduction current of the inverse reaction occurring at the disk ($[Fe(III)(CN)_6]^{3-} + e^- \rightarrow [Fe(II)(CN)_6]^{4-}$), using a similar procedure described in the work of Paulus et al.[173]. Additional information on the experimental determination of the collection efficiency can be found in the Annex Figure A2. To ensure the formation of a reproducible and smooth thin electrocatalyst film on the glassy carbon electrode substrate, the ink was dried by means of the rotational drying method[174]. The total mass loading of the catalyst composite on the glassy carbon substrate was 0.1 mg. Before the start of each measurement, the 0.1 M KOH electrolyte (Reag. Ph Eur, Merck) was N_2-saturated upon vigorous bubbling for 30 min to record base cyclic voltammograms in absence of dissolved O_2. Then, for both ORR and OER investigations, the electrolyte was O_2-saturated upon vigorous O_2 bubbling during 30 min. A gentle O_2 flow was maintained over the electrolyte during the measurement. To account for the ohmic resistance of the electrolyte, all CVs were *iR*-compensated during the measurement by using the built-in ZIR technique available in the EC-Lab® software. This technique consists of performing a electrochemical impedance spectroscopy (EIS) measurement at 100 KHz frequency. The scan rates for all potentiodynamic measurements was 5 $mV \cdot s^{-1}$.

2.3.2. GDE Testing

The electrocatalysts were loaded by spraying method on a PTFE-treated Toray™ carbon paper, which serves both as support for the active layer (AL, see Introduction for more details), and as gas diffusion

layer (GDL) for the transport of the active species. To tune the hydrophobicity/hydrophilicity of the electrode, a commercial PTFE suspension (59 wt.%, 3M™ Dyneon™ PTFE TF 5060GZ) was employed. The hydrophobization of the GDL was carried out by immersing the Toray™ carbon paper into a solution of deionized water and the PTFE suspension for 2 min and 30 seconds. The concentration of PTFE in the solution determines the PTFE loading on the GDL. Then, the GDL was dried in ambient air overnight and finally, heat-treated at 330°C for 30 min. For the AL case, 83 mg α-MnO2, 83 mg commercial carbon black and 83 mg Ni/NiO NPs were dispersed into 9 mL ethanol and water (volume ratio 1:1) solution, which already contains variable amount of colloidal PTFE suspension. The solution was stirred for 10 minutes, followed by other 10 minutes of sonication. Then the ink was emulsified for 1 min at 30000 rpm (to ensure an optimum homogenization of the particulates) and finally sprayed using a standard airbrush onto a 25 cm^2 PTFE-treated GDL until the desired catalyst loading was reached.

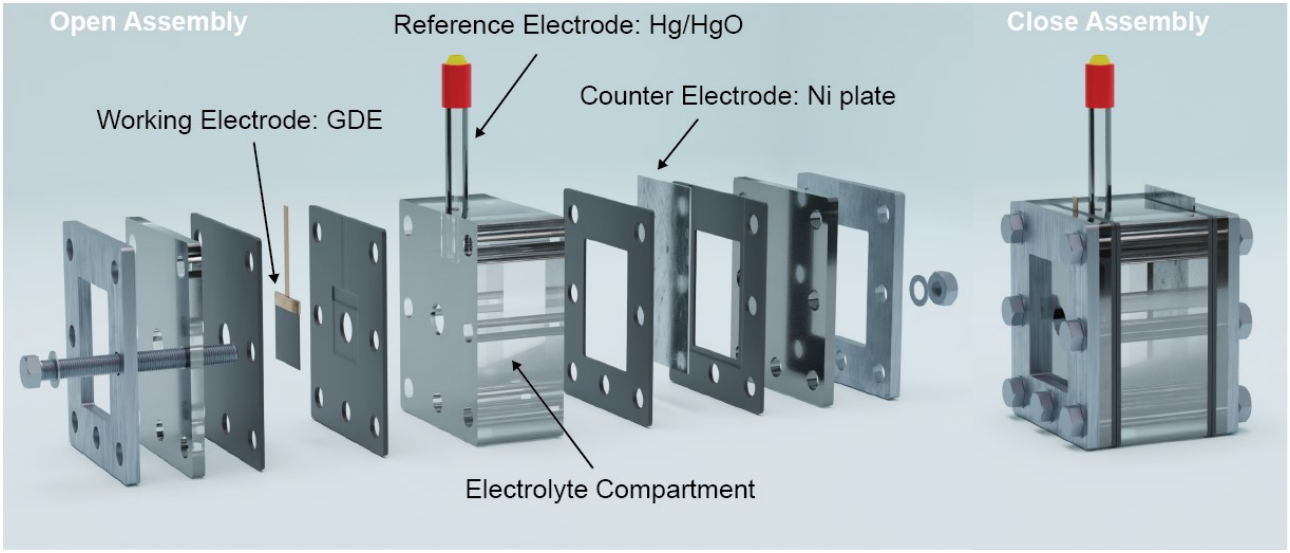

Figure 18: Schematic of the electrochemical cell setup employed to evaluate performance and stability of the GDEs prepared in this study.

Prior electrode's testing, the air electrode was heat treated at 320°C for 30 min. The air electrode was then assembled into a half-cell setup having a nickel plate and a Hg/HgO electrode used as counter and reference electrodes, respectively (see Figure 18). The use of nickel as counter electrode allow

for quantitative assessment of bifunctional air cathode properties without drawbacks from poor Zn anode properties. To sustain high current loads reversibly in a stable manner, Zn anodes require a very refined/advanced tuning of their microstructural and chemical characteristics that are significantly dependent on complex electrolyte composition and on the refinement of the additives composition. This being still challenging, Zn anode properties should not be the limiting parameter in probing bifunctional air GDE performances. The electrochemical cell was tested with 6 M KOH solution freshly prepared from potassium hydroxide pellets (for analysis, ≥ 85.0 %, Merck) and ultrapure water. All the measurements were performed under ambient atmosphere and at regulated room temperature (T = 21 °C). The electrocatalytic performances towards the ORR/OER were evaluated by applying a stepwise increasing cathodic/anodic current with densities ranging from 1 $mA \cdot cm^{-2}$ to 200 $mA \cdot cm^{-2}$ (10 min for each current step), as shown in Figure 19a. The stability of the electrode was measured by alternatively applying constant cathodic (2h) and anodic (2h) current steps at a current density of 10 $mA \cdot cm^{-2}$. Between each step, 5 min interruption at open circuit potential (OCP) was applied. This was repeated for a total of 100 charge/discharge cycles, which approximatively corresponds to 400 h of measurement. A schematic of the galvanostatic stability test is illustrated in Figure 19b. The potentiostat/galvanostat was a multichannel potentiostat (VMP3, Bio-logic Science Instruments). In order to gain insights on the main ageing mechanisms of the air cathode, Galvano electrochemical impedance spectroscopy (EIS) were recorded using a the same potentiostat/galvanostat instrument under 10 $mA \cdot cm^{-2}$ current load during the ORR and superimposing a sinusoidal current input on dc current applied to the electrode (amplitude: 100 μA, frequency range: 10 mHz to 100 kHz). Fitting of the EIS data with an analog equivalent circuit was performed with Zahner Analysis software.

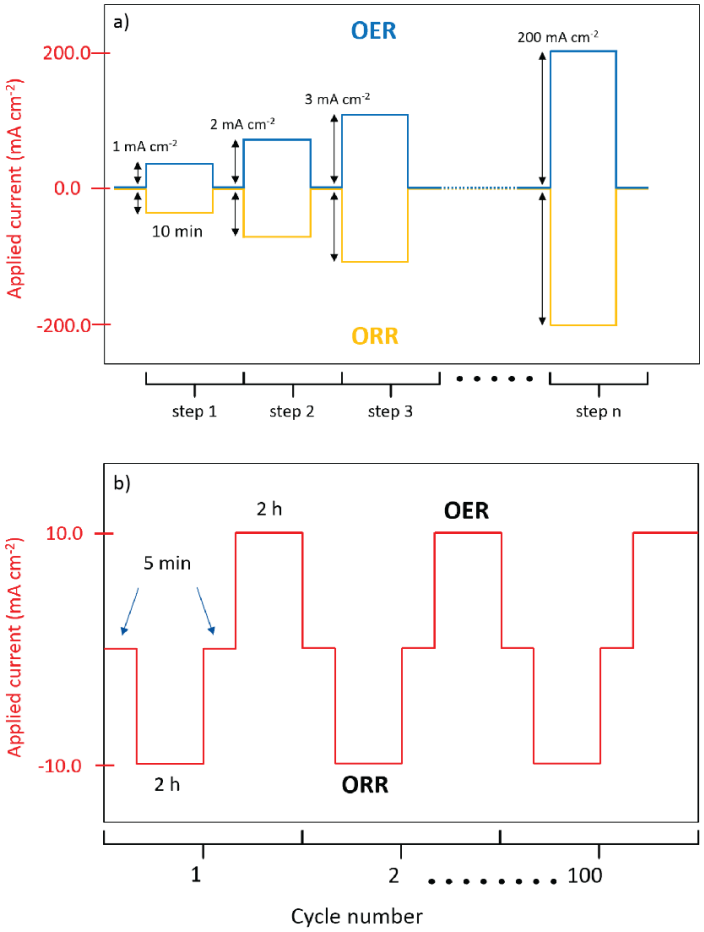

Figure 19: Schematics of the electrochemical methods used to test the **(a)** ORR (yellow) and OER (blue) activity and **(b)** the stability during cycling at application relevant conditions of the O_2-electrode.

2.3.3. Electrochemical setup for *in operando* XAS

A dedicated electrochemical setup (including electrodes and electrochemical cell) has been developed in-house for the *operando* XAS measurement. XAS data were collected using the electrochemical cell illustrated in the schematic of Figure 20. Each setup is equipped with two parallel Zn-GDE cells, which can be used independently, hence reducing the time needed to switch from one measurement/experiment to another. The setup also includes a channel for the insertion of a reference electrode, which enables to simultaneously monitor the evolution of cathode and anode potentials of the electrochemical cell. *Operando* XAS analysis has been performed at the Mn and Ni K-edges. Both the architecture and composition of the electrodes, as well as the configuration of the electrochemical setup, have been designed to achieve optimal edge-jumps and signal-to-noise ratio

in the absorption spectra for the Mn and Ni K-edges, without sacrificing the current densities applied during testing (electrode performance). Two electrodes with different composition were fabricated. For the electrodes tested at the Mn K-edge (XAS), the AL composition was 3.0 mg·cm^{-2} α-MnO_2, 1.3 mg·cm^{-2} Ni/NiO NPs, 3.0 mg·cm^{-2} carbon black and 1.8 mg·cm^{-2} PTFE. For the electrodes probed at the Ni K-edge, instead, the AL was composed of 1.3 mg·cm^{-2} α-MnO_2, 2.7 mg·cm^{-2} Ni/NiO NPs, 1.3 mg·cm^{-2} carbon black and 1.3 mg·cm^{-2} PTFE. Both formulations ensure an optimal absorption (edge-jump) of 0.47 at the corresponding K-edge energy for Mn and Ni, respectively. This enabled to perform high-quality *operando* XAS spectroscopy under practical GDE operating conditions.

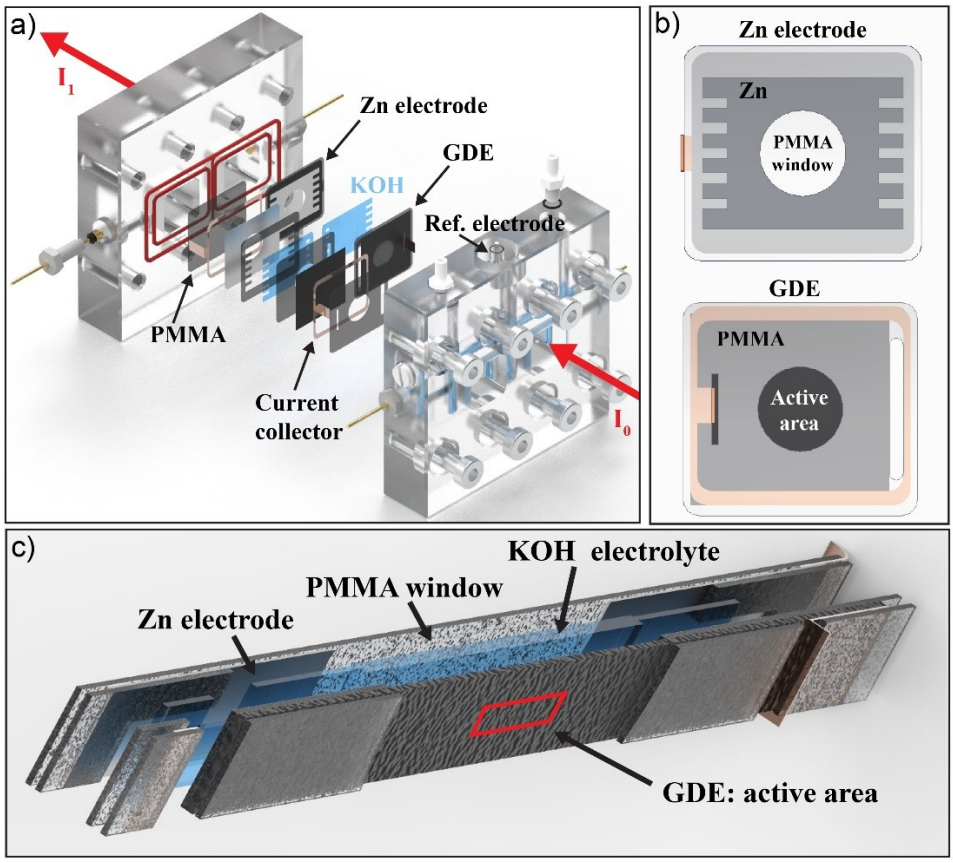

Figure 20: (a) Sketch of the *in situ* XAS setup, with the GDE side facing the incoming X-ray beam of intensity I_0. Upon transmission through the entire sample, consisting of the GDE, the 6 M KOH electrolyte and the Zn electrode, part of the X-rays is absorbed by the different materials and the resulting X-ray intensity is I_1. **(b)** Top view of the GDE and Zn electrode assemblies. **(c)** Schematic of the expanded cross-section of the electrodes/cell assembly.

The *operando* XAS experiment, devised to follow discharge/charge cycles, consists of a sequence of cathodic (ORR) and anodic (OER) current density of $j = 5\ mA \cdot cm^{-2}$, carried out in ambient air without CO_2 trap. The experimental setup used for XAS experiments is shown in Figure 21. After each change in current density / direction, the system could equilibrate for 10 minutes (to ensure that the system reached a stable/plateau potential) before starting the acquisition of XAS spectra. It should be noted that the current densities used are one-to two orders of magnitude higher than other *operando* XAS studies performed on similar electrodes[70,175,176]. We therefore consider that our research can provide valuable and reliable information on structural, chemical and electronic modifications occurring when electrocatalysts are subjected to application-relevant conditions. Further information on the various electrochemical conditions applied are given in the Annex (Table A3).

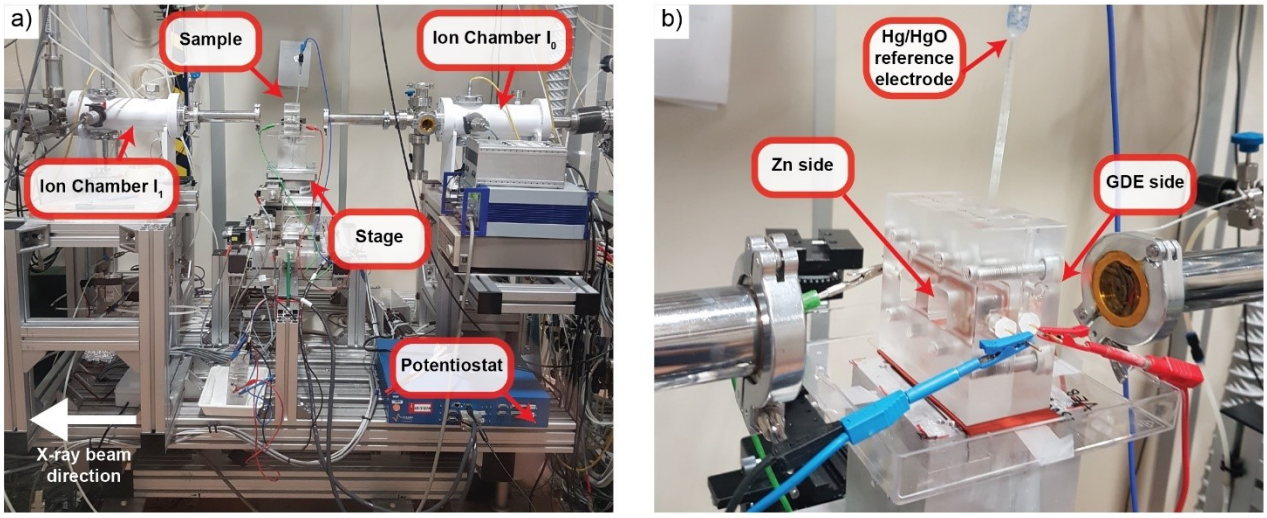

Figure 21: Digital photograph of **(a)** the XAFS beamline at the Synchrotron ELETTRA (Trieste, IT) equipped with our electrochemical setup for *operando* XAS measurements. **(b)** Magnification of the XAS electrochemical cell used.

3. Results and Discussion

3.1. Synthesis and chemical-physical characterization of α-MnO_2

According to Wang and coworkers[148,177], the formation of template-free 1 dimensional (i.e. crystals with only one dimension larger than 100 nm[178]) MnO_2 nanostructures results from the redox reaction between species $S_2O_8^{2-}$ and Mn^{2+}. The chemical equation describing the redox process can be formulated as follows:

Eq. 1) $$MnSO_4 + K_2S_2O_8 + 2H_2O \rightarrow MnO_2 + K_2SO_4 + 2H_2SO_4$$

That comprises the following two half reactions:

Eq. 2) $$Mn^{2+} + 2H_2O \rightarrow MnO_2 + 4H^+ + 2e^-,\ E^0 = 1.23\ \text{V vs. SHE}$$

Eq. 3) $$S_2O_8{}^{2-} + 2e^- \rightarrow 2SO_4{}^{2-},\ E^0 = 2.01\ \text{V vs. SHE}$$

The calculated standard Gibbs free energy change ΔG^0 of the chemical reaction is -151 kJ·mol^{-1}, which implies that the process occurs spontaneously with a very strong tendency to progress toward the formation of the MnO_2 phase[177]. However, several polymorphs of manganese dioxide MnO_2 exists, such as Ramsdellite (α), Pyrolusite (β), Electrolytic (γ), Birnessite (δ), Epsilon (ε) and Spinel type (λ). These share as a common building block MnO_6 octahedra that are linked in different ways to produce the different crystallographic species. The formation of a specific crystal structure depends on several experimental parameters, such as reaction time and temperature, reagents, etc. For the chemical reaction described above, it has been shown that the addition of sulfates in the reaction mixture (such as K_2SO_4 or $(NH_4)_2SO_4$) triggers the selective formation of cryptomelane-type α-MnO_2[148]. It seems that the potassium ions liberated during the chemical reaction serves to stabilize its structure, while an increase of the concentration of $SO_4{}^{2-}$ may be responsible for decreasing the formation rate of different crystal facets, thus facilitating the growth of 1D crystals. A digital camera installed in the microwave reactor enabled to follow (monitor) *in situ* the chemical reaction, as shown by the image sequence illustrated in Figure 22. A picture of the solution was taken before starting the

thermal treatment and it appeared transparent, but as soon as the chemical reaction started (about 2 s), the color changed to a dark violet and after 6 s no additional visible color changes can be further observed. Therefore, we expect that the formation of MnO_2 may take less than 10 s, that is a reasonable time since similar reaction times have already been reported by other studies[148].

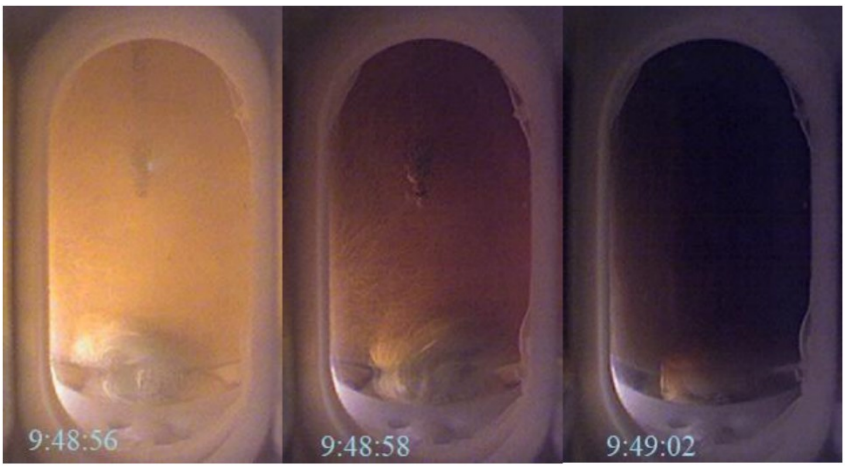

Figure 22: Images acquired *in situ* during the synthesis of the α-MnO_2 following the chemical reaction of Eq. 1. Taken from [179].

The crystal structure of cryptomelane-type α-MnO_2 with formula $K_xMn_8O_{16}$ was reported for the first time by Byström in 1949[180] and it consists of double chains of edge-sharing MnO_6 octahedra, which are linked at their corners to form 1D (2x2) and (1x1) tunnels that extend in a direction parallel to the c axis of the tetragonal unit cell.[181] A schematic representation of the crystal structure of cryptomelane-type α-MnO_2 along the c axis shown in Figure 23.

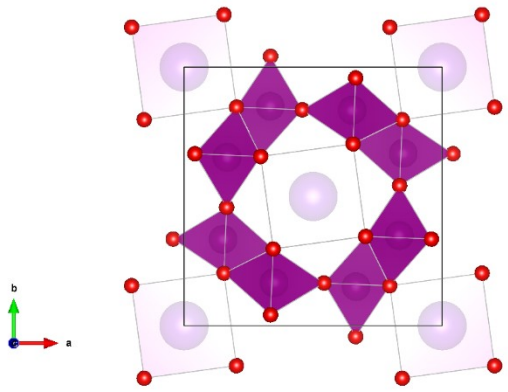

Figure 23: Schematic (visualized with VESTA[163]) displaying the 2x2 tunnel structure of the α-MnO_2 crystal lattice.

The (2x2) tunnel structures have a diameter of about 4.6 Å and are stabilized by the insertion of K^+ ions[182]. The K^+ content of synthetized $K_xMn_8O_{16}$ was determined by calculating the K/Mn molar ratio obtained via ICP-OES method, where the elemental composition (in wt.%) of the sample is indicated in Table 1. The calculated K/Mn ratio is 0.095, which corresponds to 0.76 K^+ ions per structural formula, i.e. $K_{0.76}Mn_8O_{16}$. The ICP-OES analysis also revealed minor traces of S, Ni and Co in the synthetized material (see Tab. 1), may be present in the reagent's solution. Due to the inherent structure of α-MnO_2, metal cations other than K+, such as Ni^{2+} and Co^{2+}, may be also incorporated into the (2x2) tunnels without destroying the original lattice structure.

Table 1: Elemental analysis (in wt. %) of α-MnO_2 determined via ICP-OES technique.

Element	**Mn**	**K**	**S**	**Ni**	**Co**
Percentage (wt.%)	60.5 ± 0.6	4.1 ± 0.6	0.3 ± 0.3	0.2 ± 4.3	0.1 ± 1.6

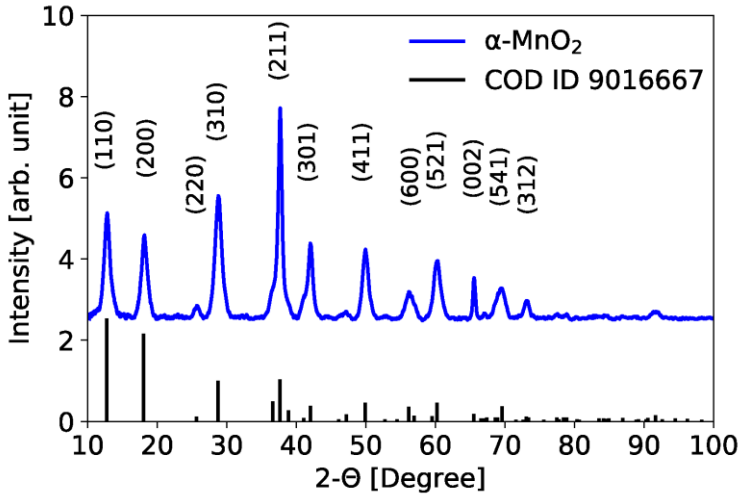

Figure 24: XRD powder pattern of MnO_2 prepared by microwave-assisted hydrothermal synthesis. Taken from [183].

The phase purity of the synthesis product was examined by XRD (Figure 24), where all detected diffraction peaks are indexed by standard α-MnO_2 (COD ID 9016667) with lattice parameters a = 9.815 Å, b = 9.815 Å, c = 2.847 Å. α-MnO_2 has a cryptomelane structure with the space-group *I4/m*, consisting of edge- and corner sharing MnO_6 octahedra. The diffractogram of the as-synthetized α-

MnO_2 powder is characterized by low diffraction intensities and broad peaks, which are indications for small crystallite size and/or high microstructural defect density such as microtwinning or De Wolff disorder[184,185]. The absence of additional peaks, such as those for segregates crystalline phases of other manganese dioxides, indicates that pure α-MnO_2 can be obtained through a rapid and simple microwave-assisted synthesis route. As indicated by Wang and coworkers[186], the difference in relative intensities between the observed diffraction peaks and those of the standard may suggest that the as-synthetized α-MnO_2 have a preferential growth along the [001] direction.

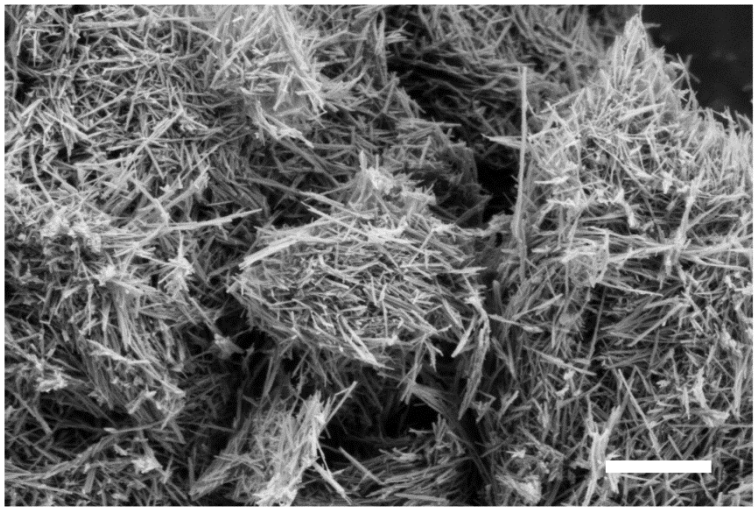

Figure 25: Representative scanning electron micrograph of the as-synthetized manganese dioxide α-MnO_2. Scale bar: 1 μm.

Representative electron micrograph shown in Figure 25 of the synthetized powder indicates that the α-MnO_2 has a fibrous, needle-like morphology. The powder comprises large aggregates of needles, which may be connected by simple electrostatic forces, since their release can be obtained by simply immersing them into an aqueous solution. The measured average length of the MnO_2 particles is about 600 nm and a diameter of 40 nm with low polydispersity attributed to the rapid and uniform heating of the reaction of the microwave-assisted hydrothermal method used for the synthesis of the cryptomelane structure. It has been previously reported that a longer reaction time increases the length of the α-MnO_2 needles, thus indicating a higher crystallinity[148], while the temperature of the reaction is important in determining the polymorphism of the MnO_2. It was observed that by

performing the synthesis of MnO_2 at 150°C (rather than 200°C) for the same reaction time (10 min), the birnessite type δ-MnO_2 is formed, as confirmed by the XRD analysis shown in Figure 26a. However, the XRD pattern also shows the appearance of small diffraction peaks ($2\theta \approx 16°$ and $2\theta \approx 28°$) that belong to the α-MnO_2 phase. These findings are supported by the experimental study of Birgisson et al.[187] who used different *in situ* diffraction techniques to identify the mechanism of formation and the polymorph evolution of manganese dioxide during hydrothermal synthesis. The reaction process includes the initial formation δ-MnO_2, which then transforms into α-MnO_2 and this is finally converted into β-MnO_2. In the same study, both the initiation and the rate of phase transformation have been shown to be temperature dependent, where higher temperatures provide higher reaction rates. A schematic representation of the proposed phase transformation mechanism of manganese dioxide is shown in Figure 27.

Interestingly, the morphology of the synthesized δ-MnO_2 phase also differs significantly from that of the α-MnO_2 phase, where the particles have flower-like morphologies (Figure 26b).

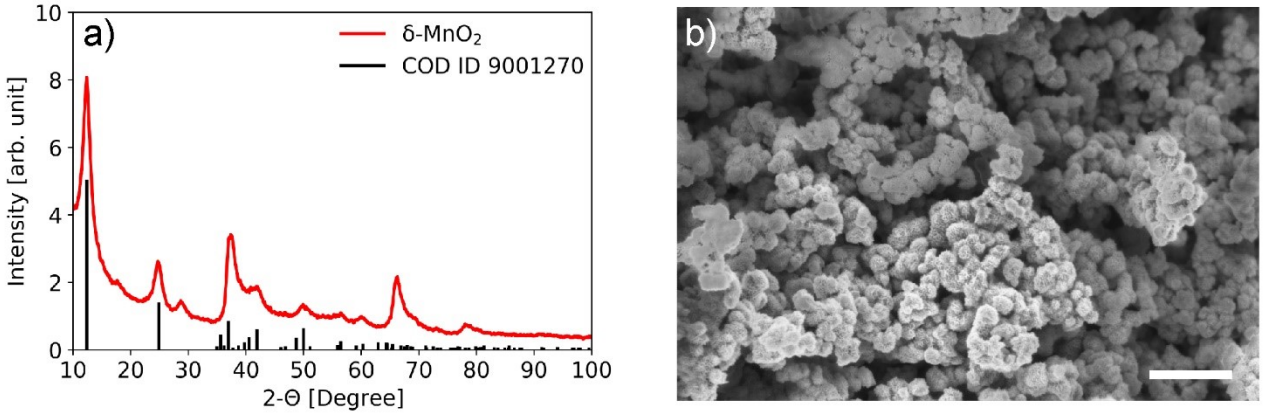

Figure 26: (a) XRD pattern and **(b)** representative SEM image of the synthetized δ-MnO_2 phase. Scale bar: 1 µm.

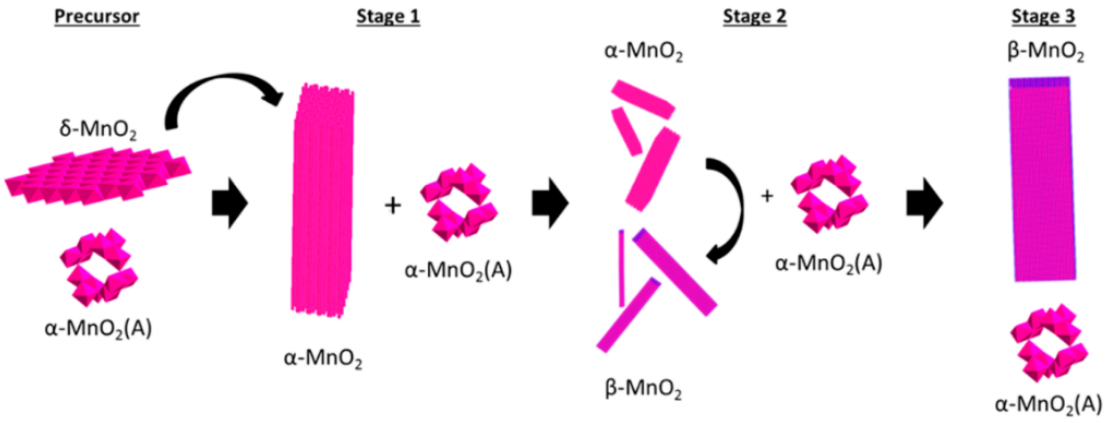

Figure 27: Schematic representation of the transformation mechanism of manganese dioxide proposed by Birgisson et al. Taken from [187].

The nitrogen adsorption isotherm of α-MnO_2 (Figure 28) belongs to type IV (IUPAC classification), characterized by the formation of a hysteresis loop at high relative pressure close to saturation (p/p^o = 0.8-1.0). The origin of the latter is due to capillary condensation in the mesopores[157], indicative for the mesoporous nature of the sample. At low relative pressures the N_2-sorption profile indicates that monolayer formation is the dominant process, whereas multilayer formation takes place at high partial pressures[148,149]. The specific surface area estimated by the BET method is approximately 86.1 ± 0.1 $m^2 \cdot g^{-1}$ that is in well agreement with other reported study that prepared α-MnO_2 by microwave-assisted method[148]. In catalysis, a high specific surface area is usually required as the reaction occurs on the catalytic surface. As a result, higher specific area results in higher reaction rates.

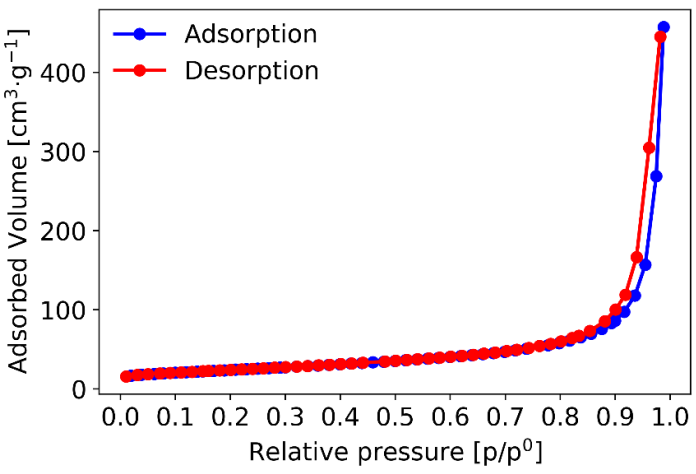

Figure 28: N_2-soprtion isotherms of the as-synthetized manganese dioxide α-MnO_2.

3.2. A Comprehensive study on the ORR activity and selectivity of α-MnO_2/C catalyst composite via RDE and RRDE techniques

The purpose of this section is to illustrate the experimental RDE and RRDE procedure used to evaluate the electrochemical activity towards ORR of different electrocatalysts. This also includes a discussion on the reproducibility and accuracy of this technique in reporting the relevant electrochemical data. The material used for this study is the synthetized cryptomelane-type α-MnO_2 mixed with carbon C65 with nominal ratio 50:50. The detailed description on the preparation of the catalyst layer can be found in the chapter Experimental Methods (*2.3. Electrochemical techniques and electrode preparation methods*). The Annex includes a discussion on the refinement of the catalysts layer composition for RDE and RRDE measurements, where the optimum active mass loading on the GC disk was found to be 10 mg. The influence of the cycle number on the shape of the voltammogram recorded in N_2-saturated 0.1 M KOH electrolyte is shown in Figure 29, where the two black arrows indicate the shift direction of the CV curves with cycle number. To obtain representative voltammograms and to compare the data, only the third cycle of the entire CV test was considered, since extensive cycling would cause substantial modification of the original composition and structure of MnO_2[184], as also evidenced in Figure 29. On the other hand, the initial two CV cycles were considered as a surface cleaning step that may serve to remove impurities, as well as to activate the surfaces of the electrocatalyst.

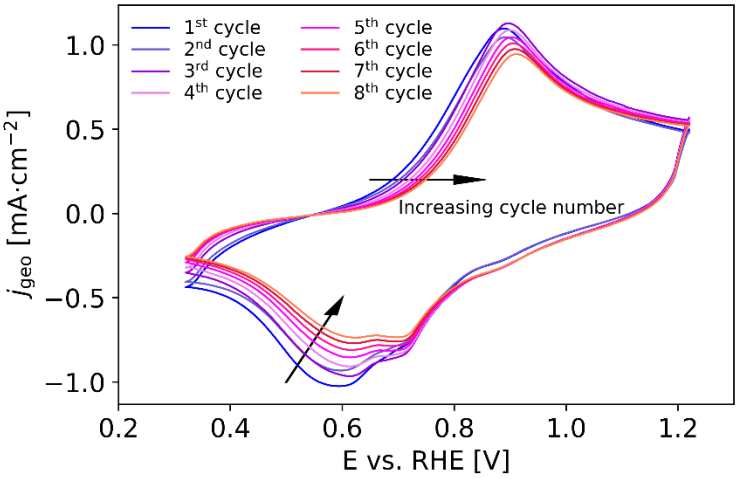

Figure 29: Cyclic voltammograms at 5 mV·s^{-1} in in N_2-saturated 0.1 KOH of α-MnO_2/C catalyst composite mixture.

To show the reproducibility of the RDE and RRDE techniques, each measurement was repeated three times by drop-casting a new catalyst layer on the RDE tip. The averaged CV curve of three catalyst layers α-MnO_2/C with nominal ratio 50:50 is shown in Figure 30.

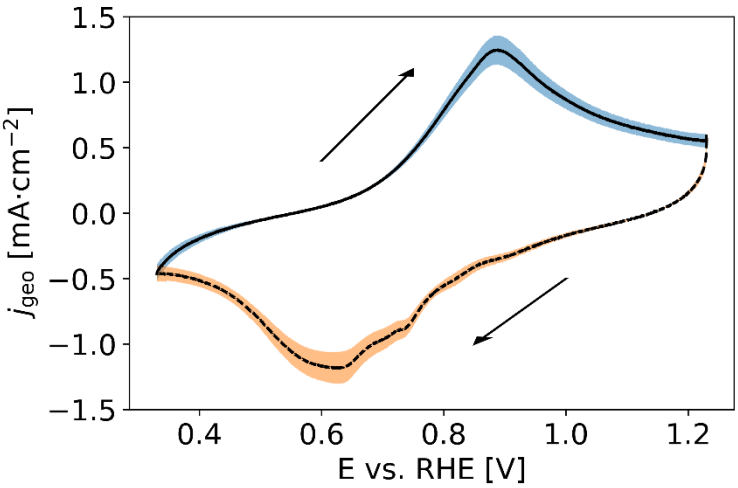

Figure 30: Cyclic voltammogram at 5 mV·s^{-1} in in N_2-saturated 0.1 KOH of α-MnO_2/C averaged over three catalyst layers. The arrows and the shadow area represent the potential sweep direction and the confidence interval, respectively.

In order to differentiate the sweep directions of the electrode potential, the voltammograms were indicated with a black dashed line to represent the scan from high to low potential (defined as cathodic sweep), and with a black solid line for the opposite scan direction (anodic sweep), respectively. In the same plot the measurement uncertainty (equal to the standard deviation, which is defined as the

square root of the average of the squared deviations from the mean[188]) is shown by a blue and an orange area depending on the potential sweep direction. The voltammogram exhibits two mayor anodic and cathodic peaks, which are located at electrode potentials of 0.63 V and 0.89 V vs. RHE, respectively. The largest deviation between the three measurements was observed at the position of the two main peaks, with values of -1.2 ± 0.1 $mA \cdot cm^{-2}$ for the cathodic peak and 1.2 ± 0.1 $mA \cdot cm^{-2}$ for the anodic peak, respectively. Several studies[184,189] reported similar anodic and cathodic peaks, which are attributed mainly to a pseudocapacitive process, which consists of a faradaic redox reaction occurring within and at the surface of the MnO_2. This differs from a pure capacitive non-faradaic process, which is based on the separation of charges at the electrode/solution interface. In the case of MnO_2, the two peaks can be assigned to different mechanisms that occur simultaneously, first being the pseudocapacitive transition of the redox couple MnO_2 and MnOOH corresponding to a reversible proton insertion, as described by the following redox reaction[189]:

Eq. 4) $$MnO_2 + H_2O + e^- \leftrightarrow MnOOH + OH^-$$

And the second being an effect from the KOH electrolyte, which can be further classified in i) a capacitive (non-faradaic) process that involves the adsorption and desorption of K^+ ions on the surface of the MnO_2 catalyst[190,191]:

Eq. 5) $$(MnO_2) + K^+ + e^- \leftrightarrow (MnO_2{}^-K^+)_{surface}$$

and ii) a second pseudocapacitive redox process in which the K^+ ions intercalate inside the interstitial sites of the MnO_2 structure[192]:

Eq. 6) $$MnO_2 + K^+ + e^- \leftrightarrow MnO.OK$$

Furthermore, a small voltammetric wave preceding the main reduction peak is also visible in Figure 30. According to the work of Chabre and Pannetier[185], the latter may be attributed to easily reducible Mn^{4+} sites incompletely coordinated by oxygen. It is believed that these surface active Mn^{4+} sites could play an important part in the ORR catalysis.

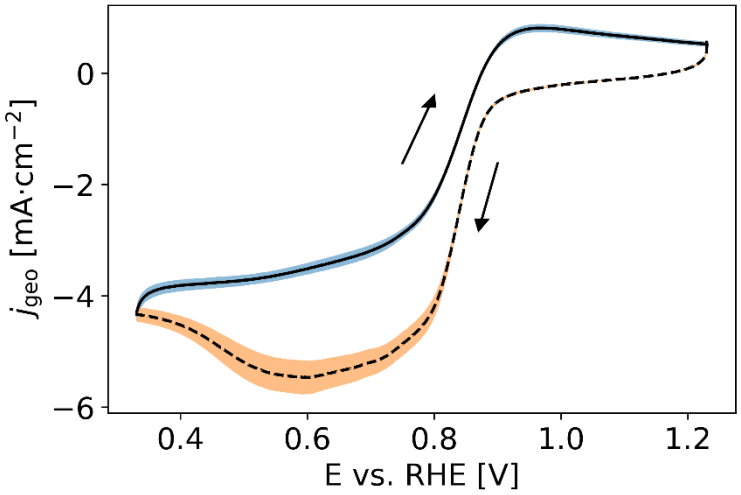

Figure 31: Cyclic voltammogram at 5 mV·s^{-1} in O_2-saturated 0.1 KOH at 1600 rpm.

The voltammogram in O_2-saturated 0.1 M KOH electrolyte is shown in Figure 31. At potentials > 0.9 V the current density is close to zero (neglecting the background current due to the pseudo-capacitive processes previously described), indicating that no major electrochemical reaction is taking place. This corresponds to an infinite resistance of the electrode/electrolyte interface. At potentials ≤ 0.9 V vs. RHE, the situation changes drastically, where the measured cathodic current density increases, indicating that the MnO_2/C composite is highly active towards ORR. The short region of the voltammogram that follows the net zero current, is the so-called activation-controlled region, i.e. when the reaction rate is only limited by the kinetic of the catalyst, which is proportional to the applied potential. The potential at which the current begins to increase is usually referred as the onset potential (here defined as the potential where the current density j_{geo} ≤ - 0.1 mA·cm^{-2}). A mixed-controlled region is observed in the potential region of 0.8 - 0.9 V vs. RHE. At potentials ≤ 0.8 V vs. RHE a plateau is formed, suggesting that the reaction is under O_2-reactant mass transport control. The cathodic current density in the O_2-reactant mass-transport limiting region (at 0.6 V vs. RHE) is -5.46 ± 0.30 mA·cm^{-2} and -3.51 ± 0.11 mA·cm^{-2} for the forward and reverse scan, respectively. According to the Levich equation, the main parameter that influence the magnitude of current density in the diffusion limiting region is the concentration of O_2 reactant that is controlled by diffusion. On the other hand, it can be seen from Figure 31 that there is only a minor deviation in the measured current

densities in the activation region between the three samples. That is not surprising since the reaction rate in the kinetic region is predominantly controlled by the intrinsic activity of the electrocatalyst and the three catalyst layers have identical composition and the loading is the main parameter affecting the measured current density.

Interestingly, the forward and reverse scans do not overlap in O_2-saturated electrolyte, where the magnitude of the current density of the cathodic sweep is larger than the reverse one. Moreover, the slope of the two curves differs in the mixed-controlled region, which is may indicative for a different rate determining step or mechanism that governs the electrochemical reaction. This may be attributed to structural changes occurring on the catalyst surface, which is also supported by the asymmetric redox couple observed in the CV in N_2-saturated electrolyte (Figure 30). However, the common practice in the literature[124] for the description of the ORR activity is to report the slope for the anodic potential sweep, thus avoiding an overestimation of the catalytic activity due to additional contributions, which do not belong to the ORR process. However, the voltammogram shown in Figure 31 still contains the capacitive and/or pseudocapacitive contributions of MnO_2. To separate these additional effects from the ORR current, the CV under N_2 atmosphere (Figure 30) is subtracted from the CV recorded in O_2 (Figure 31), resulting in the background corrected CV, as shown in Figure 32. It may be noted that the region of infinite resistance (i.e. at potentials higher than the ORR onset potential, $E > 0.9$ V vs. RHE) flattens, and the recorded current approaches to zero. Moreover, the onset potential can be more readily detected, as well as located at the point where the current density increases abruptly. The onset potentials for the ORR are 0.95 V and 0.94 V vs. RHE for the cathodic and anodic sweeps, respectively. Although the literature uses various definitions for the onset potential, common reported values for MnO_2/C-based catalysts are usually in the range of 0.8-0.9 V vs. RHE[117], which is in good agreement with our findings. It can also be noticed that, as a result of the background subtraction, the amplitude of the current density in the diffusion limiting area is slightly reduced.

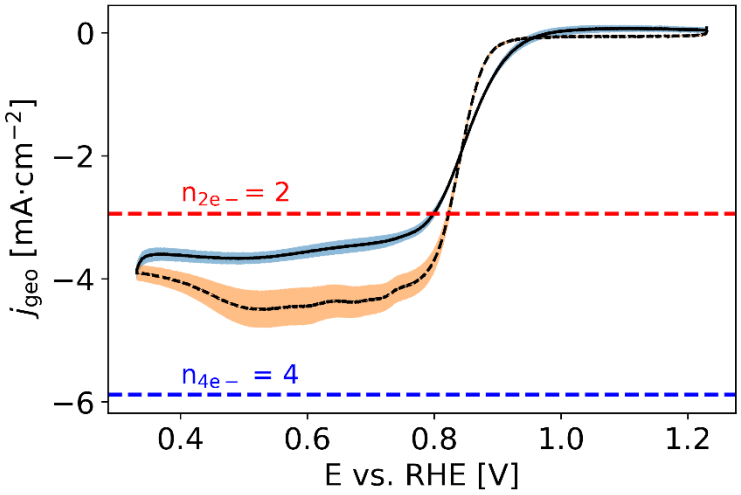

Figure 32: N_2-background corrected cyclic voltammogram of MnO_2/C mixture in O_2 saturated 0.1 M KOH. The horizontal red and blue dashed lines represent the theoretical current densities for the $2e^-$ and $4e^-$ ORR processes at 1600 rpm, respectively.

According to the Levich theory, the theoretical limiting currents at rotation speed of 1600 rpm for the $2e^-$ ($j_L^{2e^-} = -2.94\ mA \cdot cm^{-2}$) and $4e^-$ ($j_L^{4e^-} = -5.88\ mA \cdot cm^{-2}$) ORR process can be calculated using the following parameters in the Levich equation, in accordance with the experimental conditions applied:

The diffusion coefficient of O_2 in 0.1 M KOH is $D_{O_2} = 2 \times 10^{-5}\ cm^2 \cdot s^{-1}$

The kinematic viscosity of the electrolyte is $\nu = 1 \times 10^{-5}\ cm^2 \cdot s^{-1}$

The concentration of O_2 in the bulk electrolyte is $C_{O_2} = 1.2 \times 10^{-6}\ mol \cdot cm^{-3}$

The rotation speed of the working electrode is $\omega = 1600\ rpm = 167.5\ rad \cdot s^{-1}$

The two limiting cases of the diffusion limiting currents are represented in Figure 32 by two parallel horizontal lines. It can be noticed that the measured average diffusion limiting current density of MnO_2/C is somehow centered between the two limiting cases. For the full estimation of the number of transferred electrons (n), the same voltammogram was acquired at different rotation rates: 400, 900, 1600 and 2500 rpm. The set of N_2-background subtracted voltammograms in O_2 atmosphere at variable rotation speeds is depicted in Figure 33a. To perform the K-L study, the current was sampled

at 0.8 V vs. RHE, that is located in the rising portion of the voltammogram (mix-controlled region). The K-L plot of the reciprocal current $\frac{1}{I}$ against the reciprocal root of the angular rotation rate $\omega^{-1/2}$ yields to a linear relationship (Figure 33b). The same figure also includes the calculated K-L lines of theoretical 2e- and a 4e- processes. For the cathodic and anodic sweep, the fits of the experimental data with the K-L equation give the experimental value of n=3.5 and n=3.7, respectively. This finding is consistent with previous literature studies[128,129] that reported values of n ≈ 4, indicative for the 4-electron ORR pathway.

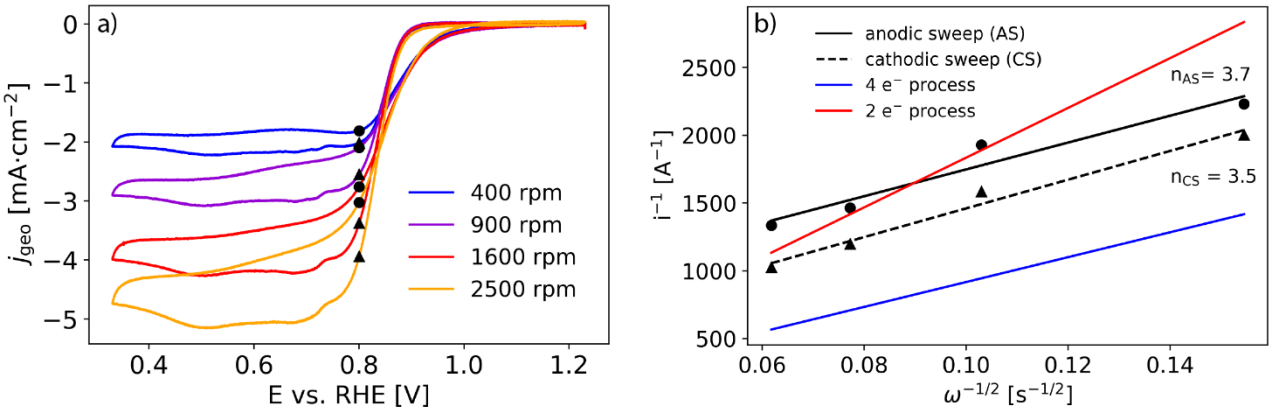

Figure 33: (a) N_2-background corrected cyclic voltammograms of MnO_2/C in O_2-saturated 0.1 M KOH at different electrode rotation rates. **(b)** Koutecký-Levich plots calculated at 0.8 V vs. RHE. The red and blue solid lines represent the theoretical K-L plots for the $2e^-$ and $4e^-$ ORR processes, respectively.

As previously mentioned, a more reliable method for the estimation of n, is the RRDE technique. In addition of being a relatively simple method, RRDE allows a straightforward determination of the peroxide HO_2^- yield, which is directly proportional to the apparent electron transfer number of the ORR process. The percentage of HO_2^- and the equivalent electron transfer number n are shown in Figure 34, as a function of the applied disk potential. The potential window considered for the estimation of HO_2^- and n is between 0.34 and 0.85 V vs. RHE, since at E_{disk} > 0.85 V the measurement is no longer reliable due to the extremely low current densities recorded at the ring (< 1 μA·cm^{-2}). The electron transfer number calculated using this method gives a value of n= 3.97 and 3.93 for the cathodic and anodic sweep at the disk electrode potential E_{disk} = 0.8 vs. RHE, respectively, meaning

that the MnO_2/C mixture follows the 4 e- ORR pathway. Similarly, the peroxide HO_2^- yield of the reaction is in the range of 5.0 ± 0.5 %, thus indicating that most of the O_2 molecules participating to the ORR are reduced into OH^-.

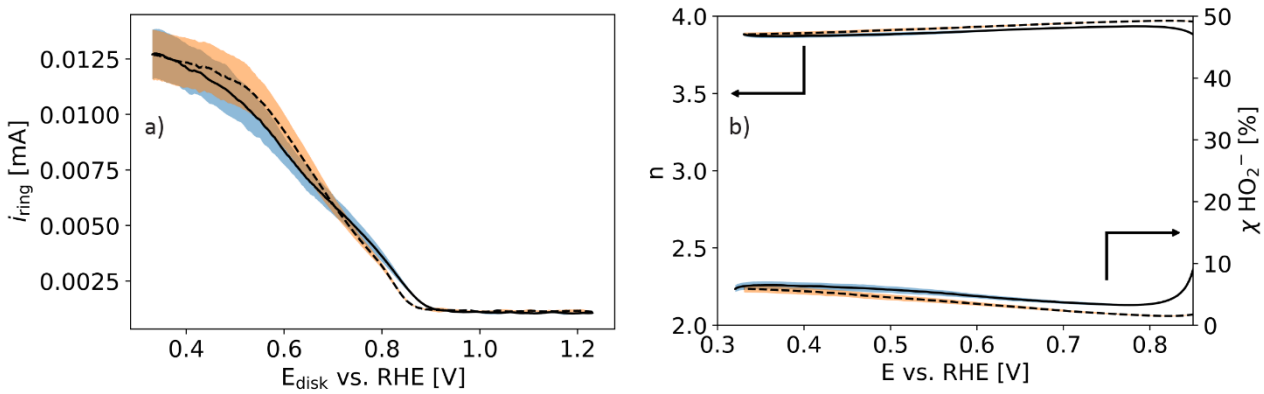

Figure 34: (a) Ring current as a function of (disk) electrode potential. **(b)** Measured number of transferred electrons n (left) and hydrogen peroxide HO_2^- yield (right) vs. electrode potential.

While the mechanistic for the oxygen reduction reaction on MnO_x/C-based electrodes has been extensively studied and it is still being under exploration, one the most accepted and likely mechanism for manganese dioxide-based material consists of a so-called series pathway[122,128,193]. In the series pathway, the oxygen is first reduced to peroxide through a 2e- process at the carbon surface:

Eq. 7) $$O_2 + H_2O + 2e^- \rightarrow HO_2^- + OH^-,\ E_0 = -0.065\ \text{V vs. SHE}$$

After the completion of the first 2e- reduction step, the peroxide is either reduced into OH^- via a 2e- process:

Eq. 8) $$HO_2^- + H_2O + 2e^- \rightarrow 3OH^-,\ E_0 = 0.867\ \text{V vs. SHE}$$

or transformed to O_2 in half the original amount via a chemical disproportionation reaction, as indicated by the following equation:

Eq. 9) $$HO_2^- \rightarrow \frac{1}{2}O_2 + OH^-$$

The produced O_2 is reduced back to HO_2^-, which then undergoes another disproportionation to O_2, thus generating a cycle loop that is repeated until reaching the theoretical limit of an apparent 4e- process (2 + 1 + ½ + ¼ + … ≈ 4)[194].

In order to compare the ORR activity of different catalyst mixtures, the intrinsic kinetic current density was considered. The kinetic currents were retrieved via mass-transport correction of the background corrected voltammograms by rearranging the Koutecký-Levich equation as follows:

Eq. 10) $$j_{kin} = \frac{j_L \cdot j}{j_L - j}$$

where the value of the diffusion limiting current density j_L was taken at the recorded disk electrode potential of 0.34 V vs. RHE, that is (≤ -3.82 mA·cm^{-2} at 1600 rpm), see Figure 32. The kinetic current density (averaged over three separate measurements) is shown in Figure 35, where the mass-transport correction is evidenced by the absence of the plateau at higher current densities (≤ -3.82 mA·cm^{-2}), whilst the onset potential of the two curves remained virtually unchanged. It may be noticed that the cut-off potential and current density in Figure 35 was arbitrarily chosen to be 0.8 V vs. RHE and -10 mA·cm^{-2}, respectively.

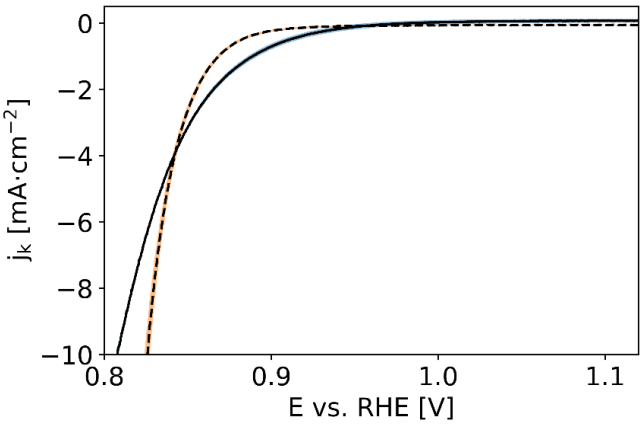

Figure 35: Potential dependence of the ORR activity in terms of kinetic current density. The black dashed- and solid lines represent the cathodic and anodic sweep direction, respectively. Potential sweep rate: 5 mV·sec^{-1}. O_2-saturated 0.1 M KOH electrolyte. Rotation rate: 1600 rpm.

3.3. Optimization of a ternary catalyst composite for enhanced ORR and OER activities

Part of this chapter has been published in Journal of Power Sources [183].

Herein, a systematic study about the influence of the catalyst material composition for the promotion of the ORR and OER activities based on α-MnO_2, commercial carbon black (C) and Ni(core)/NiO(shell) nanoparticles, and that are very simply mixed together in aqueous alcohol solution, is presented. Binary mixtures, namely $(C)_{100-x}(MnO_2)_x$, $(Ni/NiO)_{100-x}(C)_x$ and $(Ni/NiO)_{100-x}(MnO_2)_x$ at different weight ratios, allowed for the identification of the best material composition for both ORR and OER taken separately. We detail synergetic effects taking place on both activity and stability of the materials by means of rotating ring disk electrode (RRDE) technique. A stable and highly ORR/OER active ternary composite catalyst $(C)_{100-x}(MnO_2)_{100-y}(Ni/NiO)_{100-x-y}$ derives from these findings and such design strategy.

3.3.1. Physical-chemical characteristics of the catalyst materials

The change in properties towards ORR and OER for three families of $A_{100-x}B_x$ catalyst materials, namely $(C)_{100-x}(MnO_2)_x$, $(Ni/NiO)_{100-x}(C)_x$, and $(Ni/NiO)_{100-x}(MnO_2)_x$, were investigated as function of the nominal composition of the binary mixtures in a systematic fashion. The subscripts 100-x and x indicate the weight fraction for component A and B, respectively. Preparation procedures for these low-cost catalysts materials where kept as simple as possible to facilitate future scale-up, details are given in the Experimental Methods chapter. Briefly, the catalyst materials involve both commercially available carbon black (C) and 5-20 nm Ni/NiO core-shell nanoparticles (NPs) and an α-MnO_2 prepared in-house (see chapter 3. Synthesis and chemical-physical characterization of α-MnO_2) that are simply mixed together in aqueous ethanol solution and deposited on an electrode substrate. Low to moderate specific surface areas, as-measured by N_2-adsorption are 80 $m^2 \cdot g^{-1}$, 60 $m^2 \cdot g^{-1}$ and 8 $m \cdot g^{-1}$ for α-MnO_2, C and Ni/NiO NPs, respectively, alleviate for, in principle, an optimal dispersion between the components aiming at the maximization of the useful fraction of the active material. Representative scanning electron micrographs, acquired prior electrochemical investigations, for the

whole set of catalyst materials are displayed in Figure 36. The $(C)_{100-x}(MnO_2)_x$ composite (Figure 36, top row) exhibits a mesoscopic evolution in its morphology as the weight fraction of MnO_2 increases, from a more porous and corpuscular structure dictated by the carbon particles for C weight percentage above 50 % towards a more fibrous architecture for the highest MnO_2 content that is typical for α-MnO_2[125,149]. On the other hand, $(Ni/NiO)_{100-x}(MnO_2)_x$ and $(Ni/NiO)_{100-x}(C)_x$ composites (in Figure 36 middle row and bottom row, respectively) exhibit both a highly compact/dense structure at high Ni/NiO contents. For MnO_2 content in $(Ni/NiO)_{100-x}(MnO_2)_x$ above 25 wt.% the needle-like structure of the manganese dioxide becomes clearly predominant. At lower MnO_2 weight fraction, the Ni/NiO NPs seem to fill the voids between the anisotropic MnO_2 particles giving rise to a more compact and continuous matrix. Nevertheless, it can be seen from Figure 36 (bottom) that Ni/NiO and carbon does not form a homogeneous mixture in $(Ni/NiO)_{100-x}(C)_x$ composites, but rather segregate in two separate/immiscible phases. The variation of weight ratio between the two species results in an equivalent change in the relative fraction of the two phases. Hence, the simple mixing of the components in aqueous ethanol solution delivers materials presenting a morphological evolution consistent with changes in their compositional characteristics. This, in turn, confirms a preparation of the electrocatalyst materials easy to control, which, furthermore, does not present any demanding steps impeding future scale-up.

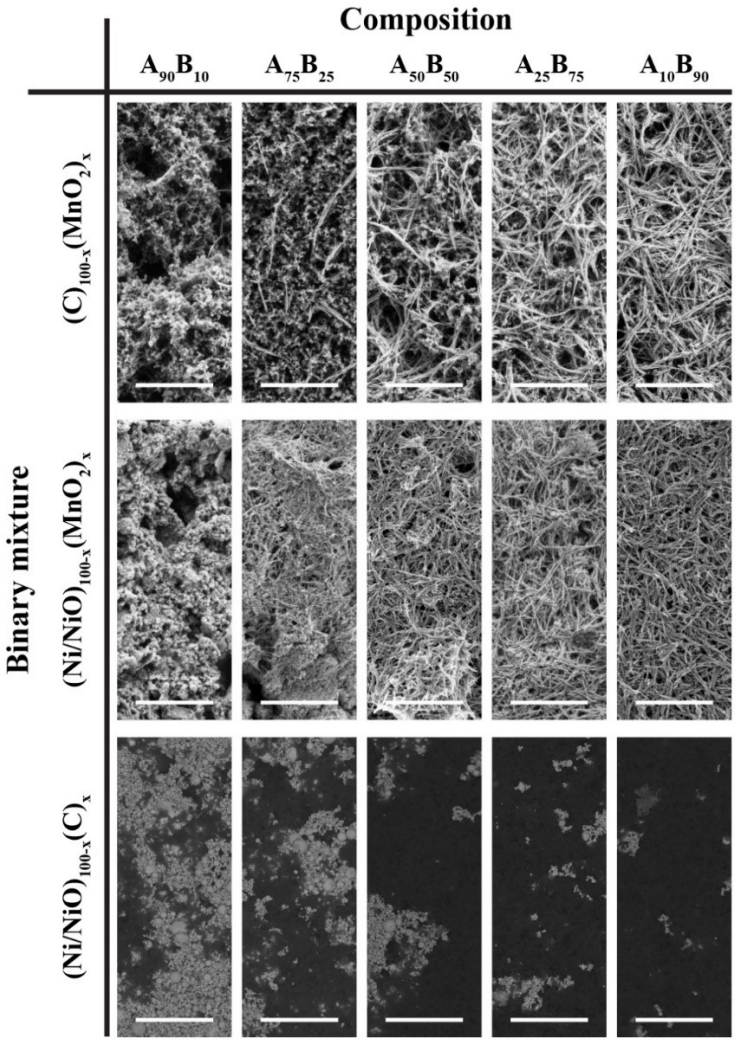

Figure 36: Evolution of mesoscopic morphology of binary electrocatalysts. Set of SEM images representative of the morphological evolution of the binary composites catalyst materials $(C)_{100-x}(MnO_2)_x$ (top row), $(Ni/NiO)_{100-x}(MnO_2)_x$ (middle row), $(Ni/NiO)_{100-x}(C)_x$ (bottom row) as a function of nominal composition. Scale bar: 2 µm. Taken from [183].

3.3.2. Electrocatalytic properties of binary mixtures

The activity for the ORR of each catalyst materials in contact with 0.1 M KOH solution was evaluated by potentiodynamic polarization methods at 5 $mV \cdot s^{-1}$ under well-defined mass transport conditions. Information relative the electrode preparation and applied experimental conditions are described in the chapter Experimental Methods. Polarization curves obtained experimentally are exemplified in Figure 37 and exhibit very similar characteristics to previously reported data on analogous catalyst materials[123,195,196].

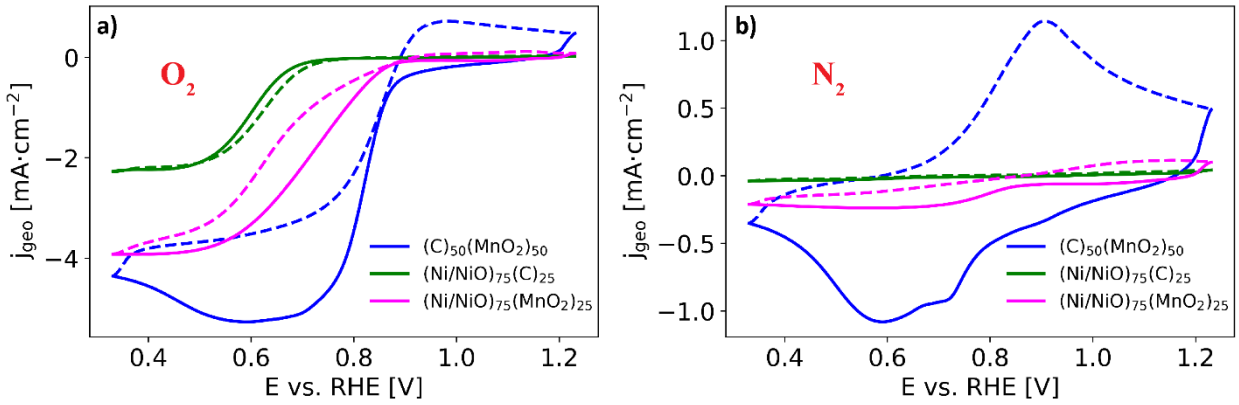

Figure 37: Cyclic voltammograms at 5 $mV \cdot s^{-1}$ in O_2 **(a)** and in N_2 **(b)** saturated 0.1 KOH. In order to differentiate the sweep directions of the electrode potential, we indicated the voltammograms with a dashed line, representing the scan from low to high potential (positive-going potential scan), and with a solid line for the opposite scan direction, respectively. Taken from [183].

Peroxide production resulting from incomplete O_2 reduction stayed minor, with very little dependence on the electrode potential, over the whole potential range investigated, and is also barely influenced by the nominal composition for all the samples investigated, see Figure 38. Thus, the total amount of electron exchanged by the reaction above 0.6 V was found equal to 3.89 ± 0.02, 3.85 ± 0.07 and 3.52 ± 0.06 for $(C)_{100-x}(MnO_2)_x$, $(Ni/NiO)_{100-x}(MnO_2)_x$ and $(Ni/NiO)_{100-x}(C)_x$, respectively, indicating almost complete O_2 reduction reaction on all samples. Figure 39a exemplifies kinetic current densities for the ORR obtained during the positive-going potential scan for three selected binary composites. ORR is initiated at 1.05 V, 0.70 V and 0.85 V for $(C)_{50}(MnO_2)_{50}$, $(Ni/NiO)_{75}(C)_{25}$, and $(Ni/NiO)_{75}(MnO_2)_{25}$, respectively, and the currents increase exponentially as the electrode potential is further lowered. By plotting the potential against the logarithm of the kinetic current, the Tafel slope can be obtained. Tafel slopes (Figure 39b) are found very similar for $(C)_{50}(MnO_2)_{50}$, $(Ni/NiO)_{75}(C)_{25}$, 106 $mV \cdot dec^{-1}$ and 96 $mV \cdot dec^{-1}$, respectively and in good agreement with the literature[196,197], while it differs significantly for $(Ni/NiO)_{75}(MnO_2)_{25}$ with two Tafel slopes of 200 $mV \cdot dec^{-1}$ and 150 $mV \cdot dec^{-1}$ in the low and high overpotential ranges, respectively. This suggests for the latter catalyst material either a change in the ORR rate-determining step or a different reaction mechanism for the ORR than for the two former ones.

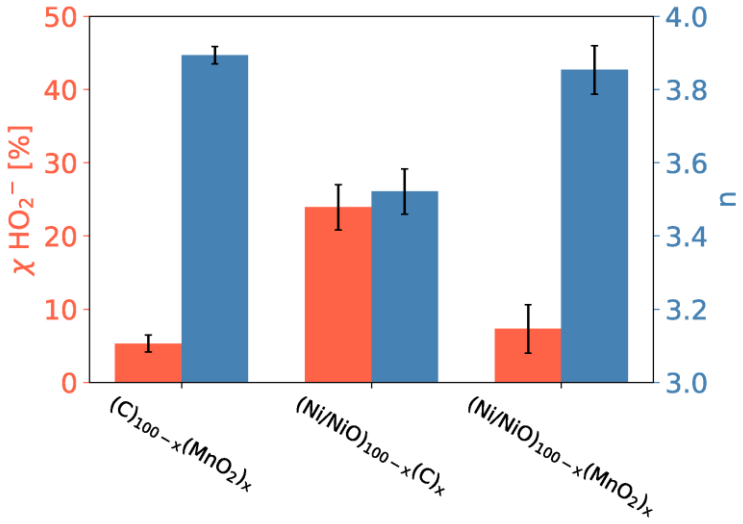

Figure 38: Average number of transferred electrons (n) and hydrogen peroxide yield (χ HO_2^-) for $(C)_{100-x}(MnO_2)_x$, $(C)_{100-x}(Ni/NiO)_x$, $(Ni/NiO)_{100-x}(MnO_2)_x$. Taken from [183].

In order to compare the whole set of compositions for the catalyst materials, we defined as a general descriptor for the ORR activity the overpotential at the kinetic current density j_k = -1 mA·cm^{-2}, which is represented by a black horizontal dashed line in Figure 34a. This current density is reached for the binary mixture $(C)_{50}(MnO_2)_{50}$ at a significantly lower overpotential (η_{ORR} = 0.32 V) compared to $(Ni/NiO)_{75}(MnO_2)_{25}$ (η_{ORR} = 0.50 V) and $(Ni/NiO)_{75}(C)_{25}$ (η_{ORR} = 0.58 V). The remarkable ORR activity in alkaline solution of carbon/MnO_2 materials compares well with previous results reported in the literature[123,129,195,197]. Even though a very limited number of studies detailing ORR activities for mixtures C/Ni and Ni/MnO_2 composites is available, the general trend for the activity of the different binary mixtures $(C)_{50}(MnO_2)_{50}$ > $(Ni/NiO)_{75}(MnO_2)_{25}$ > $(Ni/NiO)_{75}(C)_{25}$ is in good agreement with previous reports[123,125,196].

Figure 39c shows plots of the overpotential for the ORR at j_k = -1 mA·cm^{-2} for all the binary systems $(C)_{100-x}(MnO_2)_x$, $(Ni/NiO)_{100-x}(C)_x$ and $(Ni/NiO)_{100-x}(MnO_2)_x$ investigated as a function of weight ratio between the two components in the catalyst materials. First, for both $(C)_{100-x}(MnO_2)_x$ and $(Ni/NiO)_{100-x}(C)_x$ mixtures the ORR activities exhibit a volcano-shaped behavior with optima (i.e. the lowest overpotential) at the nominal composition $(C)_{50}(MnO_2)_{50}$ and $(Ni/NiO)_{50}(C)_{50}$. The $(C)_{100-x}(MnO_2)_x$ mixture largely outperforms the other two binary systems over the entire compositional

range. Furthermore, the extent in the variation of the overpotential with the nominal composition is significantly lower for $(Ni/NiO)_{100-x}(C)_x$ than for $(C)_{100-x}(MnO_2)_x$, 30 mV and 60 mV, respectively. Such low variation with the nominal composition in the case of $(Ni/NiO)_{100-x}(C)_x$ might be tentatively related to the segregation between the two components (see Figure 36) assuming that the most active catalytic site for this material is at the boundaries C-Ni/NiO (the absolute amount of boundaries should vary little with the C content due to this segregation). Second, $(Ni/NiO)_{100-x}(MnO_2)_x$ exhibits the largest variation of the overpotential as a function of composition (about 200 mV), with a continuous decay of the overpotential as the fraction of MnO_2 increases, from η_{ORR} = 0.63 V for $(Ni/NiO)_{90}(MnO_2)_{10}$ to η_{ORR} = 0.43 V for $(Ni/NiO)_{10}(MnO_2)_{90}$. Interestingly, these two values approximately match with the values of η_{ORR} = 0.60 V for $(Ni/NiO)_{90}(C)_{10}$ and η_{ORR} = 0.40 V for $(C)_{10}(MnO_2)_{90}$. This whole set of observations about the dependency of the ORR overpotential on the chemical nature and the compositional characteristics of the binary catalyst materials indicates that i) the catalytic properties of Ni/NiO for the ORR is only slightly modified by 10 wt.% of C or of MnO_2 and ii) that for 90 wt.% MnO_2 content the intrinsic ORR catalytic properties of MnO_2 are barely modified by 10 wt.% of Ni/NiO or of C. Furthermore, the addition of Ni/NiO in $(Ni/NiO)_{100-x}(MnO_2)_x$ only acts as a dilution of the most active catalytic site at the α-MnO_2 surface. On the other hand, the volcano-shaped dependence on the nominal composition for $(C)_{100-x}(MnO_2)_x$ and $(Ni/NiO)_{100-x}(C)_x$ suggests the creation of new catalytic sites (or catalytic ensembles) induced by the carbon addition that are more active than the catalytic sites exhibited by the surface two transition metal oxide materials.

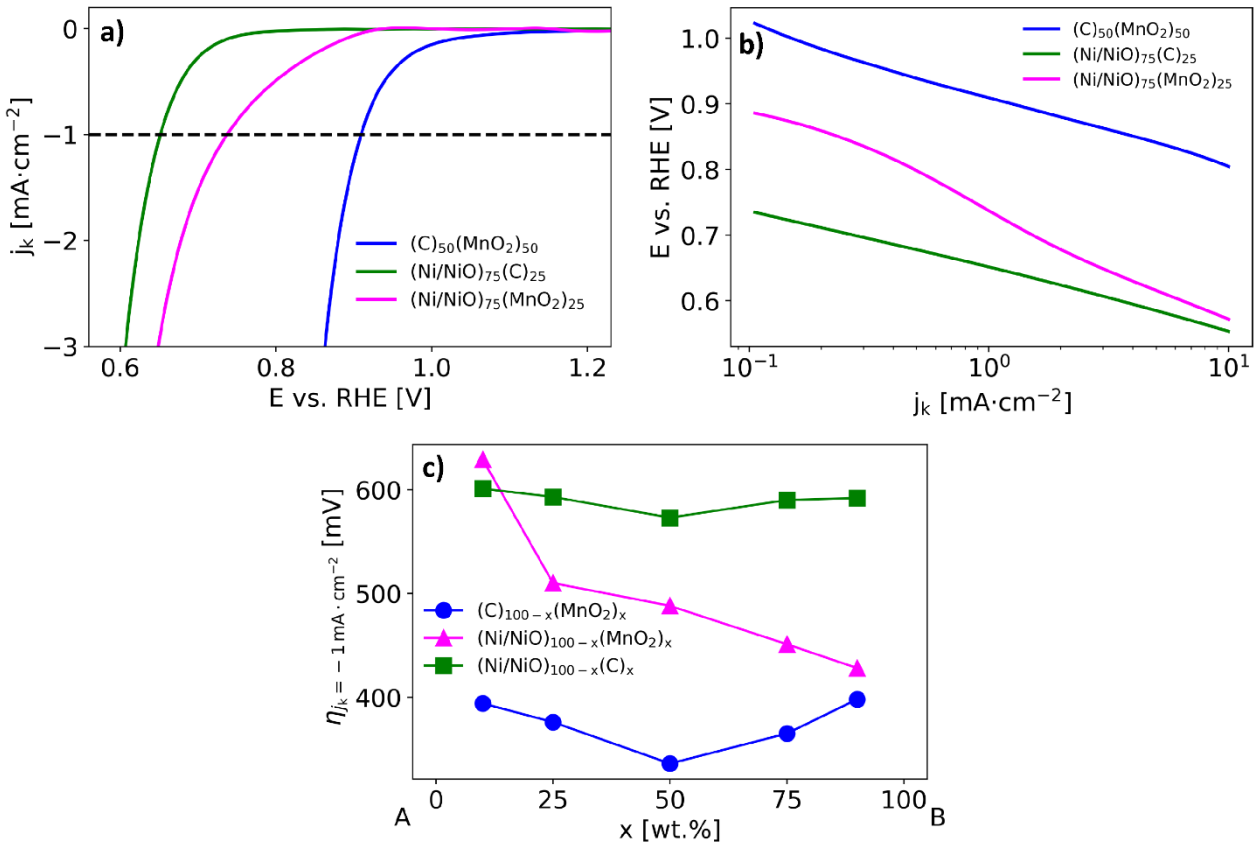

Figure 39: (a) Potential dependence of the electrocatalytic activity towards the ORR for three selected binary composites, as labelled in the figure. **(b)** ORR Tafel slopes for $(C)_{50}(MnO_2)_{50}$, $(Ni/NiO)_{75}(C)_{25}$, and $(Ni/NiO)_{75}(MnO_2)_{25}$. **(c)** Compositional dependence of the overpotential at the kinetic current density j_k = -1 mA·cm^{-2} for the ORR. All currents are normalized with the geometrical area of the electrode and all experiments were carried out in O_2-saturated 0.1 M KOH at 5 mV·s^{-1} and at 1600 rpm. Taken from [183].

We may now draw an analogy with experimental findings about the ORR, supported by a theoretical approach, on well-defined model bimetallic electrodes identifying catalytic sites down to the atomic scale level[198–200] that rationalize the reaction rate measured experimentally by the surface fraction of the most active catalytic ensemble (even though such fraction is in minority). In principle, the change in the reaction rates giving rise to volcano-shaped relationships with the nominal composition (and not a thermodynamic descriptor) in Figure 39c should not be related to a discrete creation of new, and more active, catalytic sites at each nominal composition since materials are prepared via a simple mixing in aqueous solution (see section 2.3. Electrochemical techniques and electrode preparation methods - *Preparation of the RRDE measurement*). Rather, the nominal composition

changes the surface concentration of the most active catalytic ensemble for the ORR on this family of materials. $(C)_{50}(MnO_2)_{50}$ should present the highest surface concentration, and higher or lower weight percentage of C in $(C)_{100-x}(MnO_2)_x$ reduces its surface concentration and results in lower overall material activity. Similar considerations should also apply for $(Ni/NiO)_{100-x}(C)_x$, yet at lower extent due to the phase segregation between the two components. Although mechanistic aspects remain to be fully clarified, this finding is in line with extensive works conducted by Savinova and co-workers[121,201] who have clearly evidenced a specific carbon contribution on the reactivity towards the ORR for carbon/transition metal oxides (mainly Mn-based) composites enhancing the overall reaction rate. The authors suggested a two-step reduction process with a first 2e- exchange at the carbon surface, followed by a subsequent electrochemical reduction of the HO_2^- into OH^-, and/or by a chemical disproportionation reaction, where the HO_2^- is transformed again into O_2, at the transition metal oxide surface. This proposal might, however, not provide the full picturing of the carbon support role since according to our results i) the carbon employed does indeed exhibit 2e- partial O_2 reduction but only for potentials below 0.72 V (see Figure 40a) whereas η_{ORR} is much lower on $(C)_{100-x}(MnO_2)_x$ (see Figure 39a) and ii) the peroxide yield (or the total number of electron exchanged) is independent of the carbon content (see Figure 40b) while the opposite could have been expected for the two-step ORR process. Our results rather point toward specific catalytic properties at the boundary transition metal oxide-carbon. Nonetheless, the identification of the nature of the catalytic site/ensemble at this surface boundary that drives the apparent reaction rate for the ORR has yet to be resolved down to the atomic scale level.

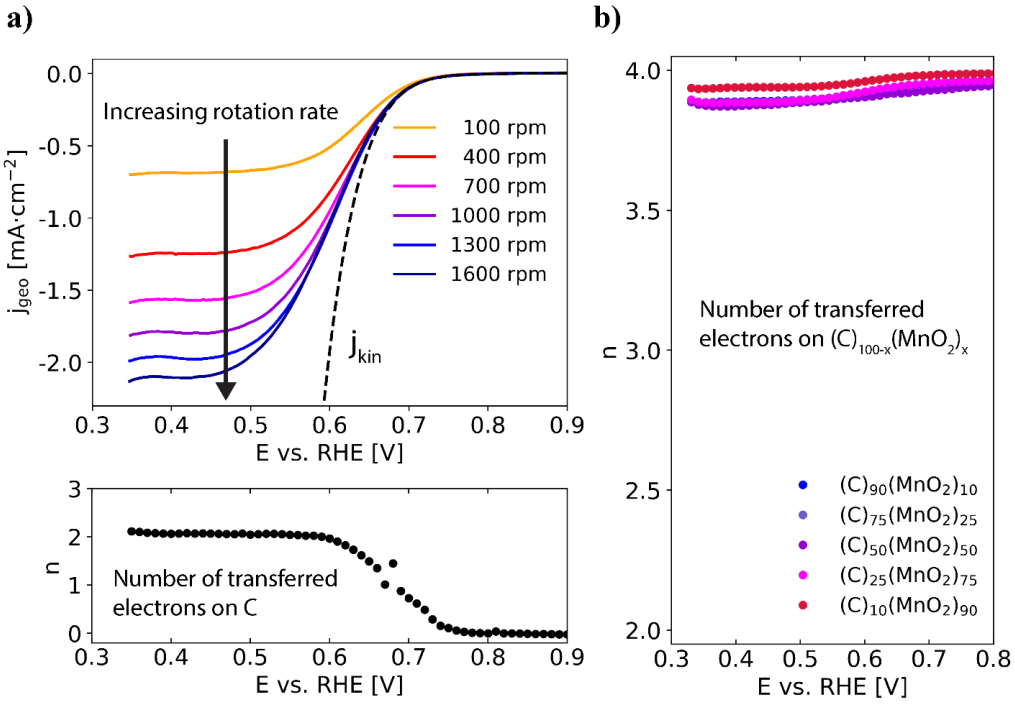

Figure 40: (a) Polarization curves and kinetic current density for the ORR on C at different rotation rates (top) and the corresponding number of transferred electrons determined with the Koutecký-Levich equation (bottom). **(b)** Number of transferred electrons for $(C)_{100-x}(MnO_2)_x$. Taken from [183].

The results on the OER activities for the same set of catalyst materials are now reported. Figure 41a shows OER polarization curves of $(C)_{50}(MnO_2)_{50}$, $(Ni/NiO)_{75}(C)_{25}$, and $(Ni/NiO)_{75}(MnO_2)_{25}$ as representative example for all binary systems investigated. Oxygen evolution reaction is initiated at similar potentials (1.58 V) for both Ni/NiO containing catalysts, which is ca. 50 mV lower than for $(C)_{50}(MnO_2)_{50}$. However, the dependency of the reaction rate on the potential is greatly affected by the nature of the composite material, and this results in trends for OER activities for $(Ni/NiO)_{75}(C)_{25}$ > $(C)_{50}(MnO_2)_{50}$ > $(Ni/NiO)_{75}(MnO_2)_{25}$ at potentials higher than 1.65 V and $(Ni/NiO)_{75}(C)_{25}$ > $(Ni/NiO)_{75}(MnO_2)_{25}$ > $(C)_{50}(MnO_2)_{50}$ at potentials lower than 1.65 V. Here again, in order to compare OER activities exhibited by the whole set of binary composites we defined a descriptor as the current density reached at η = 0.47 V (i.e. 1.70 V vs. RHE) and results are shown in Figure 41b. For $(C)_{100-x}(MnO_2)_x$ and $(Ni/NiO)_{100-x}(C)_x$, a volcano-type relationship with the nominal composition is observed, with optima at 10 mA·cm^{-2} (x = 50) and 16 mA·cm^{-2} (x = 25), respectively. Oppositely to

the case of the ORR activities, see Figure 39c, the changes in OER activities with the nominal composition is more pronounced for $(Ni/NiO)_{100-x}(C)_x$ than for $(C)_{100-x}(MnO_2)_x$. For $(Ni/NiO)_{100-x}(MnO_2)_x$ materials, the OER activities continuously drop from 10 $mA{\cdot}cm^{-2}$ to 1 $mA{\cdot}cm^{-2}$ as the fraction of MnO_2 raises from 10 to 90 wt.% The highest OER activity for the $(C)_{100-x}(MnO_2)_x$ composites is nearly identical to a C/MnO_2 compound reported recently literature[123]. Marković and co-workers[202] reported OER catalytic activity trend for transition metal oxides as Ni > Co > Fe > Mn. Furthermore it has been also shown beneficial effect of carbon addition in enhancing the OER activity of Ni-based oxides[203]. In good agreements, our results show that the nickel-containing binary mixture $(Ni/NiO)_{75}(C)_{25}$ outperforms by a large extent (more than 5 $mA{\cdot}cm^{-2}$ at η = 0.47 V) the most OER active Mn-based composite catalyst $(C)_{50}(MnO_2)_{50}$ and an increase in the OER activity upon increasing the weight fraction of carbon from 10 to 25 wt.% in $(Ni/NiO)_{100-x}(C)_x$. For this later material, if the lowest C content is left aside at an outlier data, one might also hypothesize that the most active catalytic sites are at the surface of the Ni particles and the C component acts as a dilution since the absolute amount of composite remains constant for all the compositional characteristics. Overall, as for the case of the ORR, the role of the carbon component on the enhancement of the OER activity needs to be better resolved for further development of this family of catalyst materials. These results call for further detailed investigations on O_2 electrocatalysis at the boundary/interface between transition metal oxides and carbon with structurally well-defined electrodes.

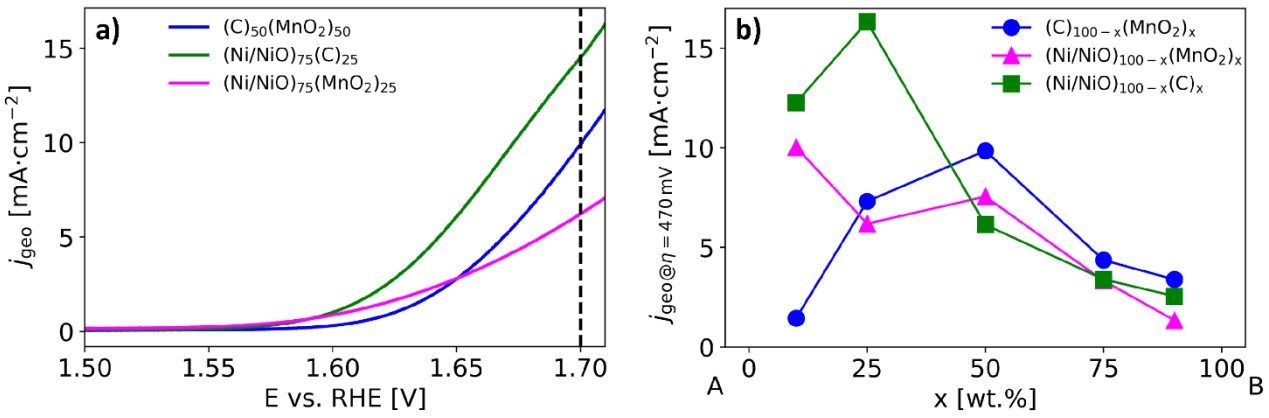

Figure 41: (a) Potential dependence of the electrocatalytic activity towards the OER for three selected binary composites, as labelled in the figure, **(b)** compositional dependence of the current densities for the OER at η = 470 mV for the same materials as in (b). All currents are normalized with the geometrical area of the electrode and all experiments were carried out in O_2-saturated 0.1 M KOH at 5 $mV \cdot s^{-1}$ and at 1600 rpm. Taken from [183].

3.3.3. Design, activity and stability of the performances of the bifunctional catalyst materials

Theoretical approach developed by Rossmeisl and co-workers[110] (see section 1.3. Oxygen electrocatalysis - *The ideal bifunctional electrocatalyst*) to rationalize changes in catalyst activities asserts that the optimum binding energies for the same reaction intermediate serving as descriptor for ORR and OER activities differs by 0.7 eV. It follows that for the development of a performant bifunctional catalyst material for an O_2 electrode the catalytic sites for both ORR and OER should differ structurally and chemically at the atomic scale level. Associating such theoretical concepts with benefits gained from the activity-composition relationships for the binary compositions described above, we designed a ternary-based catalyst $(C)_x(MnO_2)_y(Ni/NiO)_{100-x-y}$ with optimized ORR and OER activities. High concentration of Ni/NiO in the composite leads to excellent OER activity, see Figure 41b, while equal fractions of C and MnO_2 ensure the lowest overpotential for the ORR, see Figure 39c. It naturally follows that the best compromise to reach the high activities for both OER and ORR with a ternary composite should be $(C)_{33}(MnO_2)_{33}(Ni/NiO)_{33}$. We verified these design principles with the preparation of $(C)_x(MnO_2)_y(Ni/NiO)_{100-x-y}$ materials employing the same method and presenting various compositional characteristics. The resulting ORR and OER activities are shown in Figure 42a and Figure 42b, respectively.

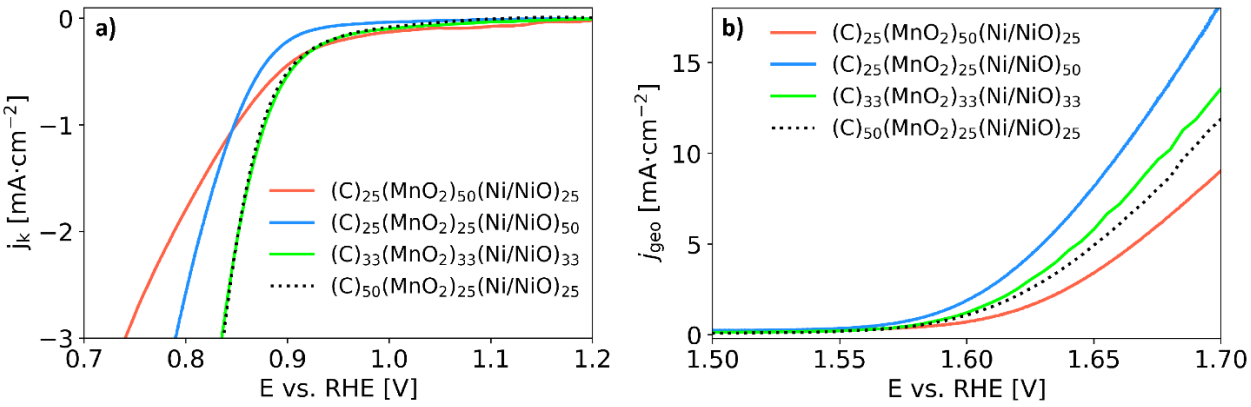

Figure 42: Compositional optimisation of a bifunctional electrocatalyst. Kinetic current densities for the ORR **(a)** and polarization curves for the OER **(b)** of ternary composites with different C : MnO_2 : Ni/NiO ratios as indicated in the figure. Same experimental conditions as in the binary composites testing. Taken from [183].

By applying our general descriptor for the ORR activity to the ternary composites, see previous section, the trend follows $(C)_{33}(MnO_2)_{33}(Ni/NiO)_{33} \approx (C)_{50}(MnO_2)_{25}(Ni/NiO)_{25} > (C)_{25}(MnO_2)_{25}(Ni/NiO)_{50} > (C)_{25}(MnO_2)_{50}(Ni/NiO)_{25}$. For the OER presented in Figure 42b the polarization curve for $(C)_{25}(MnO_2)_{25}(Ni/NiO)_{50}$ outperforms the composites with lower Ni/NiO weight content. The general trend observed for the material activity is $(C)_{25}(MnO_2)_{25}(Ni/NiO)_{50} > (C)_{33}(MnO_2)_{33}(Ni/NiO)_{33} > (C)_{50}(MnO_2)_{25}(Ni/NiO)_{25} > (C)_{25}(MnO_2)_{50}(Ni/NiO)_{25}$. The trends in OER and ORR activities with the compositional characteristics of the ternary composites follows remarkably well the composition/activity relationship reported in Figure 41b for the binary composites. As expected, high concentration of Ni/NiO NPs is beneficial for enhancing the OER activity, but it comes at the cost of sacrificing the ORR performances, and equal fraction of C and MnO_2 ensures excellent ORR activity. In Figure 43, we show that the catalytic activity of the ternary composite results from the weighted sum of the respective contributions of the binary components, confirming the relevance of the design principles exposed above and the transfer of properties from binary to ternary catalyst material still making use of the facile and low-cost preparation route. ORR performances of our ternary catalyst materials are driven by the C/MnO_2 component at 50/50 wt.% (relatively), while the OER performances are driven by the amount of Ni/NiO component. It indicates

in turns a successful transfer to a ternary composite catalyst material of the most active catalytic sites created upon the preparation of the binary composites (although these remain not identified down to the atomic scale level for the nanostructured powders). Overall, these results confirm our design principles and the ternary $(C)_{33}(MnO_2)_{33}(Ni/NiO)_{33}$ represents the best compromise in terms of high OER and ORR activities for a bi-functional O_2-electrode based on these low-cost and sustainable components.

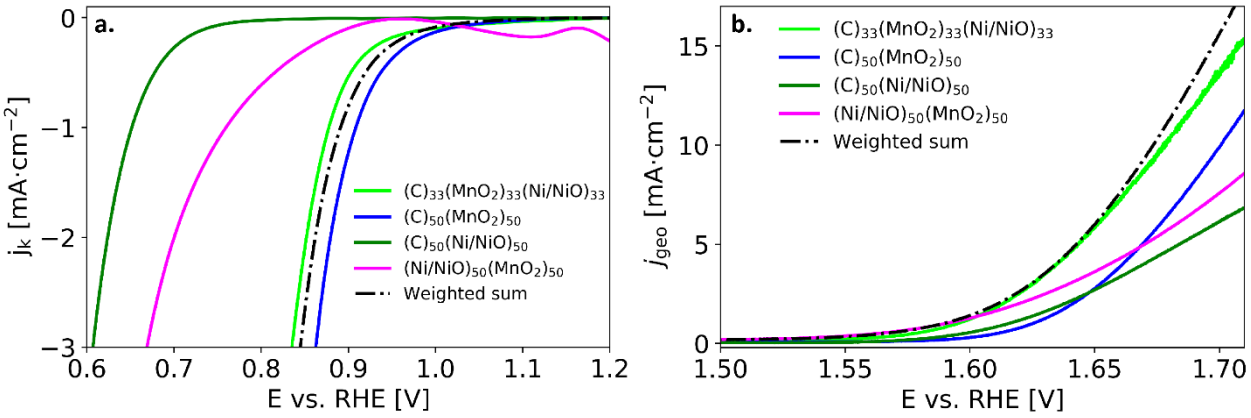

Figure 43: Transfer of performances of binary composites to ternary electrocatalyst. Plots **(a)** and **(b)** compares polarization curves for the ORR and OER, respectively, on the ternary $(C)_{33}(MnO_2)_{33}(Ni/NiO)_{33}$ and the binary composites $(C)_{50}(MnO_2)_{50}$, $(Ni/NiO)_{50}(C)_{50}$, $(Ni/NiO)_{50}(MnO_2)_{50}$. O_2-saturated 0.1 M KOH, v = 5 mV·s^{-1}, 1600 rpm. Taken from [183].

This also translates in terms of stability for the performances over 100 successive galvanostatic charge/discharge cycles, see Figure 44, where the stability of $(C)_{33}(MnO_2)_{33}(Ni/NiO)_{33}$ properties results from a synergetic association of the binary composition with high Ni/NiO content. Up to ca. 65 successive charge/discharge cycles, overpotentials remain nearly constant for both ORR and OER for all the catalyst materials, excepted for the OER on $(C)_{50}(MnO_2)_{50}$ and $(Ni/NiO)_{50}(MnO_2)_{50}$ where a small and continuous increase in the overpotentials by ca. 1 mV per charge/discharge cycle takes place. After ca. 65 cycles, the ORR and OER overpotentials for $(Ni/NiO)_{50}(MnO_2)_{50}$ suddenly rise up and stabilize after 75 cycles at 1.04 V and 0.97 V for OER and ORR, respectively, thus indicating a severe degradation of the catalyst materials followed by a stabilization upon irreversible restructuring.

For $(C)_{50}(MnO_2)_{50}$ performances degrade at a more severe rate after 65 charge/discharge cycles with an increase in the OER overpotential by ca. 9 mV per charge/discharge cycles. The ORR overpotential, after an initial sharp increase after 70 cycles, stabilizes at 0.64 V, which is about 250 mV higher than the initial value. For this latter material, losses of performances are mainly attributed to continuous removal of the C component upon corrosion/oxidation in the high potential region during OER[204–206]. It can be noticed that losses in performances are significantly more important for $(Ni/NiO)_{50}(MnO_2)_{50}$ than for $(C)_{50}(MnO_2)_{50}$. As already shown in Figure 41b, the reactivity for the OER follows $(Ni/NiO)_{50}(MnO_2)_{50}$ < $(C)_{50}(MnO_2)_{50}$. Thus, under galvanostatic tests, large overpotentials and might consequently results in larger driving force towards an irreversible restructuring on $(Ni/NiO)_{50}(MnO_2)_{50}$ compared to $(C)_{50}(MnO_2)_{50}$ and $(C)_{33}(MnO_2)_{33}(Ni/NiO)_{33}$. This might also suggests that the expected lower conductivity for $(Ni/NiO)_{50}(MnO_2)_{50}$ could also be one of the origins of the higher overpotential for the OER on this electrode. The OER overpotentials for $(Ni/NiO)_{50}(C)_{50}$ and $(C)_{33}(MnO_2)_{33}(Ni/NiO)_{33}$ remain unchanged over the entire duration of the experiment. The excellent properties of Ni/NiO towards the OER results in lower overpotentials under constant current loads and hinder potential-induced irreversible restructuring of the catalyst materials (when compared to the two other binary composites in Figure 44). It results that overpotentials for the ORR on these two materials remain also constant over the whole duration of the stability test. Additionally, and in good agreement with catalytic performances evaluated in the previous subsection, the ORR overpotential during galvanostatic charge/discharge is significantly lower for $(C)_{33}(MnO_2)_{33}(Ni/NiO)_{33}$ than for $(Ni/NiO)_{50}(C)_{50}$.

The properties of the ternary $(C)_{33}(MnO_2)_{33}(Ni/NiO)_{33}$ material combine activity performances with the lowest overpotentials for both ORR and OER at the end of the stability test (0.43 V and 0.30 V, respectively) and these overpotentials remained unchanged for 100 charge/discharge cycles. This result was achieved by simple physical/mechanical mixing the catalyst powders, and not by Ni-doping of the MnO_2 structure such as in Refs.[122,123] where enhanced stability was also demonstrated. It was assumed that a surface concentration of active catalytic sites sufficient enough

to supply the current loads for the OER with a limited overpotential (driving force) act as a protection against irreversible potential-induced restructuring of the most active catalytic ensembles for the ORR and carbon component corrosion[205,207].

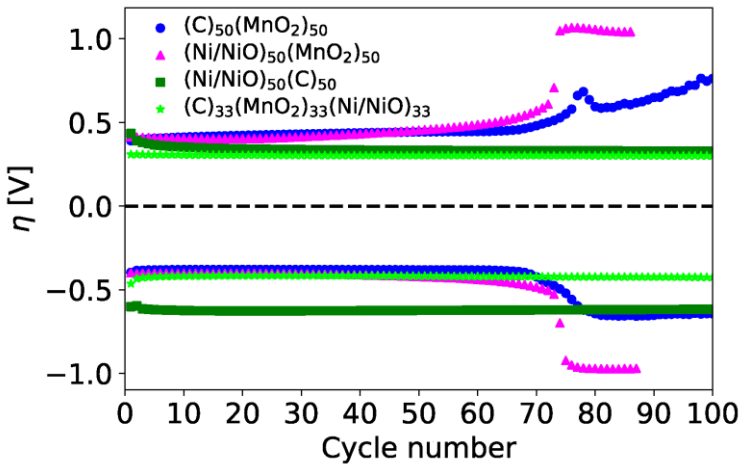

Figure 44: Stability of the catalyst materials upon successive galvanostatic charge (ORR) / discharge (OER) at 1 mA·cm^{-2} load in O_2-saturated 0.1 M KOH (1600 rpm). The stability test totalizes 100 cycles where each charge/discharge cycle consists in a 5 min discharge followed by 5 min charge. Taken from [183].

3.3.4. ORR/OER activities comparison with commercial MnO_2

To demonstrate the superior catalytic properties of the newly developed ternary catalyst composite, the latter has been compared with other catalyst mixtures containing commercial MnO_2.

The commercial MnO_2 (Manganese(IV) oxide, ReagentPlus®, ≥ 99%, Sigma Aldrich) used in this study is of the electrolytic manganese dioxide (EMD) type, which is one of the most commonly employed cathode materials for primary lithium- and alkaline manganese batteries[208]. X-ray powder diffraction measurement (**see Annex, Figure A8**) shows that the MnO_2 has a pyrolusite-type crystal structure, also known as β-MnO_2. In order to study the influence of manganese dioxide (commercial MnO_2 vs. α-MnO_2) on the ORR and OER activities, a binary catalyst composite $(C)_{50}(Pyrolusite)_{50}$, and a ternary catalyst composite $(C)_{33}(Pyrolusite)_{33}(Ni/NiO)_{33}$ were prepared and tested via RRDE measurements following the same experimental conditions described in the previous subsection. Figure 45a shows ORR kinetic current densities as a function of potential of binary

composites $(C)_{50}(\alpha\text{-}MnO_2)_{50}$, $(C)_{50}(Pyrolusite)_{50}$, and of ternaries $(C)_{33}(\alpha\text{-}MnO_2)_{33}(Ni/NiO)_{33}$, $(C)_{33}(Pyrolusite)_{33}(Ni/NiO)_{33}$. It can be seen that the ORR onset potentials of $\alpha\text{-}MnO_2$-based catalyst composites is about 200 mV lower than those of mixtures containing the commercial MnO_2.

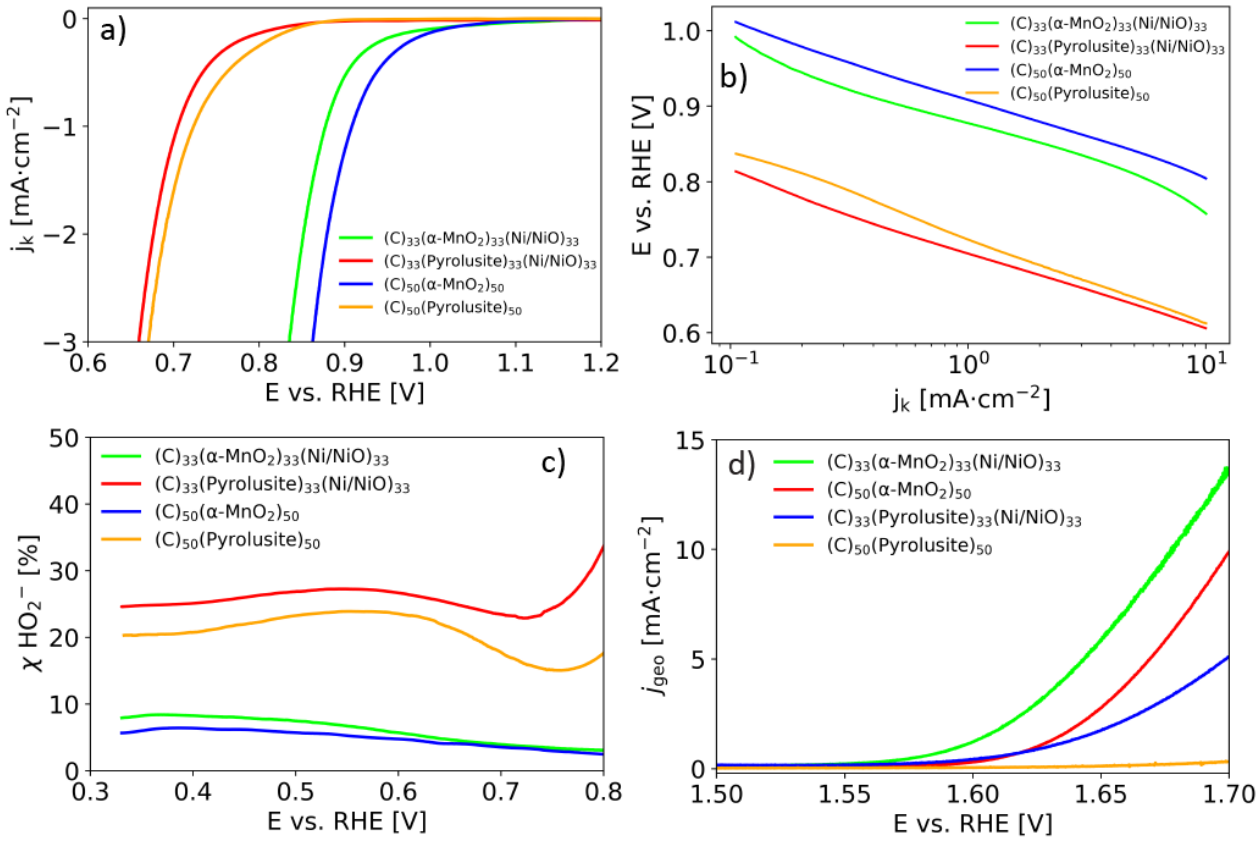

Figure 45: Kinetic current densities for the ORR **(a)** and corresponding **(b)** Tafel slopes of binary and ternary composites made of commercial MnO_2 and synthetized $\alpha\text{-}MnO_2$. **(c)** Hydrogen peroxide yields and **(d)** OER polarization curves of the same mixtures of figure (a) and (b). O_2-saturated 0.1 M KOH, v = 5 mV·s^{-1}, 1600 rpm.

In general, the catalyst composites without Ni/NiO have slightly higher activity than their containing Ni counterparts. This might be due to a lower content of MnO_2 in the catalyst mixtures with Ni/NiO (33 wt.% vs. 50 wt.%). As indicated in Figure 45b, the shift of 200 mV remains virtually constant over the entire measured potential-current density range. All catalyst mixtures have similar Tafel slopes of about -100 mV·dec^{-1} (Figure 45b), indicating that the two MnO_2 electrocatalysts might follow similar ORR pathways. However, RRDE measurements show that the selectivity towards the 4e$^-$ ORR process of $\alpha\text{-}MnO_2$-containing catalyst composites is much higher compared to pyrolusite-

based composites, where the hydrogen peroxide yield of the former is about 8 % vs. 25 % of the latter (see Figure 45c). Since the ORR process on MnO_2/C systems involves a step in which the hydrogen peroxide, that has formed on the carbon surface, is decomposed into OH^- and O_2, it can be presumed that the rate of the reaction will depend on the interaction/affinity between these two materials. The SEM image of the $(C)_{50}$(Pyrolusite)$_{50}$ composite catalyst (Figure A9) shows that the Pyrolusite particles have an amorphous morphology of 1-2 μm in size. It can be seen that, in contrast to the $(C)_{50}(\alpha\text{-}MnO_2)_{50}$ catalyst composite (Figure 36, top), the shape of the Pyrolusite particles do not favor/maximize the formation of the reaction sites where the MnO_2 is in contact with C, which are crucial for the HO_2^- decomposition. For the OER case, the ternary composite $(C)_{33}(\alpha\text{-}MnO_2)_{33}(Ni/NiO)_{33}$ outperforms all the other catalyst mixtures, as shown in Figure 45d. Interestingly, the binary mixture $(C)_{50}(\alpha\text{-}MnO_2)_{50}$ shows enhanced OER performance compared to $(C)_{33}$(Pyrolusite)$_{33}(Ni/NiO)_{33}$, although the latter contains the efficient OER electrocatalyst (Ni/NiO). At 1.70 V vs. RHE, $(C)_{50}(\alpha\text{-}MnO_2)_{50}$ reaches about j_{geo} = 10 mA·cm^{-2}, whereas $(C)_{33}(\alpha\text{-}MnO_2)_{33}(Ni/NiO)_{33}$ merely achieves j_{geo} = 5 mA·cm^{-2}. As shown in Figure 45d, the $(C)_{50}$(Pyrolusite)$_{50}$ is the least active material towards OER over all mixtures investigated. Our results are consistent with the work of Meng and co-workers[123] who synthesized various MnO_2 structures and tested their ORR/OER activities in alkaline electrolytes. They have shown that there is a strong correlation between activity towards ORR and OER, and crystal structure of the manganese dioxide, with trend for both oxygen reactions (from highest to lowest activity) $\alpha\text{-}MnO_2 > \beta\text{-}MnO_2 > \delta\text{-}MnO_2$.

3.4. Architecting and performances of gas diffusion electrode

Part of this chapter has been published in Journal of Power Sources [183].

Although model RDE experiments in three-electrode glass cell configuration allow for assessing straightforwardly the catalyst performances, environmental and operating conditions for a gas diffusion electrode (GDE) employed in rechargeable metal-air batteries are very different. Specificities and limitations related to reactant and product mass transports within the air-electrode[209,210], operation under realistic current loads[70,209,210], clogging of the air-electrode upon electrolyte carbonation[211–214], electrolyte leakage through the air-electrode[75,215], etc., generate numerous challenges for the design of a functioning air-electrode that are as important as the intrinsic catalyst material properties. As bitterly underlined in a recent report from the Department of Energy for the evaluation of hydrogen and fuel cells programs[216], the excellent properties of promising advanced electrocatalyst materials more than often do not translate into membrane-electrode assembly performances in cells probed under realistic experimental conditions relevant for practical applications. Another aspect lies in the description of the GDE preparation in the literature that frequently suffers from a lack of technical/experimental details, which impede an independent reproduction of the results or of the manufacturing process.

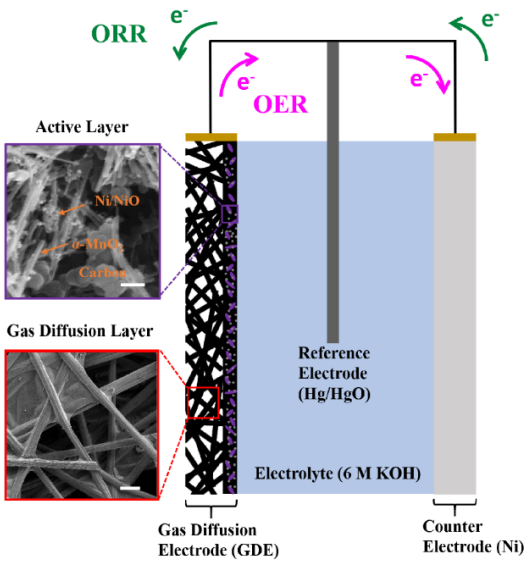

Figure 46: Sketch of the electrochemical cell setup employed to evaluate performance and stability of the GDEs prepared in this study and representative SEM imaging of the AL and the GDL (scale bars are 200 nm and 10 µm, respectively). The thickness of the GDE is 380 µm (GDL: 280 µm and AL: 100 µm). Taken from [183].

A typical design of GDE developed in our group, as depicted in Figure 46, comprises a stack of two layers: the active layer (AL) including catalyst material, and a gas diffusion layer (GDL) for the supply and the release of O_2 during discharge and charge, respectively. The AL contains polytetrafluoroethylene (PTFE), which i) makes the catalysts tightly stick to carbon supports[45] and improves the adhesion of the AL onto the GDL, thus enhancing the mechanical stability of the electrode, ii) tunes the hydrophobicity/hydrophilicity of the AL, relevant to reduce evaporation loss and leakage of the electrolyte, and iii) helps the formation of reaction sites, the so-called triple phase boundaries[22,217]. As for the AL, the GDL also contains PTFE, which acts as a physical hindrance against leakage of the electrolyte[22]. However, too high concentration of PTFE in the GDE leads to i) an increase of the charge-transfer resistance (caused by the insulating properties of the fluoropolymers) and ii) a lowering of the reactants accessibility to the active sites. Furthermore, PTFE suffers chemical decomposition over long operation times due to the strong alkaline environment, in combination with the oxidizing conditions during OER[22], resulting in collapse of the porous structure and the detachment of the AL from the GDE and ultimately to the complete battery failure.

Hence, keeping in mind these general considerations, a systematic investigation of the influence of the catalyst loading in the spray-coated AL and of the weight fraction of PTFE (in both GDL and AL) on performance and stability of the GDE was carried out, aiming at a rational optimization and design of practical electrodes. The chapter Experimental Methods provides all details on the classical spray-coating preparation method and on the nature of the material employed (see 2.3. Electrochemical techniques and electrode preparation methods - *GDE Testing*). Table 2 lists the characteristics of the GDEs prepared where the catalyst and PTFE loadings in the AL, and weight fraction of PTFE in the GDL were systematically varied in the range 3.5-8.0 $mg \cdot cm^{-2}$, 0.55-3.33 $mg \cdot cm^{-2}$, and 25-50 wt.%,

respectively. The fabricated GDEs were tested in 6 M KOH using a half-cell setup. All GDEs were tested under galvanostatic mode and under ambient atmosphere without CO_2 trap. Furthermore, the Experimental Methods described here are designed for quantitative assessment of bifunctional air cathode properties in a half-cell setup, making use of a Ni counter-electrode, in order to avoid drawbacks from poor Zn anode properties or non-optimized full cell battery design. To sustain high current loads reversibly in a stable manner, Zn anodes require a very refined/advanced tuning of their microstructural and chemical characteristics that are significantly dependent on complex electrolyte composition and on the refinement of the additives composition. This being still challenging, Zn anode properties should not be the limiting parameter in probing bifunctional air GDE performances.

Table 2: Catalyst materials and PTFE loadings in the AL, and PTFE loading in the GDL for 9 GDEs prepared with $(C)_{33}(MnO2)_{33}(Ni/NiO)_{33}$ catalyst material. Compositional characteristics of a GDE prepared with commercial reference materials Pt and IrO_2. Taken from [183].

GDE	Catalyst loading [mg·cm^{-2}]	PTFE loading in AL [mg·cm^{-2}]	Catalyst + PTFE loading in AL [mg·cm^{-2}]	Catalyst to PTFE ratio in AL: [wt.%]	PTFE in GDL [wt.%]
1	5	0.55	5.55	90:10	50
2	5	1.25	6.25	80:20	50
3	5	2.14	7.14	70:30	50
4	5	3.33	8.33	60:40	50
5	4	1.00	5	80:20	25
6	4	1.00	5	80:20	35
7	4	1.00	5	80:20	50
8	8	2.00	10	80:20	25
9	3.5	1.50	5	70:30	25
Pt/IrO_2	3.5	1.50	5	70:30	25

In order to study the influence of PTFE in the catalyst layer, the catalyst to PTFE weight ratio was systematically varied from 90:10 to 60:40 (see GDE 1-4 in Table 2), whereas the catalyst loading was kept to a constant value of 5 mg·cm^{-2}. For the ORR, at current densities ranging from 1 to 200 mA·cm^{-2} (see Annex, Figure A10a) three distinct polarization regions can be distinguished[22], namely i) the activation (1-10 mA·cm^{-2}), ii) the ohmic region (10-150 mA·cm^{-2}) and iii) the mass transport region (150-200 mA·cm^{-2}). Polarization curves for the OER with the same large current ranges are also given in Annex (see Figure A10b). The Figure 47a and Figure 47b focus on the 1-20 mA·cm^{-2} current range, for both ORR and OER, respectively. It can be noticed that increasing the PTFE to catalyst ratio scales with an increase in the overpotentials for the ORR in the activation region (and in the ohmic and mass transport regions, see Figure A10, with trend GDE 1 > GDE 2 > GDE 3 > GDE 4. On the contrary, and although the PTFE loading in the AL has an influence on the overpotentials for the OER, no clear trend is observed between PTFE loading and polarization behaviour of the GDEs in the current range considered (1-20 mA·cm^{-2}), see Figure 47b. The best performing electrode for the OER is GDE 2 (η_{OER} = 408 mV at 10 mA·cm^{-2}), may indicating an optimum wetting (hydrophobicity/hydrophilicity) of the active layer. Interestingly, GDE 2 also showed remarkable ORR activity (η_{OER} = 413 mV at 10 mA·cm^{-2}), making this electrode the most promising composition for enhanced bifunctional activity ($\Sigma\eta_{OER\text{-}ORR}$ = 821 mV at 10 mA·cm^{-2} for both charge and discharge), among all the other GDEs with similar catalyst loading (see Table 2). We then varied the PTFE loading in the GDL from 25 to 50 wt.% (GDEs 5-7), while keeping the same catalyst loading and catalyst to PTFE ratio of 80:20 for all the electrodes. As expected, no significant influence of the PTFE loading in the GDL on the overpotential in the low current loads range (below 10 mA·cm^{-2}, activation region) can be observed for both OER and ORR. However, increasing PTFE content results in a lowering of the overpotentials in the high current loads region, see Figure A10c and Figure A10d. Larger hindering of O_2 to/away from the AL follows a higher propensity for flooding of the GDL with a decrease of the hydrophobicity.

To characterize the stability of the GDE performances, we performed successive charge/discharge load cycles. For rechargeable ZAB, Parker and co-workers[70] defined the minimum metric j x $t_{discharge} \geq 11.7$ mAh·cm^{-2} for air-cathode to meet the technologically relevant threshold value of 100 Wh·kg^{-1} and therefore compete favourably with Li-ion batteries. Thus, in order to demonstrate the viability and performances of our most promising $(C)_{33}(MnO_2)_{33}(Ni/NiO)_{33}$ ternary composite catalyst material for aqueous alkaline metal-air battery application, we investigated the stability of our GDEs upon successive galvanostatic charge/discharge cycles with j x t_{charge} = j x $t_{discharge}$ = 20 mAh·cm^{-2} (2h at 10 mA·cm^{-2} each). As shown in Figure 47c the stability of the GDE performances upon successive load cycles increases with the PTFE loading for the GDE 5-7 (while catalyst loading and catalyst to PTFE ratio in the AL were kept unchanged, see also Table 2). A 10 % increase of the overpotentials for both OER and ORR was observed after 72, 64 and 58 load cycles for GDE 7, GDE 6 and GDE 5, respectively, for which the PTFE loading in the GDL (and by extension the degree of hydrophobization) was decreased from 50 to 25 wt%. Subsequent cycles result in further performance drop. The rise in overpotentials is attributed to the flooding of the GDL by the electrolyte that hinders the O_2 reactant mass transport towards and away from the AL.

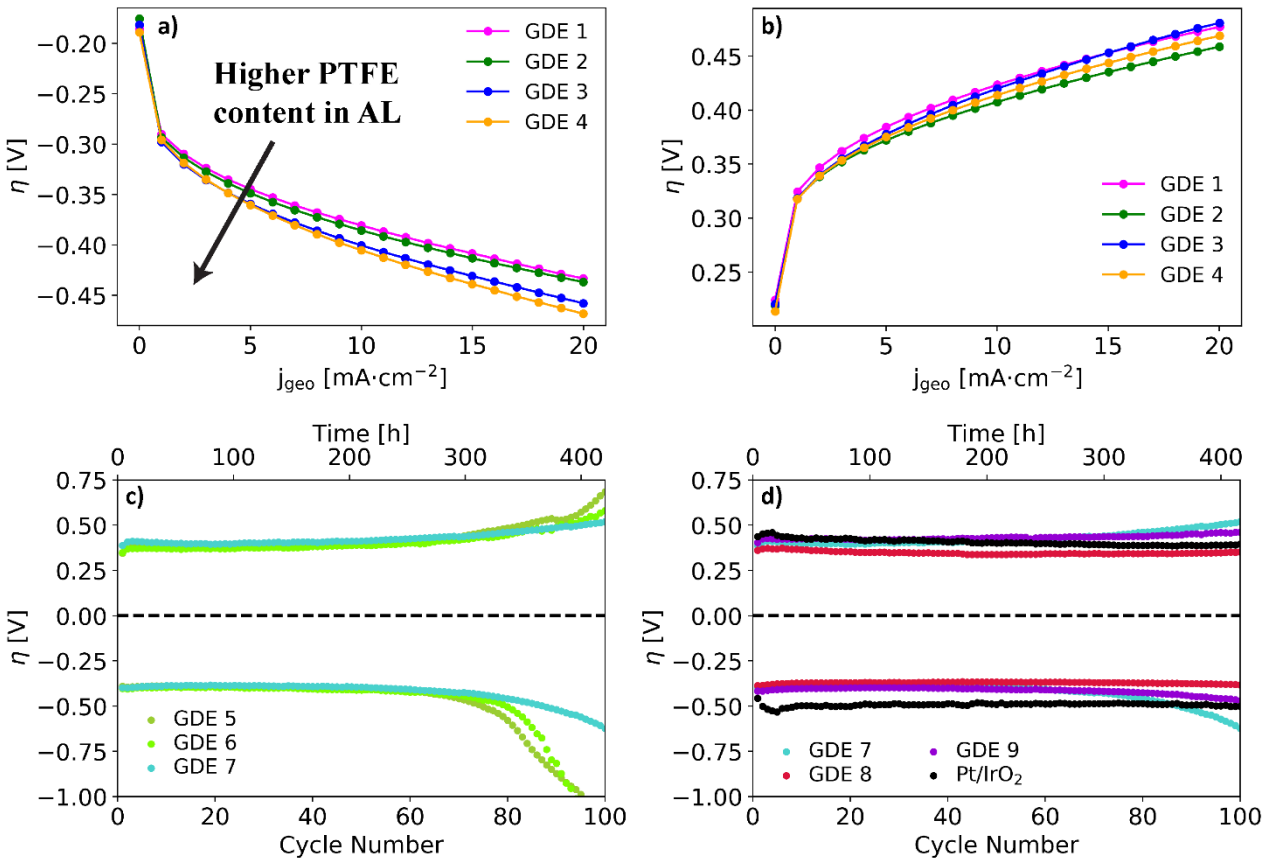

Figure 47: PTFE loading dependence on the GDEs performances that embed $(C)_{33}(MnO_2)_{33}(Ni/NiO)_{33}$ catalyst material. ORR **(a)** and OER **(b)** overpotentials as a function of the galvanostatic current densities applied for GDEs 1-4 (10 min per current density step). Change in the overpotentials upon 100 successive galvanostatic charge (OER) and discharge (ORR) load cycles for GDEs 5-7 **(c)** and GDEs 7-9 **(d)**. Each load cycle consists in a 2 h discharge followed by 2 h charge both at 10 mA·cm^{-2}. For the sake of comparison, results with a GDE using benchmark Pt black and IrO_2 catalysts also shows excellent stability but a lower energy efficiency (45 %) than GDE 8 (55 %). Ambient atmospheric conditions, no CO_2 trap. See text for details. Taken from [183].

However, too large amounts of PTFE in the GDL are not satisfying from a practical perspective. With GDEs 7-9, see Table 2 and Figure 47d, we demonstrate that refining of the catalyst and PTFE loadings in the AL, while lowering by two times the PTFE loading in the GDL, allows for substantial gains in stability over long term load cycling. With larger PTFE/catalyst ratio and slightly lower catalyst loading in the AL (by 12.5 %), the stability of GDE 9 largely exceed GDE 7 at the expense of the efficiency (an increase by ca. 4 % and 7 % of the overpotentials for the ORR and the OER with respect to GDE 7, respectively). With similar catalyst/PTFE ratio but with a doubled catalyst loading

in the AL, the overpotentials for both ORR and OER with GDE 8 are lowered, as expected, but are moreover stable over 100 load cycles (< 1 % variation) while the performances of GDE 7 substantially degrade after 72 load cycles. Overall, this indicates that the optimum hydrophobization of the GDE for activity and stability are different and, depending on the duty targeted for the bifunctional air electrode, it requires a subtle balance in PTFE loading in both the AL and the GDE. Too large amount of PTFE could also significantly alter the specific energy. According to calculation detailed in the Annex, the GDE 8 will account for approximately 10 % of the total weight of Zn-air cell with specific energy density ≥ 100 $Wh \cdot kg^{-1}$ and will show an energy efficiency of 55 % with respect to thermodynamics under a current density load of 10 $mA \cdot cm^{-2}$. (The dependence of the energy efficiency on the current density loads up to 200 $mA \cdot cm^{-2}$ for GDE 8 is given in Figure A11). With an energy efficiency for ZAB technology forecasted to be at best at 65 %[113], the energy efficiency of a ZAB equipped with this bifunctional air electrode will be mostly limited by the reversibility and the coulombic efficiency of the Zn anode.

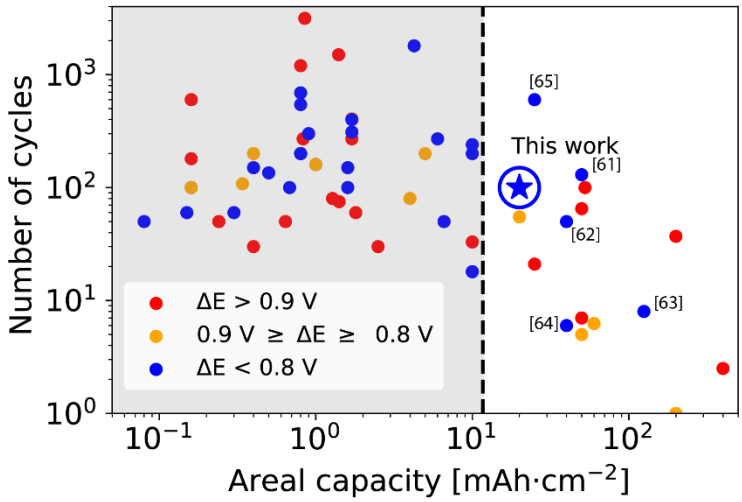

Figure 48: Overview of published bifunctional air GDE performances and stabilities. The number of stable load cycles is plotted versus the charge-discharge loads (j x t, areal capacity), and for each scatter x-y coordinates are tabulated in the Annex together with references (Table A1). The color code, namely red, orange and blue colors indicates ΔE > 0.9 V, 0.9 V ≥ ΔE ≥ 0.8, and ΔE < 0.8 V, respectively, as qualitative descriptor for the efficiency (see text for details). The vertical dashed line crossing the x-axis at 11.7 $mAh \cdot cm^{-2}$ indicates the threshold metric developed by Parker and co-workers[70]

to meet the minimum technologically relevant value of 100 Wh·kg^{-1} for ZAB. The most performant GDE prepared in this work, GDE8, is represented by a star. Taken from [183].

Finally, we compare the performance of our most promising bifunctional air cathode (GDE 8) with results reported in recent literature in Figure 48. In this figure, the number of stable load cycles is plotted versus the charge-discharge loads (j x t, areal capacity), and for each point x-y coordinates are tabulated in the Annex together with references (Table A1). The color code, namely red, orange and blue colors indicates $\Delta E > 0.9$ V, $0.9\ V \geq \Delta E \geq 0.8$, and $\Delta E < 0.8$ V, respectively, where ΔE is the sum of overpotentials for the ORR and OER at the given current load and acts as a qualitative indicator. For $\Delta E > 0.9$ V, the drop in overall efficiency would be too high to consider a practical application in ZAB for the electrode, while we consider ΔE up to 0.8 V still *reasonable* for the sum of the overpotentials with respects to a practical application. For our best performing GDE, GDE 8, the sum of the overpotentials for ORR and OER is $\Delta E = 0.70$ V at j x t = 20 mAh·cm^{-2} (see Figure 47d). Also in Figure 48, the vertical dashed line crossing the x-axis at 11.7 mAh·cm^{-2} indicates the threshold metric developed by Parker and co-workers previously mentioned to meet the technologically relevant threshold value of 100 Wh·kg^{-1} for ZAB. At first, such plot demonstrates that the vast majority of the previous reports for bifunctional air GDE do not meet the minimum requirements in terms of areal capacity to consider further applicability in ZAB for stationary storage, in good agreement with previous claims[70]. Second, ca. 70 % of the GDEs tested under conditions meeting threshold value for the areal capacity exhibit too large overpotentials for considering their potential applicability in a practical ZAB having honourable energy efficiency. Finally, the few GDEs previously reported that fulfil both criteria of j x t > 11.7 mAh·cm^{-2} and $\Delta E < 0.8$ V (blue dots in Figure 48) all include critical raw materials as defined by the E.U. commission[218], either rare-earth elements (*e.g.* La[57]) or large quantities of Co[57,67,71–73] and/or Ba[73] as catalyst materials, thus challenging their sustainability in the perspective of large-scale deployment of a ZAB infrastructure for the storage of electricity produced by intermittent renewables. Furthermore, the use of either pure oxygen[57,71] or synthetic air[73], which eliminates carbonation and clogging issues, artificially

enhances performances and stability with respect to tests under ambient air conditions. Accounting for potential additional limitations related to the scale-up of the material preparation and for the electrode manufacturing, application of the competing concepts presented in the references mentioned above[57,67,71–73] might be hampered due to the tight economic constraints associated with the stationary storage of electricity.

Benchmarking the ORR performances of the α-MnO_2-based O_2-electrode

Although bifunctional GDEs are still not available in the market, commercial O_2-electrodes that have been optimized for the ORR process (mainly for primary alkaline batteries) can readily be purchased. In this section, we compare the ORR performances of two O_2-electrodes: the first electrode is made of our best ORR catalyst mixture based of α-MnO_2 with nominal composition $(C)_{50}(MnO_2)_{50}$; the second is made of state-of-the-art ORR (based on transition metal oxides) catalyst mixture available in the market. This is mainly composed of a mixture of carbon and bixbyite (Mn_2O_3, see Figure A13) that, according to Ryabova et al.[121,201] it is one of the most active ORR catalyst among other manganese dioxides. The two electrodes were fabricated using the same manufacturing process as described in the previous section, and the mass of the active materials is the same for both electrodes (5 $mg \cdot cm^{-2}$). These were tested in 6 M KOH using the same half-cell setup described previously (see 2.3. Electrochemical techniques and electrode preparation methods - *GDE Testing* for more details). All tests were performed under galvanostatic mode and under ambient atmosphere without CO_2 trap. Figure 49a shows the polarization curves of the two GDEs. The two electrodes have similar open circuit potential of about 1 V vs. RHE. At current densities $j_{geo} \leq 50$ $mA \cdot cm^{-2}$, the potentials of the electrode made of commercial catalyst (red curve) are about 50 mV lower than those of the α-MnO_2-based electrode (blue curve). At current densities of $j_{geo} > 50$ $mA \cdot cm^{-2}$, the potential difference between the two GDEs is decreased to approximately 30 mV, but remains relatively unchanged until the end of the experiment. This finding demonstrates that our catalyst mixture can easily outperform the commercial catalyst composite designed for high ORR activities. In order to compare their

stability, as this commercial catalyst mixture has been developed for primary battery applications (i.e. where GDE only operates for O_2-cathodic reduction), the two electrodes have been evaluated by imposing a constant cathodic current at medium (10 $mA \cdot cm^{-2}$, solid lines) and high density (50 $mA \cdot cm^{-2}$, dashed lines) for a total of 500 hours, as shown in Figure 49b. At the beginning of test, the α-MnO_2-based O_2-electrode has lower overpotentials (especially at 10 $mA \cdot cm^{-2}$) than the commercial-based one. However, the α-MnO_2-based O_2-electrode shows a steady decrease in potential while the second electrode remains more stable (10 $mV \cdot day^{-1}$ vs. 5 $mV \cdot day^{-1}$). Despite this decline in efficiency, our O_2-electrode is more effective than the electrode with the commercial electrocatalyst material until the end of test, with final potentials of 0.84 V and 0.82 V vs. RHE. More interesting is the result obtained at higher current density (50 $mA \cdot cm^{-2}$). The two electrodes have similar overpotential of about η_{ORR} = 550 mV until 300 h. The commercial-based electrode reached its stability limit at times > 300 h, where its activity decreases rapidly at a rate of about 90 $mV \cdot day^{-1}$. On the other hand, the α-MnO_2-based O_2-electrode completed the 500 h experiment without any indication of activity fading, with a relative change of potential from the beginning of test.

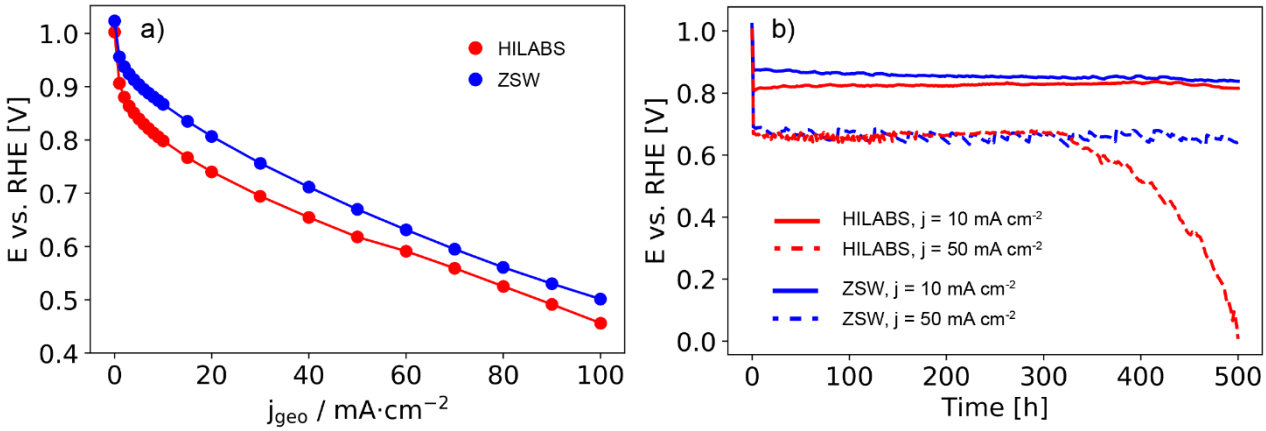

Figure 49: (a) ORR polarization curves and **(b)** chronovoltammetry tests of the O_2 electrodes manufactured with the commercial catalyst mixture (HILABS, red) and with the α-MnO_2 synthetized in-house (ZSW, blue).

These results demonstrate the superior performances, both in terms of activity and stability, of the electrocatalyst mixture developed in-house over other commercially available products that are commonly employed for applications requiring the use of O_2 electrodes in alkaline media. We believe

that α-MnO_2 is the material of choice for future O_2-electrodes intended for energy storage applications, not only because of its outstanding performance, but also because its synthesis process can be scaled-up and does not involve special handling during electrode preparation.

3.5. The influence of aging on the air electrode components

Parts of this chapter have been submitted as manuscript for publication in Journal of Power Sources.

In the previous sections, we have described in details the physical-chemical characteristics, the properties and the influence of the compositional characteristics of a ternary catalyst material composed of the carbon, α-MnO_2 and Ni/NiO nanoparticles on the electrode catalytic properties towards oxygen evolution reaction (OER) and oxygen reduction reaction (ORR). In brief, the catalyst material consisted of commercially available 5-20 nm Ni/NiO nanoparticles, commercially available 60 $m^2 \cdot g^{-1}$ carbon and in-house prepared 600 nm long fibre-like α-MnO_2, which were simply mixed together in an aqueous-alcohol solution. The study also included a detailed investigation on the influence of PTFE loading in both the active layer (AL) and the gas diffusion layer (GDL) forming together the bifunctional air gas diffusion electrode (GDE), and described the overall GDE performances over successive load cycles under conditions relevant for Zn-air battery application. Materials and processes for GDE preparation employed for this section are identical. The reader is referred to sections 3.3 and 3.4 where all the details are provided, and serving as starting point onto which we elaborate the present study focusing on the degradation processes of the GDE components. This study reports the influence of successive charge-discharge cycles on the stability of a GDE embedding the ternary catalyst composite (carbon, α-MnO_2, Ni/NiO nanoparticles) investigated by electrochemical impedance spectroscopy (EIS), scanning electron microscopy (SEM), ex situ X-ray photoelectron spectroscopy (XPS) and in situ X-ray absorption spectroscopy (XAS) measurements.

3.5.1. Electrode performance and stability upon galvanostatic charge-discharge

The stability of the GDE prepared for the present study was evaluated by applying successive galvanostatic discharge/charge cycles (galvanostatic cycling) with j x $t_{discharge}$ = j x t_{charge} = 20 $mAh \cdot cm^{-2}$ (2 h at 10 $mA \cdot cm^{-2}$ each), that is, according to the metric proposed by Parker et al.[70], well above the minimum value of 11.7 $mAh \cdot cm^{-2}$ for a Zn-air battery to meet the technologically relevant threshold of 100 $Wh \cdot kg^{-1}$. The evolution of the electrode potential (vs. RHE) as a function

of cycle number is shown in Figure 50. The discharge (η_{ORR} = 0.39 V) and charge (η_{OER} = 0.36 V) overpotentials remained constant for approximately 50 charge-discharge cycles (200 h). This results in a total charge-discharge potential gap of $\Sigma\eta$ = 0.75 V. After the completion of 58 load cycles (approximately 230 h), $\Sigma\eta$ increased by 10 %, where the OER overpotential being initially the most affected with an increase of 40 mV (η_{OER} = 0.4 V) compared to the beginning of the test. Then, the overpotentials for both OER and ORR rise faster with the number of load cycles. After 100 charge-discharge cycles, $\Sigma\eta$ increased by 170 % with respect to the initial electrode performance, corresponding to electrode failure (or end of life, E.o.L.). Galvanostatic cycling test leads to a progressive activity fading of the GDE for both reactions, yet at different rates when changes for η_{OER} and for η_{ORR} are compared, suggesting a continuous and progressive transformation of the electrode structural-chemical characteristics. Comparatively, the overpotential for the ORR increases more rapidly than the overpotential for the OER, and also to a larger extent, although the losses in GDE performances appears to be initiated simultaneously for both reactions. At a first glance, this suggests that i) the physical-chemical and structural characteristics of the GDE resulting in the given OER performances are more robust than those associated with for the ORR performances and ii) at the catalyst material level the degradation processes for the two catalytic functions are interrelated.

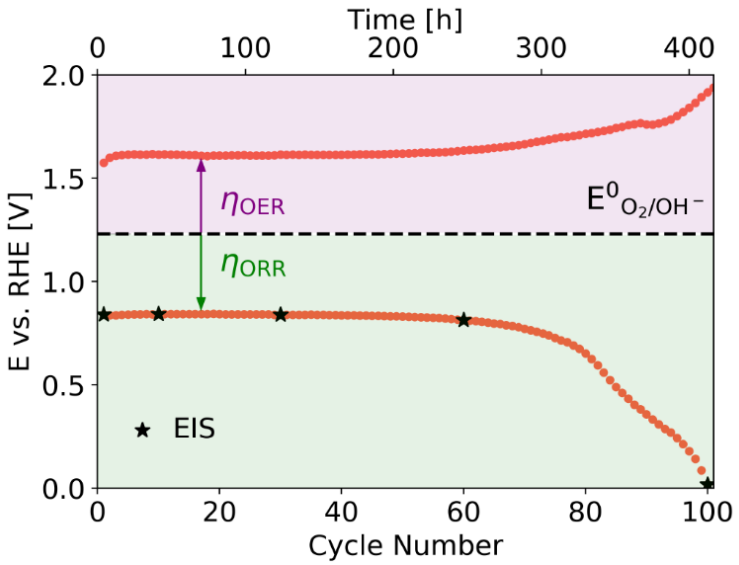

Figure 50: (a) Charge and discharge potentials upon 100 successive galvanostatic charge (OER) and discharge (ORR) load cycles. Each load cycle consists in a 2 h discharge followed by 2 h charge both at 10 $mA \cdot cm^{-2}$. Ambient atmospheric condition, no CO_2 trap. The black dashed line indicates the equilibrium potential of the water splitting (OER) and oxygen reduction reaction (ORR) at standard conditions, $E^0_{O2/OH-}$. Electrochemical impedance spectroscopy (EIS) analysis was also conducted at the 1st, 10th, 30th, 60th and 100th cycle during the discharge interval, as indicated by the black stars.

3.5.2. Insights on the processes during the electrode aging from EIS and SEM

EIS measurements were conducted at the end of the 1st, 10th, 30th, 60th, and 100th cycle during the discharge (ORR), as indicated by the black stars in Figure 50, and under current load (see Experimental Methods). The evolution of the GDE impedance, represented as Nyquist plot, as a function of cycle number is shown in Figure 51. For the 1st, 10th and 30th load cycles, impedance spectra in the complex plane are characterized by a very small, strongly depressed, semi-circle in the high frequency range (ca. between 4 Hz and 100 kHz) remaining unchanged with the number of load cycles and a larger, also depressed, semi-circle in the low frequency range (ca. between 10 mHz and 3 Hz) displaying a slightly increasing resistance with the number of load cycles. The spectrum at the 60th load cycle also presents a depressed semi-circle in the low frequency range, yet shifted towards higher real part of the impedance compared to results gained after a lower amount of load cycles, and a larger depressed semi-circle in the high frequency range. Finally, the low- and high-frequency semi-circles become significantly larger for the impedance spectrum acquired at the 100th load cycle. After Thiele[219] and Wagner[220], the low- and high-frequency arcs are related to resistances associated with diffusion and charge transfer at the electrochemical interface, respectively. The same authors proposed an analog equivalent circuit (EC) offering a satisfying approximation and comprising a resistance R_0 (sum of electrolyte, contact and cell resistances) connected in series with a second resistance R_1 being in parallel with a constant phase element (CPE 1), and a third resistance R_2 being also in parallel with a constant phase element (CPE 2), see Annex Figure A14. The CPE accounts for the electrode surface heterogeneities and the dispersion of the time constants. R_1 and R_2 are associated with charge transfer (high frequency) and diffusion (low frequency) resistances, respectively. Full

results of the EC fitting are given in the Annex (Table A2), and numerical values obtained for R_0, R_1 and R_2 and reported in Table 3. These follow obviously the trend described for the Nyquist plots in Figure 51. R_0 remained unchanged at ca. 2.5 Ω·cm upon successive load cycles, R_2 progressively increases from 3.7 to 7.5 Ω·cm upon successive load cycles and exhibit a significant rise up to 41.3 Ω·cm at the 100th load cycle. R_1 remain low, below 2.0 Ω·cm, until the 60th load cycle and significantly rises up to 29.7 Ω·cm at the end of life of the GDE.

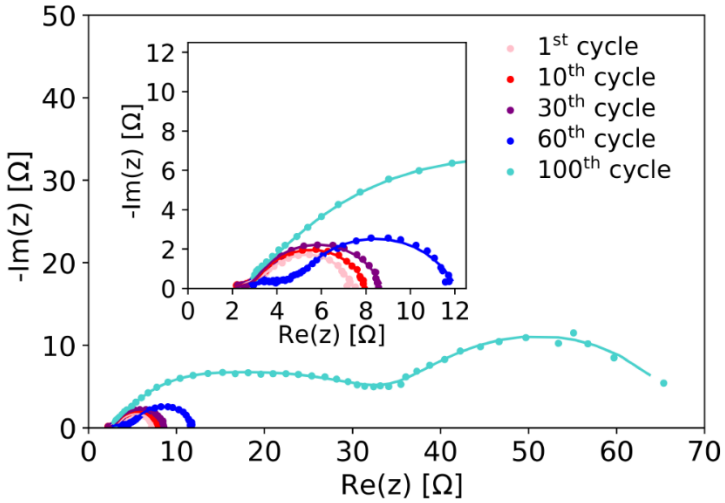

Figure 51: Changes in the Nyquist diagram for EIS of the GDE displayed in Figure 50, as a function of cycle number (scatters: experimental data points, solid lines: fitted spectrum). The insert provides a magnification of the high frequency region.

Table 3: Values of the resistances for the fitted equivalent circuit displayed in Figure A14 (see text for details).

cycle number	R_0 [Ω·cm]	R_1 [Ω·cm]	R_2 [Ω·cm]
1	2.21 ± 0.02	1.48 ± 0.05	3.69 ± 0.19
10	2.17 ± 0.06	0.95 ± 0.01	4.92 ± 0.21
30	2.21 ± 0.03	0.83 ± 0.13	5.70 ± 0.23
60	2.82 ± 0.09	1.89 ± 0.11	7.48 ± 0.45
100	2.06 ± 0.08	29.70 ± 0.41	41.30 ± 0.15

It results that changes in the impedance spectra can be qualitatively interpreted as follow:

- Up to 30 load cycles, the catalyst activity remains unchanged while the diffusional characteristics towards the catalytic sites are slightly altered upon successive load cycles;
- At the 60th cycles, the properties of the active layer for O_2-reactant diffusion become sensitively impaired, most likely upon partial flooding of the catalytic layer, and the active material become slightly less active towards the ORR probably originating from some irreversible restructuring (this will be detailed in the next subsection);
- After 100 load cycles, at the end of life of the GDE, both diffusional and catalytic properties of the GDE are significantly deteriorated upon flooding of the electrode hampering O_2-reactant diffusion toward the catalytic sites and significant irreversible restructuring of the active catalytic sites for the ORR; both leading to a large increase of the overpotential (see Figure 50).

SEM imaging was also performed at the electrode surfaces at different stages of its lifetime. To this purpose, a second and identical GDE was prepared, cycled under the same load conditions (20 mAh·cm^{-2}) and dismantled/remounted after different amount of load cycles (the same as where EIS data were acquired). Figure 52 displays the evolution of the active layer surface morphology from representative images taken after the 1st, 10th, 30th, 60th and 100th load cycles. It can be noticed that the electrode surface has a globular morphology that is most probably dictated by the spray-coating method used to deposit the catalyst layer (see Experimental Methods). More important, the presence of cracks in the catalyst layer, revealed by a black contrast and highlighted by red traces in the images, can be resolved and their amount increases with the number of load cycle already from a qualitative inspection of the images. From a quantitative evaluation, expressed as the fraction of the area attributed to cracks over the electrode area imaged (% cracks), it can be estimated that after 100 load cycles crack areas represent about 11% of the overall catalyst layer, corresponding to as much breaches allowing potentially for electrolyte flooding and leakage through the GDE. This is indicative of a severe structural degradation/wearying of the C/PTFE matrix.

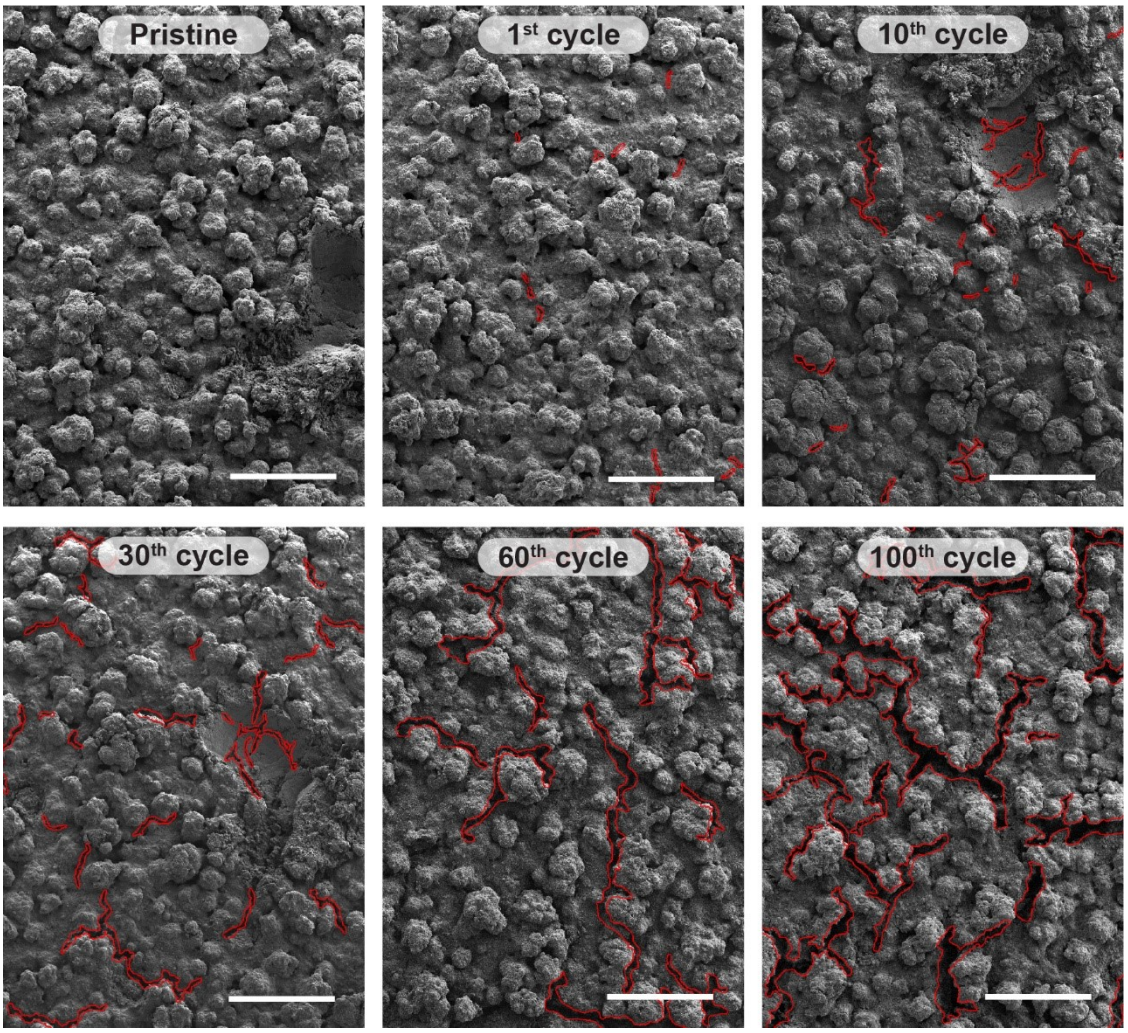

Figure 52: Representative scanning electron micrographs of the GDE in the pristine state (Pristine) and after different load cycle numbers, as indicated in the figure. Scale bar: 100 µm.

A plot of the percentage of crack areas as function of the amount of load cycles is given in Figure 53, where the trend upon successive load cycles follows remarkably well the increases of the overpotentials (compare with Figure 50) and of the resistance R_2 gained from EIS data, which is associated to the diffusional limitations.

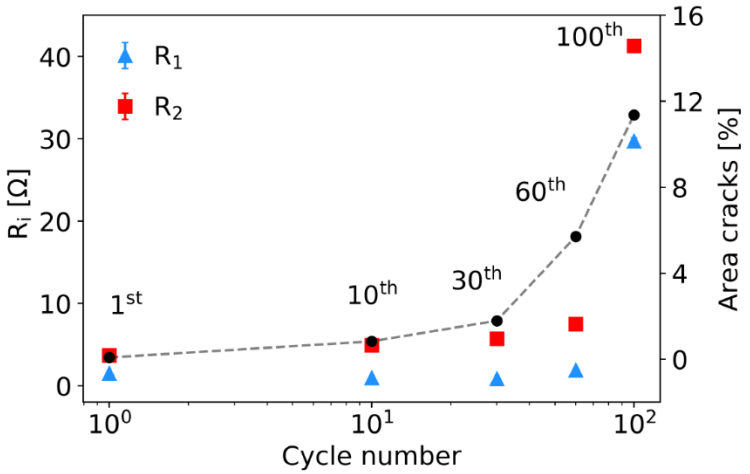

Figure 53: Fitted parameters R_1, R_2, (left-hand y-axis) from the equivalent circuit depicted in Figure A14 and percentage of cracks (projected surface area, right-hand y-axis) as a function of cycle number obtained from Nyquist plots and quantitative analysis of SEM images, respectively.

Together SEM and EIS data point towards a structural degradation of the active layer, with the apparition of cracks, leading to an electrolyte flooding of the GDE. It results a hampered access to the catalytic site for the O_2-reactant and larger overpotential for the ORR. In addition, EIS data also suggests a degradation of the catalytic properties of the active material for the ORR, as monitored by an increase upon successive load cycles of the depressed semi-circle associated with the charge-transfer resistance. In the following, the weary of the C/PTFE matrix and irreversible restructuring of the catalyst material are investigated in detail in order to disentangle chemically-driven and electrochemically-driven processes shortening the GDE lifetime.

3.5.3. Insights on electrode components degradation from ex-situ XPS and in operando XANES investigations

High-resolution XPS spectra were acquired at the active layer surface of the GDE before (pristine) and after (end-of-life, E.o.L.) the successive charge/discharge load cycles reported in Figure 50. Additional measurements were carried out on identical GDEs after having experienced either only ORR or only OER until 200 $mA \cdot cm^{-2}$ current load (polarization curves are displayed in Figure A15). The latter electrochemical measurements are comparatively fast (330 min) with respect to the stability

tests (see Figure 50), and larger current loads are expected to enhance electrochemically-driven degradations of the GDE components.

The F (1s) core level spectrum, see Figure 54, reveals two well-defined overlapping peaks centred at 689.9 eV and 692.2 eV for the pristine GDE and the for GDEs after ORR and OER. The FWHM, see Table 4, are significantly larger for the peak at higher binding energy (B.E.) than for the peak at lower B.E. In good consistency with the literature[221,222], both peaks are related to $(-CF_2-)_n$ polymeric chains of the PTFE and the presence of thicker film patches lead to a second and broader peak at higher B.E. due charging effects resulting from the insulating nature of the PTFE. The small, yet visible, changes in intensity maxima ratio between the two peaks for these three GDEs is attributed to inherent variations in the distribution and amount of thicker PTFE patches during the preparation procedure, with GDE preparation steps potentially not perfectly controlled. This suggests in turns that XPS could be employed as quality control tool to monitor the dispersion of the PTFE layer with the active layer of the GDE. For the XPS spectrum acquired at E.o.L., the F (1s) region of the spectrum is apparently characterized by a single and broad peak, but the use of a single symmetric peak leads to poor fitting quality with significantly larger Chi-square (not shown). Instead, two components can be resolved with a low-B.E. component centred at 689.9 eV, as for the three other spectra described above, and a high-B.E. component centred at 691.1 eV. FWHM for both components are also very similar to those reported for the other spectra where the two components are clearly separated, see Table 4, supporting for the deconvolution in two peaks. Assuming that the high-B.E. component at 691.1 eV also relates to charging effects for $(-CF_2-)_n$ but at a lower magnitude compared to the other samples, the shift by ca. 1 e.V. towards lower B.E. indicates a substantial thinning of the PTFE layer in the active layer at the E.o.L. of the GDE. We also note that the fraction of the high-B.E. component in the F (1s) region of the spectrum at the E.o.L. is clearly increased compared to spectra for the pristine sample and those for GDEs after either ORR or OER. Such thinning of the PTFE layer upon successive charge/discharge load cycles during 400 h should lead to losses of the hydrophobic properties of the GDE and ultimately to its flooding, in good consistency with interpretation of SEM

and EIS data (see previous section). Interestingly, the degradation of the PTFE layer appears to result from a chemical process over time rather than from a potential-induced (electrochemical) degradation. Indeed, the F (1s) spectrum obtained after either ORR or OER under significantly higher current loads than for the stability test (200 $mA \cdot cm^{-2}$ versus 20 $mA \cdot cm^{-2}$) differ significantly to the spectrum acquired at the E.o.L. GDE (and are very similar to the one for the pristine sample). A significant modifications of the F (1s) spectra after either ORR or OER with much larger overpotentials for these experiments than for the stability test would have been expected under the hypothesis of an electrochemically-driven degradation of the PTFE layer. Thus, losses of hydrophobicity over time are attributed to a chemical process, with surface chemical changes for PTFE film in contact with concentrated KOH solution. Chemical (lowering of the contact angle) and structural (roughening) changes of PTFE film surface in contact with concentrated KOH solutions and surface roughening are reported in the literature[223,224].

In the same figure, charging effects at the PTFE layer are also reflected in the C (1s) region of the spectrum for the pristine sample, with the deconvolution of two well-resolved peaks centred at 292.4 eV and 294.8 eV. The peak at lower B.E. for PTFE is in perfect agreement with the literature[225], while various shift towards higher B.E. upon charging effect are reported[222,226], and, as for the F (1s) region of the spectrum, the FWHM of the higher B.E. peak is larger than for the low B.E. peak. Importantly, the ratio of normalized peak areas F(1s)/C(1s) for the two associated $(-CF_2-)_n$ peaks in the F (1s) and C (1s) regions are approximately 2 in both cases, see Table 4, hence supporting for the overall assignment of these peaks and the deconvolution of the C 1s region above ca. 291 eV. This deconvolution revealed the presence of a third peak in this region of the spectrum, centred at 293.3 eV and relatively minor with respect to the two other peaks, which remains unidentified. Inspection of Ref.[227] suggests that this peak could be tentatively attributed to oxygenated fluorocarbons, likely impurities in the PTFE employed.

Deconvolution of the region above ca. 291 eV for the pristine sample provides guidelines for the deconvolution of the spectrum acquired after electrocatalytic investigations. Results are also provided

in Figure 54 and in Table 4, enlargements of the C (1s) regions are also provided in the Annex, Figure A16. For the E.o.L. GDE and the GDE having experienced ORR up to 200 $mA \cdot cm^{-2}$, a K (2p) component can be resolved at 294.3 eV ($2p_{3/2}$, spin-orbit splitting s.o.s. = 2.8 eV) and is attributed to intercalated K^+ ions in the α-MnO_2 resulting from the large cathodic overpotentials. Consistently, this species is absent for the GDE after OER up to 200 $mA \cdot cm^{-2}$ due to the large anodic overpotentials leading to the de-intercalation of K^+. For the E.o.L. GDE, a second K (2p) component can be resolved and is centred at 293.1 eV ($2p_{3/2}$, s.o.s. = 2.8 eV). This peak at lower B.E. is attributed to potassium carbonate / hydrogen carbonate species[228] formed after reaction of the CO_2 present in the ambient air with the strongly alkaline electrolyte. Clogging of the GDE upon carbonation, hindering O_2 reactant, is one of the major drawbacks of aqueous alkaline metal-air batteries [REF]. Also for this E.o.L. GDE, the high B.E. peak attributed to $(-CF_2-)_n$ (charging effect) is also shifted to lower binding energy by 0.70 eV compared to the other samples, in good consistency with the corresponding changes in the spectrum of the F (1s) region.

The K (2p) attributed to $K_2CO_3/KHCO_3$ is also resolved at 293.1 eV for the GDE after OER (and absent for the GDE after ORR). Although the electrocatalytic investigation was significantly shorter that for the E.o.L. GDE, see above, carbonate formation may result from the carbon support oxidation due to the large anodic overpotentials. Inspecting the region below ca. 291 eV and above the peak at 284.8 eV attributed to adventitious carbon, we found that the intensities are relatively significantly higher than for the pristine and after ORR samples, and the presence of an ill-defined broad peak maximum at ca. 288 eV, see also enlargements provided in Figure A16. This supports for a partial (electro)catalytic oxidation of the carbon support during OER at large current loads. This intermediate region of the spectrum is not further analysed since the absence of intensity maxima impedes a robust deconvolution. Nevertheless, we also noted for the E.o.L. GDE larger intensities in this poorly informative region of the spectrum and the development of a broad shoulder attached to the peak characteristic for adventitious carbon. These are also indicating a partial oxidation / degradation of

the carbon support for the E.o.L GDE, albeit comparatively more moderate due to the significantly lower anodic overpotential (see also the relative changes in the peak areas in Table 4).

Finally, the XPS spectrum of the GDE after OER presents two well resolved peaks at 295.6 eV and 298.4 eV, and peak intensities ratio as well as spin-orbit splitting match well with a K (2p) peak, see Figure 54. To the best of our knowledge, a K (2p) component at such high B.E. is not reported in the literature and further identification would require specific investigations.

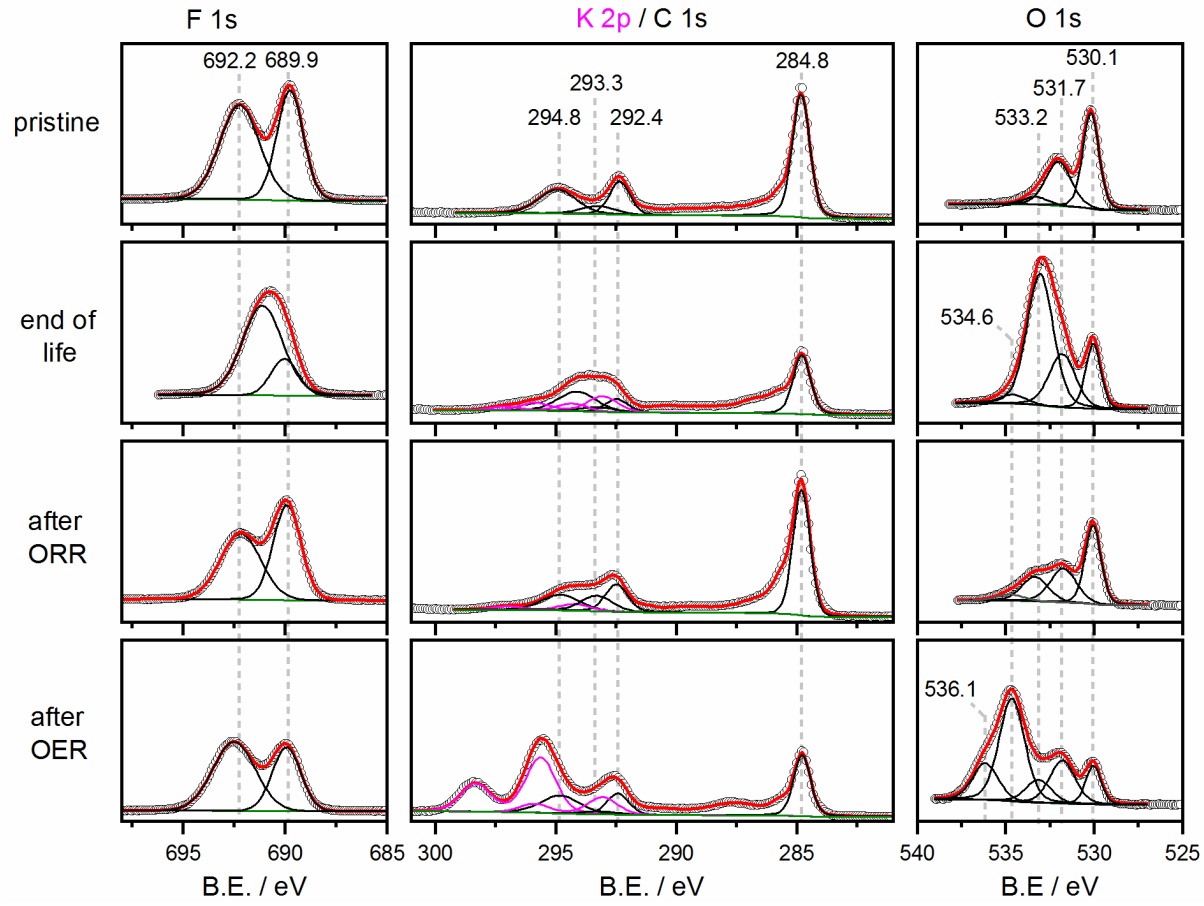

Figure 54: F 1s (left), C 1s / K 2p (center) and O 1s (right) core level XPS spectra for (from top to bottom) pristine GDE, GDE at the end of life, GDE having only experience ORR overpotentials and GDE having only experienced OER overpotentials, as indicated in the figure, see text for details. For a given spectral region, the intensity scale is identical for the four GDE samples investigated. Experimental data (open scatters), background (green solid traces), deconvoluted components (black solid traces and pink solid traces for K 2p) and fitted spectra (red solid traces). Enlargement of the C 1s regions are provided in the Annex, Figure A16.

In the O (1s) region of the spectrum, see Figure 54, peaks at 530.1 eV and 531.7 eV are well resolved for all the GDEs investigated, and are classically attributed to transition metal oxides and metal carbonates, respectively (the latter overlapping with organic C=O surface contaminations). A peak at 533.2 eV, also present for all the GDEs investigated, is attributed to organic C-O surface contaminations. The changes in the integrated areas for this peak, very small for the pristine GDE, large for the E.o.L GDE, intermediate for the GDEs after ORR and OER, see Table 4, are tentatively attributed to the time of exposure of the active layer to the electrolyte. Contaminations from the ambient air may dissolve in the electrolyte and accumulate at the surface of the active layer. More interesting is the presence of a peak at higher binding energies, centred at 534.6 eV for the three GDEs having experienced current loads and of an additional peak at 536.1 eV for the GDE after OER, both peaks being absent for the pristine GDE. The normalized area for the former is relatively low for the E.o.L. GDE and the GDE after ORR, while being large for the GDE after OER, see Table 4. Both peak positions correspond very well with previous reports on fluorocarbons incorporating O in the aliphatic chains[227,229], with (-CF)-O-(CF_2-) at 534.6 eV and (-CF)-O-C_nF_{2n+1} at 536.1 eV. These two moieties were reported after photo-oxidation of perfluoroalkoxy alkane (PFA) under ultra-high vacuum conditions[229]. Since PTFE and PFA are to some extent rather similar compounds, the detection of large amounts of these moieties specifically for the GDE after OER indicates an electrochemically-driven oxidation of the PTFE at large anodic overpotentials. Whether these moieties results from a direct electrooxidation or mediated via peroxo-type intermediates during the OER cannot be distinguished with the present investigations. The detection of comparatively small amounts of (-CF)-O-(CF_2-) for the E.o.L. GDE and the GDE after ORR up to large cathodic overpotentials points towards an additional chemical degradation (kinetically slow) of the PTFE in contact in aqueous alkaline electrolyte, as mentioned above. This indicates in turns that excessive overpotentials during the charge should be strictly avoided to limit the degradation of the PTFE binder incorporated in the active layer of the GDE and ensure long term stability of the electrode.

Table 4: Binding energies (B.E), normalized areas and full width at half maximum (FWHM) for the deconvoluted components in the C 1s, K 2p, O 1s, and F 1s XPS spectra displayed in Figure 54. In the case of K 2p, the B.E. of the 2p3/2 component is given and the spin-orbit splitting was fixed at 2.8 eV.

Spectrum region	B.E. / e.V. (± 0.1)	Normalized area (FWHM)				assignment
		pristine	E.o.L	ORR	OER	
C 1s	284.8	14934 (0.85)	7248 (0.83)	14109 (0.83)	7141 (0.83)	C-C adv. carbon
	292.4	4860 (1.00)	2041 (1.09)	4257 (1.09)	3215 (1.07)	$(-CF_2-)_n$
	293.3	1945 (1.69)	1152 (1.83)	3363 (1.53)	758 (1.83)	PTFE impurities
	294.1	-	5179 (1.86)	-	-	$(-CF_2-)_n$ *Charging effect*
	294.8	6057 (1.79)	-	4166 (1.88)	4779 (1.86)	$(-CF_2-)_n$ *Charging effect*
O 1s	530.1	3179 (1.07)	2006 (1.00)	2564 (1.05)	1224 (1.02)	Transition metal oxides
	531.8	2303 (1.68)	2875 (1.75)	1822 (1.75)	2250 (1.70)	Org. surf. cont. / metal carbonates
	533.2	400 (1.68)	7093 (1.75)	1325 (1.75)	1203 (1.70)	Org. surf. cont.
	534.6	-	490 (1.75)	340 (1.75)	5388 (1.70)	$-CF-O-(CF_2)-$
	536.1	-	-	-	1911 (1.70)	$-CF-O-C_nF_{2n+1}$
K 2p	293.1	-	1215 (1.46)		1334 (1.46)	$K_2CO_3/KHCO_3$
	294.3	-	584 (1.46)	539 (1.46)	-	intercalated K^+
	295.6	-	-	-	4319 (1.46)	unidentified
F 1s	689.9	9652 (1.50)	4312 (1.54)	8740 (1.57)	5968 (1.60)	$(-CF_2-)_n$
	691.1	-	10753 (2.16)	-		$(-CF_2-)_n$ *Charging effect*
	692.2	12307 (2.23)		8570 (2.24)	9536 (2.37)	$(-CF_2-)_n$ *Charging effect*

In the Ni (2p) region of the spectrum, Figure 55, the very complex overlapping multiplet structures and satellites, for both $2p_{1/2}$ and $2p_{3/2}$, for Ni metal, NiO, NiOOH and $Ni(OH)_2$[230–232] would impede a straightforward quantitative analysis of the XPS core level spectra for nanostructured Ni materials imbedded in a composite matrix, as for the present study. Nonetheless, a qualitative analysis, as described in the following, delivers some insights on the behaviour of the Ni component of the electrode during operation. The overall shape of the Ni 2p region of the spectrum differs significantly when pristine and E.o.L samples are compared. For the pristine sample, three peak maxima emerge

in the $2p_{3/2}$ region as indicated by dashed lines in the figure: A minor one at ca. 853.4 eV and two peaks at 855.3 eV and 856.8 eV of approximately apparent equal magnitude. This group of peaks are attributed to NiO and a mixture of $Ni(OH)_2$ and NiOOH[230], with the main contribution for NiO located at the lower B.E. than for the hydroxide-oxy-hydroxide. Ni metal would result in a significant peak below 853 eV[233] that is not observed presently. For the E.o.L sample, the Ni $2p_{3/2}$ region of the spectrum is largely dominated by an (apparent) single peak centred at ca. 856.6 eV. The absence of significant feature in the lower binding energy range would be consistent with the presence of a thicker hydroxide/oxy-hydroxide layer at the surface of the Ni/NiO particles after 100 load cycles. Now comparing with spectra acquired on electrode surfaces having experience only either ORR or OER, we found are that these are very similar to those obtained on pristine sample and at the E.o.L, respectively.

This indicates that a significant surface modification of the Ni component of the catalyst material in parallel to the increase of the overpotentials, and to the GDE failure, takes place during the OER (charge) along the load cycles with the formation of a thick hydroxides/oxy-hydroxydes layer at the surface of the Ni/NiO particles. According to our previous investigation on identical ternary catalyst materials (see section 3.3), the OER activity is mainly driven by the Ni/NiO component and the boundary/interface that it forms with the carbon support. The increase of the OER overpotential upon successive load cycles is hence attributed to the accumulation/formation of the $Ni(OH)_2$/NiOOH layer during the OER, lowering the catalyst activity. We suggest tentatively the formation of a thicker Ni hydroxide/oxy-hydroxide layer during the OER that is not fully reversible when the overpotential is lowered during the ORR under the given operating conditions, thus accumulating over successive charge/discharge load cycles and progressively lowering the catalyst activity for the OER.

In the Mn (2p) region of the spectrum for the pristine GDE, Figure 55, the $2p_{3/2}$ component is characterized by a broad peak centred at 642.5 eV, with shoulders at lower and higher binding energies. Both, shape and position, are in good agreement with literature data for MnO_2[234,235].

The overall shape of the Mn (2p) appears barely affected neither by successive charge/discharge load cycles of the GDE nor by ORR and OER up to high loads resulting in large overpotentials. This would indicate at a first glance an absence of irreversible changes of the surface oxidation state of the MnO_2 components upon electrochemical investigations. However, as for the Ni (2p) region of the spectrum, complex multiplet structure of overlapping peaks for Mn (2p) region and within a narrow binding energy range for Mn with various oxidation states (e.g. MnOOH, Mn_2O_3, Mn_3O_4)[235] impede a straightforward quantitative analysis of the spectra revealing a potential irreversible transformation of a fraction of the MnO_2 component of the GDE into other Mn compounds. Thus, the XPS data for the Mn (2p) region presented here do not allow to conclude for the stability of the α-MnO_2 component of the ternary bifunctional catalyst imbedded in the GDE upon successive charge/discharge load cycles.

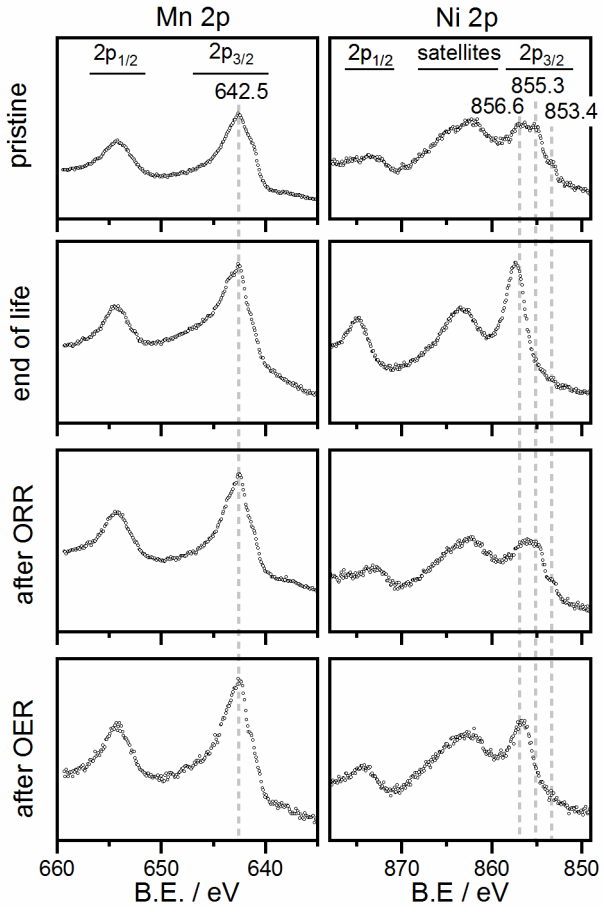

Figure 55: Mn 2p (left) and Ni 2p (right) core level XPS spectra for (from top to bottom) pristine GDE, GDE at the end of life, GDE having only experience ORR overpotentials and GDE having only experienced OER overpotentials, see text for details.

In order to elucidate further potential electrochemically driven transformation of α-MnO_2 component upon extensive electrode galvanostatic cycling, we conducted *operando* X-ray absorption near edge structure (XANES) analysis at the Mn K-edge energy range during an accelerated degradation test of the electrode, hence mimicking the effect of electrolyte flooding into the porous structure of the GDE or a clogging due to carbonates formation. This was achieved by installing a thin Kapton foil in front of the GDE, on the GDL side exposed to ambient air, during constant ORR rate (galvanostatic discharging at j = -5 $mA \cdot cm^{-2}$). We expect that the oxygen concentration inside the GDE would gradually decrease upon its constant consumption by the ORR. This experiment assumes that in a flooded electrode, the rate of oxygen consumption is faster than the transport rate of oxygen from the gas phase to the catalyst surface, hence forcing the electrode into a state of oxygen-starvation. Under these very stringent operating conditions, as expected this translates into a progressive drop of the electrode potential with time, see Figure 56a. A set of X-ray absorption spectra was acquired during the experiment simultaneously and are displayed in Figure 56b. If the access of oxygen is not hampered (ORR with O_2), the resulting XANES spectrum is identical to the one of the pristine electrode. When the electrode potential drops due to the lack of oxygen supply from ambient air (ORR without O_2), a negative shift is observed in the XANES region, indicating a lowering of the average Mn oxidation state[175]. The XANES spectrum of the starved electrode coincides well with the XANES of the Mn(II,III)oxide Mn_3O_4 reference compound, thus confirming that the α-MnO_2 component of the GDE is progressively reduced into Mn_3O_4. This is in agreement with a previous study[236], which reported the formation of Mn_3O_4 upon exposure of MnO_2-based electrodes to large ORR overpotentials. Although a clear identification of the chemical process leading to the transformation of α-MnO_2 upon the potential drop still needs to be fully resolved, our results suggest that the α-MnO_2 is stable provided that the O_2-reactant is supplied to the catalytic site at a sufficient

rate for the current given current load applied. On the other hand, if the access to oxygen is hindered (e.g. due to GDE flooding), the α-MnO_2 can be easily converted into other oxide species with lower valence state upon extended excursion towards large overpotentials, thereby altering/reducing the overall activity/stability of the electrode.

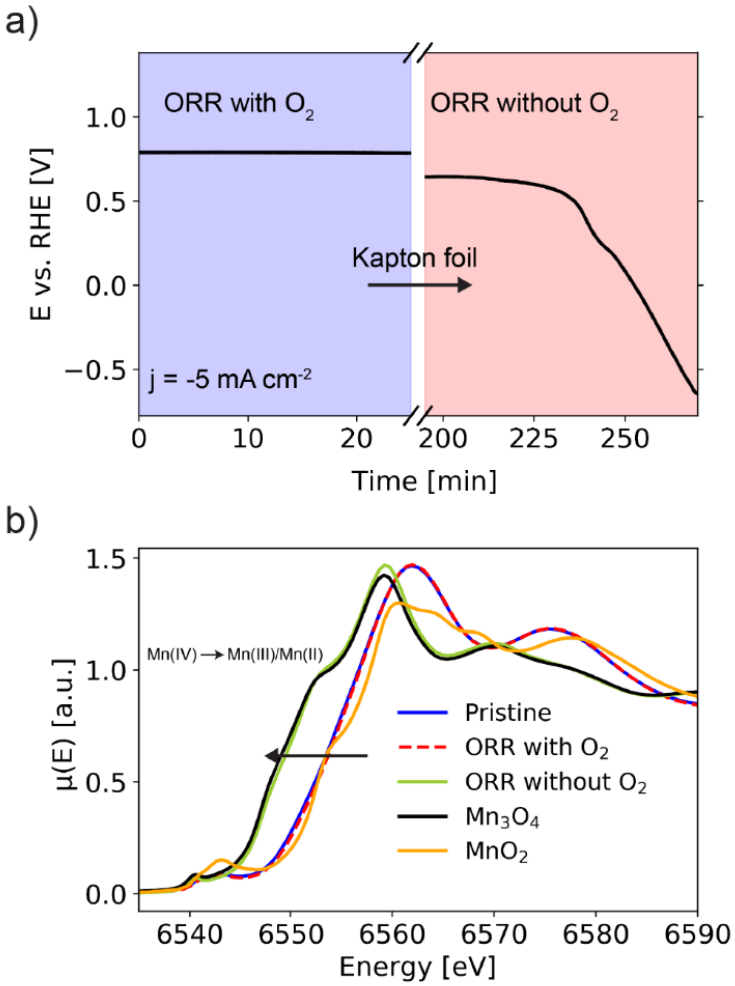

Figure 56: (a) Chronoamperometry during in situ XAS measurements at ORR relevant electrochemical conditions (j = -5 mA·cm^{-2}) before and after oxygen starvation. **(b)** Comparison of Mn K-edge XANES collected on the GDE in pristine state (blue) and on GDE after *in situ* exposure to ORR before (red) and after oxygen starvation (green). The figure also includes the reference XANES of Mn_3O_4 (black) and MnO_2 pyrolusite (orange) powder.

3.6. Monitoring the structural and electronic changes of the α-MnO_2 under battery application condition via operando extended X-ray absorption fine structure (EXAFS) analysis

Parts of this chapter have been submitted as manuscript for publication in Journal of Power Sources.

In order to provide direct information on structural changes that may occur at the electrocatalyst components under current loads characteristics for normal (standard) battery operation, particularly at OER condition, *in operando* XAS investigations at the Mn and Ni K-edges have been carried out to complete the post-mortem analyses presented above. Both the architecture and composition of the electrode, as well as the configuration of the electrochemical setup, have been slightly adapted to achieve optimal edge-jumps and signal-to-noise ratio in the absorption spectra for the Mn and Ni K-edges, but remained very similar in terms of compositional characteristics to those employed in the previous section and without sacrificing the current densities applied during testing (electrode performance). Details relative to the electrode compositions and electrochemical cell design can be found in the chapter Experimental Methods and in the Annex (Figure A17), respectively. The *in operando* XAS experiment, devised to follow discharge/charge cycles, consists of a sequence of cathodic (ORR) and anodic (OER) current density of j = 5 $mA \cdot cm^{-2}$, carried out in ambient air without CO_2 trap. In this way we could perform high-quality *operando* XAS spectroscopy under practical GDE operating conditions. It should be emphasized that the current densities used in this study are one to two orders of magnitude higher than other *operando* XAS studies performed on other GDE design concepts[175,176,237]. We therefore consider that our results provide information on structural, chemical and electronic modifications occurring when electrocatalyst material is subjected to application-relevant operating conditions. Further information on the electrochemical conditions applied are given in Table A3 and Figure A17.

3.6.1. *In operando* EXAFS investigation of the α-MnO_2 GDE component

As shown in Figure A18, variations in the XANES regions of the absorbance spectrum under polarization (either during ORR or OER) normalized with the spectrum acquired at OCP can be clearly resolved for the Mn K-edge, while no change takes place for the Ni K-edge. This first indicates

that under the current loads of 5 $mA \cdot cm^{-2}$ (for both ORR and OER), significant structural/chemical changes occur at the α-MnO_2 component of the GDE, and apparently in a reversible manner since respective spectra acquired during ORR and OER nearly overlap along successive load cycles. Conversely, the Ni/NiO component of the GDE appears remaining unaffected structurally under these operating conditions or the changes remain below the detection limit during the first load cycles. To some extent the opposite has been observed at the E.o.L. GDE from chemical surface analysis by XPS, see subsection 3.5.3. Therefore, only the evolution of the local chemical environment of the α-MnO_2 electrocatalyst during ORR and OER processes will be addressed in this subsection by Mn K-edge EXAFS analysis. To this aim, a fitting analysis was conducted on results gained from two GDEs (prepared in an identical fashion, see Experimental Methods): one with and a second one without incorporating the Ni/NiO nanoparticle component during the fabrication of the GDE, this in order to resolve better their role in stabilizing the α-MnO_2 component under current loads. To perform such analysis of the EXAFS oscillation, we fixed the amplitude reduction factor (S_0^2, which accounts for the intrinsic losses accompanying the electron scattering processes) to 0.8, following the report of Calvin Scott[238]. Edge energy (E_0, providing information on the relative changes of the average Mn oxidation state), the coordination numbers (CN), the mean squared relative displacements (σ^2, accounting for static and thermal disorders) and interatomic distances (R) were set as refinement variables. For the latter, our model contains four contributions (scattering paths), leading to four adsorber-scatterer interactions. These include two Mn-O contributions that account for i) the Jahn-Teller distortion of the MnO_6 octahedra (Mn-$O_{lattice}$, contributing to a relative asymmetric oxygen distribution around the Mn^{4+} ions[239], and ii) possible adsorbed oxygen-containing molecules/species (e.g. intercalated water molecules)[240] or hydroxide end groups on the catalyst surface[241] (Mn-O_{ads}). The two remaining contributions relate to the Mn-Mn distances with the edge-sharing MnO_6 octahedra (Mn-Mn_{edge}) and the corner-sharing MnO_6 octahedra (Mn-Mn_{corner})[239,242]. The fitting procedure was always carried out within the same R- and k-ranges (intervals) of 1.25-3.25 Å and 2.3-15.3 $Å^{-1}$, respectively. The structural model representing the α-

MnO_2 employed for the fit of the EXAFS data is displayed in Figure 58. Comparison of the experimental data with the fitted model in R- and q-spaces for the GDEs with Ni/NiO and without Ni/NiO nanoparticles are shown in Figure A19 and Figure A20, respectively. All fitted parameters resulting from the refinement procedure are reported in Table A4 (some of the data tabulated are also given as plots in the Figure A21), which also includes the R-factor estimating the goodness of the fits. Qualitatively, the fitted model matches very well with the experimental data (see Figure A19 and Figure A20), as also witnessed by the very low R-factors (ca. 0.004, see Table A4). This strengthening overall the choice of the model applied.

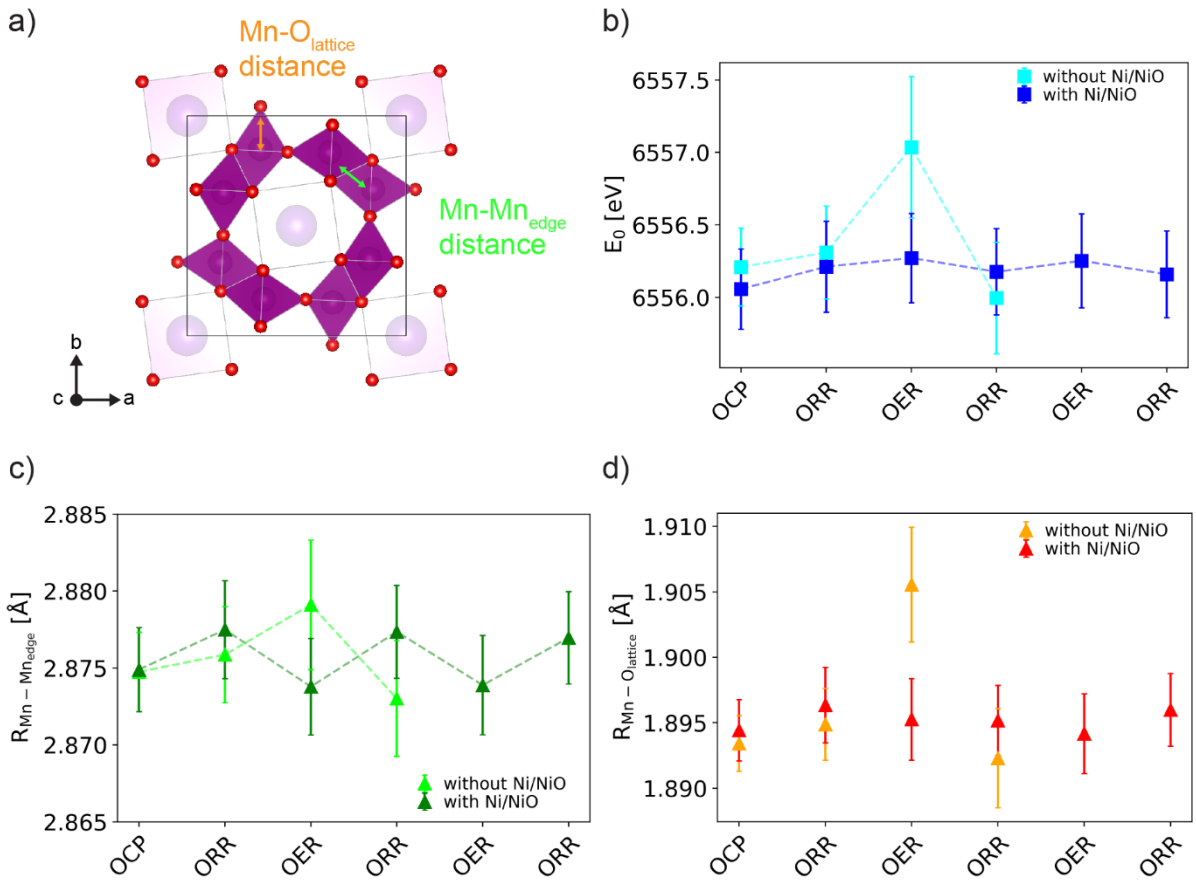

Figure 57: (a) Schematic (visualized with VESTA[163]) displaying the α-MnO_2 crystal lattice. **(b-d)** Experimental data resulting from fitting of EXAFS spectra measured under the aforementioned current load conditions (see Experimental Methods chapter): **(b)** Mn K-edge energy E_0, **(c)** radial distances R of Mn-Mn edge-sharing octahedra $R_{(Mn\text{-}Mn)edge}$ and **(d)** $Mn\text{-}O_{lattice}$. Error bars represent the fit uncertainties, as delivered by the ARTEMIS software[164].

Figure 57b-d shows the evolution of the most relevant fitted parameters during OER and ORR current loads. The first current load for the ORR (discharge) results in an initial slight raise of E_0 with respect to OCP, Figure 57b, for both GDE either or not including Ni/NiO nanoparticles. This is tentatively attributed to an initial reorganization/forming/restructuring of the pristine α-MnO_2 component, which results in a slightly higher average oxidation degree of the Mn centres. Indeed, changes in the oxidation degree for manganese oxide compounds have been related to shifts of the XANES region on the absorption energy scale and the corresponding edge energy[175]. For the GDE including Ni/NiO nanoparticles, subsequent OER (charge) leads to a further slight increase of the oxidation degree of Mn, as expected from higher electrode potentials, followed by a small down-shift of E_0 during the next ORR step translating a relatively lower degree of oxidation of the Mn centres, as expected from the lowering of the electrode potential (see Figure A17). E_0 remains established at 6556.2 eV and 6556.3 during ORR and OER, respectively, during successive load cycle steps (see also Table A4). Although this small difference of ca. 0.1 eV in E_0 during ORR and OER remains lower than the error bar calculated (0.3 eV), periodicity and constant respective E_0 values for ORR and OER upon successive load cycles suggest a reversible change in the oxidation degree of the α-MnO_2 component in the GDE including Ni/NiO nanoparticles during charge and discharge steps. This result is obviously in good agreement with the XANES data in Figure A18, and with other XANES data[142,175] and Soft XAS data[176,243] previously published on other MnO_x-based compounds). The situation appears different for the GDE without Ni/NiO nanoparticles. The first OER step is characterized by a significant up-shift of E_0 by 0.7 eV, with respect to E_0 at ORR. This shows that the α-MnO_2 is comparatively more oxidized for the GDE without Ni/NiO that for the GDE including Ni/NiO nanoparticles, in good consistency with η_{OER} about 30 mV higher for the former than for the latter GDE (all data relative to the measured electrode potentials are provided in the Annex, Table A3). Thus, in absence of Ni/NiO particles, the α-MnO_2 component of the GDE undergoes more severe oxidative stress during OER in supplying the current load, this supporting our

previous findings that the most active sites for the OER are located at the Ni/NiO particles for such ternary C-MnO_2-Ni/NiO catalyst composites (see subsection 3.3). E_0 for the second ORR step is lower by 0.3 eV in absence of Ni/NiO compared to the first ORR step, while this value remained unchanged with the GDE including Ni/NiO nanoparticles (see above). This indicates that the (relatively) larger Mn oxidation degree during OER in absence of Ni/NiO nanoparticles impedes the reversibility of the E_0 variation during successive load cycles, suggesting an irreversible restructuring. Structural characteristics, as probed by the changes in average $R_{(Mn\text{-}Mn)edge}$ displayed in Figure 57c, follows a similar pattern. Including Ni/NiO in the GDE, the distance for edge sharing MnO_6 octahedra reversibly oscillates from 2.877 Å down to 2.874 Å during successive ORR and OER ($\Delta R_{(Mn\text{-}Mn)edge}$ ≈ 0.003 Å), respectively. Inspecting previously reported data on Fe-exchanged α-MnO_2[239], a relative shortening of this radial distance has been also resolved during potentiostatic OER. Furthermore, a relationship (with the identification of an optimum) between $R_{(Mn\text{-}Mn)edge}$ and the adsorption of reactive intermediates during ORR has been proposed from electrochemical and X-ray absorption investigations[242]. In absence of Ni/NiO nanoparticles $R_{(Mn\text{-}Mn)edge}$ increases up to 2.879 Å during the first OER, higher by 0.003 Å compared to the preceding ORR, while in presence of Ni/NiO nanoparticles this distance was decreasing during the OER following the ORR. Also for the GDE without Ni/NiO nanoparticles, the Mn-Mn distance for edge sharing octahedral is even lower by 0.002 Å compared to the initial OCP value during the second ORR current step. Similar influence of the presence (or the absence) of Ni/NiO component in the GDE can be observed on the variations at the Mn-Mn distance for corner sharing MnO_6 octahedra (see Figure A21 and Table A4).

For the GDE including Ni/NiO nanoparticles, the value of $R_{(Mn\text{-}O)lattice}$ remained nearly unchanged during successive load cycles (≈ 1.895 Å), see Figure 57d. On the other hand, $R_{(Mn\text{-}O)lattice}$ increased to ca. 1.905 Å at OER condition when Ni/NiO is not present in the GDE. Consequently, it results significant drop in the average Mn-O coordination number (Table A4 and Figure A21). Similar dependence on the presence (or absence) of Ni/NiO nanoparticles in the GDE can be monitored on the $R_{(Mn\text{-}O)ads}$ parameter, see Table A4 and Figure A21.

From this first analysis of the EXAFS data, it can be concluded the following:

- The presence of Ni/NiO nanoparticles in the GDE stabilizes and/or makes reversible the variations in the structural characteristics and in the Mn oxidation degree of the α-MnO_2 component during the first successive ORR/OER (discharge/charge) galvanostatic current steps (5 $mA \cdot cm^{-2}$). In providing the most active catalytic sites for the OER in the ternary catalyst composite, Ni/NiO nanoparticles enables the reversibility of the α-MnO_2 component in lowering the overpotential during the OER current load.
- The reversible structural modification at the α-MnO_2 component taking place during the ORR and the OER are resolved at the level of the Mn-Mn distances rather than at the averaged Mn-O bond length, with an increase of the distance between both edge- and corner- sharing MnO_6 octahedra during ORR, and, oppositely, a lowering during the OER. This effect is qualitatively more pronounced for the former distance than for the latter one and suggests a sort of potential-induced 'breathing' of the α-MnO_2 structure at the level of the MnO_6 octahedra structural units. Our data also suggest that significant variation on the averaged Mn-O bond length is concomitant with an irreversible restructuring.

Yet, electrocatalytic reactions occur at the catalyst material surface while hard X-rays with energies higher than 5 keV penetrate deeply into the sample, therefore making XAS technique not inherently surface sensitive that delivers averaged information including the bulk of the material. Nevertheless, the higher penetrating power of hard X-rays enables *in situ* studies with realistic battery electrodes that would not be readily feasible with alternative surface-sensitive approaches. To overcome this limitation, we attempt in the following a differential analysis of the same EXAFS data in order to resolve better structural/chemical modifications at the surface of the α-MnO_2 component of the GDE during successive load cycles.

3.6.2. Probing oxidation state and local structural changes at the α-MnO_2 surface via differential EXAFS analysis

For such differential analysis, the main hypothesis assumes that the structural/chemical characteristic of the bulk of the α-MnO_2 component during current load results in EXAFS spectrum can be approximated by the whole EXAFS spectrum (bulk + surface) acquired at OCP. This is illustrated in Figure 58.

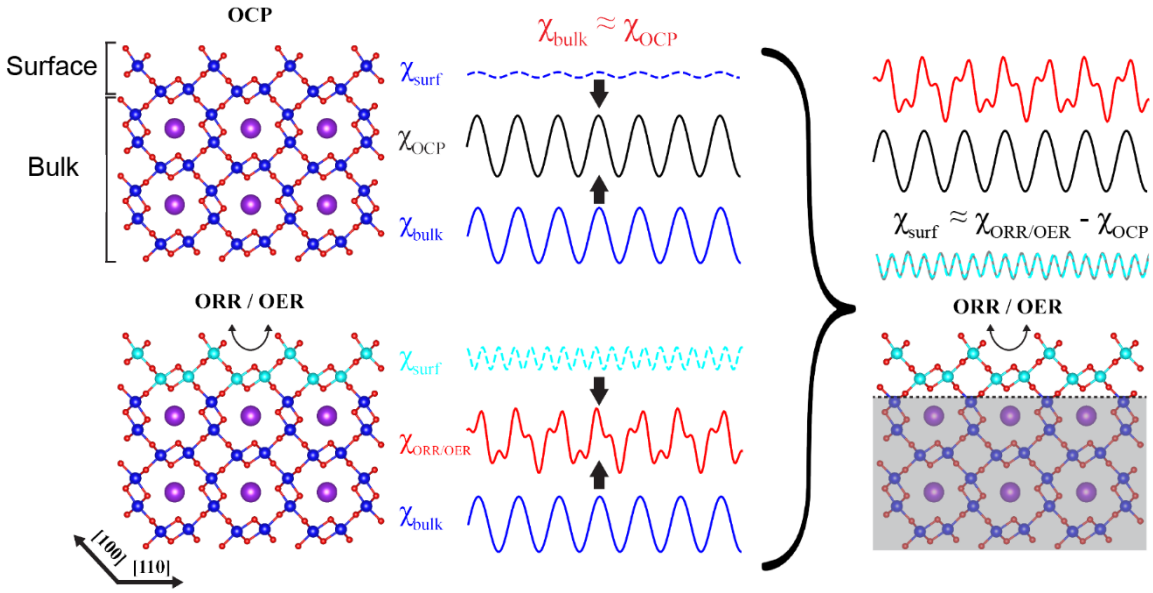

Figure 58: Schematic representation (visualized with VESTA[163]) displaying the bulk and (110) surface structure of α-MnO_2, where the Mn ions are represented in blue, the oxygen in red and K^+ ions in purple and representation of the main underlying hypothesis for the differential surface analysis (see text for details).

Computational[244,245] and experimental[241] studies on the atomic configuration and topography of the α-MnO_2 surface show that Mn oxide (110) crystal plane, which is one of the most abundant, is very stable (does not undergo reconstruction) and can be superimposed to the bulk structure. Therefore, it is presumed that, apart from the presence of hydroxyl (-OH) groups populating the outermost layer of Mn oxide, the surface would have similar general structural characteristics of the bulk at OCP (Figure 58, left). Hence, we assume that the Mn K-edge EXAFS oscillations χ(k) measured at OCP condition might be a good approximation of the signal associated with the bulk of the material under current loads. The OCP is located within the rather narrow electrode potential

window defined from galvanostatic loads, see Table A3, and so processes such as, e.g., a significant potential-induced cationic intercalation/de-intercalation modifying the bulk structural characteristics under current load with respect to the situation at OCP should not take place. Therefore, to resolve structural/chemical changes at the α-MnO_2 surface that we expect undergoing during ORR and OER processes, we calculated the difference between Mn K-edge EXAFS oscillations $\chi_i(k) - \chi_{OCP}(k)$, where i = ORR or OER, as illustrated in Figure 58.

In addition, it should be noticed that the fitting procedure was carried out on the differential EXAFS spectra within the R- and k-ranges of 2.3-3.3 Å and 2.2-14.0 $Å^{-1}$ for the GDE with Ni/NiO and 2.3-2.9 Å and 2.0-15.6 $Å^{-1}$ for the GDE without Ni/NiO, respectively. Consequently, the refinement focuses over the ranges for Mn-Mn_{edge} and Mn-Mn_{corner} interactions, thus omitting oxygen contributions at shorter radial distances (R < 2 Å). Owing to their complex interpretations, which directly correlate with the ORR and OER electrode processes, they should be addressed in detail in a separate and dedicated study.

Figure 59a shows the Fourier transforms (FT) of the differential Mn K-edge EXAFS spectra $\chi_i(k) - \chi_{OCP}(k)$. The figure also includes the FT at OCP condition (black dots), which was obtained from the bulk EXAFS measurement, used here for qualitative comparison.

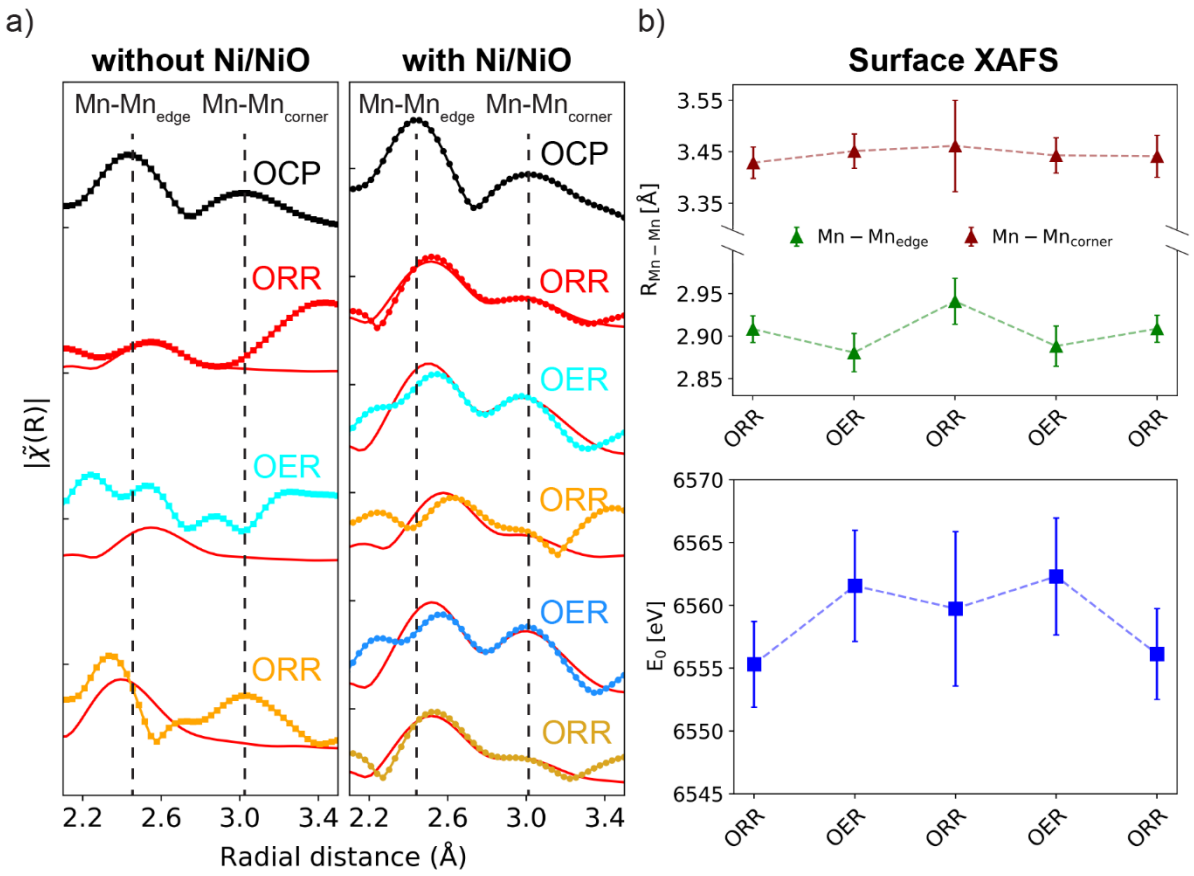

Figure 59: **(a)** Differential EXAFS spectra in the R-space (scatters) and curve fitting (solid line) of the Mn K-edge for GDE without- (left) and with Ni/NiO nanoparticles (right) at OCP and under current loads as indicated in the figure. **(b)** Mn-Mn interatomic distance for edge-sharing and corner-sharing MnO_6 octahedra (top) and edge energy E_0 (bottom) as a function of applied electrochemical condition as indicated in the figure.

Interestingly, the two FT peaks of the Mn-Mn_{edge} and Mn-Mn_{corner} at OCP (bulk) are still clearly visible in the FTs in the differential EXAFS spectra, especially in the case of the GDE including Ni/NiO (right-hand side panel). This strongly supports the assumption that the α-MnO_2 surface retains a crystal structure rather similar to that of the bulk. Under current loads, see Figure 59a, refinement of the model delivers satisfactory fits for the experiments conducted with the GDE including Ni/NiO nanoparticles for both ORR and OER, R-factors remains below ca. 0.1 (see Table 5). Larger R-factors obtained with the differential analysis most likely results from the lower amount degrees of freedom (less parameters are refined) and inherently from the spectra subtraction operated. Oppositely, for the GDE without Ni/NiO nanoparticles, no reasonable fits can be obtained after the first ORR current load (see also the very large R-factor obtained). Hence, the model can still track the surface structural

changes of MnO_2 when Ni/NiO is included in the GDE, while, on the other hand, this is not the case in the absence of Ni/NiO. It can be concluded for this latter GDE that a larger restructuring undergoes at the α-MnO_2 surface (in good consistency with the larger overpotentials, see Table A3). Therefore, these results demonstrate that traditional hard XAS and suitable cell design enable a surface probing, provided that the potential-induced restructuring is not too large, for catalyst materials embedded in an electrode under current loads that are realistic with respect to practical application.

Table 5: Results of the non-linear least-squares curve-fittings for the differential EXAFS spectra shown in Figure 59a measured under different electrochemical conditions. To perform the analysis, the amplitude reduction factor (S_0^2), as well as the mean relative squared displacement (σ^2) were keep fixed at 0.8 and at $5 \cdot 10^{-4}$ Å^2, respectively.

GDE without Ni/NiO

Condition	$R_{(Mn\text{-}Mn)edge}$ [Å]	$R_{(Mn\text{-}Mn)corner}$ [Å]	CN_{edge}/CN_{corner}	E_0 [eV]	R-factor
ORR (1st)	2.907 ± 0.018	-	-	6555.7 ± 4.6	0.05
OER (1st)	2.905 ± 0.117	-	-	6559.0 ± 29.5	0.71
ORR (2nd)	2.807 ± 0.073	-	-	6538.2 ± 24.9	0.34

GDE with Ni/NiO

Condition	$R_{Mn\text{-}Mn\ edge}$ [Å]	$R_{(Mn\text{-}Mn)corner}$ [Å]	CN_{edge}/CN_{corner}	E_0 [eV]	R-factor
ORR (1st)	2.908 ± 0.016	3.429 ± 0.031	2	6555.3 ± 3.4	0.05
OER (1st)	2.881 ± 0.023	3.451 ± 0.034	1	6561.6 ± 4.4	0.10
ORR (2nd)	2.930 ± 0.033	3.461 ± 0.089	3	6558.4 ± 5.6	0.10
OER (2nd)	2.888 ± 0.024	3.443 ± 0.034	1	6562.3 ± 4.7	0.12
ORR (3rd)	2.910 ± 0.016	3.441 ± 0.041	3	6556.1 ± 3.6	0.05

Radial distances for edge- and corner-sharing octahedra for the GDE including Ni/NiO nanoparticles under current loads for ORR and OER are plotted in Figure 59b (see also Table 5). The Mn-Mn radial distance for edge-sharing MnO_6 octahedra changes reversibly from ca. 2.91 Å (ORR) and 2.88 Å (OER), $\Delta R_{(Mn\text{-}Mn)edge} \approx 0.03$ Å, while it remains nearly constant at ca. 3.44 Å for corner-sharing octahedra, independently of the direction of the current. With the differential analysis the reversible

changes $\Delta R_{(Mn\text{-}Mn)edge}$ are now clearly resolved with respect to fit uncertainties (errors bars, compare with Figure 57c). We also observed that the reversible changes in the ratio of radial distances edge/corner follow the one for the ratio of the CNs, increasing during the ORR and decreasing during the OER (see Table 5 and the variations of amplitude of the two corresponding FT peaks in Figure 59a). Following the interpretation proposed Lee and co-workers[239] with an Fe-exchange α-MnO_2 material, this increase in the intensity of the FT peak attributed to the $Mn\text{-}Mn_{corner}$ radial distance evidences an improved collinear alignment of corner-sharing MnO_6 octahedra during OER.

Compared to the conventional analysis, see previous subsection, $R_{(Mn\text{-}Mn)edge}$ during OER and $R_{(Mn\text{-}Mn)corner}$ values are found very similar, and the main difference lies in the significantly larger $R_{(Mn\text{-}Mn)edge}$ during the ORR current load. It results that for the differential analysis $\Delta R_{(Mn\text{-}Mn)edge}$ is larger by one order of magnitude (0.03 Å vs. 0.003 Å). An approximation for calculating the surface-to-volume ratio (S/V) of elongated nanostructures (that is the case for the α-MnO_2 employed in this study) has been proposed by He et al.[246]. As shown in the SEM micrograph (Figure 25), our α-MnO_2 particles have a fibrous, needle-like morphology with an average length (l) of approximately 600 nm and a width (d) of about 40 nm. Making use of cylinder model delivers a S / V ratio of ca. 10 % (Eq. 1).

Eq. 1) $$\frac{S}{V} = \frac{4l+2d}{dl} = \frac{4\times600+2\times40}{600\times40} \approx 10\ \%$$

Thus, if we assume for our sample that the structural characteristics of the α-MnO_2 bulk represents about 90 % of the EXAFS spectrum (S / V = 10 %), the increase by one order of magnitude of the average variation for $\Delta R_{(Mn\text{-}Mn)edge} \approx 0.003$ Å between ORR and OER that was obtained from the conventional EXAFS fitting analysis (see previous subsection) to $\Delta R_{(Mn\text{-}Mn)edge} \approx 0.03$ Å obtained by differential analysis is perfectly consistent. This strengthens the main initial assumption for the differential analysis, naming that the structural characteristics of the bulk of the α-MnO_2 component under current loads are very similar to those at OCP, provided obviously that the overpotentials remain moderated. It also indicates that the (reversible) structural changes are confined within the

surface of the α-MnO_2 during the two electrocatalytic reactions for charge and discharge. It should be mentioned that these surface structural changes might not be directly related to the electrocatalytic processes per se, e.g. either ORR or OER through the bonding of reaction intermediate(s), but rather be an electrode potential-induced mechanism, such as, for example, the initial stage of the dissolution process. Indeed, as shown in section 3.4, the intrinsic catalytic properties of the α-MnO_2 strongly relates to the fraction of carbon support embedded, suggesting interfacial C/α-MnO_2 sites as the most active catalytic site towards the ORR. Further detailed investigation are needed, including a full analysis/modelling of the Mn-O radial distances, to resolve this point.

Now inspecting the changes in E_0, Figure 59b, these are again much larger ($\Delta E_0 \approx 5$ eV, although the broader error bar) than the variation in E_0 obtained by the conventional EXAFS fitting approach presented in Figure 57b ($\Delta E_0 \approx 0.1$ eV). The large variation in E_0 suggests that the surface may be exposed to a more severe oxidative stress than estimated from the conventional analysis. Previous XAS studies on multivalent manganese oxide materials suggests that there is a (linear) relationship between the position of the Mn K-edge energy, E_0, and the Mn oxidation state[247]. Hence, in order to probe the oxidation state of the α-MnO_2 surface at ORR and OER conditions, such relationship between E_0 and the oxidation state can be used, as shown in Figure 60. Commercial Mn compounds MnO (+2), Mn_3O_4 (+2.7[175]), Mn_2O_3 (+3), pyrolusite MnO_2 (+4) were used for the calibration. Figure 60 also includes two colored areas that represent the formation of soluble Mn compounds MnO_4^{2-} and MnO_4^- with valences +6 and +7, respectively, where the edge energy range was estimated from the oxidation degree. The positions of the latter on the E_0 scale remains only qualitative at best, since Gilbert and co-workers[248] have shown that the shifts in E_0 deviate from linear, particularly when the +7 valence is included. Nevertheless, we believe that this qualitative approximation provides already a good indication of the Mn valence state as a function of the E_0 shift. It can be shown that the fitted E_0 values obtained by the differential EXAFS during the ORR give a valence of around +3.9, which matches well to the value obtained by the conventional EXAFS fitting method

(Figure 57b). On the other hand, during the OER E_0 moves towards values that are near to the range where dissolution of Mn is expected. This emphasizes the critical role of the Ni/NiO nanoparticles in providing the most active sites for the OER, and consequently lowering the overpotential, to avoid partial dissolution of the α-MnO_2 component. This also indicates that the surface structural changes probed by the radial distance Mn-Mn_{edge} (Figure 59c) might be as well associated with the initial stage of the dissolution process, as previously suggested. In lowering the overpotential during the OER, the Ni/NiO nanoparticles prevent excessive increase of the oxidative stress at the surface of the α-MnO_2 component leading to its irreversible restructuring / partial dissolution.

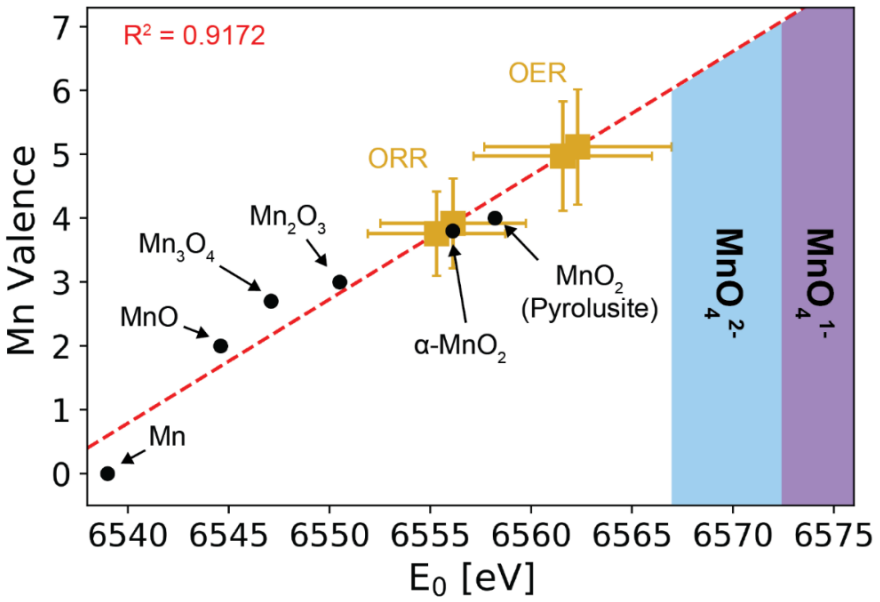

Figure 60: Determination of the α-MnO_2 surface oxidation state at ORR and OER conditions using the Mn K-edge energy shift of the reference Mn compounds. See text for details.

3.7. Mapping of the different degradation processes occurring at the GDE under successive charge/discharge current loads

Parts of this chapter have been submitted as manuscript for publication in Journal of Power Sources.

In the following, we attempt a mapping of the different degradation processes occurring at the GDE under successive charge/discharge current loads, and of their interactions/relationships. These are also illustrated in the Figure 61.

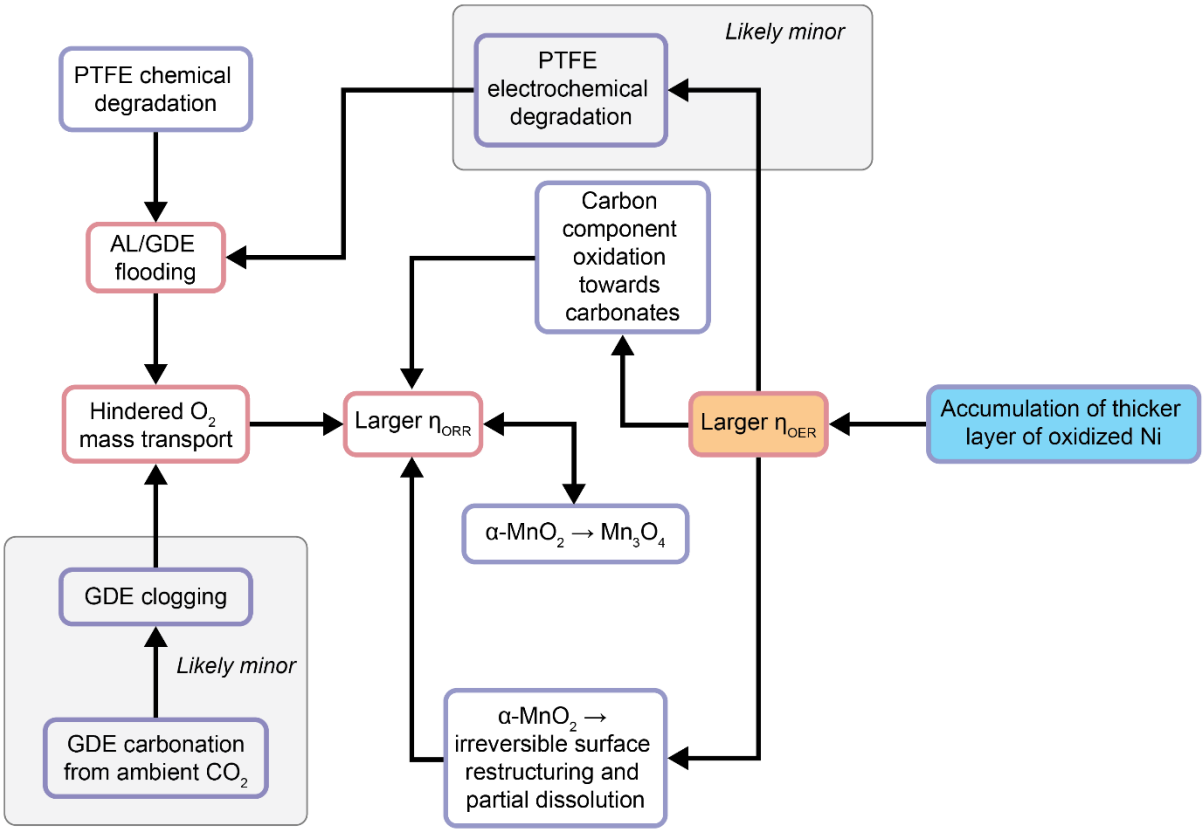

Figure 61: Mapping of the different degradation processes occurring at the GDE under successive charge/discharge current loads, and of their interactions/relationships. See text for details.

Bringing together the insights gain from the various physical-chemical methods applied and described in sections 3.5. and 3.6., we can determine four main degradation paths:

- The chemical degradation of the PTFE component of the active layer with the formation of cracks and the thinning of the PTFE layer, as observed from *ex situ* SEM imaging and XPS data, respectively, appears consistent with an increase of the reactant mass transport

limitations during the ORR probed by EIS. According to XPS data, it is suggested a degradation resulting from a chemical process rather than an electrochemical (potential-induced) process. Losses in the hydrophobic properties of the GDE enables a flooding of the GDE that hinders the O_2-reactant mass transport towards the catalytic sites and results consequently in larger overpotentials. XANES data acquired under forced O_2-starving conditions indicated that larger overpotentials result in the irreversible reduction of the α-MnO_2 into Mn_3O_4. Consistently, our previous results (see section 3.4) indicated that larger PTFE loadings led to an enhanced stability of the GDE upon successive charge/discharge cycles, however at the cost of the GDE efficiency (higher overpotentials for the ORR and the OER). Electrochemically-induced degradation of the PTFE was found only for too large overpotentials during the OER.

- EXAFS data highlights the role of the Ni/NiO nanoparticles in stabilizing or, more precisely, in enabling reversible structural changes and variations in the oxidation degree of the Mn centers at (the surface of) the α-MnO_2 component during the OER. In providing the most active catalytic sites for the former reaction, the presence of Ni/NiO nanoparticles in the GDE results in lower overpotentials at the given current load. A progressive surface restructuring of the Ni/NiO nanoparticle surface towards the formation (accumulation) of a thicker hydroxide/oxy-hydroxide layer upon successive load cycles, as suggested by the *ex-situ* XPS investigations, will result either in a lowering of the surface concentration of these most active sites for the OER or to an increased impedance for the electron transfer during the reaction (or a combination of both) since oxidized Ni is less conductive than Ni metal. Both anyway have for consequences to lead to larger overpotentials during the OER, this being detrimental for the reversible restructuring of the α-MnO_2. Since the latter provides the most active catalytic sites (in association with the carbon component) for the ORR, it results larger overpotentials during discharge current loads. This degradation of the material properties for

the ORR was also probed by EIS with an increase of the charge transfer resistance. This scheme also provides a rational explanation for the simultaneous degradation of the GDE performances for both the charge and discharge with an increase of the overpotentials for the ORR and OER initiated at the same load cycle, see Figure 50.

- As shown by the XPS study, the carbon component also suffers from degradation. Too large overpotentials during the OER leads to its oxidation, likely towards the formation of carbonate / hydrogen carbonate. Section 3.4. pointed towards the boundary carbon / α-MnO_2 components as the most active catalytic site for the ORR. Degradation of the carbon component would consequently result in a lowering of the catalyst activity. Investigation on the degradation mechanism of the carbon component and of its relative impact on the GDE performance still need to be addressed in detail. Nonetheless, here again and as for the α-MnO_2 component, the role of the Ni/NiO nanoparticles, and the stability of their properties in lowering the overpotential for the OER, appears critical.

- The XPS data also suggest the chemical formation of potassium carbonate / hydrogen carbonate from the reaction of the CO_2 present in the air with the alkaline electrolyte. This could lead to clogging of the porous structure[211–214], impeding the O_2 mass transport and thereby increasing the overpotentials of the electrocatalytic reactions. Nonetheless, the relative weight of this specific degradation process with respect to the other degradation processes remains to be addressed in detail. We might here hypothesize that with the GDE design employed, and with the results presented, carbonation of the active layer upon reaction with the CO_2 from the ambient air stays relatively minor compared to the other degradation processes.

4. Conclusion and outlook

In this work, we optimized a facile, reproducible, rapid and scalable method for the synthesis of one most promising earth-abundant transition metal oxide-based catalyst for the ORR, the cryptomelane type manganese dioxide, α-MnO_2. A systematic physical, chemical and electrochemical characterization of the latter was then carried out. Investigation the ORR activity was carried out by the RDE and RRDE techniques. This included the optimization of key parameters, such as the preparation of catalyst layer, as well as the refinement of the experimental electrochemical conditions. The simple mixture aqueous alcohol solution of abundant components, and with two out of three that are furthermore commercially available, delivered with $(C)_{33}(MnO_2)_{33}(Ni/NiO)_{33}$ a highly active and stable bifunctional composite electrocatalyst for both ORR and OER. Such low-cost path, including the catalysts embedding within a GDE whose structural composition has been refined, delivered results outperforming in terms of activity and stability the vast majority of previous reports for bifunctional air cathode when ZAB applications are targeted, still accounting for preparation procedure designed to ease a scale-up process. Performances of the optimized GDEs, with overpotentials of ca. 0.35 V for both ORR and OER (55 % energy efficiency), were found stable over 400 hours at 20 $mAh \cdot cm^{-2}$ load cycles (j x t = 10 $mA \cdot cm^{-2}$ x 2 h) for both charge and discharge reactions. The results presented demonstrates the relevance of the methodological approach implemented in this study, bridging also the gap between the preparation of efficient catalyst and the development of performant electrode, for the design of electrodes for catalytic conversion that could potentially find their path towards practical application. In particular, the definition of relevant metrics, as those proposed by Parker et al., to assess electrode properties that are relevant when one considers a potential practical application of the electrode/material under development appears essential to nurture a technology transfer towards industry.

The degradation of a bifunctional O_2 GDEs in contact with aqueous alkaline solutions upon successive galvanic charge-discharge cycles has been extensively investigated by a set of complementary physical-chemical methods, either *ex-situ* (XPS and SEM) or *in-situ* (EIS, XAS). The

whole set of data were acquired on realistic GDEs embedding the active material in the active layer, and under current loads relevant for the practical application of metal-air batteries. This multi-technique approach resulted a detailed mapping of the degradation processes of the electrode components impairing the durability of the GDE performances, being both chemical and potential-induced, and of their respective interactions. In principle, this mapping should be representative of the processes taking place at the cathode of a metal-air aqueous alkaline battery.

Such model investigation revealed two main leverages to improve further the durability of the GDE upon successive charge/discharge cycles: i) limiting the chemical degradation of the hydrophobic binder and ii) preventing the degradation of the OER catalytic function.

The development of a cell hardware suitable for direct *in situ* XAS investigations with a GDE and under current loads that are high for the application of interest, in combination with a differential analysis of the data, revealed the essential role of the OER catalytic function in enabling reversible structural (radial distance between edge-sharing MnO_6 octahedra) and chemical (degree of oxidation of the Mn centers probed by the Mn K-edge energy) changes at the surface of the α-MnO_2 component during charge and discharge load cycles. We proposed that the lowering of the radial distance between edge-sharing MnO_6 octahedra during OER might relate to the initial stages of the MnO_2 irreversible dissolution process rather than to the electrocatalytic conversion of hydroxide ions towards molecular oxygen. Further detailed investigations on this specific topic are needed to provide a definitively disentangleing of the two processes. We have shown that the different degradation processes taking place at the bifunctional GDE under successive current loads are multiple and very much interrelated. Improving the durability of such type of electrodes for rechargeable zinc-air batteries will require a holistic approach accounting for the overall of these processes.

5. References

[1] X. Luo, J. Wang, M. Dooner, J. Clarke, Overview of current development in electrical energy storage technologies and the application potential in power system operation, Appl. Energy. 137 (2015) 511–536. https://doi.org/10.1016/j.apenergy.2014.09.081.

[2] Z.W. Seh, J. Kibsgaard, C.F. Dickens, I. Chorkendorff, J.K. Nørskov, T.F. Jaramillo, Combining theory and experiment in electrocatalysis: Insights into materials design, Science. 355 (2017) eaad4998. https://doi.org/10.1126/science.aad4998.

[3] B. Dunn, H. Kamath, J.-M. Tarascon, Electrical energy storage for the grid: a battery of choices, Science. 334 (2011) 928–935.

[4] M. Beaudin, H. Zareipour, A. Schellenberglabe, W. Rosehart, Energy storage for mitigating the variability of renewable electricity sources: An updated review, Energy Sustain. Dev. 14 (2010) 302–314. https://doi.org/10.1016/j.esd.2010.09.007.

[5] H. Chen, T.N. Cong, W. Yang, C. Tan, Y. Li, Y. Ding, Progress in electrical energy storage system: A critical review, Prog. Nat. Sci. 19 (2009) 291–312. https://doi.org/10.1016/j.pnsc.2008.07.014.

[6] H. Ibrahim, A. Ilinca, J. Perron, Energy storage systems—Characteristics and comparisons, Renew. Sustain. Energy Rev. 12 (2008) 1221–1250. https://doi.org/10.1016/j.rser.2007.01.023.

[7] D. Linden, T.B. Reddy, eds., Handbook of batteries, 3rd ed, McGraw-Hill, New York, 2002.

[8] Rastler, D., Electricity Energy Storage Technology Options: A White Paper Primer on Applications, Costs, and Benefits, ELECTRIC POWER RESEARCH INSTITUTE, 3420 Hillview Avenue, Palo Alto, California 94304-1338, 2010.

[9] J. McDowall, Integrating energy storage with wind power in weak electricity grids, J. Power Sources. 162 (2006) 959–964. https://doi.org/10.1016/j.jpowsour.2005.06.034.

[10] V.G. Lacerda, A.B. Mageste, I.J.B. Santos, L.H.M. da Silva, M. do C.H. da Silva, Separation of Cd and Ni from Ni–Cd batteries by an environmentally safe methodology employing aqueous two-phase systems, J. Power Sources. 193 (2009) 908–913. https://doi.org/10.1016/j.jpowsour.2009.05.004.

[11] Energy Storage Exchange, 2020, https://www.energystorageexchange.org/projects.

[12] W.H. Zhu, Y. Zhu, Z. Davis, B.J. Tatarchuk, Energy efficiency and capacity retention of Ni–MH batteries for storage applications, Appl. Energy. 106 (2013) 307–313. https://doi.org/10.1016/j.apenergy.2012.12.025.

[13] M.A. Fetcenko, S.R. Ovshinsky, B. Reichman, K. Young, C. Fierro, J. Koch, A. Zallen, W. Mays, T. Ouchi, Recent advances in NiMH battery technology, J. Power Sources. 165 (2007) 544–551. https://doi.org/10.1016/j.jpowsour.2006.10.036.

[14] A.S. Subburaj, P. Kondur, S.B. Bayne, M.G. Giesselmann, M.A. Harral, Analysis and Review of Grid Connected Battery in Wind Applications, in: 2014 Sixth Annu. IEEE Green Technol. Conf., IEEE, Corpus Christi, TX, USA, 2014: pp. 1–6. https://doi.org/10.1109/GREENTECH.2014.14.

[15] UK Launches Europe'S Largest Energy Storage Trial IEEE Spectrum - IEEE Spectrum, (n.d.). https://spectrum.ieee.org/energywise/energy/the-smarter-grid/uk-launches-europes-largest-energy-storage-trial (accessed December 10, 2019).

[16] Japan Looks at Recycling Vehicle Batteries for Renewable Power, 2019, https://oilprice.com/Alternative-Energy/Renewable-Energy/Japan-Looks-at-Recycling-Vehicle-Batteries-for-Renewable-Power.html.
[17] electrical energy storage project team, Electrical energy storage: white paper, International Electrotechnical Commission (IEC), 2011. <http://www.iec.ch/ whitepaper/pdf/iecWP-energystorage-LR-en.pdf>.
[18] F. Díaz-González, A. Sumper, O. Gomis-Bellmunt, R. Villafáfila-Robles, A review of energy storage technologies for wind power applications, Renew. Sustain. Energy Rev. 16 (2012) 2154–2171. https://doi.org/10.1016/j.rser.2012.01.029.
[19] S. Kim, Vanadium Redox Flow Batteries: Electrochemical Engineering, in: M. Taha Demirkan, A. Attia (Eds.), Energy Storage Devices, IntechOpen, 2019. https://doi.org/10.5772/intechopen.85166.
[20] D.H. Doughty, P.C. Butler, A.A. Akhil, N.H. Clark, J.D. Boyes, Batteries for Large-Scale Stationary Electrical Energy Storage, Electrochem. Soc. Interface. 19 (2010) 49–53. https://doi.org/10.1149/2.F05103if.
[21] Trung Nguyen, Robert F. Savinell, Flow Batteries, Electrochem. Soc. Interface. 19 (2010) 54–56.
[22] J. Fu, Z.P. Cano, M.G. Park, A. Yu, M. Fowler, Z. Chen, Electrically rechargeable zinc-air batteries: progress, challenges, and perspectives, Adv. Mater. 29 (2017) 1604685. https://doi.org/10.1002/adma.201604685.
[23] J. Fu, Z.P. Cano, M.G. Park, A. Yu, M. Fowler, Z. Chen, Electrically Rechargeable Zinc–Air Batteries: Progress, Challenges, and Perspectives, Adv. Mater. 29 (2017) n/a-n/a. https://doi.org/10.1002/adma.201604685.
[24] P. Hartmann, C.L. Bender, M. Vračar, A.K. Dürr, A. Garsuch, J. Janek, P. Adelhelm, A rechargeable room-temperature sodium superoxide (NaO2) battery, Nat. Mater. 12 (2013) 228–232. https://doi.org/10.1038/nmat3486.
[25] S.R. Narayanan, G.K.S. Prakash, A. Manohar, B. Yang, S. Malkhandi, A. Kindler, Materials challenges and technical approaches for realizing inexpensive and robust iron–air batteries for large-scale energy storage, Solid State Ion. 216 (2012) 105–109. https://doi.org/10.1016/j.ssi.2011.12.002.
[26] X. Ren, Y. Wu, A Low-Overpotential Potassium–Oxygen Battery Based on Potassium Superoxide, J. Am. Chem. Soc. 135 (2013) 2923–2926. https://doi.org/10.1021/ja312059q.
[27] M.A. Rahman, X. Wang, C. Wen, High energy density metal-air batteries: a review, J. Electrochem. Soc. 160 (2013) A1759–A1771.
[28] J. Zhang, Q. Zhou, Y. Tang, L. Zhang, Y. Li, Zinc–air batteries: are they ready for prime time?, Chem. Sci. 10 (2019) 8924–8929. https://doi.org/10.1039/C9SC04221K.
[29] A. Smee, LIII. *On the galvanic properties of the metallic elementary bodies, with a description of a new chemico-mechanical battery*, Lond. Edinb. Dublin Philos. Mag. J. Sci. 16 (1840) 315–321. https://doi.org/10.1080/14786444008650046.
[30] Richard Rennie, Jonathan Law, A Dictionary of Chemistry, 7 ed., Oxford University Press, 2016.
[31] L. Maiche, Patent number: 127069, France, 1878.
[32] G. W. Elmore, H. A. Tanner, *U.S. Patent*, Patent number: 3,419,900.
[33] A. M. Moos, *U.S. Patent*, Patent number: 3,267,909.

[34] Zinc-air Storage | NantEnergy, 2019, https://nantenergy.com/zinc-air/.
[35] Products & Technology, 2019, https://eosenergystorage.com/products-technology/.
[36] Zinc8 Energy Solutions: The Leader in Zinc Air Battery Technology, 2019, https://zinc8energy.com/.
[37] P.A. Khan, B. Venkatesh, Economic Analysis of Chemical Energy Storage Technologies, in: A. Leon-Garcia, R. Lenort, D. Holman, D. Staš, V. Krutilova, P. Wicher, D. Cagáňová, D. Špirková, J. Golej, K. Nguyen (Eds.), Smart City 360°, Springer International Publishing, Cham, 2016: pp. 277–291. https://doi.org/10.1007/978-3-319-33681-7_23.
[38] Beyond Lithium – LESC, 2020, http://smeng.ucsd.edu/supercapacitors/.
[39] M. Uchida, Y.-C. Park, K. Kakinuma, H. Yano, D.A. Tryk, T. Kamino, H. Uchida, M. Watanabe, Effect of the state of distribution of supported Pt nanoparticles on effective Pt utilization in polymer electrolyte fuel cells, Phys. Chem. Chem. Phys. 15 (2013) 11236. https://doi.org/10.1039/c3cp51801a.
[40] Noam Eliaz, Eliezer Gileadi, Physical Electrochemistry: Fundamentals, Techniques, and Applications, 1st Edition, Wiley-VCH, 2013.
[41] A.K.N. Reddy, J.O. Bockris, M.E. Gamboa-Aldeco, Modern electrochemistry, Plenum Press, New York, 1998.
[42] Julius Tafel, Über die Polarisation bei kathodischer Wasserstoffentwicklung, Zeitschrift f. physik. Chemie. (1905) 641–712.
[43] S. Srinivasan, Fuel cells: from fundamentals to applications, Springer, New York, 2006.
[44] Bard Allen J., Faulkner Larry R., Electrochemical Methods, Fundamental and Applications, J. Wiley and Sons, New York, 2000.
[45] J. Pan, Y.Y. Xu, H. Yang, Z. Dong, H. Liu, B.Y. Xia, Advanced architectures and relatives of air electrodes in Zn-air batteries, Adv. Sci. 5 (2018) 1700691. https://doi.org/10.1002/advs.201700691.
[46] J. Xiao, D. Wang, W. Xu, D. Wang, R.E. Williford, J. Liu, J.-G. Zhang, Optimization of Air Electrode for Li/Air Batteries, J. Electrochem. Soc. 157 (2010) A487. https://doi.org/10.1149/1.3314375.
[47] L. Jörissen, Bifunctional oxygen/air electrodes, J. Power Sources. 155 (2006) 23–32. https://doi.org/10.1016/j.jpowsour.2005.07.038.
[48] Y. Li, M. Gong, Y. Liang, J. Feng, J.-E. Kim, H. Wang, G. Hong, B. Zhang, H. Dai, Advanced zinc-air batteries based on high-performance hybrid electrocatalysts, Nat. Commun. 4 (2013). https://doi.org/10.1038/ncomms2812.
[49] Y. Li, H. Dai, Recent advances in zinc–air batteries, Chem Soc Rev. 43 (2014) 5257–5275. https://doi.org/10.1039/C4CS00015C.
[50] Lars Carlsson, Lars Öjefors, Bifunctional air electrode for metal-air batteries, J. Electrochem. Soc. 127 (1980) 525–528.
[51] M. Watanabe, M. Tomikawa, S. Motoo, Preparation of a High Performance Gas DIfffusion Electrode, J. Electroanal. Chem. 182 (1985) 193–196.
[52] M. Watanabe, M. Tomikawa, S. Motoo, Experimental Analysis of the Reaction Layer Structure in a Gas DIffusion Electrode, J. Electroanal. Chem. 195 (1985) 81–93.
[53] S. Motoo, M. Watanabe, N. Furuya, Gas Diffusion Electrode of High Performance, J. Electroanal. Chem. 160 (1984) 351–357.

[54] T. Kenjo, K. Kawatsu, Current-limiting factors and the location of the reaction area in PTFE-bonded double-layered oxygen electrodes, Electrochimica Acta. 30 (1985) 229–233.
[55] M. Maja, C. Orecchia, M. Strano, P. Tosco, M. Vanni, Effect of structure of the electrical performance of gas diffusion electrodes for metal air batteries, Electrochimica Acta. 46 (2000) 423–432.
[56] K. Kordesch, S. Jahangir, M. Schautz, Engineering concepts and technical performance of oxygen-reducing electrodes for batteries and electrochemical processes, Electrochimica Acta. 29 (1984) 1589–1596.
[57] S. Müller, K. Striebel, O. Haas, $La_{0.6}Ca_{0.4}CoO_3$: a stable and powerful catalyst for bifunctional air electrodes, Electrochimica Acta. 39 (1994) 1661–1668.
[58] M.S. Wilson, S. Gottesfeld, Thin-film catalyst layers for polymer electrolyte fuel cell electrodes, J. Appl. Electrochem. 22 (1992) 1–7.
[59] M.G. Park, D.U. Lee, M.H. Seo, Z.P. Cano, Z. Chen, 3D ordered mesoporous bifunctional oxygen catalyst for electrically rechargeable zinc-air batteries, Small. 12 (2016) 2707–2714. https://doi.org/10.1002/smll.201600051.
[60] I.-S. Park, W. Li, A. Manthiram, Fabrication of catalyst-coated membrane-electrode assemblies by doctor blade method and their performance in fuel cells, J. Power Sources. 195 (2010) 7078–7082. https://doi.org/10.1016/j.jpowsour.2010.05.004.
[61] Z. Wang, Y. Nagao, Effects of Nafion impregnation using inkjet printing for membrane electrode assemblies in polymer electrolyte membrane fuel cells, Electrochimica Acta. 129 (2014) 343–347. https://doi.org/10.1016/j.electacta.2014.02.133.
[62] W. Wang, S. Chen, J. Li, W. Wang, Fabrication of catalyst coated membrane with screen printing method in a proton exchange membrane fuel cell, Int. J. Hydrog. Energy. 40 (2015) 4649–4658. https://doi.org/10.1016/j.ijhydene.2015.02.027.
[63] L. Sun, R. Ran, G. Wang, Z. Shao, Fabrication and performance test of a catalyst-coated membrane from direct spray deposition, Solid State Ion. 179 (2008) 960–965. https://doi.org/10.1016/j.ssi.2008.01.081.
[64] C. Meng, T. Ling, T.-Y. Ma, H. Wang, Z. Hu, Y. Zhou, J. Mao, X.-W. Du, M. Jaroniec, S.-Z. Qiao, Atomically and electronically coupled Pt and CoO hybrid nanocatalysts for enhanced electrocatalytic performance, Adv. Mater. 29 (2017) 1604607. https://doi.org/10.1002/adma.201604607.
[65] Z. Song, X. Han, Y. Deng, N. Zhao, W. Hu, C. Zhong, Clarifying the controversial catalytic performance of $Co(OH)_2$ and Co_3O_4 for oxygen reduction/evolution reactions toward efficient Zn–air batteries, ACS Appl. Mater. Interfaces. 9 (2017) 22694–22703. https://doi.org/10.1021/acsami.7b05395.
[66] E. Davari, A.D. Johnson, A. Mittal, M. Xiong, D.G. Ivey, Manganese-cobalt mixed oxide film as a bifunctional catalyst for rechargeable zinc-air batteries, Electrochimica Acta. 211 (2016) 735–743. https://doi.org/10.1016/j.electacta.2016.06.085.
[67] J. Fu, F.M. Hassan, J. Li, D.U. Lee, A.R. Ghannoum, G. Lui, Md.A. Hoque, Z. Chen, Flexible rechargeable zinc-air batteries through morphological emulation of human hair array, Adv. Mater. 28 (2016) 6421–6428. https://doi.org/10.1002/adma.201600762.
[68] Q. Liu, Y. Wang, L. Dai, J. Yao, Scalable Fabrication of Nanoporous Carbon Fiber Films as Bifunctional Catalytic Electrodes for Flexible Zn-Air Batteries, Adv. Mater. 28 (2016) 3000–3006. https://doi.org/10.1002/adma.201506112.

[69] D.U. Lee, J.-Y. Choi, K. Feng, H.W. Park, Z. Chen, Advanced extremely durable 3D bifunctional air electrodes for rechargeable zinc-air batteries, Adv. Energy Mater. 4 (2014) 1301389. https://doi.org/10.1002/aenm.201301389.

[70] J.F. Parker, J.S. Ko, D.R. Rolison, J.W. Long, Translating materials-level performance into device-relevant metrics for zinc-based batteries, Joule. 2 (2018) 2519–2527. https://doi.org/10.1016/j.joule.2018.11.007.

[71] Z. Wang, S. Xiao, Y. An, X. Long, X. Zheng, X. Lu, Y. Tong, S. Yang, $Co(II)_{1-x}Co(0)_{x/3}Mn(III)_{2x/3}S$ nanoparticles supported on B/N-codoped mesoporous nanocarbon as a bifunctional electrocatalyst of oxygen reduction/evolution for high-performance zinc-air batteries, ACS Appl. Mater. Interfaces. 8 (2016) 13348–13359. https://doi.org/10.1021/acsami.5b12803.

[72] C. Guo, Y. Zheng, J. Ran, F. Xie, M. Jaroniec, S.-Z. Qiao, Engineering high-energy interfacial structures for high-performance oxygen-involving electrocatalysis, Angew. Chem. Int. Ed. 56 (2017) 8539–8543. https://doi.org/10.1002/anie.201701531.

[73] N. Bogolowski, O. Ngaleu, M. Sakthivel, J.-F. Drillet, Long-life bifunctional $BaSrCoFeO_3$/C gas diffusion electrode, Carbon. 119 (2017) 511–518. https://doi.org/10.1016/j.carbon.2017.04.051.

[74] Kim Kinoshita, Electrochemical Oxygen Technology, John Wiley & Sons, 1992.

[75] P. Gu, M. Zheng, Q. Zhao, X. Xiao, H. Xue, H. Pang, Rechargeable zinc–air batteries: a promising way to green energy, J Mater Chem A. 5 (2017) 7651–7666. https://doi.org/10.1039/C7TA01693J.

[76] K. L. Hsueh, D. T. Chin, S. Srinivasan, ELECTRODE KINETICS OF OXYGEN REDUCTION A THEORETICAL AND EXPERIMENTAL ANALYSIS OF THE ROTATING RING-DISC ELECTRODE METHOD, J Electroanal Chem. 153 (1983) 79–95.

[77] D.S. Gnanamuthu, J.V. Petrocelli, A Generalized Expression for the Tafel Slope and the Kinetics of Oxygen Reduction on Noble Metals and Alloys, J. Electrochem. Soc. 114 (1967) 1036. https://doi.org/10.1149/1.2424180.

[78] A. Damjanovic, A. Dey, J.O. Bockris, Kinetics of oxygen evolution and dissolution on platinum electrodes, Electrochimica Acta. 11 (1966) 791–814. https://doi.org/10.1016/0013-4686(66)87056-1.

[79] A. Damjanovic, M.A. Genshaw, J.O. Bockris, Distinction between Intermediates Produced in Main and Side Electrodic Reactions, J. Chem. Phys. 45 (1966) 4057–4059. https://doi.org/10.1063/1.1727457.

[80] H.S. Wroblowa, Yen-Chi-Pan, G. Razumney, Electroreduction of oxygen, J. Electroanal. Chem. Interfacial Electrochem. 69 (1976) 195–201. https://doi.org/10.1016/S0022-0728(76)80250-1.

[81] A. J. Appleby, M. Savy, KINETICS OF OXYGEN REDUCTION REACTIONS INVOLVING CATALYTIC DECOMPOSITION OF HYDROGEN PEROXIDE, J Electroanal Chem. 92 (1978) 15–30.

[82] R.W. Zurilla, R.K. Sen, E. Yeager, The Kinetics of the Oxygen Reduction Reaction on Gold in Alkaline Solution, J Electrochem Soc. (1978) 7.

[83] V. S. Bagotskii, M. R. Tarasevich, VY Filinovskii, Calculation of the kinetic parameters of conjugated reactions of oxygen and hydrogen peroxide, Elektrokhimiya. 5 (1969).

[84] N. A. Anastasijevic', S. Strbac, R.R. Adzic', J Electroanal Chem. 40 (1978).

[85] J.K. Nørskov, J. Rossmeisl, A. Logadottir, L. Lindqvist, J.R. Kitchin, T. Bligaard, H. Jónsson, Origin of the Overpotential for Oxygen Reduction at a Fuel-Cell Cathode, J. Phys. Chem. B. 108 (2004) 17886–17892. https://doi.org/10.1021/jp047349j.

[86] A. Kulkarni, S. Siahrostami, A. Patel, J.K. Nørskov, Understanding Catalytic Activity Trends in the Oxygen Reduction Reaction, Chem. Rev. 118 (2018) 2302–2312. https://doi.org/10.1021/acs.chemrev.7b00488.

[87] V. Tripković, E. Skúlason, S. Siahrostami, J.K. Nørskov, J. Rossmeisl, The oxygen reduction reaction mechanism on Pt(111) from density functional theory calculations, Electrochimica Acta. 55 (2010) 7975–7981. https://doi.org/10.1016/j.electacta.2010.02.056.

[88] G.S. Karlberg, J. Rossmeisl, J.K. Nørskov, Estimations of electric field effects on the oxygen reduction reaction based on the density functional theory, Phys. Chem. Chem. Phys. 9 (2007) 5158. https://doi.org/10.1039/b705938h.

[89] N.M. MarkovicÂ, P.N.R. Jr, Surface science studies of model fuel cell electrocatalysts, Surf. Sci. Rep. (2002) 113.

[90] N.M. Marković, R.R. Adžić, B.D. Cahan, E.B. Yeager, Structural effects in electrocatalysis: oxygen reduction on platinum low index single-crystal surfaces in perchloric acid solutions, J. Electroanal. Chem. 377 (1994) 249–259. https://doi.org/10.1016/0022-0728(94)03467-2.

[91] R.R. Adzic, N.M. Markovi, V.B. Vesovic, STRUCTURAL EFFECTS IN ELECTROCATALYSIS OXYGEN REDUCTION ON THE Au (100) SINGLE CRYSTAL ELECTRODE, (n.d.) 16.

[92] J. Greeley, I.E.L. Stephens, A.S. Bondarenko, T.P. Johansson, H.A. Hansen, T.F. Jaramillo, J. Rossmeisl, I. Chorkendorff, J.K. Nørskov, Alloys of platinum and early transition metals as oxygen reduction electrocatalysts, Nat. Chem. 1 (2009) 552–556. https://doi.org/10.1038/nchem.367.

[93] H.-Y. Su, Y. Gorlin, I.C. Man, F. Calle-Vallejo, J.K. Nørskov, T.F. Jaramillo, J. Rossmeisl, Identifying active surface phases for metal oxide electrocatalysts: a study of manganese oxide bi-functional catalysts for oxygen reduction and water oxidation catalysis, Phys. Chem. Chem. Phys. 14 (2012) 14010. https://doi.org/10.1039/c2cp40841d.

[94] D.F. Abbott, S. Mukerjee, V. Petrykin, Z. Bastl, N.B. Halck, J. Rossmeisl, P. Krtil, Oxygen reduction on nanocrystalline ruthenia – local structure effects, RSC Adv. 5 (2015) 1235–1243. https://doi.org/10.1039/C4RA10001H.

[95] M. Lehtimäki, H. Hoffmannová, O. Boytsova, Z. Bastl, M. Busch, N.B. Halck, J. Rossmeisl, P. Krtil, Targeted design of α-MnO2 based catalysts for oxygen reduction, Electrochimica Acta. 191 (2016) 452–461. https://doi.org/10.1016/j.electacta.2016.01.070.

[96] J. Suntivich, H.A. Gasteiger, N. Yabuuchi, H. Nakanishi, J.B. Goodenough, Y. Shao-Horn, Design principles for oxygen-reduction activity on perovskite oxide catalysts for fuel cells and metal–air batteries, Nat. Chem. 3 (2011) 546–550. https://doi.org/10.1038/nchem.1069.

[97] G.A. Tritsaris, J.K. Nørskov, J. Rossmeisl, Trends in oxygen reduction and methanol activation on transition metal chalcogenides, Electrochimica Acta. 56 (2011) 9783–9788. https://doi.org/10.1016/j.electacta.2011.08.045.

[98] A. Seifitokaldani, O. Savadogo, M. Perrier, Density Functional Theory (DFT) Computation of the Oxygen Reduction Reaction (ORR) on Titanium Nitride (TiN) Surface, Electrochimica Acta. 141 (2014) 25–32. https://doi.org/10.1016/j.electacta.2014.07.027.

[99] J.W.F. To, J.W.D. Ng, S. Siahrostami, A.L. Koh, Y. Lee, Z. Chen, K.D. Fong, S. Chen, J. He, W.-G. Bae, J. Wilcox, H.Y. Jeong, K. Kim, F. Studt, J.K. Nørskov, T.F. Jaramillo, High-performance oxygen reduction and evolution carbon catalysis: From mechanistic studies to device integration, Nano Res. (2017) 15.

[100] Yasumichi Matsumoto, Eiichi Sato, Electrocatalytic properties of transition metal oxides for oxygen evolution reaction, 14 (1986) 397–426. https://doi.org/10.1016/0254-0584(86)90045-3.

[101] J.O. Bockris, Kinetics of Activation Controlled Consecutive Electrochemical Reactions: Anodic Evolution of Oxygen, J. Chem. Phys. 24 (1956) 817–827. https://doi.org/10.1063/1.1742616.

[102] M. Bursell, M. Pirjamali, Y. Kiros, La 0.6 Ca 0.4 CoO 3, La 0.1 Ca 0.9 MnO 3 and LaNiO 3 as bifunctional oxygen electrodes, Electrochimica Acta. 47 (2002) 1651–1660.

[103] X. Lu, C. Zhao, Highly efficient and robust oxygen evolution catalysts achieved by anchoring nanocrystalline cobalt oxides onto mildly oxidized multiwalled carbon nanotubes, J. Mater. Chem. A. 1 (2013) 12053. https://doi.org/10.1039/c3ta12912h.

[104] J. Rosen, G.S. Hutchings, F. Jiao, Ordered Mesoporous Cobalt Oxide as Highly Efficient Oxygen Evolution Catalyst, J. Am. Chem. Soc. 135 (2013) 4516–4521. https://doi.org/10.1021/ja400555q.

[105] H. Jin, J. Wang, D. Su, Z. Wei, Z. Pang, Y. Wang, In situ Cobalt–Cobalt Oxide/N-Doped Carbon Hybrids As Superior Bifunctional Electrocatalysts for Hydrogen and Oxygen Evolution, J. Am. Chem. Soc. 137 (2015) 2688–2694. https://doi.org/10.1021/ja5127165.

[106] C. Zhu, D. Wen, S. Leubner, M. Oschatz, W. Liu, M. Holzschuh, F. Simon, S. Kaskel, A. Eychmüller, Nickel cobalt oxide hollow nanosponges as advanced electrocatalysts for the oxygen evolution reaction, Chem. Commun. 51 (2015) 7851–7854. https://doi.org/10.1039/C5CC01558H.

[107] V. Neburchilov, H. Wang, J.J. Martin, W. Qu, A review on air cathodes for zinc–air fuel cells, J. Power Sources. 195 (2010) 1271–1291. https://doi.org/10.1016/j.jpowsour.2009.08.100.

[108] X. Cai, L. Lai, J. Lin, Z. Shen, Recent advances in air electrode for Zn-air Batteries: electrocatalysis and structural design, Mater. Horiz. 4 (2017) 945–976.

[109] D. Chen, C. Chen, Z.M. Baiyee, Z. Shao, F. Ciucci, Nonstoichiometric oxides as low-cost and highly-efficient oxygen reduction/evolution catalysts for low-temperature electrochemical devices, Chem. Rev. 115 (2015) 9869–9921. https://doi.org/10.1021/acs.chemrev.5b00073.

[110] M. Busch, N.B. Halck, U.I. Kramm, S. Siahrostami, P. Krtil, J. Rossmeisl, Beyond the top of the volcano? – A unified approach to electrocatalytic oxygen reduction and oxygen evolution, Nano Energy. 29 (2016) 126–135. https://doi.org/10.1016/j.nanoen.2016.04.011.

[111] M.T.M. Koper, Thermodynamic theory of multi-electron transfer reactions: Implications for electrocatalysis, J. Electroanal. Chem. (2011) 7.

[112] I.C. Man, H.-Y. Su, F. Calle-Vallejo, H.A. Hansen, J.I. Martínez, N.G. Inoglu, J. Kitchin, T.F. Jaramillo, J.K. Nørskov, J. Rossmeisl, Universality in Oxygen Evolution Electrocatalysis on Oxide Surfaces, ChemCatChem. 3 (2011) 1159–1165. https://doi.org/10.1002/cctc.201000397.

[113] Y. Li, J. Lu, Metal–air batteries: will they be the future electrochemical energy storage device of choice?, ACS Energy Lett. 2 (2017) 1370–1377. https://doi.org/10.1021/acsenergylett.7b00119.
[114] W. Xiao, D. Wang, X.W. Lou, Shape-controlled synthesis of MnO2 nanostructures with enhanced electrocatalytic activity for oxygen reduction, J. Phys. Chem. C. 114 (2009) 1694–1700.
[115] C. Wei, L. Yu, C. Cui, J. Lin, C. Wei, N. Mathews, F. Huo, T. Sritharan, Z. Xu, Ultrathin MnO2 nanoflakes as efficient catalysts for oxygen reduction reaction, Chem. Commun. 50 (2014) 7885. https://doi.org/10.1039/c4cc02781g.
[116] J. Vondrák, B. Klapste, J. Velická, M. Sedlarikova, J. Reiter, I. Roche, E. Chainet, J.F. Fauvarque, M. Chatenet, Electrochemical activity of manganese oxide/carbon-based electrocatalysts, J. New Mater. Electrochem. Syst. 8 (2005) 209.
[117] J.A. Vigil, T.N. Lambert, J. Duay, C.J. Delker, T.E. Beechem, B.S. Swartzentruber, Nanoscale carbon modified α-MnO_2 nanowires: highly active and stable oxygen reduction electrocatalysts with low carbon content, ACS Appl. Mater. Interfaces. 10 (2018) 2040–2050. https://doi.org/10.1021/acsami.7b16576.
[118] R.B. Valim, M.C. Santos, M.R.V. Lanza, S.A.S. Machado, F.H.B. Lima, M.L. Calegaro, Oxygen reduction reaction catalyzed by ε-MnO2: Influence of the crystalline structure on the reaction mechanism, Electrochimica Acta. 85 (2012) 423–431. https://doi.org/10.1016/j.electacta.2012.08.075.
[119] A. Sumboja, X. Ge, F.W.T. Goh, B. Li, D. Geng, T.S.A. Hor, Y. Zong, Z. Liu, Manganese Oxide Catalyst Grown on Carbon Paper as an Air Cathode for High-Performance Rechargeable Zinc–Air Batteries, ChemPlusChem. 80 (2015) 1341–1346. https://doi.org/10.1002/cplu.201500183.
[120] K.A. Stoerzinger, M. Risch, B. Han, Y. Shao-Horn, Recent insights into manganese oxides in catalyzing oxygen reduction kinetics, ACS Catal. 5 (2015) 6021–6031. https://doi.org/10.1021/acscatal.5b01444.
[121] A.S. Ryabova, A. Bonnefont, P.A. Simonov, T. Dintzer, C. Ulhaq-Bouillet, Y.G. Bogdanova, G.A. Tsirlina, E.R. Savinova, Further insights into the role of carbon in manganese oxide/carbon composites in the oxygen reduction reaction in alkaline media, Electrochimica Acta. 246 (2017) 643–653. https://doi.org/10.1016/j.electacta.2017.06.017.
[122] I. Roche, E. Chaînet, M. Chatenet, J. Vondrák, Carbon-supported manganese oxide nanoparticles as electrocatalysts for the oxygen reduction reaction (ORR) in alkaline medium: physical characterizations and ORR mechanism, J. Phys. Chem. C. 111 (2007) 1434–1443. https://doi.org/10.1021/jp0647986.
[123] Y. Meng, W. Song, H. Huang, Z. Ren, S.-Y. Chen, S.L. Suib, Structure–property relationship of bifunctional MnO_2 nanostructures: highly efficient, ultra-stable electrochemical water oxidation and oxygen reduction reaction catalysts identified in alkaline media, J. Am. Chem. Soc. 136 (2014) 11452–11464. https://doi.org/10.1021/ja505186m.
[124] A.R. Mainar, L.C. Colmenares, O. Leonet, F. Alcaide, J.J. Iruin, S. Weinberger, V. Hacker, E. Iruin, I. Urdanpilleta, J.A. Blazquez, Manganese oxide catalysts for secondary zinc air batteries: from electrocatalytic activity to bifunctional air electrode performance, Electrochimica Acta. 217 (2016) 80–91. https://doi.org/10.1016/j.electacta.2016.09.052.

[125] T.N. Lambert, J.A. Vigil, S.E. White, C.J. Delker, D.J. Davis, M. Kelly, M.T. Brumbach, M.A. Rodriguez, B.S. Swartzentruber, Understanding the effects of cationic dopants on α-MnO_2 oxygen reduction reaction electrocatalysis, J. Phys. Chem. C. 121 (2017) 2789–2797. https://doi.org/10.1021/acs.jpcc.6b11252.
[126] K.-N. Jung, A. Riaz, S.-B. Lee, T.-H. Lim, S.-J. Park, R.-H. Song, S. Yoon, K.-H. Shin, J.-W. Lee, Urchin-like α-MnO2 decorated with Au and Pd as a bi-functional catalyst for rechargeable lithium–oxygen batteries, J. Power Sources. 244 (2013) 328–335. https://doi.org/10.1016/j.jpowsour.2013.01.028.
[127] Z. Huang, M. Zhang, J. Cheng, Y. Gong, B. Chi, J. Pu, L. Jian, Silver decorated alpha-manganese oxide nanostructured electrocatalyst for rechargeable lithium–oxygen battery, Catal. Commun. 61 (2015) 44–47. https://doi.org/10.1016/j.catcom.2014.12.009.
[128] Y. Gorlin, C.-J. Chung, D. Nordlund, B.M. Clemens, T.F. Jaramillo, Mn_3O_4 supported on glassy carbon: an active non-precious metal catalyst for the oxygen reduction reaction, ACS Catal. 2 (2012) 2687–2694. https://doi.org/10.1021/cs3004352.
[129] F. Cheng, Y. Su, J. Liang, Z. Tao, J. Chen, MnO_2-based nanostructures as catalysts for electrochemical oxygen reduction in alkaline media, Chem. Mater. 22 (2010) 898–905. https://doi.org/10.1021/cm901698s.
[130] P.H. Benhangi, A. Alfantazi, E. Gyenge, Manganese dioxide-based bifunctional oxygen reduction/evolution electrocatalysts: effect of perovskite doping and potassium ion insertion, Electrochimica Acta. 123 (2014) 42–50. https://doi.org/10.1016/j.electacta.2013.12.102.
[131] E. Fabbri, A. Habereder, K. Waltar, R. Kötz, T.J. Schmidt, Developments and perspectives of oxide-based catalysts for the oxygen evolution reaction, Catal Sci Technol. 4 (2014) 3800–3821. https://doi.org/10.1039/C4CY00669K.
[132] M. Gao, W. Sheng, Z. Zhuang, Q. Fang, S. Gu, J. Jiang, Y. Yan, Efficient water oxidation using nanostructured α-nickel-hydroxide as an electrocatalyst, J. Am. Chem. Soc. 136 (2014) 7077–7084. https://doi.org/10.1021/ja502128j.
[133] I.J. Godwin, M.E.G. Lyons, Enhanced oxygen evolution at hydrous nickel oxide electrodes via electrochemical ageing in alkaline solution, Electrochem. Commun. 32 (2013) 39–42. https://doi.org/10.1016/j.elecom.2013.03.040.
[134] X. Li, F.C. Walsh, D. Pletcher, Nickel based electrocatalysts for oxygen evolution in high current density, alkaline water electrolysers, Phys Chem Chem Phys. 13 (2011) 1162–1167. https://doi.org/10.1039/C0CP00993H.
[135] M.W. Louie, A.T. Bell, An Investigation of Thin-Film Ni–Fe Oxide Catalysts for the Electrochemical Evolution of Oxygen, J. Am. Chem. Soc. 135 (2013) 12329–12337. https://doi.org/10.1021/ja405351s.
[136] M.E.G. Lyons, M.P. Brandon, A comparative study of the oxygen evolution reaction on oxidised nickel, cobalt and iron electrodes in base, J. Electroanal. Chem. 641 (2010) 119–130. https://doi.org/10.1016/j.jelechem.2009.11.024.
[137] E.L. Miller, R.E. Rocheleau, Electrochemical and electrochromic behavior of reactively sputtered nickel oxide, J. Electrochem. Soc. 144 (1997) 1995–2003.
[138] O. Diaz-Morales, D. Ferrus-Suspedra, M.T.M. Koper, The importance of nickel oxyhydroxide deprotonation on its activity towards electrochemical water oxidation, Chem. Sci. 7 (2016) 2639–2645. https://doi.org/10.1039/C5SC04486C.

[139] L. Trotochaud, J.K. Ranney, K.N. Williams, S.W. Boettcher, Solution-Cast Metal Oxide Thin Film Electrocatalysts for Oxygen Evolution, J. Am. Chem. Soc. 134 (2012) 17253–17261. https://doi.org/10.1021/ja307507a.
[140] V. Vij, S. Sultan, A.M. Harzandi, A. Meena, J.N. Tiwari, W.-G. Lee, T. Yoon, K.S. Kim, Nickel-based electrocatalysts for energy-related applications: oxygen reduction, oxygen evolution, and hydrogen evolution reactions, ACS Catal. 7 (2017) 7196–7225. https://doi.org/10.1021/acscatal.7b01800.
[141] A. Pendashteh, J. Palma, M. Anderson, R. Marcilla, $NiCoMnO_4$ nanoparticles on N-doped graphene: highly efficient bifunctional electrocatalyst for oxygen reduction/evolution reactions, Appl. Catal. B Environ. 201 (2017) 241–252. https://doi.org/10.1016/j.apcatb.2016.08.044.
[142] S. Gul, J.W.D. Ng, R. Alonso-Mori, J. Kern, D. Sokaras, E. Anzenberg, B. Lassalle-Kaiser, Y. Gorlin, T.-C. Weng, P.H. Zwart, J.Z. Zhang, U. Bergmann, V.K. Yachandra, T.F. Jaramillo, J. Yano, Simultaneous detection of electronic structure changes from two elements of a bifunctional catalyst using wavelength-dispersive X-ray emission spectroscopy and in situ electrochemistry, Phys. Chem. Chem. Phys. 17 (2015) 8901–8912. https://doi.org/10.1039/C5CP01023C.
[143] S. Dąbrowska, T. Chudoba, J. Wojnarowicz, W. Łojkowski, Current Trends in the Development of Microwave Reactors for the Synthesis of Nanomaterials in Laboratories and Industries: A Review, Crystals. 8 (2018) 379. https://doi.org/10.3390/cryst8100379.
[144] I. Bilecka, I. Djerdj, M. Niederberger, One-minute synthesis of crystalline binary and ternary metal oxide nanoparticles, Chem Commun. (2008) 886–888. https://doi.org/10.1039/B717334B.
[145] M.S. Mohajerani, M. Mazloumi, A. Lak, A. Kajbafvala, S. Zanganeh, S.K. Sadrnezhaad, Self-assembled zinc oxide nanostructures via a rapid microwave-assisted route, J. Cryst. Growth. 310 (2008) 3621–3625. https://doi.org/10.1016/j.jcrysgro.2008.04.045.
[146] N.E. Leadbeater, C.B. McGowan, Laboratory experiments using microwave heating, CRC Press, Taylor & Francis Group, Boca Raton, 2013.
[147] H.J. Kitchen, S.R. Vallance, J.L. Kennedy, N. Tapia-Ruiz, L. Carassiti, A. Harrison, A.G. Whittaker, T.D. Drysdale, S.W. Kingman, D.H. Gregory, Modern Microwave Methods in Solid-State Inorganic Materials Chemistry: From Fundamentals to Manufacturing, Chem. Rev. 114 (2014) 1170–1206. https://doi.org/10.1021/cr4002353.
[148] H. Huang, S. Sithambaram, C.-H. Chen, C. King'ondu Kithongo, L. Xu, A. Iyer, H.F. Garces, S.L. Suib, Microwave-Assisted Hydrothermal Synthesis of Cryptomelane-Type Octahedral Molecular Sieves (OMS-2) and Their Catalytic Studies, Chem. Mater. 22 (2010) 3664–3669. https://doi.org/10.1021/cm100220g.
[149] L.R. Pahalagedara, S. Dharmarathna, C.K. King'ondu, M.N. Pahalagedara, Y.-T. Meng, C.-H. Kuo, S.L. Suib, Microwave-assisted hydrothermal synthesis of α-MnO_2: lattice expansion via rapid temperature ramping and framework substitution, J. Phys. Chem. C. 118 (2014) 20363–20373. https://doi.org/10.1021/jp505306q.
[150] C. Hammond, The basics of crystallography and diffraction, 3rd ed, Oxford University Press, Oxford ; New York, 2009.
[151] J.P. Glusker, K.N. Trueblood, Crystal structure analysis: a primer, 3rd ed, Oxford University Press, Oxford ; New York, 2010.

[152] X. Hou, R.S. Amais, B.T. Jones, G.L. Donati, Inductively coupled plasma optical emission spectrometry, Encycl. Anal. Chem. Appl. Theory Instrum. (2006) 1–25.
[153] Stephen Brunauer, P. H. Emmett, Edward Teller, Adsorption of Gases in Multimolecular Layers, J. Am. Chem. Soc. 60 (1938) 309–319.
[154] Langmuir I., The constitution and fundamental properties of solids and liquids. Part I, Solids. J. Am. Chem. Soc. 38 (1916) 2221–2295.
[155] Langmuir I., The adsorption of gases on plane surfaces of glass, mica and platinum, J. Am. Chem. Soc. 40 (1918) 1361–1403.
[156] D. Dollimore, P. Spooner, A. Turner, The BET method of analysis of gas adsorption data and its relevance to the calculation of surface areas, Surf. Technol. 4 (1976) 121–160.
[157] F. Béguin, E. Frąckowiak, eds., Carbons for electrochemical energy storage and conversion systems, CRC Press, Boca Raton, 2010.
[158] S. Oswald, X-Ray Photoelectron Spectroscopy in Analysis of Surfaces, in: R.A. Meyers (Ed.), Encycl. Anal. Chem., John Wiley & Sons, Ltd, Chichester, UK, 2013. https://doi.org/10.1002/9780470027318.a2517.pub2.
[159] Attenuation Coefficient, 2019, https://www.nde-ed.org/EducationResources/CommunityCollege/Radiography/Physics/attenuationCoef.htm.
[160] J.J. Rehr, R.C. Albers, Theoretical approaches to x-ray absorption fine structure, Rev. Mod. Phys. 72 (2000) 621.
[161] ATHENA: XAS Data Processing — Athena 0.9.26 documentation, 2020, https://bruceravel.github.io/demeter/documents/Athena/index.html.
[162] A.E. Russell, A. Rose, X-ray Absorption Spectroscopy of Low Temperature Fuel Cell Catalysts, Chem. Rev. 104 (2004) 4613–4636. https://doi.org/10.1021/cr020708r.
[163] K. Momma, F. Izumi, *VESTA* : a three-dimensional visualization system for electronic and structural analysis, J. Appl. Crystallogr. 41 (2008) 653–658. https://doi.org/10.1107/S0021889808012016.
[164] Artemis: EXAFS Data Analysis using Feff with Larch or Ifeffit — Artemis 0.9.26 documentation, 2020, https://bruceravel.github.io/demeter/documents/Artemis/index.html.
[165] A.D. Cicco, G. Aquilanti, M. Minicucci, E. Principi, N. Novello, A. Cognigni, L. Olivi, Novel XAFS capabilities at ELETTRA synchrotron light source, J. Phys. Conf. Ser. 190 (2009) 012043. https://doi.org/10.1088/1742-6596/190/1/012043.
[166] The FEFF Project - FEFF, 2020, http://monalisa.phys.washington.edu/feffproject-feff-xafsdataanalysis.html.
[167] Jean Vicat, Eric Fanchon, Pierre Strobel, Duc Tran Qui, The Structure of Ki.33Mn8O16 and Cation Ordering in Hollandite-Type Structures, Acta Cryst. B42 (1986) 162–167.
[168] Springer handbook of electrochemical energy, 1st edition, Springer Berlin Heidelberg, New York, NY, 2016.
[169] Carl H. Hamann, Andrew Hamnett, Wolf Vielstich, Electrochemistry, 2nd, Completely Revised and Updated Edition, John Wiley & Sons, Inc, 2007.
[170] R. Zhou, Y. Zheng, M. Jaroniec, S.-Z. Qiao, Determination of the Electron Transfer Number for the Oxygen Reduction Reaction: From Theory to Experiment, ACS Catal. 6 (2016) 4720–4728. https://doi.org/10.1021/acscatal.6b01581.

[171] A. Frumkin, L. Nekrasov, B. Levich, Ju. Ivanov, Die anwendung der rotierenden scheibenelektrode mit einem ringe zur untersuchung von zwischenprodukten elektrochemischer reaktionen, J. Electroanal. Chem. 1 (1959) 84–90.
[172] Brief introduction for the principles of hydrodynamic voltammetry , the basic instruments configuration for RDE/RRDE measurements, 2020,https://www.als-japan.com/1559.html.
[173] U.A. Paulus, T.J. Schmidt, H.A. Gasteiger, R.J. Behm, Oxygen reduction on a high-surface area Pt/Vulcan carbon catalyst: a thin-film rotating ring-disk electrode study, J. Electroanal. Chem. (2001) 12.
[174] Y. Garsany, I.L. Singer, K.E. Swider-Lyons, Impact of film drying procedures on RDE characterization of Pt/VC electrocatalysts, J. Electroanal. Chem. 662 (2011) 396–406. https://doi.org/10.1016/j.jelechem.2011.09.016.
[175] Y. Gorlin, B. Lassalle-Kaiser, J.D. Benck, S. Gul, S.M. Webb, V.K. Yachandra, J. Yano, T.F. Jaramillo, In Situ X-ray Absorption Spectroscopy Investigation of a Bifunctional Manganese Oxide Catalyst with High Activity for Electrochemical Water Oxidation and Oxygen Reduction, J. Am. Chem. Soc. 135 (2013) 8525–8534. https://doi.org/10.1021/ja3104632.
[176] M. Risch, K.A. Stoerzinger, B. Han, T.Z. Regier, D. Peak, S.Y. Sayed, C. Wei, Z. Xu, Y. Shao-Horn, Redox Processes of Manganese Oxide in Catalyzing Oxygen Evolution and Reduction: An *in Situ* Soft X-ray Absorption Spectroscopy Study, J. Phys. Chem. C. 121 (2017) 17682–17692. https://doi.org/10.1021/acs.jpcc.7b05592.
[177] X. Wang, Y. Li, Selected-Control Hydrothermal Synthesis of α- and β-MnO_2 Single Crystal Nanowires, J. Am. Chem. Soc. 124 (2002) 2880–2881. https://doi.org/10.1021/ja0177105.
[178] Nanotechnology Introduction - new materials, 2020, https://www.nanowerk.com/nanotechnology/introduction/introduction_to_nanotechnology_2.php.
[179] Marian Steininger, Darstellung von α-MnO2 für Zink-Luft-Batterien und ökonomische Bewertun, Bachelor Thesis, Ulm University, 2018.
[180] Anders Byström, Crystal Structure of Hollandite, Nature. 164 (1949) 1128.
[181] S. Devaraj, N. Munichandraiah, Effect of Crystallographic Structure of MnO_2 on Its Electrochemical Capacitance Properties, J. Phys. Chem. C. 112 (2008) 4406–4417. https://doi.org/10.1021/jp7108785.
[182] S.L. Suib, Structure, porosity, and redox in porous manganese oxide octahedral layer and molecular sieve materials, J. Mater. Chem. 18 (2008) 1623. https://doi.org/10.1039/b714966m.
[183] E. Marini, L. Jörissen, S. Brimaud, Rational design of a low-cost, durable and efficient bifunctional oxygen electrode for rechargeable metal-air batteries, J. Power Sources. 482 (2021) 228900. https://doi.org/10.1016/j.jpowsour.2020.228900.
[184] E.L. Gyenge, J.-F. Drillet, The electrochemical behavior and catalytic activity for oxygen reduction of MnO_2/C–Toray gas diffusion electrodes, J. Electrochem. Soc. 159 (2011) F23–F34.
[185] Y. Chabre, J. Pannetier, Structural and electrochemical properties of the proton γ-MnO_2 system, Prog. Solid State Chem. 23 (1995) 1–130.
[186] H. Wang, Z. Lu, D. Qian, Y. Li, W. Zhang, Single-crystal α-MnO_2 nanorods: synthesis and electrochemical properties, Nanotechnology. 18 (2007) 115616. https://doi.org/10.1088/0957-4484/18/11/115616.

[187] S. Birgisson, D. Saha, B.B. Iversen, Formation Mechanisms of Nanocrystalline MnO_2 Polymorphs under Hydrothermal Conditions, Cryst. Growth Des. 18 (2018) 827–838. https://doi.org/10.1021/acs.cgd.7b01304.
[187] numpy.std — NumPy v1.19 Manual, 2020, https://numpy.org/doc/stable/reference/generated/numpy.std.html.
[189] P. Ruetschi, Discharge mechanism of MnO2 electrodes as influenced by the solubility of the reaction products, J. Electrochem. Soc. 123 (1976) 495–500.
[190] M. Toupin, T. Brousse, D. Bélanger, Charge Storage Mechanism of MnO_2 Electrode Used in Aqueous Electrochemical Capacitor, Chem. Mater. 16 (2004) 3184–3190. https://doi.org/10.1021/cm049649j.
[191] S.-C. Pang, M.A. Anderson, T.W. Chapman, Novel electrode materials for thin-film ultracapacitors: comparison of electrochemical properties of sol-gel-derived and electrodeposited manganese dioxide, J. Electrochem. Soc. 147 (2000) 444–450.
[192] N. Kumar, K. Guru Prasad, A. Sen, T. Maiyalagan, Enhanced pseudocapacitance from finely ordered pristine α-MnO2 nanorods at favourably high current density using redox additive, Appl. Surf. Sci. 449 (2018) 492–499. https://doi.org/10.1016/j.apsusc.2018.01.025.
[193] L. Mao, Mechanistic study of the reduction of oxygen in air electrode with manganese oxides as electrocatalysts, Electrochimica Acta. 48 (2003) 1015–1021. https://doi.org/10.1016/S0013-4686(02)00815-0.
[194] Ernest Yeager, Dioxygen electrocatalysis: mechanisms in relation to catalyst structure, J. Mol. Catal. 38 (1986) 5–25. https://doi.org/10.1016/0304-5102(86)87045-6.
[195] G. Chen, J. Sunarso, Y. Zhu, J. Yu, Y. Zhong, W. Zhou, Z. Shao, Highly active carbon/α-MnO_2 hybrid oxygen reduction reaction electrocatalysts, ChemElectroChem. 3 (2016) 1760–1767. https://doi.org/10.1002/celc.201600433.
[196] E. Farjami, L.J. Deiner, Kinetic study of the oxygen reduction reaction on α-Ni(OH_2 and α-$Ni(OH)_2$ supported on graphene oxide, J. Electrochem. Soc. 162 (2015) H571–H578.
[197] M. Wang, K. Chen, J. Liu, Q. He, G. Li, F. Li, Efficiently enhancing electrocatalytic activity of α-MnO_2 nanorods/N-doped Ketjenblack carbon for oxygen reduction reaction and oxygen evolution reaction using facile regulated hydrothermal treatment, Catalysts. 8 (2018) 138. https://doi.org/10.3390/catal8040138.
[198] S. Beckord, S. Brimaud, R. J. Behm, The performance of structurally well-defined Ag_xPt_{1-x}/Pt(111) surface alloys in the oxygen reduction reaction – An atomic-scale picture, J. Electroanal. Chem. 819 (2018) 401–409.
[199] S. Brimaud, A. K. Engstfeld, O. B. Alves, R. J. Behm, Structure–reactivity correlation in the oxygen reduction reaction: Activity of structurally well defined Au_xPt_{1-x}/Pt(111) monolayer surface alloys, J. Electroanal. Chem. 716 (2014).
[200] S. Brimaud, A. K. Engstfeld, O. B. Alves, H. E. Hoster, R. J. Behm, Oxygen reduction on structurally well defined, bimetallic PtRu surfaces: monolayer Pt_xRu_{1-x}/Ru(0001) surface alloys versus Pt film covered Ru(0001), Top. Catal. 57 (2014) 222–235.
[201] A.S. Ryabova, F.S. Napolskiy, T. Poux, S.Ya. Istomin, A. Bonnefont, D.M. Antipin, A.Ye. Baranchikov, E.E. Levin, A.M. Abakumov, G. Kéranguéven, E.V. Antipov, G.A. Tsirlina, E.R. Savinova, Rationalizing the influence of the Mn(IV)/Mn(III) red-ox transition on the electrocatalytic activity of manganese oxides in the oxygen reduction reaction, Electrochimica Acta. 187 (2016) 161–172. https://doi.org/10.1016/j.electacta.2015.11.012.

[202] R. Subbaraman, D. Tripkovic, K.-C. Chang, D. Strmcnik, A.P. Paulikas, P. Hirunsit, M. Chan, J. Greeley, V. Stamenkovic, N.M. Markovic, Trends in activity for the water electrolyser reactions on 3d M(Ni,Co,Fe,Mn) hydr(oxy)oxide catalysts, Nat. Mater. 11 (2012) 550–557. https://doi.org/10.1038/nmat3313.

[203] M. Srivastava, Md. Elias Uddin, J. Singh, N.H. Kim, J.H. Lee, Preparation and characterization of self-assembled layer by layer $NiCo_2O_4$–reduced graphene oxide nanocomposite with improved electrocatalytic properties, J. Alloys Compd. 590 (2014) 266–276. https://doi.org/10.1016/j.jallcom.2013.12.111.

[204] J. Yang, S. Park, K. young Choi, H.-S. Park, Y.-G. Cho, H. Ko, H.-K. Song, Activity-durability coincidence of oxygen evolution reaction in the presence of carbon corrosion: case study of $MnCo_2O_4$ spinel with carbon black, ACS Sustain. Chem. Eng. 6 (2018) 9566–9571. https://doi.org/10.1021/acssuschemeng.8b01879.

[205] Y. Yi, G. Weinberg, M. Prenzel, M. Greiner, S. Heumann, S. Becker, R. Schlögl, Electrochemical corrosion of a glassy carbon electrode, Catal. Today. 295 (2017) 32–40. https://doi.org/10.1016/j.cattod.2017.07.013.

[206] T. Thippani, S. Mandal, G. Wang, V.K. Ramani, R. Kothandaraman, Probing oxygen reduction and oxygen evolution reactions on bifunctional non-precious metal catalysts for metal–air batteries, RSC Adv. 6 (2016) 71122–71133. https://doi.org/10.1039/C6RA13414A.

[207] N. Staud, H. Sokol, P.N. Ross, The corrosion of carbon black anodes in alkaline electrolyte IV. Current efficiencies for oxygen evolution from metal oxide-impregnated graphitized furnace blacks, J. Electrochem. Soc. 136 (1989) 3570–3576.

[208] A. Biswal, B. Chandra Tripathy, K. Sanjay, T. Subbaiah, M. Minakshi, Electrolytic manganese dioxide (EMD): a perspective on worldwide production, reserves and its role in electrochemistry, RSC Adv. 5 (2015) 58255–58283. https://doi.org/10.1039/C5RA05892A.

[209] M. Inaba, A.W. Jensen, G.W. Sievers, M. Escudero-Escribano, A. Zana, M. Arenz, Benchmarking high surface area electrocatalysts in a gas diffusion electrode: measurement of oxygen reduction activities under realistic conditions, Energy Environ. Sci. 11 (2018) 988–994. https://doi.org/10.1039/C8EE00019K.

[210] S. Martens, L. Asen, G. Ercolano, F. Dionigi, C. Zalitis, A. Hawkins, A. Martinez Bonastre, L. Seidl, A.C. Knoll, J. Sharman, P. Strasser, D. Jones, O. Schneider, A comparison of rotating disc electrode, floating electrode technique and membrane electrode assembly measurements for catalyst testing, J. Power Sources. 392 (2018) 274–284. https://doi.org/10.1016/j.jpowsour.2018.04.084.

[211] M.A. Al-Saleh, S. Gültekin, A.S. Al-Zakri, H. Celiker, Effect of carbon dioxide on the performance of Ni/PTFE and Ag/PTFE electrodes in an alkaline fuel cell, J. Appl. Electrochem. 24 (1994) 575–580.

[212] J.-F. Drillet, F. Holzer, T. Kallis, S. Müller, V.M. Schmidt, Influence of CO_2 on the stability of bifunctional oxygen electrodes for rechargeable zinc/air batteries and study of different CO_2filter materials, Phys. Chem. Chem. Phys. 3 (2001) 368–371. https://doi.org/10.1039/b005523i.

[213] Erich Gülzow, Alkaline fuel cells: a critical view, J. Power Sources. 61 (1996) 99–104.

[214] D. Schröder, U. Krewer, Model based quantification of air-composition impact on secondary zinc air batteries, Electrochimica Acta. 117 (2014) 541–553. https://doi.org/10.1016/j.electacta.2013.11.116.

[215] P. Pei, K. Wang, Z. Ma, Technologies for extending zinc–air battery's cyclelife: A review, Appl. Energy. 128 (2014) 315–324. https://doi.org/10.1016/j.apenergy.2014.04.095.
[215] DOE Hydrogen and Fuel Cells Program: Annual Merit Review and Peer Evaluation, 2020, https://www.hydrogen.energy.gov/annual_review.html.
[217] V.R. Stamenkovic, D. Strmcnik, P.P. Lopes, N.M. Markovic, Energy and fuels from electrochemical interfaces, Nat. Mater. 16 (2017) 57–69. https://doi.org/10.1038/nmat4738.
[217] EUR-Lex - 52017DC0490 - EN - EUR-Lex, 2020, https://eur-lex.europa.eu/legal-content/EN/TXT/?uri=CELEX%3A52017DC0490.
[219] D. Thiele, A. Züttel, Electrochemical characterisation of air electrodes based on La0.6Sr0.4CoO3 and carbon nanotubes, J. Power Sources. 183 (2008) 590–594. https://doi.org/10.1016/j.jpowsour.2008.05.042.
[220] N. Wagner, Characterization of membrane electrode assemblies in polymer electrolyte fuel cells using a.c. impedance spectroscopy, J. Appl. Electrochem. 32 (2002) 859–863.
[221] P. Cadman, Gossedge, G. M., Studies of polytetrafluoroethylene transfer layers produced by rubbing in ultrahigh vacuum using a relatively simple apparatus, Wear. 51 (1978) 57–65.
[222] X. Lu, K.C. Wong, P.C. Wong, K.A.R. Mitchell, J. Cotter, D.T. Eadie, Surface characterization of polytetrafluoroethylene (PTFE) transfer films during rolling–sliding tribology tests using X-ray photoelectron spectroscopy, Wear. 261 (2006) 1155–1162. https://doi.org/10.1016/j.wear.2006.03.020.
[223] Y. Rotenberg, S. Srinivasan, E. I. Vargha-Butler, A. W. Neumann, Effects of KOH solution on the surface properties of teflon, J. Electroanal. Chem. Interfacial Electrochem. 213 (1986) 43–51.
[224] K. Tomantschger, R. Findlay, M. Hanson, K. Kordesch, S. Srinivasan, Degradation modes of alkaline fuel cells and their components, J. Power Sources. 39 (1992) 21–41. https://doi.org/10.1016/0378-7753(92)85003-S.
[225] G. Nansé, E. Papirer, P. Fioux, F. Moguet, A. Tressaud, Fluorination of carbon blacks: An X-ray photoelectron spectroscopy study: I. A literature review of XPS studies of fluorinated carbons. XPS investigation of some reference compounds, Carbon. 35 (1997) 175–194. https://doi.org/10.1016/S0008-6223(96)00095-4.
[226] T.A. Blanchet, F.E. Kennedy, D.T. Jayne, XPS Analysis of the Effect of Fillers on PTFE Transfer Film Development in Sliding Contacts, Tribol. Trans. 36 (1993) 535–544. https://doi.org/10.1080/10402009308983193.
[227] G. Beamson, D. Briggs, High resolution XPS of organic polymers—the scienta ESCA 300 data base., Beamson and Briggs, John Wiley & Sons, Ltd, Chichester, 1992.
[228] A. V. Shchukarev, D. V. Korolkov, XPS Study of group IA carbonates, Cent. Eur. J. Chem. 2 (2004) 347–362.
[229] W. Dasilva, A. Entenberg, B. Kahn, T. Debies, G.A. Takacs, Surface modification of Teflon® PFA with vacuum UV photo-oxidation, J. Adhes. Sci. Technol. 20 (2006) 437–455. https://doi.org/10.1163/156856106777144318.
[230] M.C. Biesinger, B.P. Payne, L.W.M. Lau, A. Gerson, R.St.C. Smart, X-ray photoelectron spectroscopic chemical state quantification of mixed nickel metal, oxide and hydroxide systems, Surf. Interface Anal. 41 (2009) 324–332. https://doi.org/10.1002/sia.3026.

[231] M.C. Biesinger, L.W.M. Lau, A.R. Gerson, R.St.C. Smart, The role of the Auger parameter in XPS studies of nickel metal, halides and oxides, Phys. Chem. Chem. Phys. 14 (2012) 2434. https://doi.org/10.1039/c2cp22419d.
[232] A.P. Grosvenor, M.C. Biesinger, R.St.C. Smart, N.S. McIntyre, New interpretations of XPS spectra of nickel metal and oxides, Surf. Sci. 600 (2006) 1771–1779. https://doi.org/10.1016/j.susc.2006.01.041.
[233] J. Chastain, Handbook of X-ray Photoelectron Spectroscopy, Perkin-Elmer Corporation, 1992.
[234] V. Di Castro, G.Polzonetti, XPS study of MnO oxidation, J. Electron Spectrosc. Relat. Phenom. 48 (1989) 117–123.
[235] M.C. Biesinger, B.P. Payne, A.P. Grosvenor, L.W.M. Lau, A.R. Gerson, R.St.C. Smart, Resolving surface chemical states in XPS analysis of first row transition metals, oxides and hydroxides: Cr, Mn, Fe, Co and Ni, Appl. Surf. Sci. 257 (2011) 2717–2730. https://doi.org/10.1016/j.apsusc.2010.10.051.
[236] F.H.B. Lima, M.L. Calegaro, E.A. Ticianelli, Electrocatalytic activity of manganese oxides prepared by thermal decomposition for oxygen reduction, Electrochimica Acta. 52 (2007) 3732–3738. https://doi.org/10.1016/j.electacta.2006.10.047.
[237] E.M. Erickson, M.S. Thorum, R. Vasic, S. Marinkovic, A.I. Frenkel, A.A. Gewirth, R.G. Nuzzo, In Situ Electrochemical X-ray Absorption Spectroscopy of Oxygen Reduction Electrocatalysis with High Oxygen Flux, J Am ChemSoc. (2012) 4.
[238] Scott Calvin, XAFS for Everyone, 1st Edition, CRC Press, 2013.
[239] J.M. Lee, S.B. Patil, B. Kang, S. Lee, M.G. Kim, S.-J. Hwang, Understanding the crucial role of local crystal order in the electrocatalytic activity of crystalline manganese oxide, J. Mater. Chem. A. 6 (2018) 12565–12573. https://doi.org/10.1039/C8TA00502H.
[240] Z. Yang, D.C. Ford, J.S. Park, Y. Ren, S. Kim, H. Kim, T.T. Fister, M.K.Y. Chan, M.M. Thackeray, Probing the Release and Uptake of Water in α-$MnO_2 \cdot x H_2O$, Chem. Mater. 29 (2017) 1507–1517. https://doi.org/10.1021/acs.chemmater.6b03721.
[241] S. Yamamoto, O. Matsuoka, I. Fukada, Y. Ashida, T. Honda, N. Yamamoto, Using atomic force microscopy to image the surface of the powdered catalyst KMn8O16, J. Catal. 159 (1996) 401–409.
[242] K. Selvakumar, S.M. Senthil Kumar, R. Thangamuthu, K. Ganesan, P. Murugan, P. Rajput, S.N. Jha, D. Bhattacharyya, Physiochemical Investigation of Shape-Designed MnO_2 Nanostructures and Their Influence on Oxygen Reduction Reaction Activity in Alkaline Solution, J. Phys. Chem. C. 119 (2015) 6604–6618. https://doi.org/10.1021/jp5127915.
[243] B. Bozzini, P. Bocchetta, A. Gianoncelli, Coelectrodeposition of Ternary Mn-Oxide/Polypyrrole Composites for ORR Electrocatalysts: A Study Based on Micro-X-ray Absorption Spectroscopy and X-ray Fluorescence Mapping, Energies. 8 (2015) 8145–8164. https://doi.org/10.3390/en8088145.
[244] Y. Liu, L. Yu, M. Sun, G. Diao, B. Lan, G. Cheng, A theoretical investigation of the α-MnO2 (110) surface, Comput. Theor. Chem. 1031 (2014) 1–6. https://doi.org/10.1016/j.comptc.2014.01.003.
[245] D.A. Tompsett, S.C. Parker, M.S. Islam, Surface properties of α-MnO_2: relevance to catalytic and supercapacitor behaviour, J Mater Chem A. 2 (2014) 15509–15518. https://doi.org/10.1039/C4TA00952E.

[246] Q. He, G. Li, X. Liu, J. Liu, P. Deng, D. Chen, Morphologically Tunable MnO2 Nanoparticles Fabrication, Modelling and Their Influences on Electrochemical Sensing Performance toward Dopamine, Catalysts. 8 (2018) 323. https://doi.org/10.3390/catal8080323.
[247] K.-W. Nam, M.G. Kim, K.-B. Kim, *In Situ* Mn K-edge X-ray Absorption Spectroscopy Studies of Electrodeposited Manganese Oxide Films for Electrochemical Capacitors, J. Phys. Chem. C. 111 (2007) 749–758. https://doi.org/10.1021/jp063130o.
[248] B. Gilbert, B.H. Frazer, A. Belz, P.G. Conrad, K.H. Nealson, D. Haskel, J.C. Lang, G. Srajer, G. De Stasio, Multiple Scattering Calculations of Bonding and X-ray Absorption Spectroscopy of Manganese Oxides, J. Phys. Chem. A. 107 (2003) 2839–2847. https://doi.org/10.1021/jp021493s.
[249] V.B. Baez, D. Pletcher, Preparation and characterization of carbon/titanium dioxide surfaces—the reduction of oxygen, J. Electroanal. Chem. 382 (1995) 59–64.

6. Annex

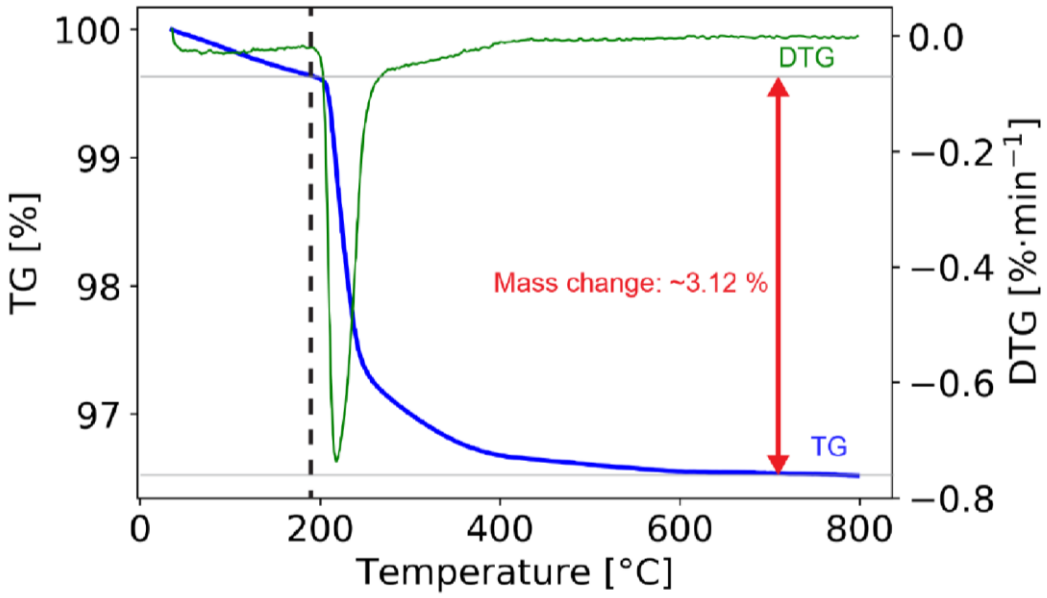

Figure A1: Thermogravimetric TGA/DTA analysis of the commercial Ni/NiO core/shell NPs. The TGA/DTA thermal properties were obtained by using the thermogravimetric analyzer NETZSCH STA 449 (Jupiter®). The temperature was increased from room temperature to 800°C with an increment of 10 °C·min^{-1} in a reducing atmosphere with composition 95 % N_2 and 5 % H_2. The flow rate was 90 mL·min^{-1}. This method enables to determine the nominal (weight) ratio between Ni and NiO by converting all the NiO (of the shell) into metallic Ni using a reducing atmosphere at elevated temperatures, following the reaction described in Equation 1:

Eq. 1) $$NiO + H_2 \rightarrow Ni + H_2O$$

Equation 2 shows the correlation between the measured weight loss (measured by the TGA technique) and to the Ni/NiO nominal ratio:

Eq. 2) $$NiO : Ni = \frac{4.7 \times \text{mass change}}{1 - 4.7 \times \text{mass change}}$$

The measured mass change (weight loss) of about 3.12 %, corresponds to a NiO:Ni ratio of 1:5, that is well compatible with the values reported by the Ni/NiO NPs producer.

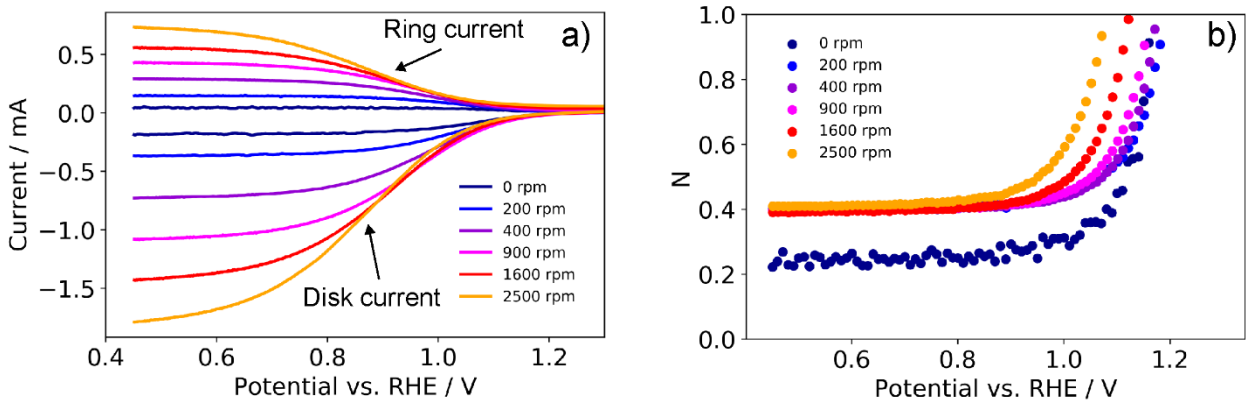

Figure A2: Determination of the collection efficiency N of the RRDE tip used in this work. The collection efficiency was obtained from the ratio of the oxidation current of potassium ferrocyanide at the ring ($[Fe(II)(CN)_6]^{4-} \rightarrow [Fe(III)(CN)_6]^{3-} + e^-$) versus the reduction current of the inverse reaction occurring at the disk ($[Fe(III)(CN)_6]^{3-} + e^- \rightarrow [Fe(II)(CN)_6]^{4-}$), see Figure A2a. The ratio between the two currents is shown in Figure A2b. Electrolyte: N_2-saturated solution of 10 mM $K_4[Fe(CN)_6]\cdot 3H_2O$ in 0.1 M NaOH. Potential scan rate: 5 $mV\cdot s^{-1}$. Reference electrode: Ag/AgCl.

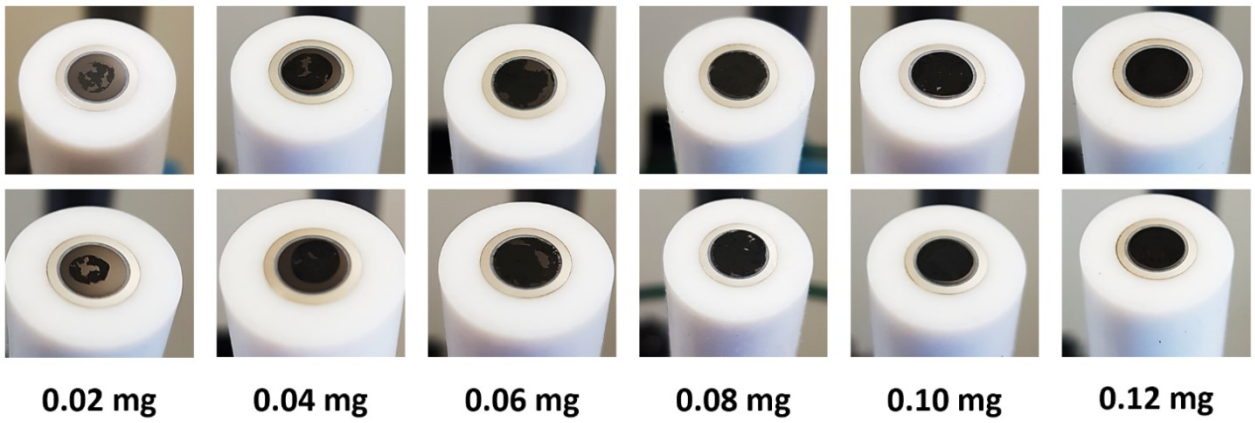

Figure A3: Optimization of the catalyst layer composition for RDE and RRDE measurements. To select the most suitable amount of catalyst to be deposited on the disk electrode for the RDE and RRDE methods, a set of measurement was performed, where the quantity of MnO_2/C catalyst composite was varied from 0.02 mg to 0.14 mg. The morphology of the catalyst layer as a function of mass loading is shown in Figure A3. It can be noticed that at loadings lower than 0.08 mg, the active material is not sufficient to cover the entire surface of the GC substrate. At composition 0.10 mg, the active layer results more uniform and it covers completely the GC surface. However, no further visible/macroscopic improvements on the quality of the catalyst layer were found at loadings above 0.10 mg.

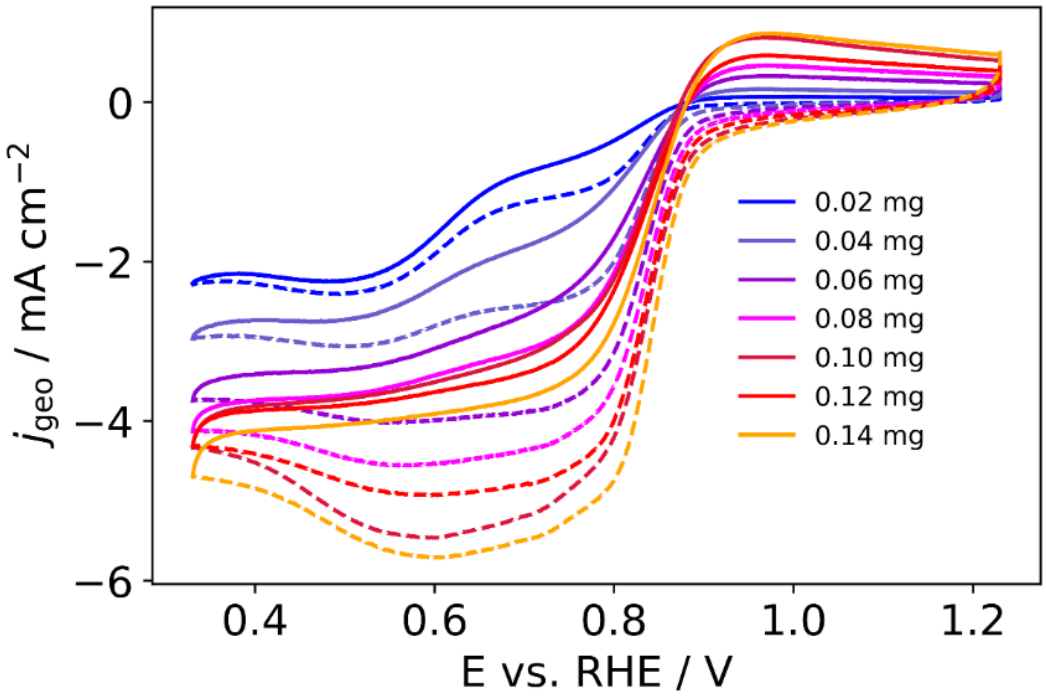

Figure A4: Cyclic voltammogram at 5 mV·s^{-1} in O_2-saturated 0.1 KOH at 1600 rpm of MnO_2/C catalyst composite with loadings 0.02 mg to 0.14 mg. The same electrochemical procedure was applied to each catalyst layer, in order to examine the effect of mass loading on the activity and selectivity towards the 4e- ORR pathway. The voltammograms recorded in the O_2 atmosphere of the different MnO_2/C mixtures are shown in Figure A4. Two consecutive reduction waves are noticeable for the ORR when the mass of active material on the disk is below 0.06 mg, while only one sharp reduction waves is observed at loadings equal to or above 0.06 mg. The first reduction step (at lower overpotentials) belongs to the reduction of oxygen on to the MnO_2/C surface, while the second reduction step (at higher overpotentials) can be ascribed to the occurrence of ORR on the bare glassy carbon (GC) substrate, since at loadings < 0.06 mg the latter was largely exposed to the electrolyte. Likewise, ORR voltammograms of a polished GC disk electrode were reported in alkaline electrolyte by Baez and coworkers[249], and two waves were also detected, both due to the reduction of O_2 to HO_2^- via the 2e-ORR pathway at different types of site on the GC surface. In their study, the formation of HO_2^- was confirmed by the relatively high anodic current that was detected at the ring electrode. The measured HO_2^- yield as a function of disk electrode potential (anodic sweep direction) of the various catalyst layers is shown in Figure A5.

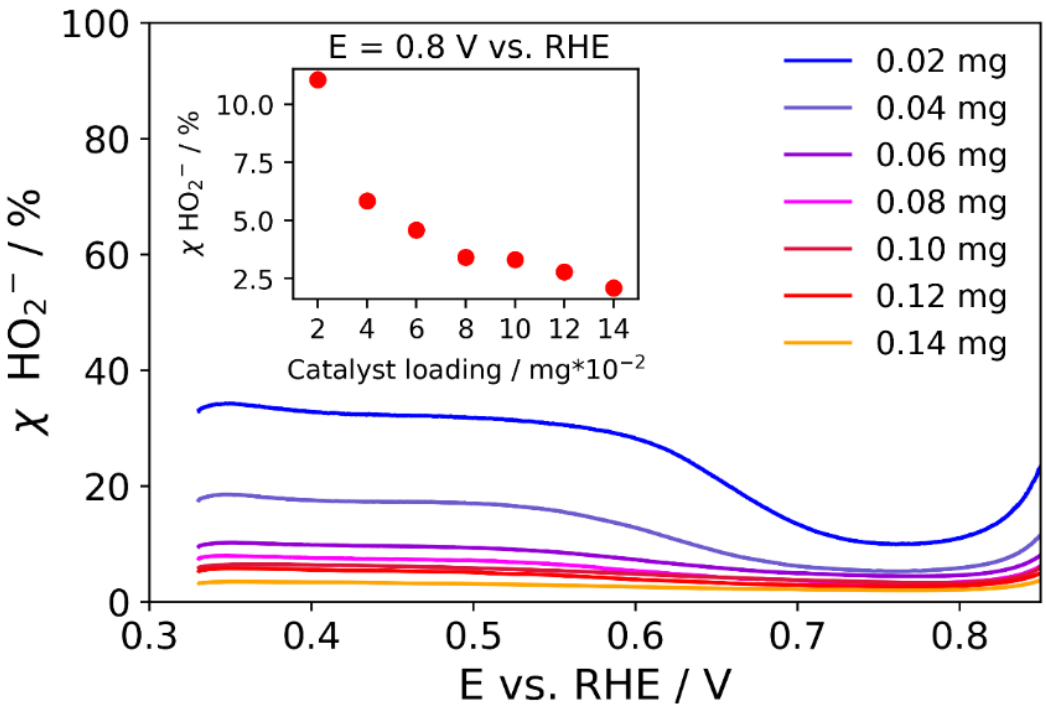

Figure A5: HO_2^- yield (%) as a function of disk electrode potential (anodic potential sweep direction) of catalyst layers with loadings 0.02 mg to 0.14 mg. At loadings < 0.06 mg (i.e. the case where a part of the GC substrate was still exposed to the solution) the HO_2^- yield is not constant, but it varies as a function of the applied potential, with a sharp increase at potentials lower than 0.7 V vs. RHE. Representative is the case of 0.02 mg, where the percentage of detected HO_2^- changes from about 13 to 33 % by varying the potential from 0.8 to 0.4 V vs. RHE, respectively. Moreover, this was the only case in which the concentration of HO_2^- was higher than 10 % in the low overpotential region (E = 0.8 V vs. RHE), indicative for a mixed 2e- and 4e- ORR pathway. For all the other cases, the low concentration of detected HO_2^- (< 5 %) may be ascribed to an apparent 4e- pathway. Although the overall trend is that the HO_2^- yield decreases with increasing catalyst loading (see inlet Figure A5), at m = 0.10 mg a plateau is formed with HO_2^- of about 3 %.

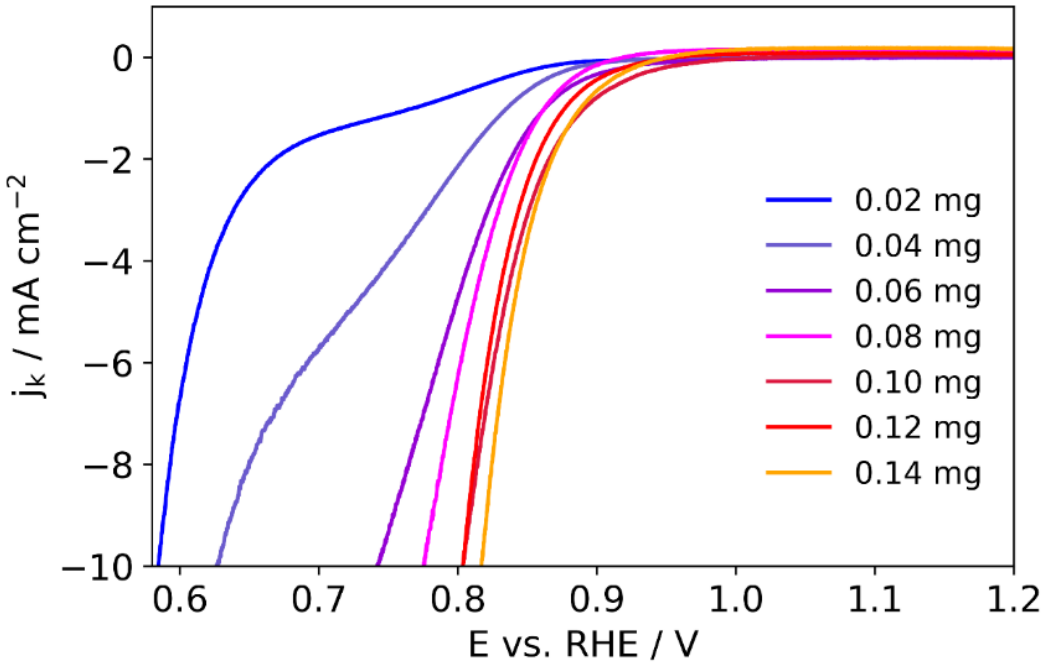

Figure A6: Potential dependence of the ORR activity in terms of kinetic current density (normalized by the geometric surface area of the GC disk electrode) as a function of MnO_2/C catalyst composite loading. It can be noticed that the voltammogram shifts to the right-hand side (lower overpotentials) by increasing the mass of the catalyst layer. At values higher than 0.10 mg, however, there is no direct evidence of further improvement related to an increase of the catalyst loading.

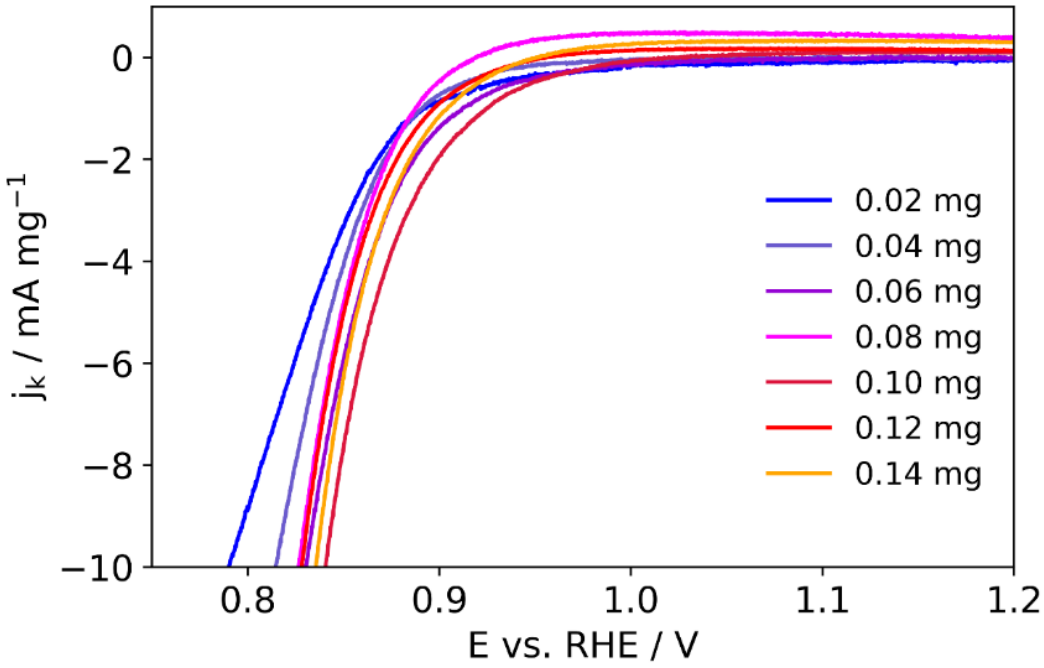

Figure A7: Potential dependence of the ORR activity in terms of kinetic current density normalized by mass of the MnO_2/C catalyst composite. The performance of the various catalyst compositions become very similar, thus suggesting that the kinetic activity is directly proportional to the mass of active material used. Again, the measurements which deviate slightly from the others are those which belong to the active layers with mass 0.02 and 0.04 mg, where the contribution of the GC substrate to the ORR may become relevant.

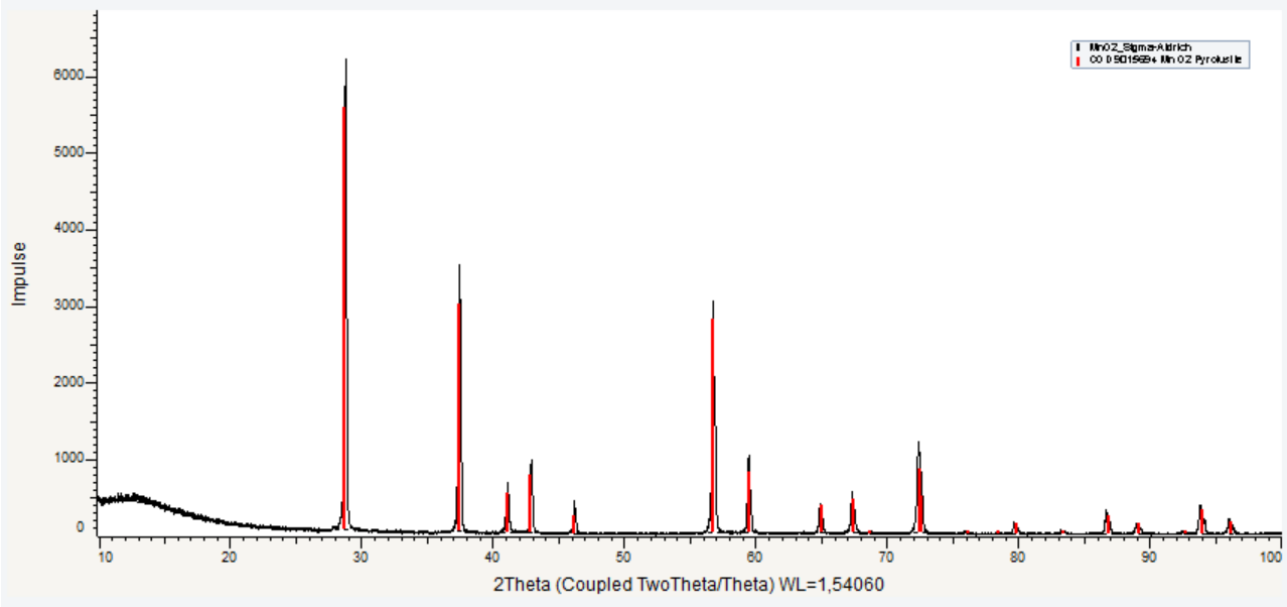

Figure A8: XRD powder pattern of MnO_2 obtained from Sigma-Aldrich. The MnO_2 has a pyrolusite-type crystal structure, also known as β-MnO_2.

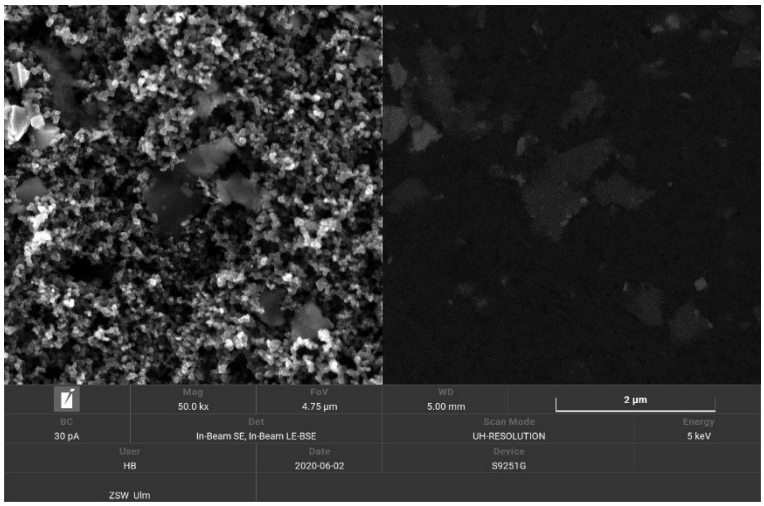

Figure A9: Scanning electron micrograph obtained via secondary electron detector (left) and via back-scattered electron detector (right) of the binary catalyst composite $(C)_{50}(Pyrolusite)_{50}$. Scale bar: 2 µm.

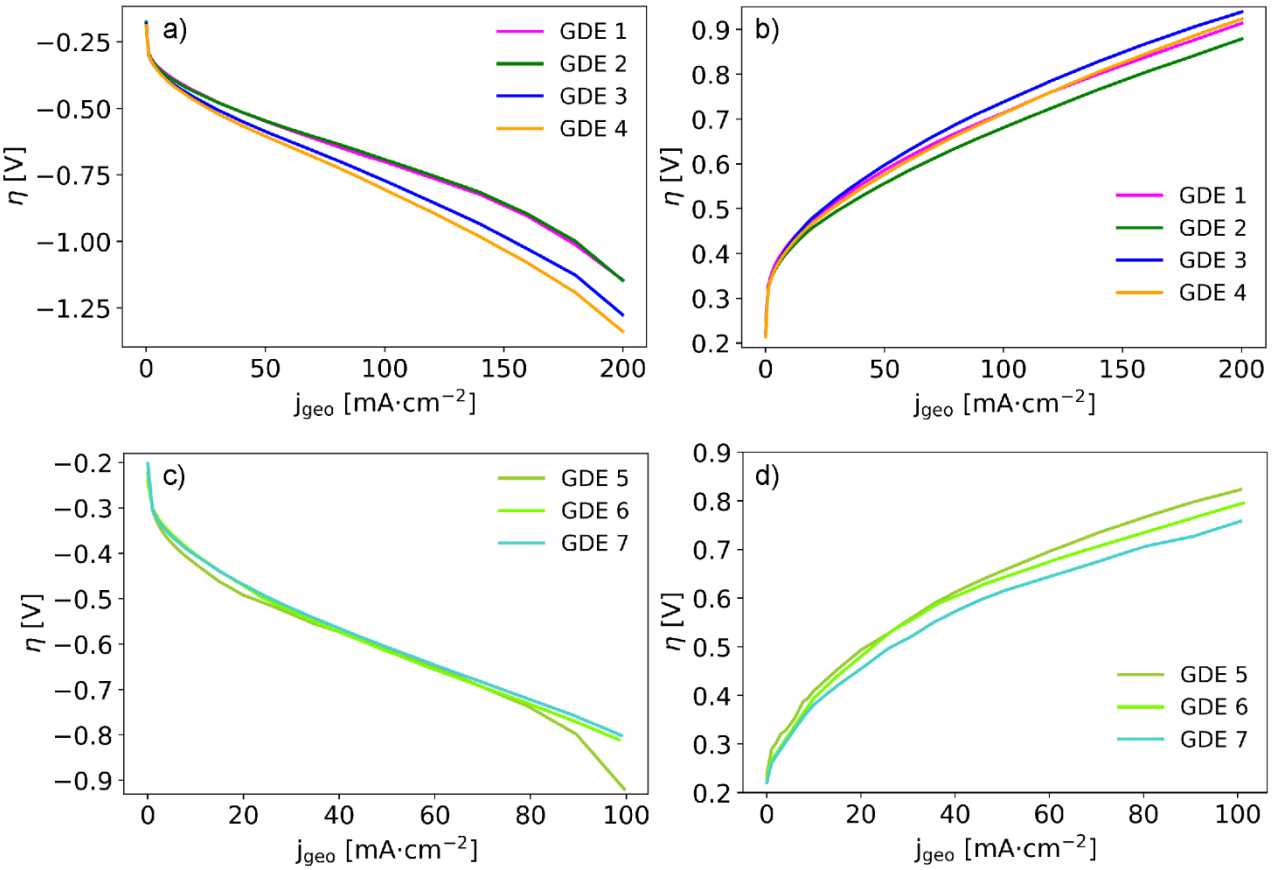

Figure A10: ORR (a, c) and OER (b, d) polarization curves of GDE 1-4 and GDE 5-7.

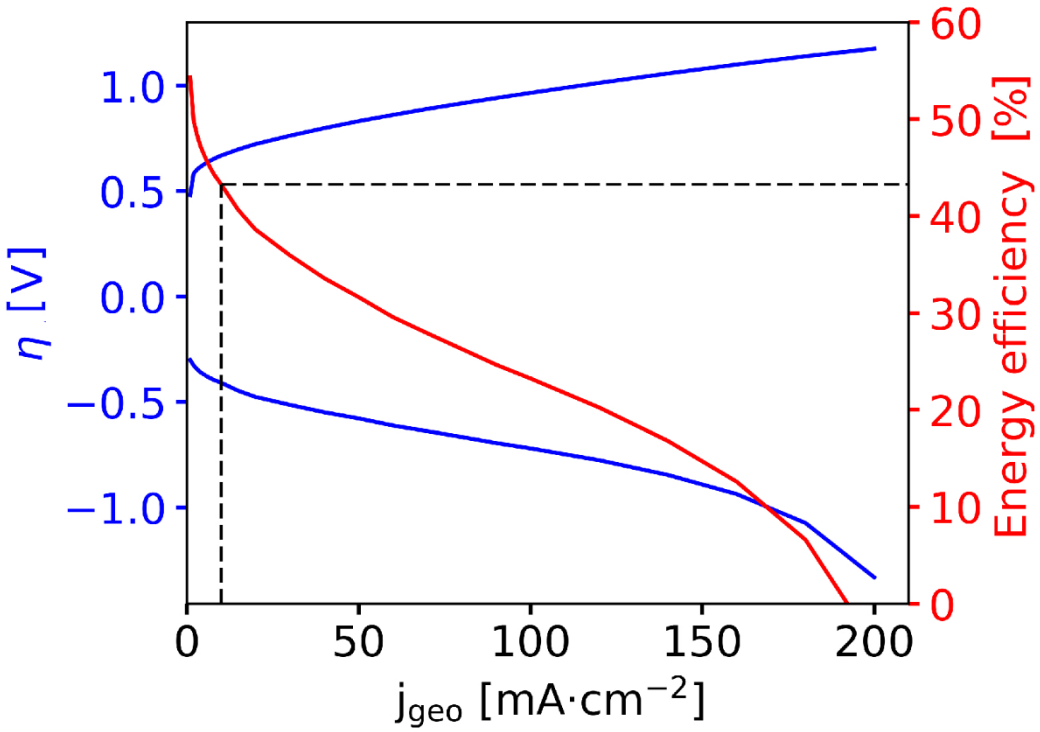

Figure A11: ORR and OER polarization curves (blue solid lines), as well as energy efficiency (defined as (1.23 V + η_{ORR}) / (1.23 V + η_{OER}), see red solid line) of GDE 8 (see Figure 47, main text). Interestingly, the energy efficiency of the same

electrode obtained during the stability test at j_{geo} = 10 mA·cm^{-2} (see Figure 47d) is higher than that measured during the polarization test (see black dashed lines, with values of 55 % and 43 %, respectively. The surface of the GDE was exposed to the electrolyte over a prolonged period of time (200-400 h) during the stability test (Figure 47d, main text), while the performance / polarization test showed in Fig. A11 only took a few hours (approx. 25 hours) to complete. As mentioned by Müller and co-workers[42], an improvement of surface area wetting of the electrode is expected with time, which in turn increases the overall efficiency of the electrode. Therefore, this difference in performances may be ascribed to such effect that modifies the performance. Nevertheless, we suggest that the energy efficiency obtained during the stability test was the most relevant, since the experimental conditions were similar to practical application.

Calculation of the specific capacity and specific energy density of a Zn-air cell

Total capacity of a Zn-air cell with an air cathode of area, $A_{cathode}$ in cm^2, cycling current density, j in mA·cm^{-2} for individual discharge time, t in hour (Equation 3):

Eq. 3) $$C_{Zn-air} = i \times t = A \times j \times t$$

Theoretical capacity of the Zn anode (which defines the total discharge capacity of the Zn-air cell) (Equation 4):

Eq. 4) $$C_{Zn,\ theo} = m_{Zn} \times 819.73 = V_{Zn} \times \rho_{Zn} \times 819.73$$

As anode material we consider a Zn foil with thickness of 0.01 cm, area= 1 cm^2 ($A_{Zn} = A_{cathode}$) and density of $\rho_{Zn} = 7.14\ g \cdot cm^{-3}$. Parker et. al[1] showed that the deep-of-discharge of the Zn foil electrode can be deduced by rationing Equation 3 and Equation 4 (Equation 5):

Eq. 5) $$DOD_{Zn} = \frac{C_{Zn-air}}{C_{Zn,\ theo}} = \frac{A_{cathode} \times j \times t}{V_{Zn} \times \rho_{Zn} \times 819.73}$$

Applying a load cycle of $j \times t = 20\ mAh \cdot cm^{-2}$ to Equation 5 results in a $DOD_{Zn} = 34\ \%$, thus giving an effective specific capacity of the Zn-air cell (without considering the weight of other cell components) of about $280\ mAh \cdot g^{-1}$ (Equation 6):

Eq. 6) $$c_{Zn-air,\ eff} = \frac{C_{Zn,\ theo} \times DOD_{Zn}}{m_{Zn}} = 819.73\ mAh \cdot g^{-1} \times 34\ \% \approx 280\ mAh \cdot g^{-1}$$

By multiplying $c_{Zn-air,\ eff}$ with the mass of the zinc anode $m_{Zn} = V_{Zn} \times \rho_{Zn}$ we obtain the effective capacity of the Zn-air cell (Equation 7):

Eq. 7) $$C_{Zn,\ eff} \times m_{Zn} = 280\ mAh \cdot g^{-1} \times 0.07\ g \approx 20\ mAh$$

To meet the technologically relevant threshold of 100 Wh·kg^{-1} and by considering an average discharge voltage of 1.25 V, the packaged Zn-air cell should have a minimum specific capacity of (Equation 8):

Eq. 8) $$c_{Zn-air,\ min} = \frac{100\ mWh \cdot g^{-1}}{1.25\ V} = 80\ mAh \cdot g^{-1}$$

Therefore, the maximum weight allowed of the packaged Zn-air cell ($m_{Zn} + m_{1-Zn}$) can be found by rationing Equation 7 and Equation 8, where m_{1-Zn} is the sum of all the other cell components:

Eq. 9) $$\frac{20\ mAh}{m_{Zn}+m_{1-Zn}} = 80\ mAh \cdot g^{-1}$$

Since the mass of the anode is known ($m_{Zn} = 0.07$ g), we found that $m_{Zn} + m_{1-Zn} = 0.25$ g. The average areal density of the fabricated GDEs is 0.03 g · cm^{-2} that is about~10 % (12 %) of the total weight of the Zn-air cell.

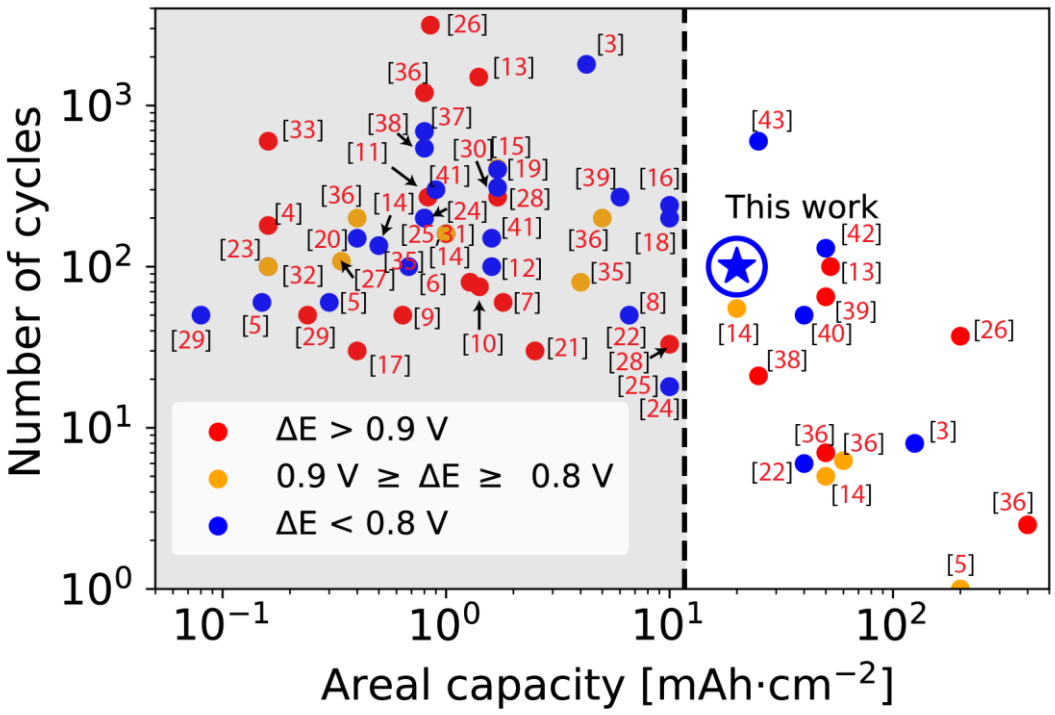

Figure A12: Same as Figure 48, but including reference numbers from the reference list in supporting information and Table A1.

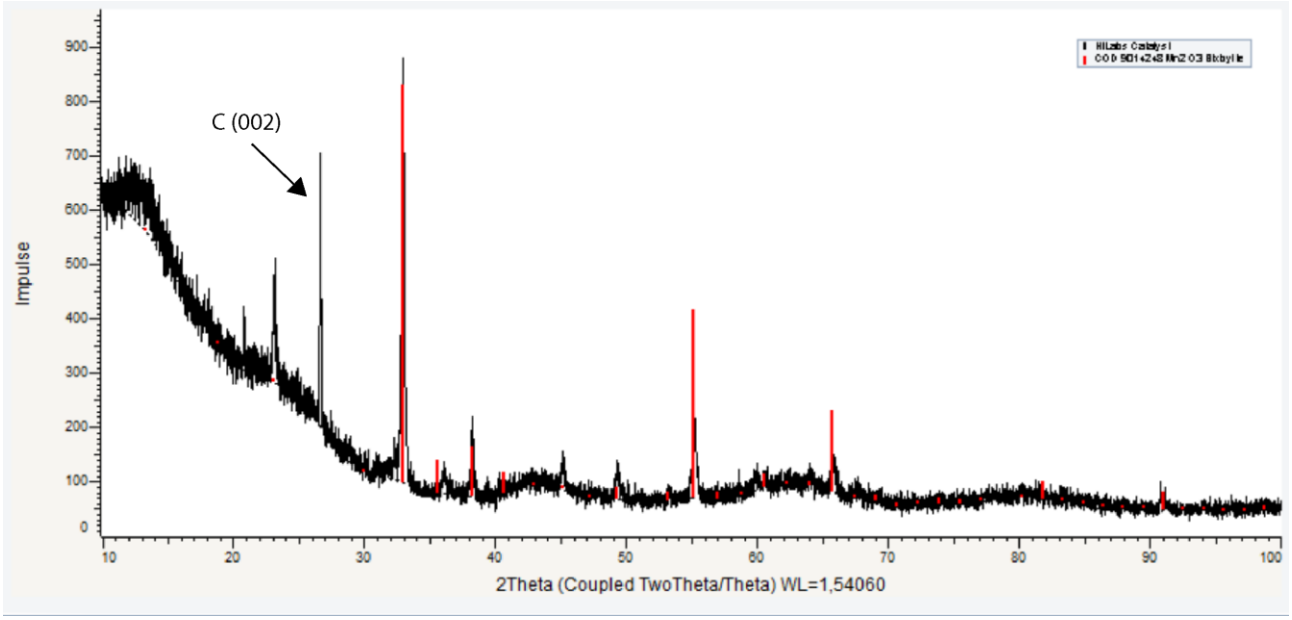

Figure A13: XRD powder diffraction of the commercial electrocatalyst mixture. The powder is composed of Mn_2O_3 (Bixbyite) and graphitic carbon (characterized by the presence of a sharp diffraction peak at 2-theta angle of about 25°).

Table A1: Performance comparison with reported GDEs in the literature.

GDE	**Total number of cycles**	**j x t [mAh·cm^{-2}]**	**Sum of charge-discharge overpotential ΔE [V]**	**Reference**
MnO_2/C/Ni	100	20	0.7	[2]
Co_3O_4-NCNT on stainless steel	1800 8	4.25 125	0.75 0.75	[3]
N-doped carbon fiber film	180	0.16	1.81	[4]
CoO/N-CNT and NiFe LDH/CNT	60 60 1	0.3 0.15 200	0.7 0.6 0.8	[5]
B, N co-doped CNT	80	1.28	1.4	[6]
MnO_2/Co_3O_4	60	1.8	0.95	[7]
$NiCo_2O_4$	50	6.6	0.7	[8]
MnO_2/NCNT	50	0.64	1.66	[9]
$LaNiO_3$ supported on N-CNTs	75	1.41	1.3	[10]

Ag–MnO2	270	0.83	1.37	[11]
$CoMn_2O_4$/N-reduced graphene oxide	100	1.6	0.7	[12]
Co_3O_4 on stainless steel	1500 100	1.4 52.5	0.98 1.1	[13]
Co_3O_4 decorated carbon nanofiber	135 5 160 55	0.5 50 1 20	0.7 0.9 0.7 0.85	[14]
Co_4N/intertwined carbon fibers on carbon cloth	408	1.7	0.84	[15]
Ni_3FeN-ordered Fe3Pt intermetallic nanoalloy	240	10	0.72	[16]
Pt nanoparticles/single crystal CoO Nanorods hybrid catalysts	30	0.4	1.35	[17]
3D ordered mesoporous cobalt oxide (3D DOM Co_3O_4)	200	10	0.76	[18]
$Co(OH)_2$ and Co_3O_4 nanosheets (NS) supported on carbon cloth (CC)	400	1.7	0.7	[19]
Mesoporous $PrBa_{0.5}Sr_{0.5}Co_{2-x}Fe_xO_{5+\delta}$ nanofiber (PBSCF-NF)	150	0.4	0.75	[20]
Fibrous hybrid Mn-Co oxides	30	2.5	1.08	[21]
Hybrid CoO nanoclusters and high-index facet Mn_3O_4 nano-	6	40	0.79	[22]

octahedrons (hi-$Mn3O_4$)				
$NiFeO@MnO_x$ core-shell structure supported on graphene	100	0.16	0.56	[23]
Single crystalline pyrochlore nanoparticles with metallic conduction ($Pb_2Ru_2O_{6.5}$)	200 18	0.8 10	0.75 0.75	[24]
Yttrium ruthenate nanoparticles ($Y_2[Ru_{2-x}Y_x]O_{7-y}$, referred as YRO)	200 18	0.8 10	0.71 0.71	[25]
Co-doped TiO_2 nanoparticles (best electrochemical performance with 5 % Co-TiO_2)	37 3150	200 0.85	1 0.94	[26]
Graphene (N-doped)-supported CoFe-based metal hydroxysulfides $Co_3FeS_{1.5}(OH)_6$	108	0.34	0.84	[27]
NiMn layered double hydroxide	270 33	1.7 10	0.96 0.92	[28]
NiO/CoN porous nanowires	50 50	0.08 0.24	0.6 1.26	[29]
Ni_3FeN	310	1.7	0.64	[30]
Eggplant-derived microporous carbon sheets	160	1	0.85	[31]
Spherical nitrogen-doped hollow mesoporous carbon	100	0.16	0.81	[32]
B-N codpoded porous carbon (BNPC)	600	0.16	1.03	[33]
N,S- doped porous carbon	300	0.9	0.77	[34]

RuO_2-coated ordered mesoporous carbon nanofiber	100 80	0.68 4	0.65 0.8	[35]
Co_3O_4/MnO_2-CNTs	1200 2.5 200 200 6.25 7	0.8 400 0.4 5 60 50	1.65 1.02 0.8 0.8 0.9 1.25	[36]
MnO_x-NiFe LDH/Ni foam	690	0.8	0.66	[37]
$La_2O_3/Co_3O_4/MnO_2$-CNTs	543 21	0.8 25	0.7 1	[38]
Ni_3FeN/Co, N-CNF	270 65	6 50	0.79 1.29	[39]
$Co(II)_{1-x}Co(0)_{x/3}Mn(III)_{2x/3}S$ NPs supported on B/N-codoped mesoporous carbon	50	40	0.72	[40]
$CoIn_2S_4$/S-rGO	150	1.6	0.65	[41]
$La_{0.6}Ca_{0.4}CoO_3$/C	130	50	0.75	[42]
$BaSrCoFeO_3$/C	600	25	0.69	[43]

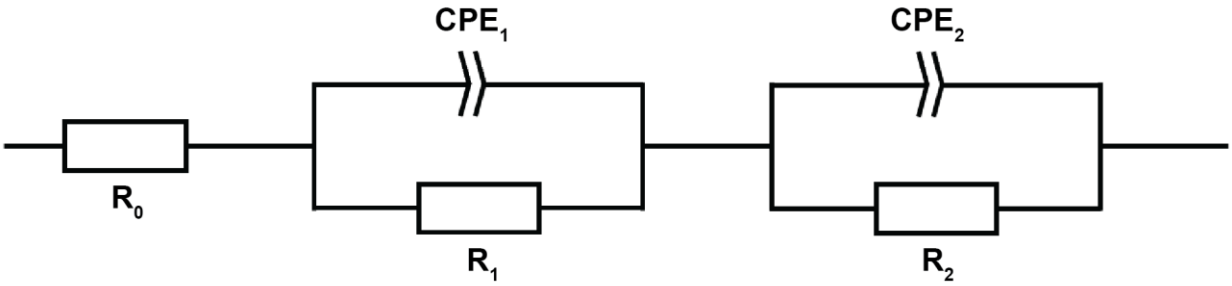

Figure A14: Equivalent model used for the fit of the measured impedances. The experimental EIS spectra could be accurately fitted with seven adjustable parameters, namely R_0, R_1, R_2, CPE_1, n_1, CPE_2 and n_2.

Table A2: Results of the equivalent circuit fitting depicted in Figure A14 and Figure 50b.

Cycle number	R_0 [Ω]	CPE_1 [$F \cdot s^{n1}$]	n_1	R_1 [Ω]	CPE_2 [$F \cdot s^{n2}$]	n_2	R_2 [Ω]
1	2.21 ± 0.02	0.060 ± 0.003	0.50 ± 0.02	1.48 ± 0.05	0.111 ± 0.002	0.90 ± 0.03	3.69 ± 0.19
10	2.17 ± 0.06	0.035 ± 0.003	0.50 ± 0.05	0.95 ± 0.01	0.084 ± 0.003	0.84 ± 7e-3	4.92 ± 0.21
30	2.21 ± 0.03	0.042 ± 0.007	0.50 ± 0.02	0.83 ± 0.13	0.082 ± 0.002	0.83 ± 0.03	5.70 ± 0.23
60	2.82 ± 0.09	0.007 ± 0.001	0.50 ± 0.02	1.89 ± 0.11	0.070 ± 0.005	0.73 ± 0.02	7.48 ± 0.45
100	2.06 ± 0.08	0.001 ± 4e-5	0.55 ± 3e-3	29.70 ± 0.41	0.045 ± 0.002	0.59 ± 0.09	41.30 ± 0.15

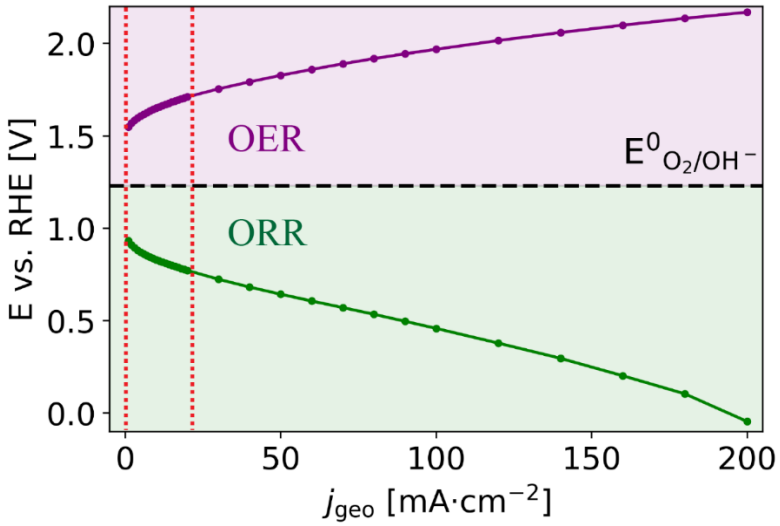

Figure A15: ORR (green) and OER (purple) polarization curves of the GDE tested for *ex-situ* XPS (10 min per current density step). The black dashed line indicates the equilibrium potential of the oxygen reactions. The large increase of overpotentials at low current densities ($j \leq 25$ mA·cm^{-2}, see region between red dotted lines) is typical for systems that are mainly under kinetic control, i.e. when the rate of the reaction is controlled by the charge transfer process.

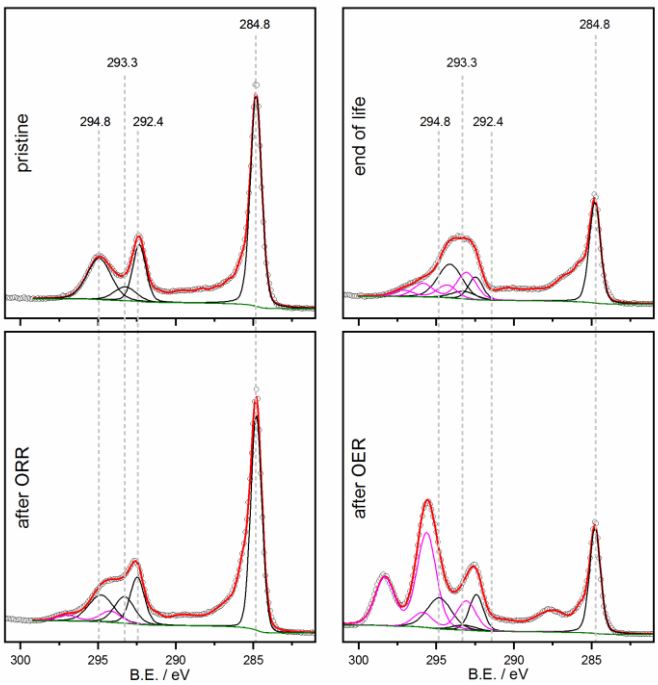

Figure A16: Enlargements of the XPS C (1s) regions. See text for more details.

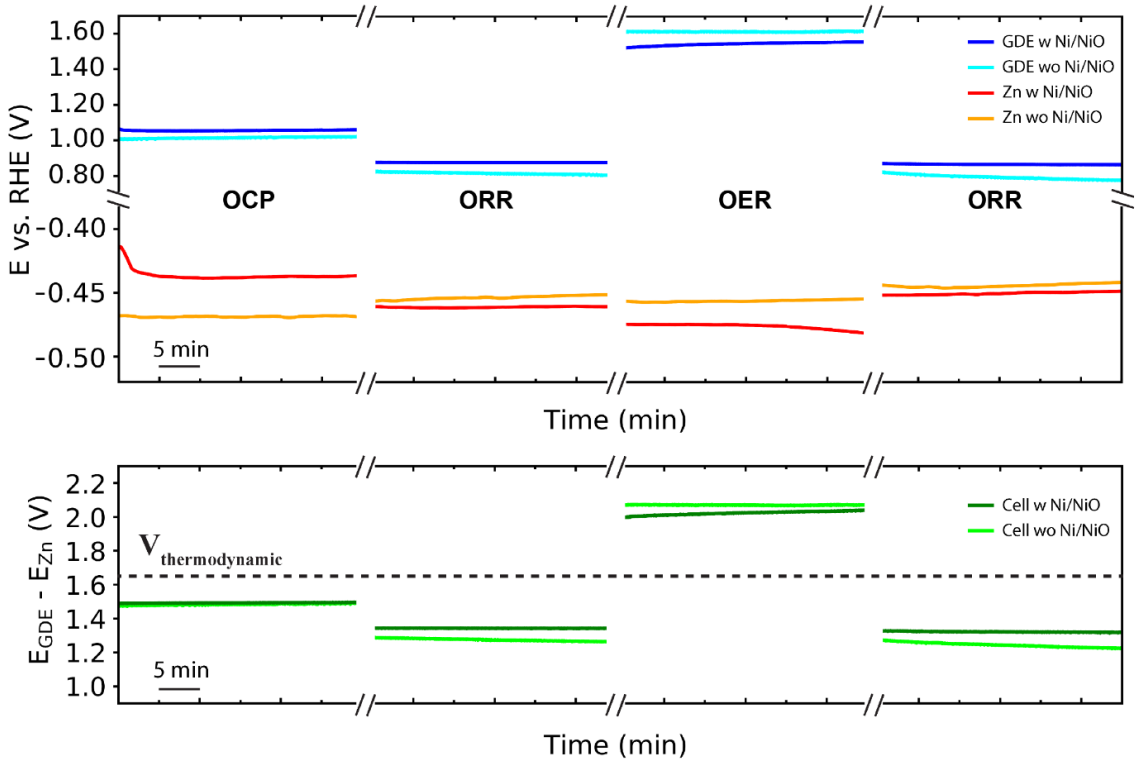

Figure A17: Chronopotentiometries of electrodes with- (**w Ni/NiO**) and without Ni/NiO (**wo Ni/NiO**) during *operando* XAS measurements under open circuit potential (OCP), ORR and OER conditions (with current density j = 5.0 mA·cm^{-2}) in air. We measured the potentials of the GDE (blue and cyan) and of the Zn electrode (red and orange), as well as the corresponding cell voltage (green and lime). Each XAS scan took about 30 min and the electrode potentials were stable

over the entire acquisition time, thus allowing to perform strictly *operando* measurements. The cell voltage at OCP of both electrodes was 1.47 V, which is very close to its theoretical value (V_{theo} = 1.66 V) and compatible with the typical, limited self-discharge rate found in practical batteries. The isolation of the two electrode contributions (GDE and Zn) indicates that the Zn electrode has a minor effect on the observed potential drop, whereas the GDE tends to have the largest deviation from its equilibrium potential (E_0 = 1.23 V vs. RHE). When a cathodic current of j = -5.0 mA·cm^{-2} is applied, the electrode potential drops to about 0.81 V and 0.82 V vs. RHE for GDE without and with Ni/NiO, respectively, indicating outstanding battery behaviour, notwithstanding the constrains dictated by the cell's and electrode designs. In particular, the thin layer of free electrolyte, required for the minimization of the X-ray beam-path through the cell, is certainly in favour of performance. Moreover, the Zn electrode corrodes actively for the whole duration of the measurements, exhibiting a very low polarization. By imposing an anodic current to the GDEs (OER, j = 5.0 mA·cm^{-2}), the electrode potentials reach plateaus of about $E_{GDE@OER}$ = 1.61 V (wo Ni/NiO) and 1.59 V vs. RHE (with Ni/NiO), whereas the Zn potentials of both electrodes shift in the cathodic direction by few mV, with a slight tendency to grow over the measurement time, yielding charge cell voltages of 2.06 V and 2.05 V, respectively.

Table A3: Information relative to the various electrochemical conditions (chronopotentiometry tests) applied during *operando* XAS to the electrode without- (top) and with Ni/NiO (bottom).

GDE without Ni/NiO

Condition	Current density [mA·cm^{-2}]	GDE potential [V vs. RHE]	Zn potential [V vs. RHE]	Cell voltage [V]
OCP	0	1.01 ± 0.01	-0.46 ± 0.04	1.48 ± 0.01
ORR (1st)	-5.0	0.81 ± 0.01	-0.45 ± 0.04	1.27 ± 0.02
OER (1st)	+5.0	1.61 ± 0.03	-0.45 ± 0.04	2.06 ± 0.03
ORR (2nd)	-5.0	0.79 ± 0.03	-0.43 ± 0.04	1.23 ± 0.03

GDE with Ni/NiO

Condition	Current density [mA·cm^{-2}]	GDE potential [V vs. RHE]	Zn potential [V vs. RHE]	Cell voltage [V]
OCP	0	1.05 ± 0.01	-0.44 ± 0.01	1.49 ± 0.01
ORR (1st)	-5.0	0.82 ± 0.01	-0.44 ± 0.04	1.26 ± 0.01
OER (1st)	+5.0	1.59 ± 0.01	-0.45 ± 0.01	2.05 ± 0.01
ORR (2nd)	-5.0	0.82 ± 0.01	-0.45 ± 0.01	1.26 ± 0.01
OER (2nd)	+5.0	1.60 ± 0.01	-0.46 ± 0.01	2.06 ± 0.03
ORR (3rd)	-5.0	0.79 ± 0.01	-0.44 ± 0.01	1.22 ± 0.01

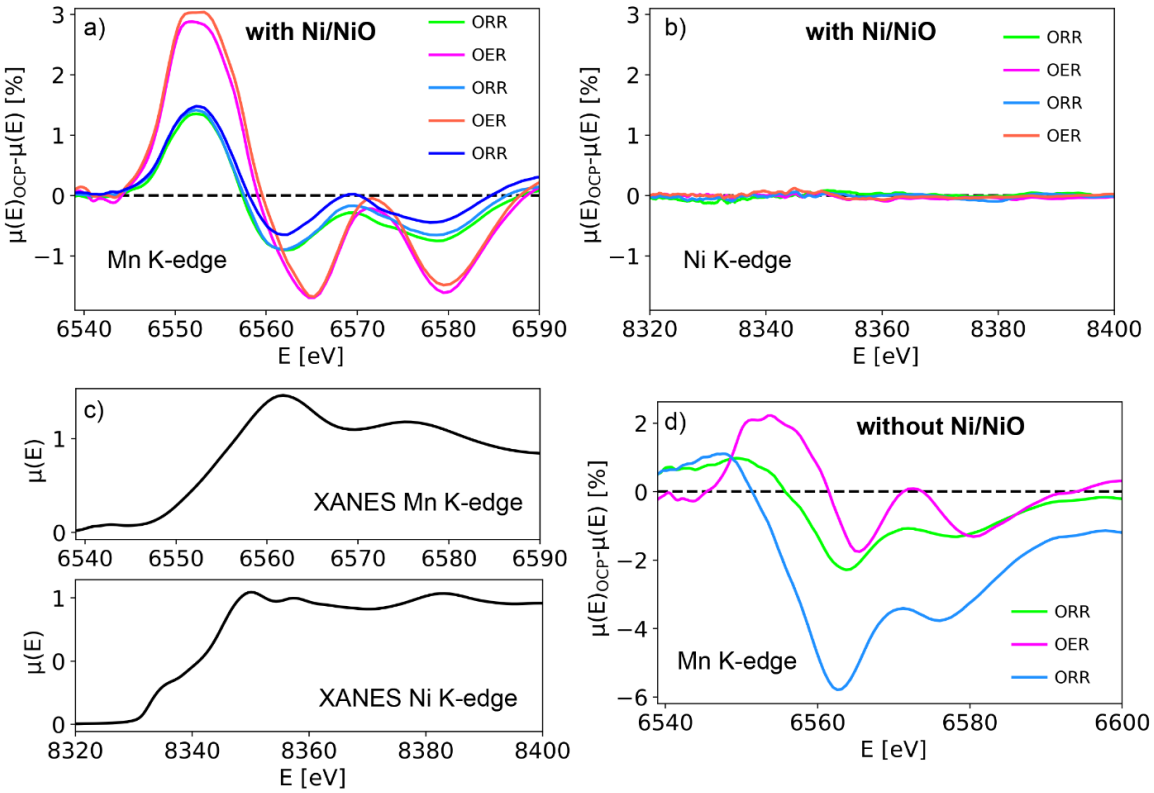

Figure A18: (a) Mn K-edge and **(b)** Ni K-edge difference XANES absorbance spectra of GDE with Ni/NiO, obtained under different electrochemical conditions. In the case of bulk metal oxides, a shift in the edge position of the XANES spectrum usually entails a change in the oxidation state of the element, where a shift to lower / higher energies correlates to a lower / higher oxidation state of the element, respectively. Since the relative energy change of the Mn and Ni K-edges are very small, no distinct differences can be identified between the measurements by analysis of the absolute XANES spectra. Direct inspection of difference spectra, instead, highlights clear, systematic and reproducible spectral changes. An effective way of representing a difference spectrum $\Delta\mu$ is to subtract the normalized absorbance XANES measured when a net current is applied (i.e. during ORR and OER) $\mu_{ORR/OER}$, from that measured at OCP μ_{OCP} **(c)**, thus: $\Delta\mu = \mu_{OCP} - \mu_{ORR/OER}$. Figure A18a shows the difference spectra $\Delta\mu$ of the Mn K-edge XANES region for exemplary ORR/OER conditions. In general, it can be seen that all Mn K-edge difference spectra show a main positive peak in the energy range of about 6542-6560 eV, which corresponds the rising portion of the XANES preceding the top of the edge; and two shallower ones at higher energies (> 6560 eV). The $\Delta\mu$ plot changes according to the electrochemical condition applied. When the ORR is applied, the positive peak appears with an amplitude of about $\Delta\mu_{ORR}$ = 1 %. By switching the reaction to OER, the amplitude of $\Delta\mu$ increases to a value of $\Delta\mu_{1stOER}$ = 3 %. By inverting the current direction again (2nd ORR), the amplitude of $\Delta\mu$ decreases to $\Delta\mu_{2ndORR}$ = 1 % again. By further switching the current direction, $\Delta\mu$ changes between 3 and 1 %, corresponding to OER and ORR, respectively. Of course, in keeping with energy shifts in the $\Delta\mu$ maximum are due to a shift of the rising portion of the XANES spectrum to higher energies by approximately 0.1 eV

(ORR) and 0.3 eV (OER) with respect to that at OCP. These findings might indicate that the chemical environment of the Mn atoms of α-MnO_2 is sensitive (follows) to the electrochemical condition applied, but the behavior seems to be reversible for GDE with Ni/NiO. In the case of nickel (Ni / NiO), no significant changes (lower than 0.1 %) can be observed in the Ni difference spectra Δμ analysis of the K-edge XANES (Figure A18b), suggesting that the Ni / NiO is either less sensitive (prompt to transformations) to the applied electrochemical conditions than α-MnO_2 or (and) that electronic and structural changes occurring on the Ni/NiO surface are below detection limit of the XAS technique. Therefore, only the evolution of the local chemical environment of the α-MnO_2 electrocatalyst during ORR and OER processes will be addressed henceforth. **(d)** Difference spectra Δμ analysis of the Mn K-edge XANES of GDE without Ni/NiO. Again, Δμ is sensitive to the ORR/OER condition. The shape of these spectra, though, is very different from the ones acquired for GDE with Ni/NiO (Figure A18a): the Δμ spectra obtained during the 1st- and 2nd ORR do not coincide. This result (juxtaposed to the above discussion for GDE with Ni/NiO) might indicate that, in the absence of Ni/NiO, the α-MnO_2 undergoes irreversible chemical (electronic) and structural transformation upon OER.

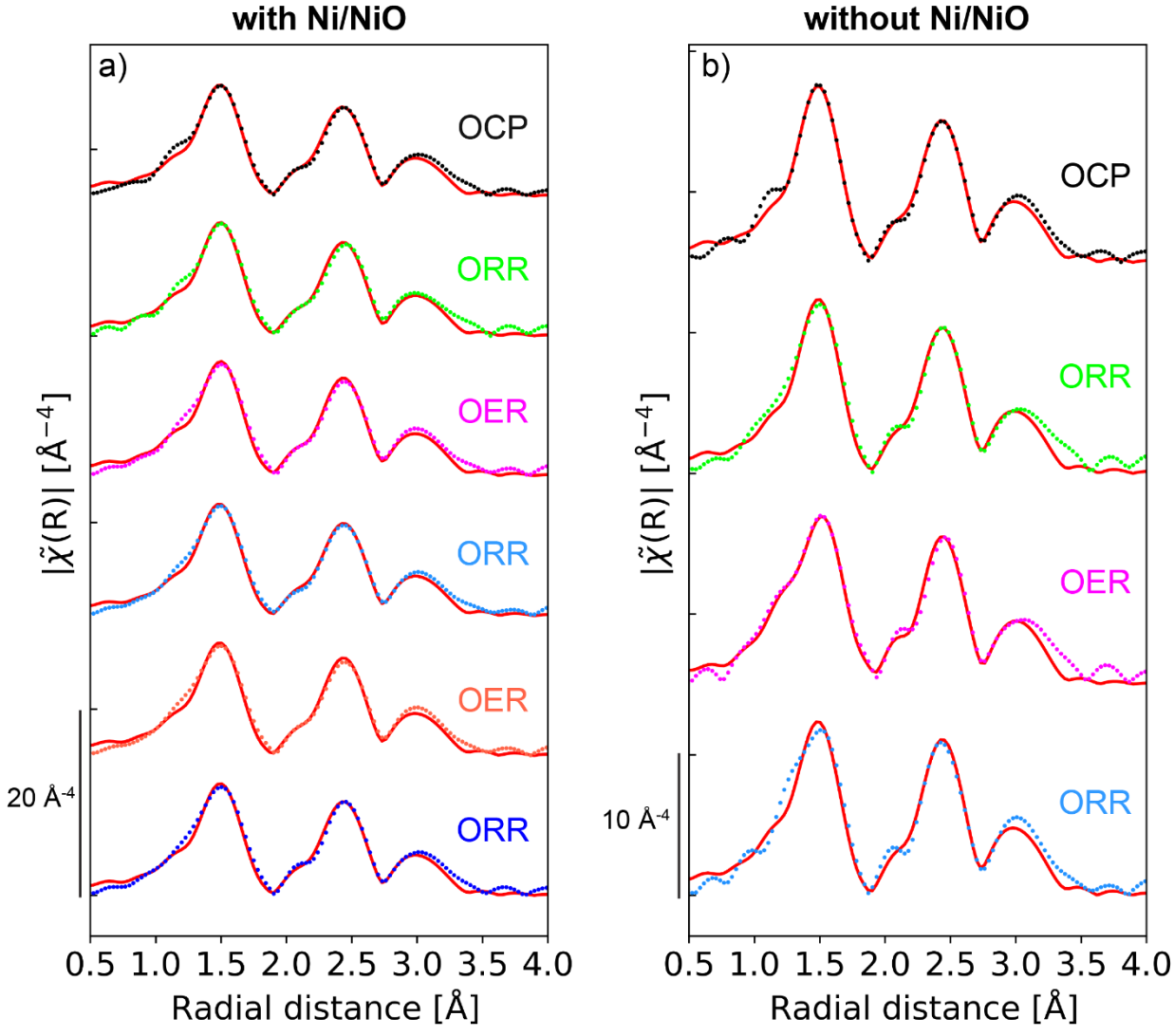

Figure A19 Magnitude of the Fourier transforms of the k^3-weighted experimental *operando* Mn K-edge EXAFS spectra and corresponding structural fits of the **(a)** GDE with Ni/NiO and **(b)** GDE without Ni/NiO, in OCP state, and at different ORR and OER conditions. The experimental data is marked by dots, while the fits, which are based on theoretical bonding paths generated by FEFF, are indicated by red solid lines. The fits were performed over the R-space range1.15-3.25 Å.

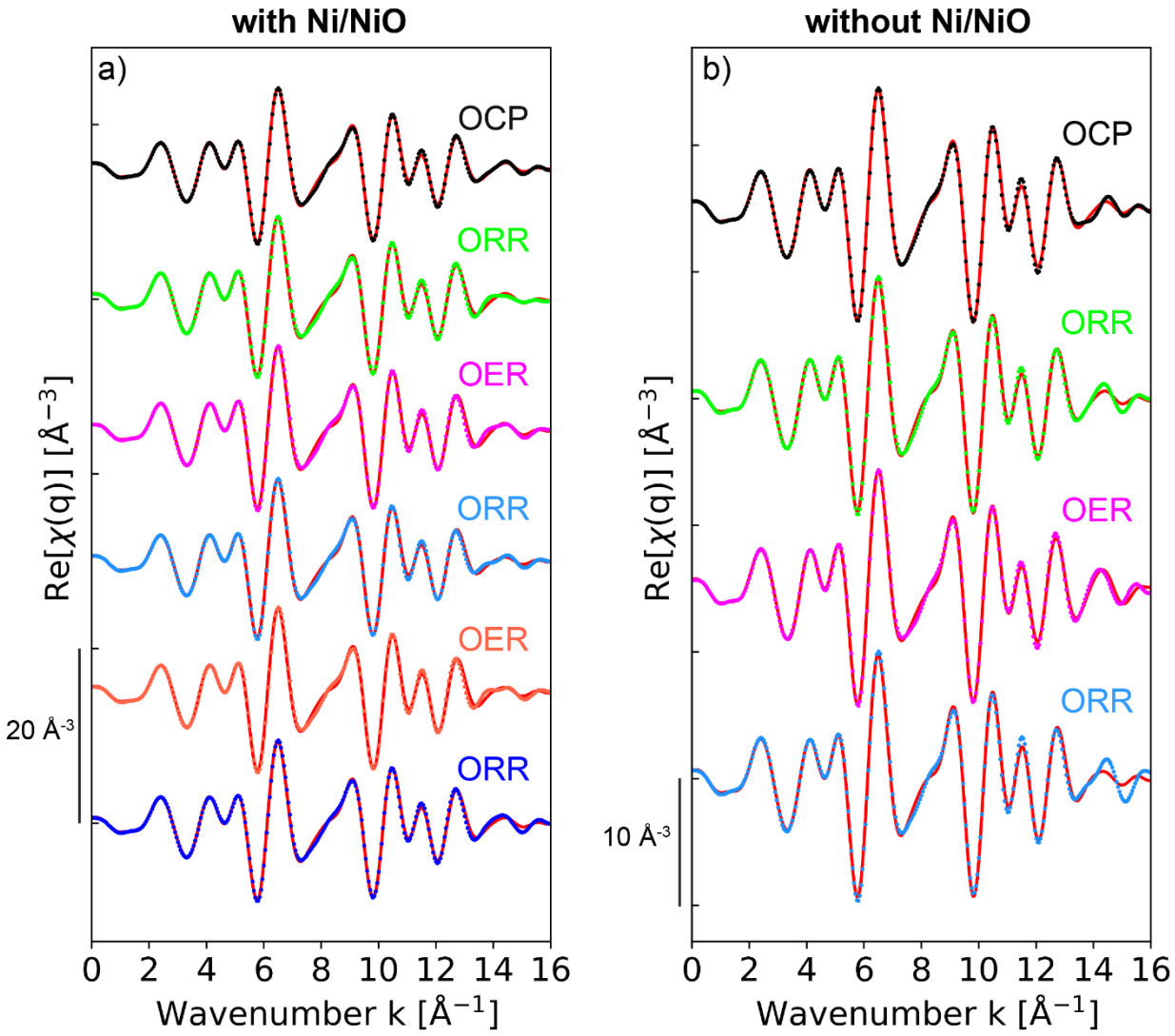

Figure A20: Real part of the inverse Fourier transforms of the k^3-weighted experimental *operando* Mn K-edge EXAFS spectra (q-space) and corresponding structural fits of the **(a)** GDE with Ni/NiO and **(b)** GDE without Ni/NiO, in OCP state, and at different ORR and OER conditions. The experimental data is marked by dots, while the fits, which are based on theoretical bonding paths generated by FEFF, are indicated by red solid lines. The fits were performed over the R-space range1.15-3.25 Å.

Table A4: Results of non-linear least-squares fittings for the EXAFS spectra shown in Figure A19 and Figure A20 for electrodes with- and without Ni/NiO, measured *in situ* at different electrochemical conditions. Fitting was performed for

the following ranges of wavenumber and radial distances: k = 2.3 - 15.3 $Å^{-1}$ and R = 1.25 - 3.25 Å. Constrained parameters are indicated in **bold**.

GDE without Ni/NiO

Condition	Path	R [Å]	CN	σ^2 [$Å^2$]	E_0 [eV]	R-factor*
OCP	Mn-O_{ads}	1.639 ± 0.016	**1.0**	0.005 ± 4e-4	6556.2 ± 0.3	0.002
	Mn-$O_{lattice}$	1.893 ± 0.002	7.6 ± 0.2			
	Mn-Mn_{edge}	2.875 ± 0.003	**4.9**	0.006 ± 2e-4		
	Mn-Mn_{corner}	3.436 ± 0.005	**3.7**			
ORR (1st)	Mn-O_{ads}	1.649 ± 0.022	**1.0**	0.006 ± 5e-4	6556.3 ± 0.3	0.004
	Mn-$O_{lattice}$	1.895 ± 0.003	7.7 ± 0.3			
	Mn-Mn_{edge}	2.876 ± 0.003	**4.9**	0.006 ± 2e-4		
	Mn-Mn_{corner}	3.438 ± 0.006	**3.7**			
OER (1st)	Mn-O_{ads}	1.777 ± 0.027	**1.0**	0.003 ± 6e-4	6557.0 ± 0.5	0.004
	Mn-$O_{lattice}$	1.906 ± 0.004	5.7 ± 0.5			
	Mn-Mn_{edge}	2.879 ± 0.004	**4.9**	0.006 ± 3e-4		
	Mn-Mn_{corner}	3.442 ± 0.008	**3.7**			
ORR (2nd)	Mn-O_{ads}	1.659 ± 0.034	**1.0**	0.006 ± 8e-4	6556.0 ± 0.4	0.007
	Mn-$O_{lattice}$	1.892 ± 0.004	8.2 ± 0.5			
	Mn-Mn_{edge}	2.873 ± 0.004	**4.9**	0.005 ± 3e-4		
	Mn-Mn_{corner}	3.433 ± 0.007	**3.7**			

GDE with Ni/NiO

Condition	Path	R [Å]	CN	σ^2 [$Å^2$]	E_0 [eV]	R-factor*
OCP	Mn-O_{ads}	1.655 ± 0.018	**1.0**	0.006 ± 4e-4	6556.1 ± 0.3	0.003
	Mn-$O_{lattice}$	1.894 ± 0.002	7.5 ± 0.3			
	Mn-Mn_{edge}	2.875 ± 0.003	**4.9**	0.006 ± 2e-4		
	Mn-Mn_{corner}	3.435 ± 0.005	**3.7**			
ORR (1st)	Mn-O_{ads}	1.662 ± 0.023	**1.0**	0.005 ± 0.001	6556.2 ± 0.3	0.004
	Mn-$O_{lattice}$	1.896 ± 0.003	7.6 ± 0.3			
	Mn-Mn_{edge}	2.878 ± 0.003	**4.9**	0.006 ± 3e-4		
	Mn-Mn_{corner}	3.436 ± 0.006	**3.7**			
OER (1st)	Mn-O_{ads}	1.669 ± 0.026	**1.0**	0.005 ± 0.001	6556.3 ± 0.3	0.004
	Mn-$O_{lattice}$	1.895 ± 0.003	7.6 ± 0.4			
	Mn-Mn_{edge}	2.874 ± 0.003	**4.9**	0.006 ± 3e-4		
	Mn-Mn_{corner}	3.434 ± 0.006	**3.7**			
ORR (2nd)	Mn-O_{ads}	1.649 ± 0.022	**1.0**	0.006 ± 0.001	6556.2 ± 0.3	0.003
	Mn-$O_{lattice}$	1.895 ± 0.003	7.8 ± 0.3			
	Mn-Mn_{edge}	2.877 ± 0.003	**4.9**	0.006 ± 2e-4		
	Mn-Mn_{corner}	3.436 ± 0.006	**3.7**			
OER (2nd)	Mn-O_{ads}	1.656 ± 0.026	**1.0**	0.006 ± 0.001	6556.3 ± 0.3	0.004
	Mn-$O_{lattice}$	1.894 ± 0.003	7.9 ± 0.4			
	Mn-Mn_{edge}	2.874 ± 0.003	**4.9**	0.006 ± 3e-4		
	Mn-Mn_{corner}	3.433 ± 0.006	**3.7**			
ORR (3rd)	Mn-O_{ads}	1.661 ± 0.023	**1.0**	0.006 ± 0.001	6556.2 ± 0.3	0.004
	Mn-$O_{lattice}$	1.896 ± 0.003	7.7 ± 0.3			
	Mn-Mn_{edge}	2.877 ± 0.003	**4.9**	0.006 ± 2e-4		
	Mn-Mn_{corner}	3.436 ± 0.006	**3.7**			

* Paths with similar adsorber-scatterer interactions (i.e. Mn-O_1 and Mn-O_2 or Mn-Mn_{edge} and Mn-Mn_{corner}) share the same mean squared relative displacements: $\sigma^2_{O_1\ \&\ O_2}$ and $\sigma^2_{Mn-Mn_{edge}\ \&\ Mn-Mn_{corner}}$, respectively. In all curve fitting processes,

the goodness of fit was estimated by calculating the averaged R-factor, defined as $\frac{\sum_{i=1}^{3}\{[\sum_{j=1}^{N}(k^i \cdot \chi_{data,j} - k^i \cdot \chi_{model,j})^2]/[\sum_{j=1}^{N}(k^i \cdot \chi_{data,j})^2]\}}{3}$.

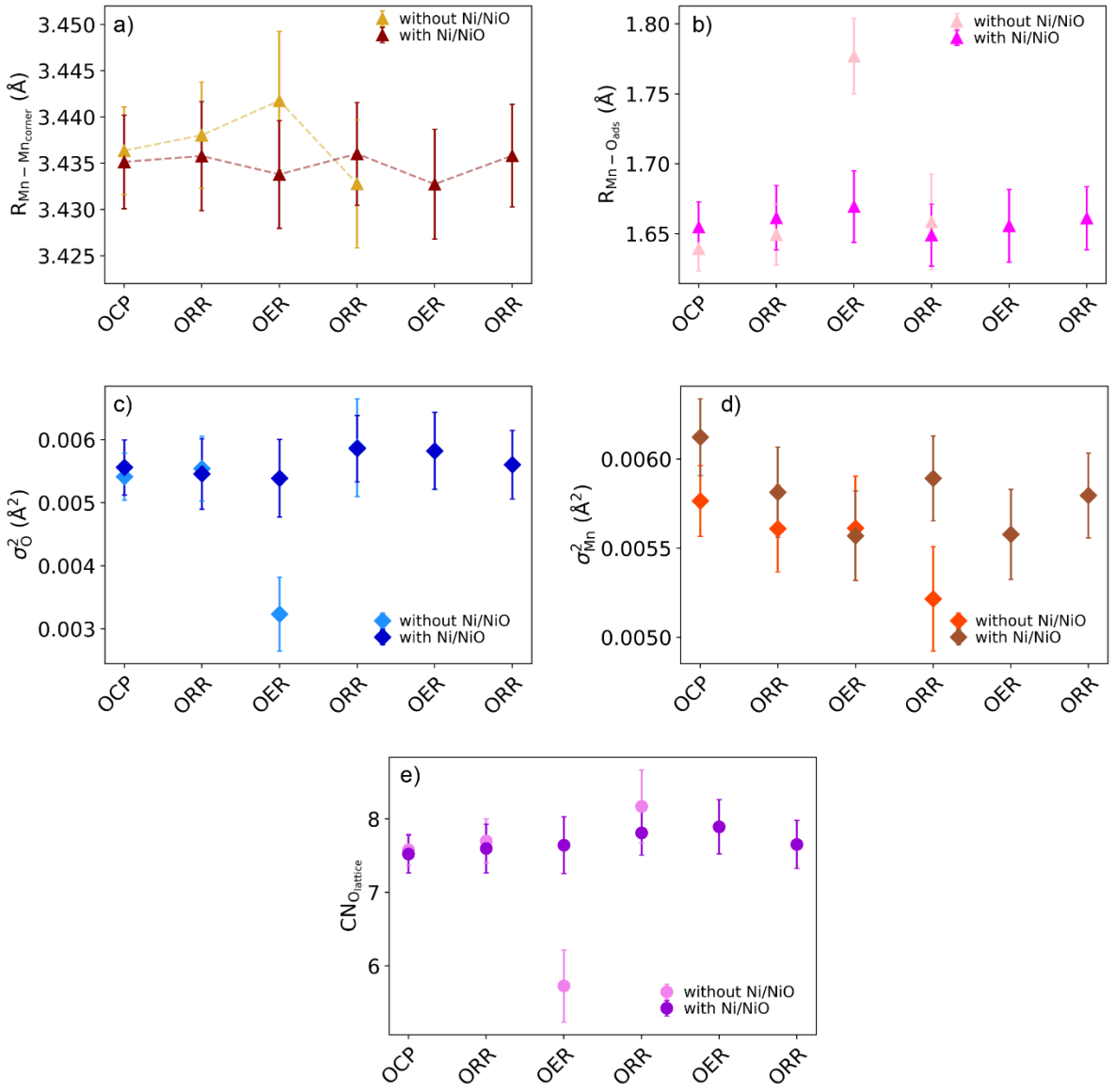

Figure A21: Experimental data and structural fitting results of in situ EXAFS spectra, measured under the indicated electrochemical conditions. **(a)** Experimentally determined interatomic distance R of Mn-Mn corner-sharing octahedra and **(b)** of the first manganese-oxygen shell Mn-O_{ads}; mean squared relative displacements (Debye-Waller factor) of the Mn-O **(c)** and Mn-Mn **(d)** interaction pairs; **(e)** coordination number of the second Mn-O shell ($CN_{O\ lattice}$). The error bars represent fit uncertainties calculated by the Artemis software.

References – Annex

The following has been added for the reference numbers included in Figure A12 and Table A1.

[1] J.F. Parker, J.S. Ko, D.R. Rolison, J.W. Long, Translating materials-level performance into device-relevant metrics for zinc-based batteries, Joule. 2 (2018) 2519–2527. https://doi.org/10.1016/j.joule.2018.11.007.

[2] Emanuele Marini, Jörissen Ludwig, Brimaud Sylvain, Rational design of durable and efficient gas diffusion bifunctional oxygen electrode for rechargeable metal-air batteries, J. Power Sources. 482 (2021).

[3] J. Fu, F.M. Hassan, J. Li, D.U. Lee, A.R. Ghannoum, G. Lui, Md.A. Hoque, Z. Chen, Flexible rechargeable zinc-air batteries through morphological emulation of human hair array, Adv. Mater. 28 (2016) 6421–6428. https://doi.org/10.1002/adma.201600762.

[4] J. Zhang, Z. Zhao, Z. Xia, L. Dai, A metal-free bifunctional electrocatalyst for oxygen reduction and oxygen evolution reactions, Nat. Nanotechnol. 10 (2015) 444–452. https://doi.org/10.1038/nnano.2015.48.

[5] Y. Li, M. Gong, Y. Liang, J. Feng, J.-E. Kim, H. Wang, G. Hong, B. Zhang, H. Dai, Advanced zinc-air batteries based on high-performance hybrid electrocatalysts, Nat. Commun. 4 (2013). https://doi.org/10.1038/ncomms2812.

[6] Y. Liu, S. Chen, X. Quan, H. Yu, H. Zhao, Y. Zhang, G. Chen, Boron and nitrogen vodoped nanodiamond as an efficient metal-free catalyst for oxygen reduction reaction, J. Phys. Chem. C. 117 (2013) 14992–14998. https://doi.org/10.1021/jp4044094.

[7] G. Du, X. Liu, Y. Zong, T.S.A. Hor, A. Yu, Z. Liu, Co_3O_4 nanoparticle-modified MnO_2 nanotube bifunctional oxygen cathode catalysts for rechargeable zinc–air batteries, Nanoscale. 5 (2013) 4657. https://doi.org/10.1039/c3nr00300k.

[8] M. Prabu, K. Ketpang, S. Shanmugam, Hierarchical nanostructured $NiCo_2O_4$ as an efficient bifunctional non-precious metal catalyst for rechargeable zinc–air batteries, Nanoscale. 6 (2014) 3173. https://doi.org/10.1039/c3nr05835b.

[9] Z. Chen, A. Yu, R. Ahmed, H. Wang, H. Li, Z. Chen, Manganese dioxide nanotube and nitrogen-doped carbon nanotube based composite bifunctional catalyst for rechargeable zinc-air battery, Electrochimica Acta. 69 (2012) 295–300. https://doi.org/10.1016/j.electacta.2012.03.001.

[10] Z. Chen, A. Yu, D. Higgins, H. Li, H. Wang, Z. Chen, Highly active and durable core–corona structured bifunctional catalyst for rechargeable metal–air battery application, Nano Lett. 12 (2012) 1946–1952. https://doi.org/10.1021/nl2044327.

[11] F.W.T. Goh, Z. Liu, X. Ge, Y. Zong, G. Du, T.S.A. Hor, Ag nanoparticle-modified MnO_2 nanorods catalyst for use as an air electrode in zinc–air battery, Electrochimica Acta. 114 (2013) 598–604. https://doi.org/10.1016/j.electacta.2013.10.116.

[12] M. Prabu, P. Ramakrishnan, S. Shanmugam, $CoMn_2O_4$ nanoparticles anchored on nitrogen-doped graphene nanosheets as bifunctional electrocatalyst for rechargeable zinc–air battery, Electrochem. Commun. 41 (2014) 59–63. https://doi.org/10.1016/j.elecom.2014.01.027.

[13] D.U. Lee, J.-Y. Choi, K. Feng, H.W. Park, Z. Chen, Advanced extremely durable 3D bifunctional air electrodes for rechargeable zinc-air batteries, Adv. Energy Mater. 4 (2014) 1301389. https://doi.org/10.1002/aenm.201301389.

[14] B. Li, X. Ge, F.W.T. Goh, T.S.A. Hor, D. Geng, G. Du, Z. Liu, J. Zhang, X. Liu, Y. Zong, Co_3O_4 nanoparticles decorated carbon nanofiber mat as binder-free air-cathode for high performance rechargeable zinc-air batteries, Nanoscale. 7 (2015) 1830–1838. https://doi.org/10.1039/C4NR05988C.

[15] F. Meng, H. Zhong, D. Bao, J. Yan, X. Zhang, In situ coupling of strung Co_4N and intertwined N–C fibers toward free-standing bifunctional cathode for robust, efficient, and flexible Zn–air batteries, J. Am. Chem. Soc. 138 (2016) 10226–10231. https://doi.org/10.1021/jacs.6b05046.

[16] Z. Cui, G. Fu, Y. Li, J.B. Goodenough, Ni_3FeN-supported Fe_3Pt intermetallic nanoalloy as a high-performance bifunctional catalyst for metal-air batteries, Angew. Chem. Int. Ed. 56 (2017) 9901–9905. https://doi.org/10.1002/anie.201705778.
[17] C. Meng, T. Ling, T.-Y. Ma, H. Wang, Z. Hu, Y. Zhou, J. Mao, X.-W. Du, M. Jaroniec, S.-Z. Qiao, Atomically and electronically coupled Pt and CoO hybrid nanocatalysts for enhanced electrocatalytic performance, Adv. Mater. 29 (2017) 1604607. https://doi.org/10.1002/adma.201604607.
[18] M.G. Park, D.U. Lee, M.H. Seo, Z.P. Cano, Z. Chen, 3D ordered mesoporous bifunctional oxygen catalyst for electrically rechargeable zinc-air batteries, Small. 12 (2016) 2707–2714. https://doi.org/10.1002/smll.201600051.
[19] Z. Song, X. Han, Y. Deng, N. Zhao, W. Hu, C. Zhong, Clarifying the controversial catalytic performance of $Co(OH)_2$ and Co_3O_4 for oxygen reduction/evolution reactions toward efficient Zn–air batteries, ACS Appl. Mater. Interfaces. 9 (2017) 22694–22703. https://doi.org/10.1021/acsami.7b05395.
[20] Y. Bu, O. Gwon, G. Nam, H. Jang, S. Kim, Q. Zhong, J. Cho, G. Kim, A highly efficient and robust cation ordered perovskite oxide as a bifunctional catalyst for rechargeable zinc-air batteries, ACS Nano. 11 (2017) 11594–11601. https://doi.org/10.1021/acsnano.7b06595.
[21] E. Davari, A.D. Johnson, A. Mittal, M. Xiong, D.G. Ivey, Manganese-cobalt mixed oxide film as a bifunctional catalyst for rechargeable zinc-air batteries, Electrochimica Acta. 211 (2016) 735–743. https://doi.org/10.1016/j.electacta.2016.06.085.
[22] C. Guo, Y. Zheng, J. Ran, F. Xie, M. Jaroniec, S.-Z. Qiao, Engineering high-energy interfacial structures for high-performance oxygen-involving electrocatalysis, Angew. Chem. Int. Ed. 56 (2017) 8539–8543. https://doi.org/10.1002/anie.201701531.
[23] Y. Cheng, S. Dou, J.-P. Veder, S. Wang, M. Saunders, S.P. Jiang, Efficient and durable bifunctional oxygen catalysts based on $NiFeO@MnO_x$ core–shell structures for rechargeable Zn–air batteries, ACS Appl. Mater. Interfaces. 9 (2017) 8121–8133. https://doi.org/10.1021/acsami.6b16180.
[24] J. Park, M. Risch, G. Nam, M. Park, T.J. Shin, S. Park, M.G. Kim, Y. Shao-Horn, J. Cho, Single crystalline pyrochlore nanoparticles with metallic conduction as efficient bi-functional oxygen electrocatalysts for Zn–air batteries, Energy Environ. Sci. 10 (2017) 129–136. https://doi.org/10.1039/C6EE03046G.
[25] J. Park, M. Park, G. Nam, M.G. Kim, J. Cho, Unveiling the catalytic origin of nanocrystalline yttrium ruthenate pyrochlore as a bifunctional electrocatalyst for Zn–air batteries, Nano Lett. 17 (2017) 3974–3981. https://doi.org/10.1021/acs.nanolett.7b01812.
[26] L.-N. Han, L.-B. Lv, Q.-C. Zhu, X. Wei, X.-H. Li, J.-S. Chen, Ultra-durable two-electrode Zn–air secondary batteries based on bifunctional titania nanocatalysts: a Co^{2+} dopant boosts the electrochemical activity, J. Mater. Chem. A. 4 (2016) 7841–7847. https://doi.org/10.1039/C6TA02143C.
[27] H.-F. Wang, C. Tang, B. Wang, B.-Q. Li, Q. Zhang, Bifunctional transition metal hydroxysulfides: room-temperature sulfurization and their applications in Zn-air batteries, Adv. Mater. 29 (2017) 1702327. https://doi.org/10.1002/adma.201702327.
[28] A. Sumboja, J. Chen, Y. Zong, P.S. Lee, Z. Liu, NiMn layered double hydroxides as efficient electrocatalysts for the oxygen evolution reaction and their application in rechargeable Zn–air batteries, Nanoscale. 9 (2017) 774–780. https://doi.org/10.1039/C6NR08870H.
[29] J. Yin, Y. Li, F. Lv, Q. Fan, Y.-Q. Zhao, Q. Zhang, W. Wang, F. Cheng, P. Xi, S. Guo, NiO/CoN Porous nanowires as efficient bifunctional catalysts for Zn–air batteries, ACS Nano. 11 (2017) 2275–2283. https://doi.org/10.1021/acsnano.7b00417.
[30] G. Fu, Z. Cui, Y. Chen, L. Xu, Y. Tang, J.B. Goodenough, Hierarchically mesoporous nickel-iron nitride as a cost-efficient and highly durable electrocatalyst for Zn-air battery, Nano Energy. 39 (2017) 77–85. https://doi.org/10.1016/j.nanoen.2017.06.029.

[31] B. Li, D. Geng, X.S. Lee, X. Ge, J. Chai, Z. Wang, J. Zhang, Z. Liu, T.S.A. Hor, Y. Zong, Eggplant-derived microporous carbon sheets: towards mass production of efficient bifunctional oxygen electrocatalysts at low cost for rechargeable Zn–air batteries, Chem. Commun. 51 (2015) 8841–8844. https://doi.org/10.1039/C5CC01999K.
[32] L. Hadidi, E. Davari, M. Iqbal, T.K. Purkait, D.G. Ivey, J.G.C. Veinot, Spherical nitrogen-doped hollow mesoporous carbon as an efficient bifunctional electrocatalyst for Zn–air batteries, Nanoscale. 7 (2015) 20547–20556. https://doi.org/10.1039/C5NR06028A.
[33] Y. Qian, Z. Hu, X. Ge, S. Yang, Y. Peng, Z. Kang, Z. Liu, J.Y. Lee, D. Zhao, A metal-free ORR/OER bifunctional electrocatalyst derived from metal-organic frameworks for rechargeable Zn-Air batteries, Carbon. 111 (2017) 641–650. https://doi.org/10.1016/j.carbon.2016.10.046.
[34] Z. Pei, H. Li, Y. Huang, Q. Xue, Y. Huang, M. Zhu, Z. Wang, C. Zhi, Texturing in situ: N,S-enriched hierarchically porous carbon as a highly active reversible oxygen electrocatalyst, Energy Environ. Sci. 10 (2017) 742–749. https://doi.org/10.1039/C6EE03265F.
[35] Z. Guo, C. Li, W. Li, H. Guo, X. Su, P. He, Y. Wang, Y. Xia, Ruthenium oxide coated ordered mesoporous carbon nanofiber arrays: a highly bifunctional oxygen electrocatalyst for rechargeable Zn–air batteries, J. Mater. Chem. A. 4 (2016) 6282–6289. https://doi.org/10.1039/C6TA02030E.
[36] N. Xu, Y. Liu, X. Zhang, X. Li, A. Li, J. Qiao, J. Zhang, Self-assembly formation of bi-functional Co_3O_4/MnO_2-CNTs hybrid catalysts for achieving both high energy/power density and cyclic ability of rechargeable zinc-air battery, Sci. Rep. 6 (2016). https://doi.org/10.1038/srep33590.
[37] Lei Wan, Peican Wang, Yuqun Lin, Baoguo Wang, Janus-typed integrated bifunctional air electrode with MnO_x-NiFe LDH/Ni foam for rechargeable zinc-air batteries, J. Electrochem. Soc. 166 (2019) A3409–A3415.
[38] N. Xu, J. Qiao, X. Zhang, C. Ma, S. Jian, Y. Liu, P. Pei, Morphology controlled $La_2O_3/Co_3O_4/MnO_2$–CNTs hybrid nanocomposites with durable bi-functional air electrode in high-performance zinc–air energy storage, Appl. Energy. 175 (2016) 495–504. https://doi.org/10.1016/j.apenergy.2016.04.036.
[39] Q. Wang, L. Shang, R. Shi, X. Zhang, G.I.N. Waterhouse, L.-Z. Wu, C.-H. Tung, T. Zhang, 3D carbon nanoframe scaffold-immobilized Ni_3FeN nanoparticle electrocatalysts for rechargeable zinc-air batteries' cathodes, Nano Energy. 40 (2017) 382–389. https://doi.org/10.1016/j.nanoen.2017.08.040.
[40] Z. Wang, S. Xiao, Y. An, X. Long, X. Zheng, X. Lu, Y. Tong, S. Yang, $Co(II)_{1-x}Co(0)_{x/3}Mn(III)_{2x/3}S$ nanoparticles supported on B/N-codoped mesoporous nanocarbon as a bifunctional electrocatalyst of oxygen reduction/evolution for high-performance zinc-air batteries, ACS Appl. Mater. Interfaces. 8 (2016) 13348–13359. https://doi.org/10.1021/acsami.5b12803.
[41] G. Fu, J. Wang, Y. Chen, Y. Liu, Y. Tang, J.B. Goodenough, J.-M. Lee, Exploring indium-based ternary thiospinel as conceivable high-potential air-cathode for rechargeable Zn-air batteries, Adv. Energy Mater. 8 (2018) 1802263. https://doi.org/10.1002/aenm.201802263.
[42] S. Müller, K. Striebel, O. Haas, $La_{0.6}Ca_{0.4}CoO_3$: a stable and powerful catalyst for bifunctional air electrodes, Electrochimica Acta. 39 (1994) 1661–1668.
[43] N. Bogolowski, O. Ngaleu, M. Sakthivel, J.-F. Drillet, Long-life bifunctional $BaSrCoFeO_3$/C gas diffusion electrode, Carbon. 119 (2017) 511–518. https://doi.org/10.1016/j.carbon.2017.04.051.

Table of Figures

Figure 1: **(a)** Discharge time vs. power rate comparison of various electrical energy storage technologies. **(b)** Comparison of specific power and energy densities for various secondary battery systems currently being studied for grid storage applications. Figures taken from [3]. 10
Figure 2: Comparison between different types of secondary battery according to their theoretical- and practical specific energy density. Data taken from [7,22]. 11
Figure 3: Schematic representation of the main components of a zinc air cell under discharge, adapted from[38,39]. 17
Figure 4: Schematics of the different resistances that affect the operating cell voltage. Taken from[7]. 19
Figure 5: Illustration of the different electrode regimes, from activation (kinetics) to mass transport control process. Taken from [40]. 21
Figure 6: Design strategies of the bifunctional gas diffusion electrodes. Taken from[47]. 22
Figure 7: Overview of published bifunctional GDE performances and stabilities. The number of stable load cycles is plotted versus the charge-discharge loads (j x t, areal capacity), and for each scatter x-y coordinates are tabulated in Annex Table A1 together with references. The color code, namely red, orange and blue colors indicates $\Delta E > 0.9$ V, 0.9 V $\geqslant \Delta E \geqslant 0.8$, and $\Delta E < 0.8$ V, respectively, as qualitative descriptor for the efficiency (see text for details). The vertical dashed line crossing the x-axis at 11.7 mAh·cm^{-2} indicates the threshold metric developed by Parker and co-workers[70] to meet the minimum technologically relevant value of 100 Wh·kg^{-1} for ZAB. 25
Figure 8: a) Different models proposed by Damjanovic et al.[79], Wroblowa et al.[80], Appleby and Savy[81], Zurilla et al.[82], and Bagotskii et al.[83], for the oxygen reduction reactions. The subscript "a" stands for species adsorbed on the electrode surface; "*" in the proximity of the surface and "b" in the bulk solution. b) Reaction scheme for the ORR in alkaline electrolyte[84]. Subscripts "sa" and "wa" refer to species that are strongly and weakly adsorbed to the electrode surface, respectively. Taken from [74]. 28
Figure 9: Free energy diagram for the four-electron associative ORR on Pt(111) for three different electrode potential vs. SHE. Taken from[86]. 30
Figure 10: Scaling relationships for the *OOH and *O binding energies for the Pt(111) surface of different transition metals (black circles) with *OH chemisorption energy as descriptor. The two solid black lines represent binding energies ΔG_{OOH} and ΔG_O as a function of ΔG_{OH}. (b) Limiting potentials for individual steps including the strongly bound*OH region (solid blue line) and weakly bound*OOH region (solid green line) for the 4e-pathway. Taken from[86]. 31
Figure 11: Schematic of the potential energy diagrams for the electrochemical oxide path described in Eq. 54-56 where the rate determining step is the desorption of oxygen from the metal surface. Taken from[100]. 33
Figure 12: (a) Two pyramids that represent the best possible ORR- (blue) and OER (green) potentials for the determining step as a function of function reaction free energies ΔG_1 and ΔG_3. **(b)** Same plot shown in (a) but including a red plane representing the restriction imposed by the constant offset of 3.2 eV between ΔG_1 and ΔG_3. **(c)** Two-dimensional cross-section of the two pyramids at the intersection with the red plane. This forms two volcanos, one for the ORR (blue) and the other for the OER (green). The black dotted line visualizes the theoretical electrode potential of 1.23 V for both ORR and OER processes. Adapted from[110]. 35
Figure 13: Schematic of the X-ray absorption measurement in transmission configuration. Taken from[160]. 46
Figure 14: Acquired XAS spectrum at the Mn-K edge before **(a)** and after **(b)** normalization (Software: Athena[161]). 47
Figure 15: (a) 3D crystal structure of the electrocatalyst material used to create the model of the X-ray interaction paths (Software: VESTA[163]) and **(b)** example of the fit of the experimental k^2-weighted EXAFS oscillations $\chi(k)$ (top, blue) with the model (blue), as well as its Fourier transform components (bottom). Software: Artemis[164]. 48
Figure 16: Sketch of the hydrodynamic flow over the rotating disk electrode tip in solution. Taken from [168]. 50
Figure 17: Schematic of the working principle of the RRDE technique. Adapted from[172]. 52

Figure 18: Schematic of the electrochemical cell setup employed to evaluate performance and stability of the GDEs prepared in this study. 54
Figure 19: Schematics of the electrochemical methods used to test the **(a)** ORR (yellow) and OER (blue) activity and **(b)** the stability during cycling at application relevant conditions of the O_2-electrode. 56
Figure 20: (a) Sketch of the *in situ* XAS setup, with the GDE side facing the incoming X-ray beam of intensity I_0. Upon transmission through the entire sample, consisting of the GDE, the 6 M KOH electrolyte and the Zn electrode, part of the X-rays is absorbed by the different materials and the resulting X-ray intensity is I_1. **(b)** Top view of the GDE and Zn electrode assemblies. **(c)** Schematic of the expanded cross-section of the electrodes/cell assembly. 57
Figure 21: Digital photograph of **(a)** the XAFS beamline at the Synchrotron ELETTRA (Trieste, IT) equipped with our electrochemical setup for *operando* XAS measurements. **(b)** Magnification of the XAS electrochemical cell used. 58
Figure 22: Images acquired *in situ* during the synthesis of the α-MnO_2 following the chemical reaction of Eq. 1. Taken from[179]. 60
Figure 23: Schematic (visualized with VESTA[163]) displaying the 2x2 tunnel structure of the α-MnO_2 crystal lattice. 60
Figure 24: XRD powder pattern of MnO_2 prepared by microwave-assisted hydrothermal synthesis. 61
Figure 25: Representative scanning electron micrograph of the as-synthetized manganese dioxide α-MnO_2. Scale bar: 1 µm. 62
Figure 26: (a) XRD pattern and **(b)** representative SEM image of the synthetized δ-MnO_2 phase. Scale bar: 1 µm. 63
Figure 27: Schematic representation of the transformation mechanism of manganese dioxide proposed by Birgisson et al. Taken from[186]. 64
Figure 28: N_2-soprtion isotherms of the as-synthetized manganese dioxide α-MnO_2. 65
Figure 29: Cyclic voltammograms at 5 $mV \cdot s^{-1}$ in in N_2-saturated 0.1 KOH of α-MnO_2/C catalyst composite mixture. 66
Figure 30: Cyclic voltammogram at 5 $mV \cdot s^{-1}$ in in N_2-saturated 0.1 KOH of α-MnO_2/C averaged over three catalyst layers. The arrows and the shadow area represent the potential sweep direction and the confidence interval, respectively. 66
Figure 31: Cyclic voltammogram at 5 $mV \cdot s^{-1}$ in O_2-saturated 0.1 KOH at 1600 rpm. 68
Figure 32: N_2-background corrected cyclic voltammogram of MnO_2/C mixture in O_2 saturated 0.1 M KOH. The horizontal red and blue dashed lines represent the theoretical current densities for the $2e^-$ and $4e^-$ ORR processes at 1600 rpm, respectively. 70
Figure 33: (a) N_2-background corrected cyclic voltammograms of MnO_2/C in O_2-saturated 0.1 M KOH at different electrode rotation rates. **(b)** Koutecký-Levich plots calculated at 0.8 V vs. RHE. The red and blue solid lines represent the theoretical K-L plots for the $2e^-$ and $4e^-$ ORR processes, respectively. 71
Figure 34: (a) Ring current as a function of (disk) electrode potential. **(b)** Measured number of transferred electrons n (left) and hydrogen peroxide $HO2^-$ yield (right) vs. electrode potential. 72
Figure 35: Potential dependence of the ORR activity in terms of kinetic current density. The black dashed- and solid lines represent the cathodic and anodic sweep direction, respectively. Potential sweep rate: 5 $mV \cdot sec^{-1}$. O_2-saturated 0.1 M KOH electrolyte. Rotation rate: 1600 rpm. 73
Figure 36: Evolution of mesoscopic morphology of binary electrocatalysts. Set of SEM images representative of the morphological evolution of the binary composites catalyst materials $(C)_{100-x}(MnO_2)_x$ (top row), $(Ni/NiO)_{100-x}(MnO_2)_x$ (middle row), $(Ni/NiO)_{100-x}(C)_x$ (bottom row) as a function of nominal composition. Scale bar: 2 µm. 76
Figure 37: Cyclic voltammograms at 5 $mV \cdot s^{-1}$ in O_2 **(a)** and in N_2 **(b)** saturated 0.1 KOH. In order to differentiate the sweep directions of the electrode potential, we indicated the voltammograms with a dashed line, representing the scan from low to high potential (positive-going potential scan), and with a solid line for the opposite scan direction, respectively. 77
Figure 38: Average number of transferred electrons (n) and hydrogen peroxide yield (χ HO_2^-) for $(C)_{100-x}(MnO_2)_x$, $(C)_{100-x}(Ni/NiO)_x$, $(Ni/NiO)_{100-x}(MnO_2)_x$. 78

Figure 39: (a) Potential dependence of the electrocatalytic activity towards the ORR for three selected binary composites, as labelled in the figure. **(b)** ORR Tafel slopes for $(C)_{50}(MnO_2)_{50}$, $(Ni/NiO)_{75}(C)_{25}$, and $(Ni/NiO)_{75}(MnO_2)_{25}$. **(c)** Compositional dependence of the overpotential at the kinetic current density j_k = -1 mA·cm^{-2} for the ORR. All currents are normalized with the geometrical area of the electrode and all experiments were carried out in O_2-saturated 0.1 M KOH at 5 mV·s^{-1} and at 1600 rpm. 80
Figure 40: (a) Polarization curves and kinetic current density for the ORR on C at different rotation rates (top) and the corresponding number of transferred electrons determined with the Koutecký-Levich equation (bottom). **(b)** Number of transferred electrons for $(C)_{100-x}(MnO_2)_x$. 82
Figure 41: (a) Potential dependence of the electrocatalytic activity towards the OER for three selected binary composites, as labelled in the figure, **(b)** compositional dependence of the current densities for the OER at η = 470 mV for the same materials as in (b). All currents are normalized with the geometrical area of the electrode and all experiments were carried out in O_2-saturated 0.1 M KOH at 5 mV·s^{-1} and at 1600 rpm. 84
Figure 42: Compositional optimisation of a bifunctional electrocatalyst. Kinetic current densities for the ORR **(a)** and polarization curves for the OER **(b)** of ternary composites with different C : MnO_2 : Ni/NiO ratios as indicated in the figure. Same experimental conditions as in the binary composites testing. ... 85
Figure 43: Transfer of performances of binary composites to ternary electrocatalyst. Plots **(a)** and **(b)** compares polarization curves for the ORR and OER, respectively, on the ternary $(C)_{33}(MnO_2)_{33}(Ni/NiO)_{33}$ and the binary composites $(C)_{50}(MnO_2)_{50}$, $(Ni/NiO)_{50}(C)_{50}$, $(Ni/NiO)_{50}(MnO_2)_{50}$. O_2-saturated 0.1 M KOH, v = 5 mV·s^{-1}, 1600 rpm. 86
Figure 44: Stability of the catalyst materials upon successive galvanostatic charge (ORR) / discharge (OER) at 1 mA·cm^{-2} load in O_2-saturated 0.1 M KOH (1600 rpm). The stability test totalizes 100 cycles where each charge/discharge cycle consists in a 5 min discharge followed by 5 min charge. 88
Figure 45: Kinetic current densities for the ORR **(a)** and corresponding **(b)** Tafel slopes of binary and ternary composites made of commercial MnO_2 and synthetized α-MnO_2. **(c)** Hydrogen peroxide yields and **(d)** OER polarization curves of the same mixtures of figure (a) and (b). O_2-saturated 0.1 M KOH, v = 5 mV·s^{-1}, 1600 rpm. 89
Figure 46: Sketch of the electrochemical cell setup employed to evaluate performance and stability of the GDEs prepared in this study and representative SEM imaging of the AL and the GDL (scale bars are 200 nm and 10 µm, respectively). The thickness of the GDE is 380 µm (GDL: 280 µm and AL: 100 µm). 92
Figure 47: PTFE loading dependence on the GDEs performances that embed $(C)_{33}(MnO_2)_{33}(Ni/NiO)_{33}$ catalyst material. ORR **(a)** and OER **(b)** overpotentials as a function of the galvanostatic current densities applied for GDEs 1-4 (10 min per current density step). Change in the overpotentials upon 100 successive galvanostatic charge (OER) and discharge (ORR) load cycles for GDEs 5-7 **(c)** and GDEs 7-9 **(d)**. Each load cycle consists in a 2 h discharge followed by 2 h charge both at 10 mA·cm^{-2}. For the sake of comparison, results with a GDE using benchmark Pt black and IrO_2 catalysts also shows excellent stability but a lower energy efficiency (45 %) than GDE 8 (55 %). Ambient atmospheric conditions, no CO_2 trap. See text for details. 96
Figure 48: Overview of published bifunctional air GDE performances and stabilities. The number of stable load cycles is plotted versus the charge-discharge loads (j x t, areal capacity), and for each scatter x-y coordinates are tabulated in the Annex together with references (Table A1). The color code, namely red, orange and blue colors indicates ΔE > 0.9 V, 0.9 V ⩾ ΔE ⩾ 0.8, and ΔE < 0.8 V, respectively, as qualitative descriptor for the efficiency (see text for details). The vertical dashed line crossing the x-axis at 11.7 mAh·cm^{-2} indicates the threshold metric developed by Parker and co-workers[70] to meet the minimum technologically relevant value of 100 Wh·kg^{-1} for ZAB. The most performant GDE prepared in this work, GDE8, is represented by a star. 97
Figure 49: (a) ORR polarization curves and **(b)** chronovoltammetry tests of the O_2 electrodes manufactured with the commercial catalyst mixture (HILABS, red) and with the α-MnO_2 synthetized in-house (ZSW, blue). 100
Figure 50: (a) Charge and discharge potentials upon 100 successive galvanostatic charge (OER) and discharge (ORR) load cycles. Each load cycle consists in a 2 h discharge followed by 2 h charge both at 10

$mA \cdot cm^{-2}$. Ambient atmospheric condition, no CO_2 trap. The black dashed line indicates the equilibrium potential of the water splitting (OER) and oxygen reduction reaction (ORR) at standard conditions, $E^0_{O2/OH-}$. Electrochemical impedance spectroscopy (EIS) analysis was also conducted at the 1st, 10th, 30th, 60th and 100th cycle during the discharge interval, as indicated by the black stars. 104
Figure 51: Changes in the Nyquist diagram for EIS of the GDE displayed in Figure 50, as a function of cycle number (scatters: experimental data points, solid lines: fitted spectrum). The insert provides a magnification of the high frequency region. 105
Figure 52: Representative scanning electron micrographs of the GDE in the pristine state (Pristine) and after different load cycle numbers, as indicated in the figure. Scale bar: 100 µm. 107
Figure 53: Fitted parameters R_1, R_2, (left-hand y-axis) from the equivalent circuit depicted in Figure A14 and percentage of cracks (projected surface area, right-hand y-axis) as a function of cycle number obtained from Nyquist plots and quantitative analysis of SEM images, respectively. 108
Figure 54: F 1s (left), C 1s / K 2p (center) and O 1s (right) core level XPS spectra for (from top to bottom) pristine GDE, GDE at the end of life, GDE having only experience ORR overpotentials and GDE having only experienced OER overpotentials, as indicated in the figure, see text for details. For a given spectral region, the intensity scale is identical for the four GDE samples investigated. Experimental data (open scatters), background (green solid traces), deconvoluted components (black solid traces and pink solid traces for K 2p) and fitted spectra (red solid traces). Enlargement of the C 1s regions are provided in the Annex, Figure A16. 112
Figure 55: Mn 2p (left) and Ni 2p (right) core level XPS spectra for (from top to bottom) pristine GDE, GDE at the end of life, GDE having only experience ORR overpotentials and GDE having only experienced OER overpotentials, see text for details. 117
Figure 56: (a) Chronoamperometry during in situ XAS measurements at ORR relevant electrochemical conditions ($j = -5\ mA \cdot cm^{-2}$) before and after oxygen starvation. **(b)** Comparison of Mn K-edge XANES collected on the GDE in pristine state (blue) and on GDE after *in situ* exposure to ORR before (red) and after oxygen starvation (green). The figure also includes the reference XANES of Mn_3O_4 (black) and MnO_2 pyrolusite (orange) powder. 118
Figure 57: (a) Schematic (visualized with VESTA[163]) displaying the α-MnO_2 crystal lattice. **(b-d)** Experimental data resulting from fitting of EXAFS spectra measured under the aforementioned current load conditions (see Experimental Methods chapter): **(b)** Mn K-edge energy E_0, **(c)** radial distances R of Mn-Mn edge-sharing octahedra $R_{(Mn\text{-}Mn)edge}$ and **(d)** Mn-$O_{lattice}$**.** Error bars represent the fit uncertainties, as delivered by the ARTEMIS software[164]. 121
Figure 58: Schematic representation (visualized with VESTA[163]) displaying the bulk and (110) surface structure of α-MnO_2, where the Mn ions are represented in blue, the oxygen in red and K^+ ions in purple and representation of the main underlying hypothesis for the differential surface analysis (see text for details). 125
Figure 59: **(a)** Differential EXAFS spectra in the R-space (scatters) and curve fitting (solid line) of the Mn K-edge for GDE without- (left) and with Ni/NiO nanoparticles (right) at OCP and under current loads as indicated in the figure. **(b)** Mn-Mn interatomic distance for edge-sharing and corner-sharing MnO_6 octahedra (top) and edge energy E_0 (bottom) as a function of applied electrochemical condition as indicated in the figure. 127
Figure 60: Determination of the α-MnO_2 surface oxidation state at ORR and OER conditions using the Mn K-edge energy shift of the reference Mn compounds. See text for details. 131
Figure 61: Mapping of the different degradation processes occurring at the GDE under successive charge/discharge current loads, and of their interactions/relationships. See text for details. 132

Table of Tables

Table 1: Elemental analysis (in wt. %) of α-MnO_2 determined via ICP-OES technique. 61
Table 2: Catalyst materials and PTFE loadings in the AL, and PTFE loading in the GDL for 9 GDEs prepared with $(C)_{33}(MnO2)_{33}(Ni/NiO)_{33}$ catalyst material. Compositional characteristics of a GDE prepared with commercial reference materials Pt and IrO_2. 93
Table 3: Values of the resistances for the fitted equivalent circuit displayed in Figure A14 (see text for details). 105
Table 4: Binding energies (B.E), normalized areas and full width at half maximum (FWHM) for the deconvoluted components in the C 1s, K 2p, O 1s, and F 1s XPS spectra displayed in Figure 54. In the case of K 2p, the B.E. of the 2p3/2 component is given and the spin-orbit splitting was fixed at 2.8 eV. .. 114
Table 5: Results of the non-linear least-squares curve-fittings for the differential EXAFS spectra shown in Figure 59a measured under different electrochemical conditions. To perform the analysis, the amplitude reduction factor (S_0^2), as well as the mean relative squared displacement (σ^2) were keep fixed at 0.8 and at $5 \cdot 10^{-4}$ $Å^2$, respectively. 128

Curriculum Vitae

Removed for privacy protection reasons

Removed for privacy protection reasons

List of Publications

1. E. Marini, L. Jörissen, S. Brimaud, Rational design of a low-cost, durable and efficient bifunctional oxygen electrode for rechargeable metal-air batteries, J. Power Sources. 482 (2021) 228900. https://doi.org/10.1016/j.jpowsour.2020.228900.
2. M. Zanini, C. Marschelke, S. E. Anachkov, E. Marini, A. Synytska, L. Isa, Universal emulsion stabilization from the arrested adsorption of rough particles at liquid-liquid interfaces, Nature communications. 8 (2017) 15701. https://doi.org/10.1038/ncomms15701
3. S. Ni, E. Marini, I. Buttinoni, H. Wolf, L. Isa. Hybrid colloidal microswimmers through sequential capillary assembly, Soft matter. 13 (2017) 4252–4259. https://doi.org/10.1039/C7SM00443E.
4. M. Zanini, C. P. Hsu, T. Magrini, E. Marini, L. Isa, Fabrication of rough colloids by heteroaggregation. Colloids and Surfaces A: Physicochemical and Engineering Aspects, 532 (2017) 116–124. https://doi.org/10.1016/j.colsurfa.2017.05.084.
5. S. Ni, E. Marini, I. Buttinoni, H. Wolf, L. Isa, Rational design and fabrication of versatile active colloidal molecules. arXiv preprint. (2017) 1701.08061 https://doi.org/10.48550/arXiv.1701.08061.
6. M. Zanini, I. Lesov, E. Marini, C.P. Hsu, C. Marschelke, A. Synytska, S. E. Anachkov, L. Isa. Detachment of rough colloids from liquid-liquid interfaces. Langmuir. 34 (2018) 4861-4873. https://doi.org/10.1021/acs.langmuir.8b00327.

Posters

1. E. Marini, S. Ni, I. Buttinoni, H. Wolf, L. Isa. Fabrication of hybrid colloidal clusters and investigation of their motion under electric field, SAOG, Basel, Switzerland, 2016.
2. E. Marini, C. Evangelisti, L. Jörissen. A bifunctional air electrode with a carbon free active layer for rechargeable zn-air batteries. GDCh- Wissenschaftsforum Chemie 2017, Berlin, 2017.
3. E. Marini, M. Steininger, S. Brimaud, C. Evangelisti, L. Jörissen. Changes in the preparation route of alpha-MnO2/C and resulting modification in ORR activity and selectivity in alkaline solution. GDCh- Electrochemistry 2018, Ulm, 2018.
4. E. Marini, M. Steininger, S. Brimaud, C. Evangelisti, L. Jörissen. Ternary-based composite as efficient and durable catalyst layer for alkaline reversible gas diffusion electrodes. 16th Ulm ElectroChemical Talks (UECT), Ulm, 2018.

Oral Contributions

1. E. Marini, S. Brimaud, C. Evangelisti, L. Jörissen. A Comparative Study of Catalyst-Support Material Synergies for Secondary Alkaline Metal-Air Batteries. Symposium: Behyond Lithium-Ion Batteries, AiMES Meeting, Cancun, 2018.

2. E. Marini, M. Steininger, P. Schoch, B. Bozzini, L. Jörissen, S. Brimaud. Rational Design towards a Durable, Efficient and Cost-Effective Reversible Air Electrode. Symposium on Insights into Gas Diffusion Electrodes: From Fundamentals to Industrial Applications, Magdeburg, 2019.